Performance Prediction of a Ducted Rocket Combustor*

R.A. Stowe
Defence Research Establishment Valcartier

** A doctoral thesis submitted to Laval University*

Defence Research Establishment Valcartier

Technical Report

DREV TR 2001-200

November 2001

Author

Robert A Stowe

R.A. Stowe

Approved by

G. Dumas

Head, Precision Weapons Section

Approved for release by

G. Dumas

Head, Precision Weapons Section

ROBERT STOWE

PERFORMANCE PREDICTION OF A DUCTED ROCKET COMBUSTOR

Thèse
présentée
à la Faculté des études supérieures
de l'Université Laval
pour l'obtention
du grade de Philosophiae Doctor (Ph.D.)

Département de génie mécanique
FACULTÉ DES SCIENCES ET DE GÉNIE
UNIVERSITÉ LAVAL
QUÉBEC

AOÛT 2001

UNIVERSITÉ LAVAL

Faculté des études supérieures

ATTESTATION

Ce 27e jour du mois de juillet ~~19~~ 2001, les personnes soussignées, en leur qualité de membres du jury de la thèse de Robert A. Stowe, ont assisté à la soutenance de cette thèse.

NOMS	UNIVERSITÉ	SIGNATURE
Alain De Champlain	Laval	
Detlef Kretschmer	Laval	
Michael Bardon	RMC	
Donald Gauthier	Carleton	
Guy Gadiot	Netherland Agency for Aerospace	

SIGNATURE DU PRÉSIDENT DE LA SOUTENANCE

Résumé Long

Le statofusée est un système de vol à propulsion supersonique qui prend l'échappement d'un générateur à gaz, le mélange avec de l'air, et le fait réagir dans un foyer de combustion à statoréacteur afin de produire de la poussée. Il y a beaucoup d'avantages par rapport aux moteur-fusées à propergol solide incluant une portée améliorée, une vitesse plus élevée et la capacité de varier sa poussée, mais il est plus simple que les systèmes aérobies à carburant liquide comme les turbines à gaz. Par le passé, les systèmes de vol à propulsion ont été développés avec beaucoup d'essais. Toutefois, pour réduire les coûts de développement, de plus en plus des modèles numériques ont étés développés pour concevoir, analyser, et prédire la performance. Récemment, des modèles numériques basés sur la simulation numérique des fluides (CFD) sont devenus très populaires, mais leur développement pour les écoulements réactifs pose toujours un défi important, et il faut porter attention à chaque application et bien la valider.

Une telle application est le statofusée à carburant solide, et jusqu'à date personne n'a développé aucun modèle de performance compréhensif qui tient compte, de façon rigoureuse, de tous les constituants de l'échappement du générateur à gaz. Par une étude approfondie des lois qui régissent la dynamique des fluides et la combustion, et des données expérimentales, une méthode basée sur le CFD a été développée pour prédire la performance du foyer de combustion d'un statofusée. Elle utilise un modèle de combustion préconisant l'équilibre chimique mais avec une fonction de densité des probabilités (PDF) pour tenir compte de l'influence de la turbulence, pour deux écoulements de carburant, l'un qui est gazeux et l'autre qui est solide. Basé sur des mesures de l'échappement du générateur à gaz, l'écoulement solide a été injecté dans le foyer comme des sphères en carbone de diamètre de 75 nm qui se décomposaient en oxyde de carbone, avec le taux contrôlé par des réactions chimiques à la surface. Afin de valider la méthode, la visualisation dans un tunnel

hydraulique et des expériences de combustion à connexion-directe ont été effectuées pour beaucoup de géométries et de conditions variées. L'incertitude expérimentale a aussi été étudiée de façon détaillée pour les expériences de combustion. Pour les configurations considérées, cette méthode basée sur le CFD pouvait prédire, avec une bonne précision, le rendement de combustion dans le foyer d'un statofusée.

Alain De Champlain, Ph.D.
Directeur de recherche

Detlef Kretschmer, D.Sc.
Codirecteur de recherche

Robert A. Stowe, M.Sc.A.
Étudiant gradué

Extended Abstract

The ducted rocket is a supersonic flight propulsion system that takes the exhaust from a solid fuel gas generator, mixes it with air, and burns it in a ramjet combustor to produce thrust. It has several advantages over solid propellant rocket motors including increased range, higher speed, and throttleability, and is much simpler than airbreathing liquid fuel systems such as gas turbines. In the past, flight propulsion systems have been developed through experimentation and trial and error. However, to reduce development costs more and more effort has been put into developing numerical models to design, analyze, and predict performance. Lately, numerical models based on Computational Fluid Dynamics (CFD) have become increasingly popular, but the development of these for reacting flow still poses a significant challenge, and each application requires specific attention and validation.

One such application is the solid fuel ducted rocket, and to date no comprehensive performance prediction model has been developed that properly accounts for all the components in the gas generator exhaust. Through a careful examination of the governing equations and experimental measurements, a CFD-based method was developed to predict the performance of a ducted rocket combustor. It uses an equilibrium-chemistry Probability Density Function (PDF) combustion model, with separate gaseous and solid phase fuel streams. Based on measurements of the gas generator exhaust, the solid stream was injected into the combustor as 75 nm diameter carbon spheres that gradually decomposed into carbon monoxide due to surface oxidation. To validate the method, water tunnel visualization and direct-connect combustion experiments were performed over a wide range of geometries and test conditions. A comprehensive assessment of experimental uncertainty was also carried out for the direct-connect experiments. For the configurations consid-

ered, this CFD-based method was able to predict, within a good degree of accuracy, the combustion efficiency of a ducted rocket combustor.

Alain De Champlain, Ph.D.
Research Supervisor

Detlef Kretschmer, D.Sc.
Research Co-Supervisor

Robert A. Stowe, M.A.Sc.
Graduate Student

Résumé

Le statofusée est un système de vol à propulsion supersonique qui prend l'échappement d'un générateur à gaz, le mélange avec de l'air, et le fait réagir dans un foyer de combustion à statoréacteur afin de produire de la poussée. Pour développer ces systèmes, des modèles numériques basés sur la simulation numérique des fluides (CFD) sont devenus très populaires, mais leur développement pour les écoulements réactifs pose toujours un défi important, et il faut porter attention à chaque application et bien la valider. Par une étude approfondie des lois qui régissent la dynamique des fluides et la combustion, et des données expérimentales, une méthode basée sur le CFD a été développée pour prédire la performance du foyer de combustion d'un statofusée. Elle utilise un modèle de combustion préconisant l'équilibre chimique mais avec une fonction de densité des probabilités (PDF) pour tenir compte de l'influence de la turbulence, pour deux écoulements de carburant, l'un qui est gazeux et l'autre qui est qui est composé des sphères solides en carbone de diamètre de 75 nm. Après avoir validé la méthode avec la visualisation dans un tunnel à eau et des expériences de combustion à connexion-directe pour beaucoup de géométries et de conditions variées, cette méthode basée sur le CFD pouvait prédire, avec une bonne précision, le rendement de combustion dans le foyer d'un statofusée.

Alain De Champlain, Ph.D.
Directeur de recherche

Detlef Kretschmer, D.Sc.
Codirecteur de recherche

Robert A. Stowe, M.Sc.A.
Étudiant gradué

Abstract

The ducted rocket is a supersonic flight propulsion system that takes the exhaust from a solid fuel gas generator, mixes it with air, and burns it to produce thrust. To develop such systems, the use of numerical models based on Computational Fluid Dynamics (CFD) is increasingly popular, but their application to reacting flow requires specific attention and validation. Through a careful examination of the governing equations and experimental measurements, a CFD-based method was developed to predict the performance of a ducted rocket combustor. It uses an equilibrium-chemistry Probability Density Function (PDF) combustion model, with a gaseous and a separate stream of 75 nm diameter carbon spheres to represent the fuel. After extensive validation with water tunnel and direct-connect combustion experiments over a wide range of geometries and test conditions, this CFD-based method was able to predict, within a good degree of accuracy, the combustion efficiency of a ducted rocket combustor.

Alain De Champlain, Ph.D.
Research Supervisor

Detlef Kretschmer, D.Sc.
Research Co-Supervisor

Robert A. Stowe, M.A.Sc.
Graduate Student

Foreword

The work contained in this thesis was carried out over several years while I was employed as a defence scientist at the Defence Research Establishment Valcartier (DREV). I would like to thank DREV and Defence R&D Canada for the opportunity and support to do this, and in particular my supervisors Christian Carrier, Ghislain Dumas, and Phil Twardawa. I am very grateful for the technical assistance of my colleagues at DREV, including Christian Watters, Jean-Guy Hervieux, Daniel Gilbert, Michel Côté, Dr. Charles Dubois, Rémy Coulombe, Gaston Nadeau, and Sophie Ringuette, as well as the help of several students with the water tunnel visualization, including Mark Dijkstra, Sander Niemeijer, Van Au, Frédéric Couture, and Marlene Jeffries. I would also like to especially thank my fellow scientists in the Propulsion Group, Paul Harris and Rocco Farinaccio, for their help, and Dr. Jim Margetson for his expert assistance with the statistical analysis.

Much of the experimental work for this thesis was carried out in the Netherlands during a one-year scientific posting, and I would like to thank the management of DREV and Defence R&D Canada for this wonderful experience. I am also extremely grateful for the support I received from the Dutch Ministry of Defence and TNO Prins Maurits Laboratory. I would like to thank all of my friends at TNO-PML for their help, particularly Fokke Dijkstra, Pieter Elands, and Alfons Mayer.

It has been a tremendous pleasure to have Dr. Alain De Champlain as my thesis supervisor, and I thank him for taking me on as a student and helping me out over the past few years. I would also like to thank my thesis co-supervisor, Dr. Detlef Kretschmer, for his help and valuable suggestions.

Finally, I would like to thank my parents for preparing and supporting me to take advantage of opportunities that they never had, and my family for their understanding, especially over the past few months.

Robert A. Stowe

Table of Contents

Nomenclature

A	-	Arrhenius factor [(kmol/m^3)$^{(1-n)}$/s]
A	-	Area (with a subscript) [m^2]
a	-	factor dependent on Reynolds number
B	-	body force per unit volume [N/m^3]
C_D	-	drag coefficient
C_d	-	constant for transport of the mixture fraction variance
C_g	-	constant for transport of the mixture fraction variance
C^*	-	characteristic velocity [m/s]
C_1	-	constant for diffusion controlled surface reaction rate [kg/(m·s·Pa·K$^{0.75}$)]
$C_{1\varepsilon}$	-	constant for RNG turbulence model
C_2	-	constant for surface kinetics controlled surface reaction rate [kg/(m^{2}s·Pa·K)]
$C_{2\varepsilon}$	-	constant for RNG turbulence model
C_μ	-	constant for RNG turbulence model
C_ν	-	constant for RNG turbulence model
c_D	-	nozzle discharge coefficient
c_p	-	constant pressure specific heat [J/(kg·K)]
D	-	binary diffusion coefficient [m^2/s]
$Dam1$	-	Damköhler's first dimensionless ratio
$Dam2$	-	Damköhler's second dimensionless ratio
$Dam3$	-	Damköhler's third dimensionless ratio
$Dam4$	-	Damköhler's fourth dimensionless ratio
d	-	diameter of combustor or reference length [m]
E_a	-	activation energy [J/kmol]
F	-	thrust [N]
F_D	-	drag force per unit mass per unit velocity [1/s]
Fr	-	Froude number
f	-	mixture fraction
f_h	-	fraction of H_reac absorbed by particle
f_i	-	body force per unit mass, ith species or ith direction [N/kg]
$f(x_i)$	-	function of x_i

G_k	-	generation of turbulent kinetic energy due to mean velocity gradients, RNG turbulence model [kg/(m·s^2)]
g	-	gravitational acceleration [m/s^2]
$\bar{g}$	-	variance of the mixture fraction
H	-	total enthalpy (sum of all species) per unit mass [J/kg]
H_{reac}	-	heat of surface reaction per unit mass [J/kg]
h	-	static enthalpy per unit mass [J/kg]
h	-	convective heat transfer coefficient [W/(m^{2}K)]
I	-	impulse [N·s]
I_{sp}	-	specific impulse [m/s]
k	-	thermal conductivity [W/(m·K)] or turbulent kinetic energy per unit mass [m^2/s^2]
L	-	length of combustor or reference length [m]
Le	-	Lewis number
M	-	Molar mass [kg/kmol]
M_{A}	-	Coefficient of model adequacy
Ma	-	Mach number
m	-	mass [kg]
$\dot{m}$	-	mass flow rate [kg/s]
Nu	-	Nusselt number
n	-	reaction order
O/F	-	Oxidizer/Fuel ratio
Pr	-	Prandtl number
p	-	static pressure [Pa] or partial fraction
$p(f)$	-	Probability Density Function
Q	-	heat generation per unit volume [J/m^3]
Q_R	-	stoichiometric heat of reaction per unit mass [J/kg]
q	-	heat flux [W/m^2]
q'	-	standard specific enthalpy difference between products and reactants at T_{ref} and constant pressure [J/kg]
R	-	gas constant ($\bar{R}/M$) [J/(kg·K)]
$\bar{R}$	-	universal gas constant [J/(kmol·K)]
R_{RNG}	-	term in RNG turbulence model
R_1	-	diffusion controlled surface reaction rate [kg/(m^{2}s·Pa)]
R_2	-	surface kinetics controlled surface reaction rate [kg/(m^{2}s·Pa)]
Re	-	Reynolds number
S	-	source
Sc	-	Schmidt number
S_h	-	energy sources (for energy equation used for non-adiabatic PDF models)
S_{ij}	-	strain rate tensor
S_{L}	-	laminar burning velocity [m/s]
S_m	-	mass sources (for generalized continuity equation)

T	-	static temperature [K]
T_{L}	-	fluid Lagrangian integral time [s]
t	-	time [s]
U	-	characteristic reaction frequency [1/s]
u	-	velocity component in the x-direction or ith direction [m/s] or internal energy per unit mass [J/kg]
v	-	velocity component in the y-direction [m/s] or velocity [m/s]
w	-	velocity component in the z-direction [m/s] or absolute uncertainty in the subscripted variable [relevant units]
x	-	independent variable
x, y, z	-	direction [m]
Y	-	mass fraction
y	-	experimental value
$\hat{y}$	-	predicted value
Z	-	elemental mass fraction
α_k	-	inverse effective Prandtl number due to turbulent kinetic energy, RNG turbulence model
α_s	-	swirl constant, RNG turbulence model
α_ε	-	inverse effective Prandtl number due to dissipation, RNG turbulence model
β	-	constant in RNG turbulence model
γ	-	ratio of specific heats
δ_{ij}	-	Kronecker delta
ε	-	dissipation per unit mass [m^2/s^3] or progress of reaction
ζ	-	normally-distributed random number
η	-	term in RNG turbulence model
η_0	-	constant in RNG turbulence model
$\eta_{\Delta \mathrm{T}}$	-	efficiency based on temperature rise in the combustor
μ	-	dynamic viscosity [kg/(m·s)]
ν	-	kinematic viscosity [m^2/s]
$\hat{\nu}$	-	term in RNG turbulence model
ρ	-	density [kg/m^3]
σ_t	-	constant for transport of the mixture fraction variance
τ	-	stress [N/m^2]
τ_e	-	characteristic eddy lifetime [s]
τ_i	-	fraction of time f lies between f and $f + \Delta f$ [s]
ϕ	-	conserved quantity
Ψ	-	ratio of kinetic energy to internal energy
Ω	-	characteristic swirl number, RNG turbulence model
ω	-	mass rate of production per unit volume by chemical reaction [$kg/(m^3s)$]

Subscripts and superscripts

a	-	air
D	-	drag
eff	-	effective
exp	-	experimental
f	-	fuel, flame
i	-	ith direction, function, species, or variable
ign	-	ignition
j	-	jth direction
k	-	kth direction
m	-	model
N	-	number
ox	-	oxidizer
p	-	particle or prototype
prop	-	propellant
reac	-	reaction
ref	-	reference
sec	-	secondary
stoich	-	stoichiometric
t	-	stagnation (for pressure, temperature) or turbulent (for viscosity, thermal conductivity)
theo	-	theoretical
tot	-	total
u	-	unburned
vitair	-	vitiated air
x, y, z	-	direction
$*$	-	asterisk denotes non-dimensionalized quantity
$\overline{}$	-	overline denotes time-averaged value
$'$	-	prime denotes instantaneous value
Note	-	other variables and quantities previously defined may also be subscripts

Station numbering subscripts

∞	-	freestream
0	-	immediately upstream of the inlet shocks
1	-	at the entrance to the inlet (where internal flow starts)
2	-	end of the inlet diffuser
3	-	head end of the combustor
4	-	end of the combustor just upstream of the nozzle
5	-	nozzle throat
6	-	nozzle exit

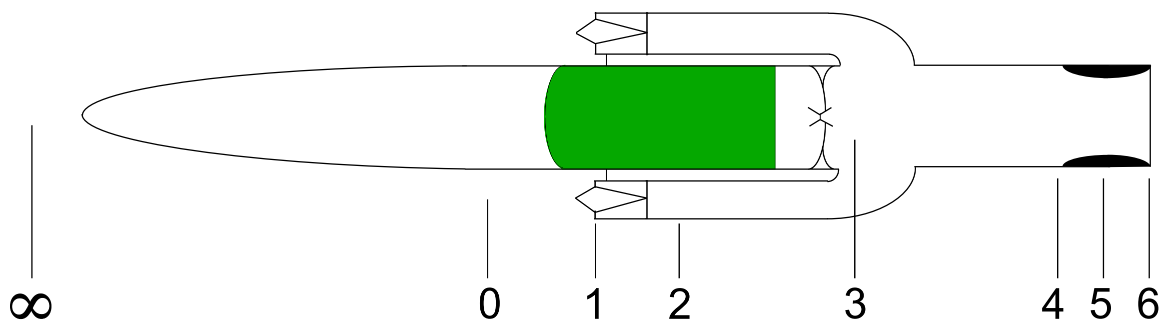

Figure 1: Ducted rocket station numbering

Acronyms

AP	-	ammonium perchlorate
ASM	-	Algebraic Reynolds Stress Model
CFD	-	Computational Fluid Dynamics
DC	-	direct-connect
DNS	-	Direct Numerical Simulation
DREV	-	Defence Research Establishment Valcartier
EBU	-	Eddy Break-Up Model
FFT	-	Fast Fourier Transform
GAP	-	glycidyl azide polymer
LDV	-	Laser Doppler Velocimetry
N-S	-	Navier-Stokes
NAWC	-	U.S. Naval Air Warfare Center
NSC	-	Nagel-Strickland-Constable
PDF	-	Probability Density Function
RNG	-	Renormalized Group Theory
RSM	-	Reynolds Stress Model
SCMC	-	Sonic Control and Measuring Choke
SEM	-	scanning electron microscope
SFRJ	-	solid fuel ramjet
TNO-PML	-	The Netherlands Organization for Applied Scientific Research, Prins Maurits Laboratory
WT	-	water tunnel

List of Figures

List of Tables

Chapter 1

INTRODUCTION

1.1 Background: Rockets and Ramjets

For hundreds of years, man has used the combustion of solid chemicals to propel rockets. In fact, the Chinese flew the first rockets around 1150 AD [1] with gunpowder as the propellant. Since then, development of the solid propellant rocket for military use took place all over the world and by the time of the War of 1812 rockets were capable of 3 km ranges [2]. During the twentieth century, the solid propellant rocket evolved into a highly reliable and powerful propulsion system capable of sending payloads anywhere on earth and into space.

The main components of a modern composite solid propellant rocket, known simply as a solid rocket, are shown in Fig. 1.1. The propellant consists of oxidizer and possibly fuel particles, all bound together by a rubbery polymer that also acts as a fuel. The propellant is cast into a grain that is housed within a structural casing. The grain shown is hollow in the middle so, once ignited, the propellant burns from the inner surface outwards to the casing. A nozzle at the tail end of the rocket accelerates the combustion products toward the rear to produce forward thrust.

The performance of a rocket propellant is often described by its specific impulse, I_{sp}, which is the impulse of the rocket per unit mass of the propellant or, at any instant in time, the thrust produced per unit mass flow rate of propellant:

$$I_{\text{sp}} = \frac{I_{\text{tot}}}{m_{\text{prop}}} = \frac{F}{\dot{m}_{\text{prop}}} \tag{1.1}$$

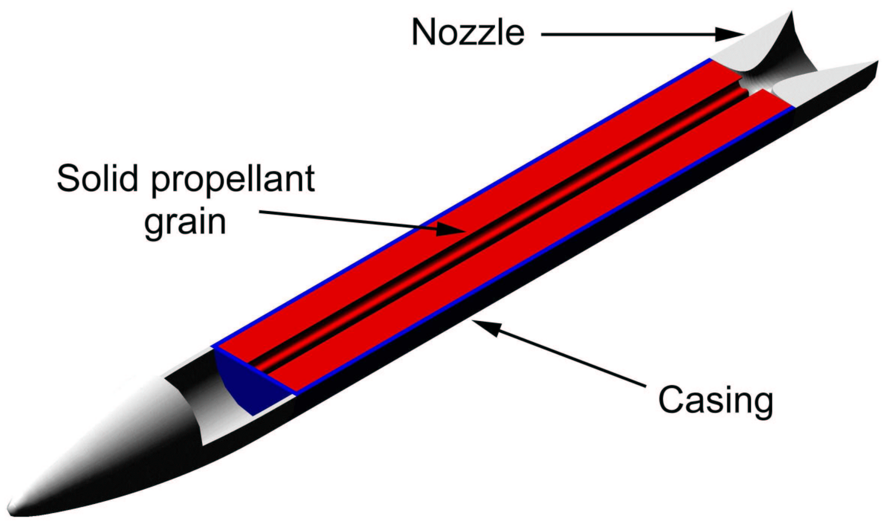

Figure 1.1: Modern solid rocket

For the composite propellant shown in Table 1.1, the theoretical I_{sp}[1] is approximately 2 500 m/s. With more energetic solid compounds, this can be improved to about 3 000 m/s, and a theoretical I_{sp} of approximately 4 500 m/s is attainable with liquid fuels and oxidizers. Because of this greater performance, as well as the ability to throttle their thrust and restart once extinguished, not possible with solid rockets, liquid fuel rockets are used to send very large payloads into space. However, their added cost and complexity mean that solid rockets still dominate atmospheric flight and military applications.

Table 1.1: Typical solid rocket propellant formulation

Ingredient	Mass fraction
Hydroxyl-terminated polybutadiene (binder)	0.12
Ammonium perchlorate (oxidizer)	0.70
Aluminum (fuel)	0.18

However, to go well beyond these values of specific impulse of even liquid propellants and to increase range dramatically, a propulsion system must take advantage of the air through which it travels to burn the fuel on board, rather than carrying

[1] "Theoretical" I_{sp} is the value calculated for perfect expansion of the combustion products from a chamber pressure of 1 000 psi (6.895 MPa) to atmospheric pressure at sea level.

an oxidizer. Such a propulsion system is termed “airbreathing”, the best known example being the gas turbine or jet engine. Its basic thermodynamic cycle includes compression of the incoming air, the addition of heat at high pressure, and subsequently the expansion of hot fluid to produce work. In a gas turbine engine, the compression of the incoming air is achieved with mechanical compressors, which means that these devices are relatively costly and complex. Furthermore, the fuel used in flight applications is usually liquid which requires pumps, valves, injectors, and related equipment. As the flight speed of a turbine-powered aircraft increases, though, mechanical compression of the incoming air becomes less and less necessary since the slowing of the air within the intake will raise its static pressure. In fact, as supersonic speeds are reached, the mechanical compressor and associated turbine can be eliminated. Such an engine without these components is called a ramjet.

The first ramjet-powered aircraft appeared during the 1950’s, the best known of these in Canada being the Bomarc air-defence missile. They all used liquid fuel, so while they were mechanically simpler than gas turbines, they still needed complicated fuel delivery systems. Many applications, however, require the inherent simplicity and reliability of solid rockets. There are solid fuel ramjets (SFRJ), but because the fuel delivery rate depends so heavily on the mass flow rate of the incoming air, they are difficult to design for a wide range of flight conditions and are used in very limited rôles. However, a practical compromise between liquid and solid fuel ramjets does exist in the form of the ducted rocket, also known as a ramrocket or integral rocket ramjet.

Figure 1.2 shows the components of a typical ducted rocket. It differs from other types of ramjets with its use of a gas generator to supply the fuel for combustion with the incoming air. This gas generator contains a fuel grain that is essentially binder, but may contain fuel particles, such as carbon or boron, and possibly some

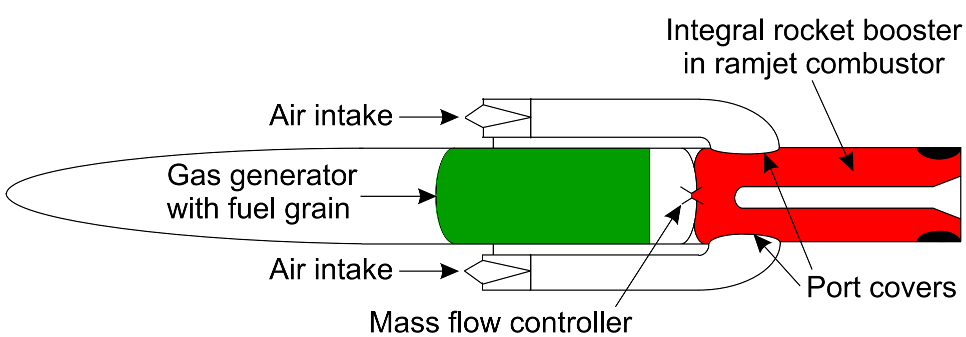

Figure 1.2: Components of a ducted rocket

oxidizer particles. The purpose of this gas generator fuel is not to directly produce thrust to propel the ducted rocket, but to decompose into a fuel-rich exhaust which can be efficiently mixed with air and burned. This exhaust not only contains gases of a wide range of molar masses, but a substantial amount of solids such as soot particles. In Fig. 1.2 the fuel grain is shown in a typical end-burner or "cigarette" configuration, as opposed to the centrally-perforated propellant grain of Fig. 1.1 which most solid rockets use. Also shown is a mass flow controller, which can throttle the gas generator exhaust to vary the thrust of the ducted rocket like liquid fuel propulsion systems, but unlike solid rockets.

The other main components include the air intakes, port covers, and the integral booster in the ramjet combustor. Their functions are best explained with reference to Fig. 1.3 which shows the phases of a ducted rocket's operation. As previously mentioned, a typical ramjet operates at supersonic speed so, if launched from rest or at subsonic speed, a means of accelerating it is needed, hence the solid rocket booster integrated into the ramjet combustor. After launch, the boost phase commences, characterized by the combustion of the rocket propellant and port covers sealing the ramjet combustor from the air intakes. Once the booster propellant is completely burned to leave an empty ramjet combustor, transition to the ramjet phase occurs. The port covers that seal the air intakes from the ramjet combustor open and, simultaneously, the gas generator ignites. Fuel-rich exhaust from the gas generator is mixed with incoming air in the ramjet combustor, reacts, and is accelerated through a nozzle to provide thrust.

By considering the ideal ramjet cycle, the theoretical specific impulse of a ducted rocket can be shown to be much higher than a rocket. The ideal ramjet cycle [3] includes isentropic compression of the incoming air, constant pressure addition of fuel and therefore heat in the combustor, and finally isentropic expansion of the exhaust products. For one-dimensional flow, constant specific heats, and perfect expansion of the exhaust to atmospheric pressure, the specific thrust is:

$$\frac{F}{\dot{m}_{\mathrm{a}}} = Ma\sqrt{\gamma R T_\infty}\left[\sqrt{\frac{\frac{T_{\mathrm{t4}}}{T_\infty}}{1+\frac{\gamma-1}{2}Ma^2}}-1\right] \tag{1.2}$$

and assuming that the velocity in the combustion chamber can be neglected and the fuel mass flow rate is much smaller than the air mass flow rate. T_∞ is the freestream static temperature and T_{t4} is the stagnation temperature in the combustor (just before the nozzle).

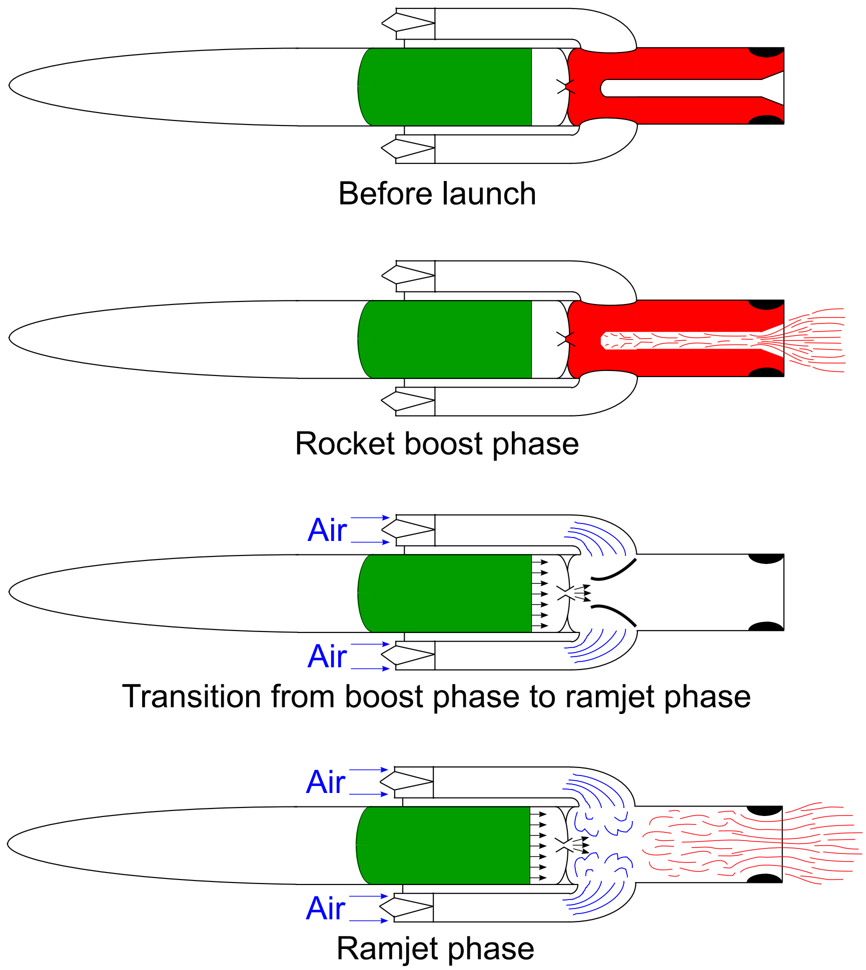

Figure 1.3: Phases of operation of a ducted rocket

Since the oxidizer is not carried on board the ramjet, the thrust should be divided by the mass flow rate of only the fuel, not the fuel *and* oxidizer as for the solid rocket. The specific thrust is therefore divided by the fuel/air ratio to get the I_{sp} of the ramjet:

$$I_{\mathrm{sp}} = \frac{F}{\dot{m}_{\mathrm{f}}} = \frac{F}{\dot{m}_{\mathrm{a}}} \frac{\dot{m}_{\mathrm{a}}}{\dot{m}_{\mathrm{f}}} \tag{1.3}$$

However, we need an expression for the fuel/air ratio. For a constant heat of reaction Q_R (no dissociation of the exhaust products), T_∞, and T_{t4}, the fuel/air ratio varies with the freestream stagnation temperature $T_{\mathrm{t}\infty}$ (and therefore flight speed). The expression is [2]:

$$\frac{\dot{m}_{\mathrm{f}}}{\dot{m}_{\mathrm{a}}} = \frac{\left(\frac{T_{\mathrm{t4}}}{T_{\mathrm{t}\infty}}\right) - 1}{\left(\frac{Q_R}{c_p T_{\mathrm{t4}}}\right) - \left(\frac{T_{\mathrm{t4}}}{T_{\mathrm{t}\infty}}\right)} \tag{1.4}$$

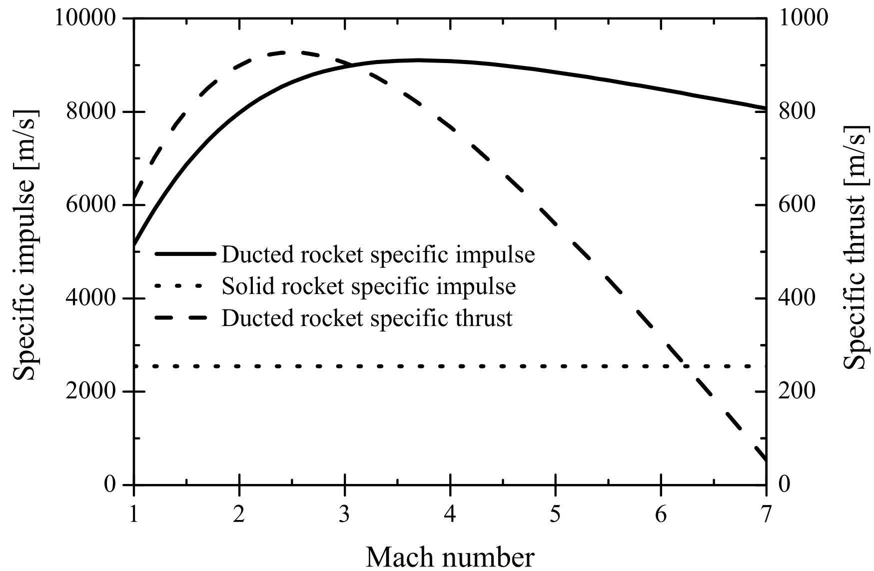

Figure 1.4: Comparison of theoretical performance, ducted rocket and solid rocket

Results for the theoretical I_{sp} of a solid rocket and a ducted rocket are shown in Fig. 1.4. The solid rocket uses the propellant listed in Table 1.1, while the ducted rocket uses a gas generator fuel of 90% glycidyl azide polymer (GAP) and 10% carbon black by mass to give an estimated Q_R of 21.3 MJ/kg. Other constants used in the equations are a c_p of 1 005 J/(kg·K), a γ of 1.4, a T_∞ of 220 K, and a T_{t4} of 2 500 K. While these are only theoretical results, real ducted and solid rockets display similar behaviour. The I_{sp} of the ducted rocket varies greatly with flight speed; it is low at Mach 1, peaks at Mach 3.7, and then falls off. The I_{sp} of the solid rocket does not depend on flight speed, but is always much lower than the ducted rocket at the speeds shown. Another important point shown on the graph, however, is that even though the I_{sp} of the ramjet is still considerably higher than the solid rocket at flight speed greater than Mach 6, its specific thrust begins to approach zero. This is because $T_{\mathrm{t}\infty}$ approaches T_{t4} so less and less fuel is needed, but there is also less and less thrust being produced. In fact, the practical limit on flight speed of a real ramjet is also Mach 6 or Mach 7, beyond which a supersonic combustion ramjet, or “scramjet” is used.

The greater specific impulse of the ducted rocket results in a propulsion system capable of much higher average speeds over vastly increased ranges than a solid rocket of similar size. While it is somewhat more mechanically complex than a solid rocket with its port covers and possibly a fuel mass flow controller to vary its thrust on demand, its use of a solid fuel means it is much simpler and therefore potentially more reliable than liquid fuel propulsion systems. Despite this, the ducted rocket has been the object of only a few development efforts and even fewer are in service. However, because of its advantages over other propulsion systems, it has enjoyed much renewed interest lately.

1.2 Research Challenges

In the past, propulsion systems have been largely developed through experimentation and trial and error. However, to reduce development costs, more and more effort has been put into building models to design, analyze, and predict propulsion system performance. Years ago, models of propulsion systems used mainly experimental techniques such as scale models and water tunnel visualization, and any numerical models were analytical or based largely on empirical data. Lately, numerical models based on Computational Fluid Dynamics (CFD) have become increasingly important, first for non-reacting flows, but now for reacting flows as well. The non-reacting flow aspect of CFD has been well validated, and special forms of the conservation equations for mass, momentum, and energy (commonly referred to as the Navier-Stokes equations) and certain turbulence models are commonly used for a wide range of applications. However, the development of accurate combustion models for CFD still poses a significant challenge, and each application requires specific attention and validation. To complicate matters, point measurements of fundamental data such as compositions, temperatures, and velocities within the hostile environment of combustors are very difficult to achieve, so CFD validation often relies on "bulk" measurements such as combustor pressure and thrust.

Because of their wide use amongst airbreathing flight propulsion systems, gas turbines have dominated research into combustion models and performance prediction. Many of the models and techniques applicable to gas turbine combustors can and have been used for other liquid fuel propulsion systems such as liquid fuel ramjets. Some of these models and techniques may also be applicable to ducted rockets, particularly those for the non-reacting flow through the intakes. Unfortunately, the available literature has only revealed simplistic treatments of the combustion within ducted rocket combustors, likely due to the difficulties in characterizing and modelling the partially reacted, particle-laden fuel exhaust from the gas generator, and none that specifically address the trajectories and decomposition of the particles in the flowfield. Because of the substantial mass fraction of solids in the gas generator exhaust, however, particles should be modelled in any prediction of combustor performance. The purpose of this thesis is therefore expressed in the following statement:

> Through a careful examination of the governing equations and experimental measurements, to develop a method based on CFD to predict the performance of a ducted rocket combustor that properly accounts for influence of the gas generator exhaust, particularly the solid phase, and validate it over a wide range of geometries and test conditions.

1.3 Scope

The development of the method to predict the performance of a ducted rocket combustor can be organized into five distinct parts. This thesis has therefore been organized into five chapters as follows:

- **Rules for combustor modelling.** Conservation equations for mass, momentum, and energy were non-dimensionalized to identify the important dimensionless parameters and establish rules for reacting flow CFD modelling. Once combined with the expected environment in a ducted rocket combustor, this helped identify what was critical to the development of a method to predict performance, and how experiments should be set up to provide test data for validation.

- **Water tunnel visualization.** Combustor geometries and test conditions identified from previous experiments in the available literature were used to create a set of configurations for water tunnel visualization. After having developed a suitable visualization technique, images for each configuration were captured and analyzed.

- **Non-reacting flow modelling.** The same geometries and test conditions used for the water tunnel visualization were modelled with a CFD code, and qualitative comparisons made of the fuel distribution in the combustor for validation purposes.

- **Direct-connect combustion experiments.** These were done for a set of geometries and test conditions that was geometrically and dynamically similar to the water tunnel experiments. Combustor performance was calculated from the data for each of the configurations. An analysis of high-frequency pressure data was also carried out, as was an estimate of experimental uncertainty.

- **Reacting flow modelling.** Two different combustion models were implemented in a CFD code, the first that treated the gas generator exhaust as a single stream, and the second that treated the exhaust as separate gaseous and particle streams. For the latter, an existing model of particle decomposition was adapted using results from experimental characterization of the particles and soot oxidation. The predictions of combustor performance were compared with the experimental results to validate the method.

Chapter 2

RULES FOR COMBUSTOR MODELLING

2.1 Scaling

As stated in the introduction, this thesis will present a CFD-based method to predict the performance of a ducted rocket combustor and validate it over a wide range of geometries and test conditions. An important first step for any type of combustor modelling, be it CFD-based or experimental, is to deduce a set of rules that can be established by deriving the relevant dimensionless parameters that should be respected between the model and the actual combustor [4]. This can be accomplished through dimensional analysis and the examination of the conservation equations for mass, momentum, and energy. For CFD modelling the geometry is usually reproduced as a full-size mesh and the boundary and test conditions reproduced as accurately as possible, so respecting most of these dimensionless parameters is already accomplished. Before the use of CFD for modelling reacting flow became widespread, however, the rules for combustor modelling were established mainly for experimental scale modelling. In fact, the best references describing dimensionless parameters for combustor modelling did indeed pertain to scale modelling. While not the principal objective of this thesis, the establishment of scaling rules to determine geometries and test conditions for the water tunnel and direct-connect combustion experiments did reveal which dimensionless parameters were crucial in the development of a CFD-based method to predict performance of ducted rocket combustors, and showed which aspects demanded special attention. An additional benefit is to establish the extent to which the experimental data and modelling techniques generated for this thesis could be applied to different size combustors and test conditions.

The main purpose of scale modelling is to allow direct comparison of test results from similar geometries of different sizes and different fluid properties, and thoroughly describe the phenomena over a wide range of test conditions. It allows experiments to be designed in such a way as to facilitate measurements and explore conditions not normally possible. Scale models of the geometries of interest can be built and, through the use of different fluids, pressures, and velocities, the same flow phenomena that occur in the full-size geometries can be accurately reproduced. This is often done because of test facility limitations and economic reasons. While usually associated with non-reacting flows, the use of dimensionless parameters and scale modelling can also be applied to reacting flows. Chemical kinetics, species transport, and thermal processes must therefore be added to the list of dimensionless parameters to describe combusting flows properly. Dimensional analysis and scale modelling of reacting flows have been applied to gas turbine [5, 6], liquid fuel ramjet [7, 8, 9], solid fuel ramjet [10], and scramjet [11] combustors, so this should also be possible for ducted rocket combustors.

Exactly which dimensionless parameters should be applied to the design of the experiments and the development of models requires a thorough knowledge of the relevant physical and chemical processes inside the combustors. For "complete" modelling of a combustor, the chosen dimensionless parameters must represent four classifications of similarity between the model and the full-size combustor; these are geometric, dynamic, thermal, and compositional similarities [12]. Geometric similarity means that all dimensions in the model are linearly related to each other in the same ratios as in the full-size combustor. For example, the L/d ratios for both the model and full-size combustors must be identical. Geometric similarity is also a prerequisite for dynamic, thermal, and compositional similarity within combustors. Dynamic similarity requires that the ratio of the dynamic pressures at corresponding points within the model and full-size combustors be constant [13]. This also implies that the ratios of the velocities at corresponding points must also be constant. For many non-reacting, isothermal flow experiments such as those proposed for the water tunnel, geometric and dynamic similarity are respected. However, combustion results in the production of temperature gradients and new chemical species so complete modelling requires that thermal and compositional similarity must also be respected. Corresponding ratios of temperature differences and chemical species concentrations must therefore be constant between any two points in the model and the full-size combustors. In general, respecting all four types of similarity for complete modelling of combustors is often impossible, but "partial" modelling can be accomplished if some approximations can be made [4, 14].

2.2 Dimensionless Parameters and the Method of Similarities

Based on the results of combustor modelling described in [5-11], partial modelling should be possible with an accurately-scaled geometry and a careful choice of operating conditions. Two techniques to establish the relevant dimensionless parameters that describe the geometry and operating conditions are dimensional analysis and the method of similarities.

Dimensional analysis begins with listing all the dimensional variables that describe a physical problem (velocity, pressure, viscosity, thermal conductivity, etc.) and the fundamental dimensions (length, time, mass, temperature, etc.) that appear in the dimensional variables. If there are n dimensional variables and m fundamental units, Buckingham's "Pi Theorem" states that the dimensional variables can be rearranged into $n-m$ dimensionless groups or parameters [12, 13] such as length-to-diameter ratios and Reynolds, Prandtl, and Mach numbers. For complete modelling, these dimensionless parameters must be the same for the scale model and full-size geometries.

While dimensional analysis does not require the equations that describe the physical problem to be known, some knowledge of the problem must exist in order to make a complete list of all the dimensionless variables. The main disadvantage of dimensional analysis is that the relative importance of each of the dimensionless parameters is not revealed, so some dimensionless parameters irrelevant to the problem are included. In the case of combustion problems with an extensive list of dimensional variables, dimensional analysis would generate several irrelevant dimensionless parameters, and much effort could be wasted in trying to respect them and ensure complete modelling. With the method of similarities [14] background knowledge and the equations that describe the problem can be exploited to identify the most important dimensionless parameters and therefore reduce the number of dimensionless parameters needed for accurate modelling.

2.3 Similitude in Combustion

A classic work on similitude for flow systems that include chemical reactions and heat transfer was written by Damköhler [15] and is detailed in [16, 17]. Damköhler proposed five dimensionless ratios that can be applied to combustion in general as long as velocities could be considered to be low (no compressibility effects) and there were no body forces. The five are:

$$Dam1 = \frac{rate\ of\ species\ formation\ by\ reaction}{rate\ of\ species\ loss\ by\ convection}$$

$$Dam2 = \frac{rate\ of\ species\ formation\ by\ reaction}{rate\ of\ species\ loss\ by\ diffusion}$$

$$Dam3 = \frac{rate\ of\ heat\ generation\ by\ chemical\ reaction}{rate\ of\ heat\ loss\ by\ convection}$$

$$Dam4 = \frac{rate\ of\ heat\ generation\ by\ chemical\ reaction}{rate\ of\ heat\ loss\ by\ conduction}$$

$$Re = \frac{inertial\ fluid\ forces}{viscous\ fluid\ forces} = \frac{\rho v d}{\mu}$$

The continuity, momentum, and energy equations for chemical processes as written by von Kármán [18] were reported and non-dimensionalized by Penner [16]. Not only do they yield the five Damköhler ratios, but additional dimensionless parameters can be extracted that are important to combustion problems in general.

2.3.1 Continuity Equation

The conservation, differential form of the continuity (conservation of mass) equation for the ith species in an infinitesimal control volume and in orthogonal coordinates following the form used by Kuo [19] is:

$$\begin{aligned} \underbrace{\rho\frac{\partial Y_i}{\partial t}}_{local\ change} \quad + \quad & \underbrace{\rho u\frac{\partial Y_i}{\partial x} + \rho v\frac{\partial Y_i}{\partial y} + \rho w\frac{\partial Y_i}{\partial z}}_{convection} \\ = \quad & \underbrace{\frac{\partial}{\partial x}\left(\rho D\frac{\partial Y_i}{\partial x}\right) + \frac{\partial}{\partial y}\left(\rho D\frac{\partial Y_i}{\partial y}\right) + \frac{\partial}{\partial z}\left(\rho D\frac{\partial Y_i}{\partial z}\right)}_{diffusion} \quad + \underbrace{\omega_i}_{production} \end{aligned} \tag{2.1}$$

since there are diffusive as well as convective velocities. The first term is the rate of accumulation of mass of the ith species in the control volume, and the second group of terms is the transport of the ith species out of the control volume through the control surface. The third group of terms is the net inflow rate of the ith species by diffusion across the control surface into the control volume, assuming that Fick's law of mass diffusion applies. The fourth term is the rate of production of the ith species inside the control volume by homogeneous chemical reactions. This equation, as well as the momentum and energy equations that will follow, are non-dimensionalized by:

$$\begin{gathered}
\rho = \rho_{\text{ref}}\rho^* \quad x = L_{\text{ref}}x^* \quad y = L_{\text{ref}}y^* \quad z = L_{\text{ref}}z^* \quad u = u_{\text{ref}}u^* \quad v = u_{\text{ref}}v^* \\
w = u_{\text{ref}}w^* \quad Y_i = Y_i^* \quad t = t^*/U_i \quad \omega_i = U_i U_i^* \rho_{\text{ref}}\rho^* Y_i^* \quad p = p_{\text{ref}}p^* \quad B_x = gB_x^* \\
f_{i,x} = gf_{i,x}^* \quad D_i = D_{\text{ref}}D^* \quad \mu = \mu_{\text{ref}}\mu^* \quad T = T_{\text{ref}}T^* \quad k = k_{\text{ref}}k^* \quad Q = Q_{\text{ref}}Q^*
\end{gathered}$$

where the "$*$" designates a non-dimensionalized quantity. The reference quantities designated "ref" are initial values for the gas mixture. After substitution and rearranging, the non-dimensionalized continuity equation is:

$$\begin{aligned}
&\frac{\partial Y_i^*}{\partial t} + \left[\frac{u_{\text{ref}}}{U_i L_{\text{ref}}}\right]\left(u^*\frac{\partial Y_i^*}{\partial x^*} + v^*\frac{\partial Y_i^*}{\partial y^*} + w^*\frac{\partial Y_i^*}{\partial z^*}\right) \\
&= \left[\frac{D_{\text{ref}}}{U_i L_{\text{ref}}^2}\right]\left(\frac{\partial}{\partial x^*}\left(\rho D^*\frac{\partial Y_i^*}{\partial x^*}\right) + \frac{\partial}{\partial y^*}\left(\rho D^*\frac{\partial Y_i^*}{\partial y^*}\right) + \frac{\partial}{\partial z^*}\left(\rho D^*\frac{\partial Y_i^*}{\partial z^*}\right)\right) + U_i^* Y_i^*
\end{aligned} \tag{2.2}$$

The term in front of the convective terms is the inverse of Damköhler's first dimensionless group which can also be thought of as the ratio of combustor residence time to a characteristic chemical reaction time. The term in front of the diffusion terms is the inverse of Damköhler's second dimensionless group and can be thought of as the ratio of a characteristic diffusion time to a characteristic chemical reaction time.

$$Dam1 = \frac{U_i L_{\text{ref}}}{u_{\text{ref}}} \qquad Dam2 = \frac{U_i L_{\text{ref}}^2}{D_{\text{ref}}}$$

2.3.2 Momentum Equation

The conservation, differential form of the linear momentum equation (conservation of linear momentum) in the x-direction for an infinitesimal control volume is, after expanding the general equation in tensor notation as used by Kuo [19] :

$$\underbrace{\frac{\partial\left(\rho u\right)}{dt}}_{local\ change} + \underbrace{\frac{\partial\left(\rho uu\right)}{\partial x} + \frac{\partial\left(\rho uv\right)}{\partial y} + \frac{\partial\left(\rho uw\right)}{\partial z}}_{convection}$$
$$= \underbrace{-\frac{\partial P}{\partial x} + \frac{\partial \tau_{xx}}{\partial x} + \frac{\partial \tau_{yx}}{\partial y} + \frac{\partial \tau_{zx}}{\partial z}}_{surface\ forces} + \underbrace{B_x}_{body\ forces} \quad (2.3)$$

The first term is the rate of accumulation of linear momentum in the x-direction within the control volume, and the second group of terms is the transport of linear momentum in the x-direction out of the control volume through the control surface. The third group of terms is the transfer of linear momentum by forces acting on the control surface, with the first term accounting for the hydrostatic pressure acting on the control volume. The fourth term is the sum of body forces in the x-direction acting on the species within the control volume. For a multicomponent system with N species, the body force term includes the sum of the body forces which act on each of the components:

$$B_x = \rho \sum_{i=1}^{N} Y_i f_{i,x} \quad (2.4)$$

Assuming that the fluid can be treated as a continuum and that the stress at any one point is linearly related to its rate of deformation (meaning that it is a Newtonian fluid), the normal and shear stresses on the fluid, contained within the surface force terms, can be related to the pressure and velocity components [20]. From Stoke's hypothesis, which assumes the bulk viscosity is zero, and after expanding the left-hand-side and simplifying by removing the terms in the continuity equation, the linear momentum equation in the x-direction is:

$$\rho\frac{\partial u}{dt} + \rho u\frac{\partial u}{\partial x} + \rho v\frac{\partial u}{\partial y} + \rho w\frac{\partial u}{\partial z}$$
$$= -\frac{\partial P}{\partial x} + \mu\left(\frac{4}{3}\frac{\partial^2 u}{\partial x^2} + \frac{\partial^2 u}{\partial y^2} + \frac{\partial^2 u}{\partial z^2} + \frac{1}{3}\frac{\partial^2 v}{\partial x \partial y} + \frac{1}{3}\frac{\partial^2 w}{\partial x \partial z}\right) + B_x \quad (2.5)$$

Non-dimensionalizing this equation and multiplying by $L_{\mathrm{ref}}/\rho_{\mathrm{ref}} u_{\mathrm{ref}}^2$ and adding the ratio of specific heats γ_{ref} yields:

$$\frac{U_i L_{\mathrm{ref}}}{u_{\mathrm{ref}}}\rho^*\frac{\partial u^*}{\partial t^*} + \rho^* u^*\frac{\partial u^*}{\partial x^*} + \rho^* v^*\frac{\partial u^*}{\partial y^*} + \rho^* w^*\frac{\partial u^*}{\partial z^*} = \left[\frac{\gamma_{\mathrm{ref}} p_{\mathrm{ref}}}{\rho_{\mathrm{ref}} u_{\mathrm{ref}}^2}\right]\left(\frac{-1}{\gamma_{\mathrm{ref}}}\frac{\partial p^*}{\partial x^*}\right)$$
$$+ \left[\frac{\mu_{\mathrm{ref}}}{\rho_{\mathrm{ref}} L_{\mathrm{ref}} u_{\mathrm{ref}}}\right]\mu^*\left(\frac{4}{3}\frac{\partial^2 u^*}{\partial x^{*2}} + \frac{\partial^2 u^*}{\partial y^{*2}} + \frac{\partial^2 u^*}{\partial z^{*2}} + \frac{1}{3}\frac{\partial^2 v^*}{\partial x^*\partial y^*} + \frac{1}{3}\frac{\partial^2 w^*}{\partial x^*\partial z^*}\right)$$
$$+ \left[\frac{L_{\mathrm{ref}} g}{u_{\mathrm{ref}}^2}\right]\frac{B_x^*}{\rho_{\mathrm{ref}}} \quad (2.6)$$

As with the continuity equation, Damköhler's first dimensionless group is also present, but is found here in front of the first group of terms describing the local change in linear momentum. The non-dimensionalization of this equation yields three new dimensionless groups plus the ratio of specific heats γ_{ref}. The square of the inverse of the Mach number is found in front of the pressure gradient term once it is multiplied and divided by the ratio of specific heats. The Mach number is the ratio of a characteristic velocity of the flow to the velocity of sound in the fluid, and is a measure of the importance of compressibility effects on the flow. The Reynolds number, which relates the importance of inertial forces to viscous forces, is present in front of the viscous stress terms. The dimensionless group in front of the body force term is the inverse of the Froude number, which relates the importance of inertial forces to gravitational body forces, which is usually the only body force of importance for fluid flow and combustion problems.

$$\gamma_{\mathrm{ref}} \qquad Ma = \sqrt{\frac{\rho_{\mathrm{ref}} u_{\mathrm{ref}}^2}{\gamma_{\mathrm{ref}} p_{\mathrm{ref}}}} \qquad Re = \frac{\rho_{\mathrm{ref}} L_{\mathrm{ref}} u_{\mathrm{ref}}}{\mu_{\mathrm{ref}}} \qquad Fr = \frac{u_{\mathrm{ref}}^2}{g L_{\mathrm{ref}}}$$

2.3.3 Energy Equation

The conservation, differential form of the energy equation (conservation of energy) for an infinitesimal control volume can be written in terms of enthalpy once the terms from the mechanical energy equation are subtracted and the following thermodynamic identity is used [19]:

$$u = h - \frac{p}{\rho} \quad (2.7)$$

where u is the internal energy per unit mass and h is the static enthalpy per unit mass. Assuming that only internal and kinetic energies are important, that this is a multicomponent system where Fick's law of mass diffusion holds, and that Stoke's hypothesis applies (the bulk viscosity is zero), the energy equation is:

$$
\begin{aligned}
&\underbrace{\rho\frac{\partial h}{\partial t}}_{local\ change} + \underbrace{\rho u\frac{\partial h}{\partial x} + \rho v\frac{\partial h}{\partial y} + \rho w\frac{\partial h}{\partial z}}_{convection} - \underbrace{\frac{\partial p}{\partial t} - u\frac{\partial p}{\partial x} - v\frac{\partial p}{\partial y} - w\frac{\partial p}{\partial z}}_{pressure\ terms} \\
&\quad = \underbrace{\frac{\partial Q}{\partial t}}_{volumetric\ heat\ sources} \underbrace{- \frac{\partial q_x}{\partial x} - \frac{\partial q_y}{\partial y} - \frac{\partial q_z}{\partial z}}_{heat\ conduction} \\
&\quad \underbrace{- \rho\sum_{i=1}^{N}\left(f_{i,x}D\frac{\partial Y_i}{\partial x}\right) - \rho\sum_{i=1}^{N}\left(f_{i,y}D\frac{\partial Y_i}{\partial y}\right) - \rho\sum_{i=1}^{N}\left(f_{i,z}D\frac{\partial Y_i}{\partial z}\right)}_{body\ force\ work} \\
&\quad + \underbrace{\mu\left(\begin{array}{c} 2\left(\frac{\partial u}{\partial x}\right)^2 + 2\left(\frac{\partial v}{\partial y}\right)^2 + 2\left(\frac{\partial w}{\partial z}\right)^2 + \left(\frac{\partial v}{\partial x} + \frac{\partial u}{\partial y}\right)^2 \\ + \left(\frac{\partial w}{\partial y} + \frac{\partial v}{\partial z}\right)^2 + \left(\frac{\partial u}{\partial z} + \frac{\partial w}{\partial x}\right)^2 - \frac{2}{3}\left(\frac{\partial u}{\partial x} + \frac{\partial v}{\partial y} + \frac{\partial w}{\partial z}\right)^2 \end{array}\right)}_{dissipation\ function}
\end{aligned}
\tag{2.8}
$$

The first term is the rate of accumulation of enthalpy within the control volume, and the second group of terms is the transport of enthalpy out of the control volume through the control surface. The pressure terms are present because of the thermodynamic identity for internal energy that was exploited. The fourth term is the rate of heat produced within the control volume by external sources, such as radiation, and internal sources, such as chemical reactions. The fifth group of terms is the conduction of heat into the control volume. The sixth group of terms is the work done on the control volume by body forces that arise from diffusion. The seventh group of terms is the energy dissipated through viscous forces, known as the dissipation function.

Assuming Fourier's law for heat conduction and neglecting thermal diffusion:

$$
q_x = -k\frac{\partial T}{\partial x} \qquad q_y = -k\frac{\partial T}{\partial y} \qquad q_z = -k\frac{\partial T}{\partial z} \tag{2.9}
$$

The non-dimensionalized energy equation becomes:

$$
\begin{aligned}
&U_i\rho_{\mathrm{ref}}q'\rho^*\frac{\partial h^*}{\partial t^*} + \frac{\rho_{\mathrm{ref}}u_{\mathrm{ref}}q'}{L_{\mathrm{ref}}}\rho^*\left(u^*\frac{\partial h^*}{\partial x^*} + v^*\frac{\partial h^*}{\partial y^*} + w^*\frac{\partial h^*}{\partial z^*}\right) - U_i p_{\mathrm{ref}}\frac{\partial p^*}{\partial t^*} \\
&\quad - \frac{u_{\mathrm{ref}}p_{\mathrm{ref}}}{L_{\mathrm{ref}}}\left(u^*\frac{\partial p^*}{\partial x^*} + v\frac{\partial p^*}{\partial y^*} + w^*\frac{\partial p^*}{\partial z^*}\right) = U_i Q_{\mathrm{ref}}\frac{\partial Q^*}{\partial t^*} \\
&\quad + \frac{k_{\mathrm{ref}}T_{\mathrm{ref}}}{L_{\mathrm{ref}}^2}\left(\frac{\partial}{\partial x^*}\left(k^*\frac{\partial T^*}{\partial x^*}\right) + \frac{\partial}{\partial y^*}\left(k^*\frac{\partial T^*}{\partial y^*}\right) + \frac{\partial}{\partial z^*}\left(k^*\frac{\partial T^*}{\partial z^*}\right)\right)
\end{aligned}
$$

$$
\begin{aligned}
&- \frac{\rho_{\text{ref}} D_{\text{ref}} g}{L_{\text{ref}}} \rho^* D^* \left(\sum_{i=1}^{N} \left(f_{i,x}^* \frac{\partial Y_i^*}{\partial x^*} \right) + \sum_{i=1}^{N} \left(f_{i,y}^* \frac{\partial Y_i^*}{\partial y^*} \right) + \sum_{i=1}^{N} \left(f_{i,z}^* \frac{\partial Y_i^*}{\partial z^*} \right) \right) \\
&+ \frac{\mu_{\text{ref}} u_{\text{ref}}^2}{L_{\text{ref}}^2} \mu^* \left(2 \left(\frac{\partial u^*}{\partial x^*} \right)^2 + 2 \left(\frac{\partial v^*}{\partial y^*} \right)^2 + 2 \left(\frac{\partial w^*}{\partial z^*} \right)^2 \right) \\
&+ \frac{\mu_{\text{ref}} u_{\text{ref}}^2}{L_{\text{ref}}^2} \mu^* \left(\begin{array}{c} \left(\frac{\partial v^*}{\partial x^*} + \frac{\partial u^*}{\partial y^*} \right)^2 + \left(\frac{\partial w^*}{\partial y^*} + \frac{\partial v^*}{\partial z^*} \right)^2 + \left(\frac{\partial u^*}{\partial z^*} + \frac{\partial w^*}{\partial x^*} \right)^2 \\ -\frac{2}{3} \left(\frac{\partial u^*}{\partial x^*} + \frac{\partial v^*}{\partial y^*} + \frac{\partial w^*}{\partial z^*} \right)^2 \end{array} \right)
\end{aligned} \tag{2.10}
$$

The equation is multiplied by:

$$
\frac{L_{\text{ref}}}{\rho_{\text{ref}} c_{p,\text{ref}} T_{\text{ref}} u_{\text{ref}}}
$$

Certain terms are also multiplied and divided by some of the dimensionless parameters that were already extracted from the continuity and momentum equations to give an additional five dimensionless parameters:

$$
Dam3 = \frac{U_i q' L_{\text{ref}}}{c_{p,\text{ref}} T_{\text{ref}} u_{\text{ref}}} \qquad \Psi = \frac{u_{\text{ref}}^2}{c_{p,\text{ref}} T_{\text{ref}} \gamma_{\text{ref}}}
$$

$$
Pr = \frac{c_{p,\text{ref}} \mu_{\text{ref}}}{k_{\text{ref}}} \qquad Sc = \frac{\mu_{\text{ref}}}{\rho_{\text{ref}} D_{\text{ref}}} \qquad \frac{Q_{\text{ref}}}{\rho_{\text{ref}} q'}
$$

The following equation results:

$$
\begin{aligned}
&\left[\frac{U_i q' L_{\text{ref}}}{c_{p,\text{ref}} T_{\text{ref}} u_{\text{ref}}} \right] \rho^* \frac{\partial h^*}{\partial t^*} + \left[\frac{U_i q' L_{\text{ref}}}{c_{p,\text{ref}} T_{\text{ref}} u_{\text{ref}}} \right] \left[\frac{u_{\text{ref}}}{U_i L_{\text{ref}}} \right] \rho^* \left(u^* \frac{\partial h^*}{\partial x^*} + v^* \frac{\partial h^*}{\partial y^*} + w^* \frac{\partial h^*}{\partial z^*} \right) \\
&- \left[\frac{u_{\text{ref}}^2}{c_{p,\text{ref}} T_{\text{ref}} \gamma_{\text{ref}}} \right] \left[\frac{U_i L_{\text{ref}}}{u_{\text{ref}}} \right] \left[\frac{\gamma_{\text{ref}} p_{\text{ref}}}{\rho_{\text{ref}} u_{\text{ref}}^2} \right] \frac{\partial p^*}{\partial t^*} \\
&- \left[\frac{u_{\text{ref}}^2}{c_{p,\text{ref}} T_{\text{ref}} \gamma_{\text{ref}}} \right] \left[\frac{\gamma_{\text{ref}} p_{\text{ref}}}{\rho_{\text{ref}} u_{\text{ref}}^2} \right] \left(u^* \frac{\partial p^*}{\partial x^*} + v^* \frac{\partial p^*}{\partial y^*} + w^* \frac{\partial p^*}{\partial z^*} \right) \\
&= \left[\frac{Q_{\text{ref}}}{\rho_{\text{ref}} q'} \right] \left[\frac{U_i q' L_{\text{ref}}}{c_{p,\text{ref}} T_{\text{ref}} u_{\text{ref}}} \right] \frac{\partial Q^*}{\partial t^*} \\
&+ \left[\frac{k_{\text{ref}}}{c_{p,\text{ref}} \mu_{\text{ref}}} \right] \left[\frac{\mu_{\text{ref}}}{\rho_{\text{ref}} u_{\text{ref}} L_{\text{ref}}} \right] \left(\frac{\partial}{\partial x^*} \left(k^* \frac{\partial T^*}{\partial x^*} \right) + \frac{\partial}{\partial y^*} \left(k^* \frac{\partial T^*}{\partial y^*} \right) + \frac{\partial}{\partial z^*} \left(k^* \frac{\partial T^*}{\partial z^*} \right) \right) \\
&- \left[\frac{\rho_{\text{ref}} D_{\text{ref}}}{\mu_{\text{ref}}} \right] \left[\frac{u_{\text{ref}}^2}{c_{p,\text{ref}} T_{\text{ref}} \gamma_{\text{ref}}} \right] \left[\frac{\mu_{\text{ref}}}{\rho_{\text{ref}} u_{\text{ref}} L_{\text{ref}}} \right] \left[\frac{g L_{\text{ref}}}{u_{\text{ref}}^2} \right] \rho^* D^* \left(\begin{array}{c} \sum_{i=1}^{N} \left(f_{i,x}^* \frac{\partial Y_i^*}{\partial x^*} \right) \\ + \sum_{i=1}^{N} \left(f_{i,y}^* \frac{\partial Y_i^*}{\partial y^*} \right) \\ + \sum_{i=1}^{N} \left(f_{i,z}^* \frac{\partial Y_i^*}{\partial z^*} \right) \end{array} \right)
\end{aligned}
$$

$$+\left[\frac{u_{\text{ref}}^2}{c_{p,\text{ref}}T_{\text{ref}}\gamma_{\text{ref}}}\right]\left[\frac{\mu_{\text{ref}}}{\rho_{\text{ref}}u_{\text{ref}}L_{\text{ref}}}\right]\gamma_{\text{ref}}\mu^*\left(\begin{array}{l} 2\left(\frac{\partial u^*}{\partial x^*}\right)^2+2\left(\frac{\partial v^*}{\partial y^*}\right)^2+2\left(\frac{\partial w^*}{\partial z^*}\right)^2 \\ +\left(\frac{\partial v^*}{\partial x^*}+\frac{\partial u^*}{\partial y^*}\right)^2+\left(\frac{\partial w^*}{\partial y^*}+\frac{\partial v^*}{\partial z^*}\right)^2 \\ +\left(\frac{\partial u^*}{\partial z^*}+\frac{\partial w^*}{\partial x^*}\right)^2 \\ -\frac{2}{3}\left(\frac{\partial u^*}{\partial x^*}+\frac{\partial v^*}{\partial y^*}+\frac{\partial w^*}{\partial z^*}\right)^2 \end{array}\right) \tag{2.11}$$

Damköhler's third dimensionless group is found in front of the first term. It relates the heat generated by chemical reaction to the heat lost by convection. It is also found in front of the second group of terms once they are multiplied and divided by Damköhler's first dimensionless group. A dimensionless parameter that Penner [16] calls Ψ relates kinetic energy to internal energy. After multiplying and dividing by Damköhler's first dimensionless group and the square of the Mach number, it is found in front of the local pressure change term. It is also found in front of the fourth group of terms after multiplying and dividing by the Mach number. The inverse of the Prandtl number, which is the ratio of momentum diffusivity to thermal diffusivity, appears in front of the conduction terms after multiplication and division by the Reynolds number. The inverse of the Schmidt number, which is the ratio of momentum diffusivity to mass diffusivity, and the parameter Ψ both appear in front of the body force work terms after multiplication and division by the Reynolds number, Froude number, and the ratio of specific heats. In front of the dissipation terms, Ψ appears once more after multiplication and division by the Reynolds number and the ratio of specific heats. The final dimensionless parameter, relating the importance of all volumetric heat sources (including radiation and chemical reaction) to the heat evolved from chemical reaction, appears after multiplication and division by Damköhler's third dimensionless group. For many reacting flow problems, however, including many types of combustors, the external contribution to the volumetric heat source term is often neglected.

From the eleven dimensionless parameters found in the continuity, momentum, and energy equations, only ten are independent since Damköhler's second dimensionless group equals $(Dam1)(Re)(Sc)$. They are:

$$Dam1 \qquad Dam3 \qquad Re \qquad Sc \qquad Pr \qquad Fr \qquad Ma \qquad \gamma_{\text{ref}} \qquad \Psi \qquad \frac{Q_{\text{ref}}}{\rho_{\text{ref}}q'}$$

These include the nine dimensionless parameters that Penner [16] extracted for reacting multicomponent gas mixtures. He left out the dimensionless parameter relating the amount of heat produced within the control volume to the heat released by chemical reaction since he assumed that the effect of radiation was negligible.

Damköhler's five dimensionless ratios are all present in the first five parameters in this group, including $Dam2$ as previously mentioned, and $Dam4$ which equals $(Dam3)(Re)(Pr)$. The next four are needed when external body forces (Fr) are important and flow speeds are high (Ma, γ_{ref}, and Ψ).

Three different methods were used in this thesis to investigate the performance of a ducted rocket combustor, including direct-connect experiments, water tunnel visualization, and CFD modelling. The ducted rocket setup and testing, being by far the most expensive part of this investigation (which is the reason behind using the water tunnel and developing a CFD-based performance prediction method), used existing 100 mm diameter hardware, and therefore the water tunnel models and CFD mesh were made to the same size, simplifying the agreement with the dimensionless parameters. However, most ducted rocket combustors of current interest are about twice this diameter, so these scaling rules are necessary to extend the applicability of the data and methods reported herein. One way that this has been done in the past with subscale and full-size gas turbine combustors is to use what is known as "PD-scaling", "P" being the static pressure in the combustor and "D" being a representative linear dimension such as the diameter. For this technique, geometric similarity and inlet temperatures, flow velocities, fuel properties, and air/fuel ratio must be maintained between the model and the full-size combustor. Then only the static pressure is changed in inverse proportion to the linear scale [5]:

$$p_{\mathrm{m}} d_{\mathrm{m}} = p_{\mathrm{p}} d_{\mathrm{p}} \tag{2.12}$$

This means that a half-scale combustor should be operated at twice the pressure in order to approach dynamic, thermal, and compositional similarity. While not the main goal of the work reported in this thesis, some direct-connect tests were done at twice the pressure to provide data that could be applied to combustors of twice the size. However, the CFD modelling was also done for these higher-pressure configurations to attempt to predict them as well.

A more thorough description of PD-scaling and how it can be applied to ducted rocket combustors is in Appendix A.

2.4 Dimensionless Parameters

The ten dimensionless ratios that should be the same in a model and the full-scale ducted rocket combustor in order to respect geometric, dynamic, thermal, and compositional similarity as closely as possible are:

$$Dam1 \quad Dam3 \quad Re \quad Sc \quad Pr \quad Fr \quad Ma \quad \gamma_{\mathrm{ref}} \quad \Psi \quad \frac{Q_{\mathrm{ref}}}{\rho_{\mathrm{ref}} q'}$$

For the CFD modelling and water tunnel visualization, geometric similarity is the first requirement and is respected by simply using accurate, full-size representations of the direct-connect combustor. The pressures, inlet velocities, vitiated air and fuel compositions, and inlet temperatures are kept the same between the direct-connect hardware and the CFD modelling in order to respect the other three types of similarity as well as possible. All reference quantities for the ten dimensionless ratios are therefore assumed to be proportional to the inlet parameters. Obviously for the water tunnel visualization, no attempt was made to respect thermal and compositional similarity since the working fluid is, by definition, water.

2.4.1 Damköhler's First Dimensionless Ratio

Damköhler's first dimensionless ratio is the ratio of the rate of species formation by chemical reaction to the rate of species loss by convection:

$$Dam1 = \frac{U_i d}{v}$$

where the reference length is d and the reference velocity is v. For the CFD modelling, we have fixed the pressures, diameter, inlet temperatures, chemical species (vitiated air and fuel compositions) and inlet velocities to be constant so these reference values will be the same. However, the challenge for the CFD modelling is to accurately model the characteristic reaction frequency U_i. Often an Arrhenius expression is used to describe a global reaction rate, but this will neglect the contribution by any solid particles present in the gas generator exhaust. The influence of turbulence on the combustion is also an important aspect that is not included in an Arrhenius representation of the reaction rate. As will be evident later, the combustion model is a critical aspect of accurately predicting the performance of a ducted rocket combustor and the object of much effort for this work.

2.4.2 Damköhler's Third Dimensionless Ratio

Damköhler's third dimensionless ratio is the ratio of the rate of heat generation by chemical reaction to the rate of heat loss by convection.

$$Dam3 = \frac{U_i q' d}{c_{p,\mathrm{ref}} T_{\mathrm{ref}} v}$$

As explained for Damköhler's first dimensionless ratio, the pressures, diameter, inlet temperatures, chemical species, and inlet velocities are the same between the CFD model and the direct-connect experiments, so d, v, and T_{ref} are the same. The constant pressure specific heat $c_{p,\mathrm{ref}}$ depends on T_{ref} and the chemical species, so this is the same as well. Since q' is a function of the chemical species and the characteristic reaction frequency U_i, this will depend on how the combustion is modelled. An additional consideration is the exchange of heat between the gaseous phase and solid particles from the gas generator exhaust; this must also be modelled accurately for the heat release.

2.4.3 Reynolds Number

The Reynolds number is the ratio of inertial fluid forces to viscous fluid forces. It is the most important dimensionless parameter for the description of the flow, both the air and the fuel, so it should be respected in both cases:

$$Re = \frac{\rho d v}{\mu_{\mathrm{ref}}}$$

The inlet temperatures and chemical species are specified to be the same for the CFD modelling and the direct-connect combustor, so the dynamic viscosity should be the same. It is a property of the gases that has to be specified when the problem is set up. However, since the flow is dominated by turbulent mixing, it is not a parameter that has to be specified too accurately, meaning that the Reynolds number does not have to be matched, as long as it is sufficiently high to respect dynamic similarity. This point is important for the water tunnel since the Reynolds numbers are typically an order of magnitude lower. Another important point, to be explained further in Chapter 4, is that the air/fuel *momentum* ratio, not the velocity or mass flow ratio, must be matched between the direct-connect combustor and the water tunnel model to properly reproduce the flowfield. The inlet turbulence parameters must also be matched to properly reproduce the mixing.

2.4.4 Schmidt Number

The Schmidt number is the ratio of momentum diffusivity to mass diffusivity:

$$Sc = \frac{\mu_{\mathrm{ref}}}{\rho_{\mathrm{ref}} D_{\mathrm{ref}}}$$

The dynamic viscosity and binary diffusion coefficients are simply functions of gas composition and temperature if the assumption of an ideal gas mixture is valid, and can be specified in the CFD model as fluid properties. However, since the flow inside the combustor is highly turbulent (Re typically 10^5 to 10^6), molecular mixing is not important compared to the turbulent mixing [10] so the Schmidt number does not have to be closely matched.

2.4.5 Prandtl Number

The Prandtl number is the ratio of momentum diffusivity to thermal diffusivity:

$$Pr = \frac{c_{p,\text{ref}}\mu_{\text{ref}}}{k_{\text{ref}}}$$

The constant pressure specific heat, dynamic viscosity, and thermal conductivity are functions of temperature and gas composition for ideal gases, and are fluid properties that must be specified in the CFD model. To model the heat transfer at the combustor walls properly, the Prandtl number should be kept the same. In an actual ducted rocket combustor, the combustor wall is insulated on the inside, so there is very little heat transfer from the gases to the wall. In these direct-connect combustor experiments, however, the combustor wall is not insulated so heat transfer to the wall may be important; this will be investigated later as part of a parametric modelling study.

2.4.6 Froude Number

The Froude number is the ratio of inertial forces to gravitational body forces:

$$Fr = \frac{v^2}{gd}$$

It will be the same in the CFD model and the direct-connect combustor since the inlet velocities and diameters are the same. For the water tunnel, the velocities are lower, but because the flow is highly turbulent the inertial forces will still overwhelm the gravitational force (buoyant effects negligible) so the Froude number can be neglected.

2.4.7 Mach Number

The Mach number is the ratio of a characteristic velocity of the flow to the velocity of sound in the fluid, and is a measure of the importance of compressibility effects on the flow:

$$Ma = \sqrt{\frac{\rho v^2}{\gamma_{\mathrm{ref}} p}}$$

Since the Mach number is less than 0.3 in most of the combustor, the flow can be classified as incompressible so the Mach number need not be respected. In fact, for the CFD modelling the density is simply a function of temperature and composition and not of pressure. Since the pressure is assumed constant within the combustor, the Mach number is effectively zero. While the ducted rocket configurations investigated for this work had unchoked fuel jets, many systems of interest have choked fuel jets and therefore there is some supersonic flow in the combustor. In these cases, compressibility cannot be ignored and the Mach number must be included as a dimensionless parameter.

2.4.8 Ratio of Specific Heats

The ratio of specific heats, γ_{ref}, can be estimated for the CFD model so that it is the same as for the direct-connect combustor. It is a property that is a function of gas composition and temperature only:

$$\gamma_{\mathrm{ref}} = constant$$

2.4.9 Ratio of Kinetic Energy to Internal Energy

The ratio that Penner [16] calls Ψ relates kinetic energy to internal energy and also determines the importance of compressibility effects, as does the Mach number:

$$\Psi = \frac{v^2}{c_{p,\mathrm{ref}} T \gamma_{\mathrm{ref}}}$$

As explained for the Mach number, the flow is assumed incompressible so this parameter need not be respected for the CFD modelling for these combustor configurations with unchoked fuel jets.

2.4.10 Volumetric Heat Sources

The ratio of heat produced within the control volume by internal (chemical reaction) and external sources (such as radiation) to the heat evolved from chemical reaction is:

$$\frac{Q_{\mathrm{ref}}}{\rho_{\mathrm{ref}} q'}$$

As explained for Damköhler's third dimensionless ratio, q' is a function of the chemical species present and the characteristic reaction frequency U_i, and depends on how the combustion is modelled. The main external contribution to Q_{ref} for typical combustion problems is radiation. Since the amount of radiative heat transfer is much smaller than the amount of convective heat transfer for ramjet combustors [8, 10], the heat release from combustion will also overwhelm the amount of radiation and will be the main contribution to Q_{ref}. This will also be investigated later as part of the parametric modelling study in Section 6.4.

2.5 Summary of Similarity and the Dimensionless Parameters

Five of the ten dimensionless parameters important for reacting flow in combustors were identified as relevant to ducted rockets with unchoked, subsonic fuel jets. They, along with some other important parameters, must be applied to ensure that geometric, dynamic, thermal, and compositional similarity will be respected as closely as possible. Geometric similarity will be achieved by using combustor models of the same dimensions as for the direct-connect experiments. For both the water tunnel and the CFD modelling, the Reynolds number is the most important dimensionless parameter to respect for dynamic similarity. In addition, the air/fuel momentum ratio and the inlet turbulence parameters are critical to properly reproduce the flowfield in the direct-connect combustor. For the CFD modelling, Damköhler's first dimensionless ratio, Damköhler's third dimensionless ratio, the Prandtl number, and the ratio of specific heats must also be respected to approach thermal and compositional similarity with the experimental combustor, and the critical aspect for this is the combustion model. Of the remaining five dimensionless parameters, the Schmidt number and the Froude number can be neglected because the Reynolds number is high, as can the Mach number and the ratio of kinetic energy to internal energy since the flow can be assumed to be incompressible. However, if there is supersonic flow in the fuel jet, then the Mach number and the ratio of kinetic energy to internal energy cannot be ignored. The amount of convective heat transfer in the combustor should be much greater than that of radiation, so the last ratio relating the importance of external heat sources to the heat released by the combustion can be neglected as well.

Chapter 3

WATER TUNNEL VISUALIZATION

3.1 Purpose of the Water Tunnel

The water tunnel was used to visualize the non-reacting flow and air/fuel mixing within model combustors at as many of the geometries and simulated test conditions that were proposed for the direct-connect combustor tests as possible. The use of a water tunnel is an accepted method to visualize flowfields within combustors, and has also been used specifically for ducted rocket combustors [21, 22, 23]. The water tunnel at Defence Research Establishment Valcartier (DREV) is basically a 560 litre plexiglass tank in which a plexiglass model of a ducted rocket combustor is installed. Water is pumped through the "fuel" and "air" inlets of the combustor - this water simulates both the fuel and the air flowing through an actual combustor. For the air/fuel mixing tests, the fuel flow was seeded with very fine bubbles to distinguish it from the air. A laser sheet illuminated a plane of interest inside the combustor so that the "air" and "fuel" mixing could be easily seen and recorded with a video camera. The main advantage of a water tunnel for flow visualization is that the Reynolds numbers for a water velocity of 1 m/s in the main part of the combustor were representative of the flow in a typical ducted rocket combustor. However, at these flow speeds the flow patterns and structures were easily seen in real time. Several combustor models were built and tested at various flow conditions to encompass many of the possible configurations for testing in the direct-connect combustion test facility at TNO Prins Maurits Laboratory (TNO-PML) in the Netherlands.

The work presented in this chapter and in Chapter 4 was presented at the 34th AIAA Joint Propulsion Conference in 1998. The paper [24] is in Appendix E.

3.2 Previous Experiments

A review of previous solid fuel ducted rocket tests in the open literature was conducted to yield data on experimental combustor configurations and test conditions. All of the configurations were of a "side dump" geometry with the air inlets feeding air from the side of the combustor (Fig. 1.2). This allows the gas generator and fuel injection to be placed adjacent to the head.[1] Boundary and test conditions were noted, and additional data were calculated, such as air and fuel velocities, Reynolds numbers based on combustor diameter, and stagnation properties to describe the flow within the combustors more completely (Table 3.1). Properties in the combustor were calculated as if the fuel were flowing, but not reacting. The influence of geometry on the flow was examined for all configurations, including the placement of the fuel injector with respect to the air flow. Of particular interest in these tests were which geometries and boundary conditions were important for efficient fuel and air mixing.

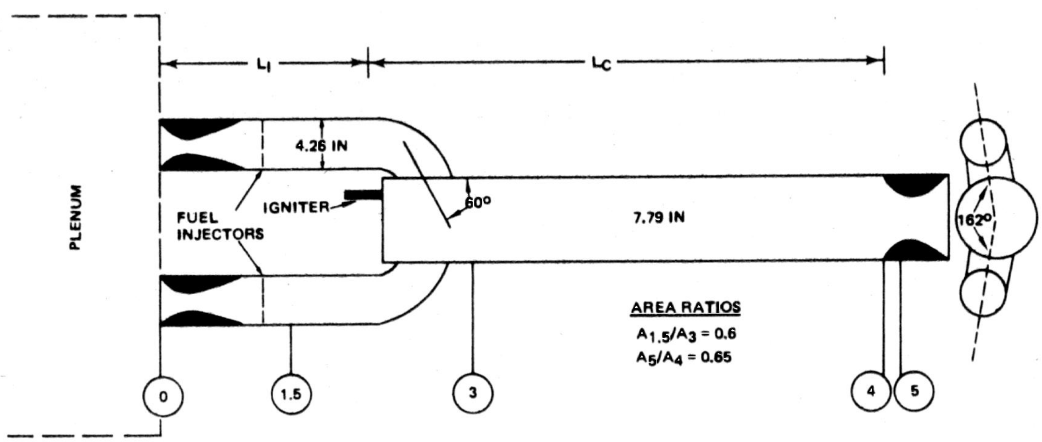

Figure 3.1: Experimental setup from Clark [25]

Clark [25] used a side dump connected pipe setup (Fig. 3.1) to study pressure oscillations within a combustor. The two inlets were opposed at 162° and used an injection angle of 60°. Liquid fuel was injected into the air inlets so some mixing would take place upstream of where the flow entered the combustor. Calculated injection velocities at the ports were about 140 m/s which yielded Mach numbers in the combustor of approximately 0.3 to 0.45. Inlet temperatures were about 600 K and

[1] An alternative to the side dump geometry is the more compact coaxial "centre dump" geometry, but this is only practical for liquid fuel and solid fuel ramjets which do not use a gas generator.

Table 3.1: Geometries and test conditions from previous experiments

Reference	Combustor diameter	Re in combustor	Air inlets	Type	Injection angles	Dome height[a]	Fuel injection type	Stagnation pressure	Stagnation temperature
Clark [25]	196.85 mm	1 850 000	2	Circular 162^{o} opposed	60^{o}	0.5 est.	In inlets	0.639 MPa	610 K
Choudhury [26]	89 mm	No T,P data	4	Circular, cantable	45^{o}, 70^{o}	0.6-4.0	Radial central	No T,P data	No T,P data
Zetterström *et al.* [23]	100 mm	1 160 000	4	Circular	60^{o}	0.75 est.	In inlets	0.714 MPa	704 K
Stull *et al.* [27]	150 mm	533 000	2	Rectangular ventral	30^{o}, 45^{o}, 60^{o}	0.4-0.9	In inlets	0.248 MPa	571 K
Chuang *et al.* [32] Hsieh *et al.* [33]	127 mm	840 000	2	Opposed 2D	45^{o}	0.48	2 off-centre ports, 2D	0.199 MPa	286 K
Dijkstra *et al.* [35] (TNO-PML)	100 mm	216 000	2	Circular ventral	45^{o}	0.7	Central nozzle protruding 30 mm	0.617 MPa	655 K
Dijkstra *et al.* [35] (NAWC)	127 mm	260 000	2	Circular ventral	45^{o}	0.96	Central nozzle protruding 51 mm	0.508 MPa	653 K
Ristori *et al.* [36]	100 mm	1 120 000	2	Square, opposed	45^{o}	0.65-1.35	2 nozzles, laterally off-centre	0.764 MPa	527 K
Schadow [37]	150 mm	270 000	2	Opposed rectangular slits	45^{o}	0-neg	Central nozzle	0.201 MPa	298 K
Tsujikado *et al.* [39]	83 mm	460 000	2	Opposed	75^{o}	0.5 est.	Central nozzle	0.464 MPa	460 K
Vigot *et al.* [40]	85 mm	1 110 000	4	Circular, shifted, deflectors	45-90^{o}	0.5 est.	Various	NA	NA
Vigot *et al.* [40]	168 mm	1 760 000	4	Circular, shifted, deflectors	45-90^{o}	0.5 est.	Various	NA	NA

[a]Dome height is given as a fraction of the combustor diameter and is the axial distance from the head of the combustor to the centre of the air inlet(s).

pressures about 0.6 MPa. While different combustor and inlet lengths, equivalence ratios, and mass flow rates were used, this study focused on pressure oscillations rather than combustor performance, so geometric effects on efficiency were not reported. However, the data are useful for establishing possible flow conditions and geometries for our tests.

Choudhury [26] studied a gaseous fuel system with four circular inlets spaced equally around the circumference of a circular tube. Air injection angles were 45^o and 70^o from the horizontal at speeds up to 150 m/s. The inlets could also be canted to induce swirl. This research focused on the importance of the fuel and air mixing at the head end of the combustor, and it was soon discovered that axial fuel injection would disrupt the head-end vortices important for mixing. All subsequent tests were then performed using radial fuel injection. Side inlet angle was found to have little effect on the head-end mixing, but the dome height (distance from the head to the air inlets) did have an optimum value. While combustion efficiency benefited from increased combustor length, the head-end mixing and stability did not. A very interesting observation was that the introduction of swirl by canting the air inlets had a negative effect on the head-end mixing, in contradiction to many other combustor configurations.

A similar four-inlet configuration (Fig. 3.2) was used in a Swedish study [23] that involved flow visualization as well as gaseous fuel and solid fuel combustion tests. The inlet angle was 60^o from horizontal. Each inlet used a vane at its end to divide the flow; this was needed to provide a stable flow pattern in the head of the combustor. Unlike Ref. [26], however, in all cases the fuel was injected directly into the inlet ducts rather than at the head of the combustor. Air inlet temperature was a maximum 700 K, pressure 0.7 MPa, and calculated inlet air velocity 90 m/s. Once again, combustion efficiency benefited from increased combustor length, while stability, which depends more on the flow in the head end of the combustor, did not. The dome height was not varied during the tests.

Stull *et al.* [27] studied a ducted rocket combustor with two rectangular air inlets (50 mm by 70 mm with the long dimension aligned with the combustor main axis) spaced 90^o apart circumferentially on a 150 mm diameter tube (Fig. 3.3). Liquid fuel (JP-4) was injected directly into the inlets rather than into the combustor. Air was injected at angles of 30^o, 45^o, and 60^o from the horizontal at a calculated speed of 180 m/s. A parallel study using a plexiglass model of the same geometry was also done. Dome height was varied from 25 mm to 150 mm measured from the upstream

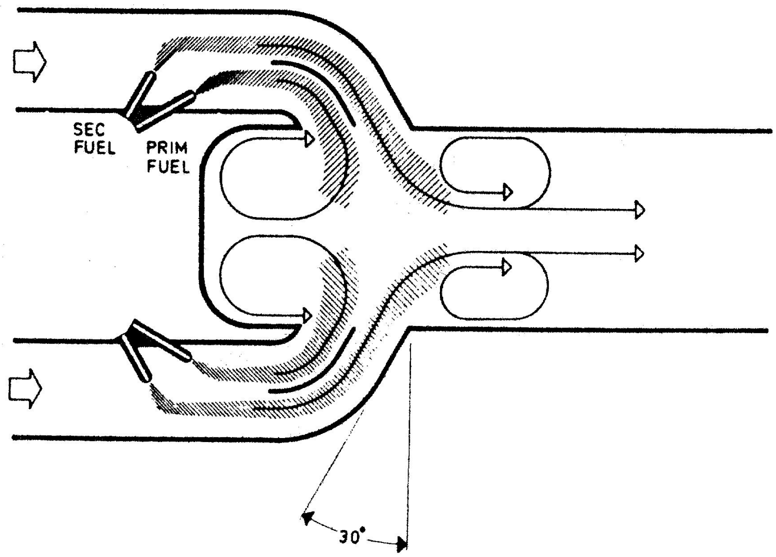

Figure 3.2: Four inlet combustor from Zetterström *et al.* [23]

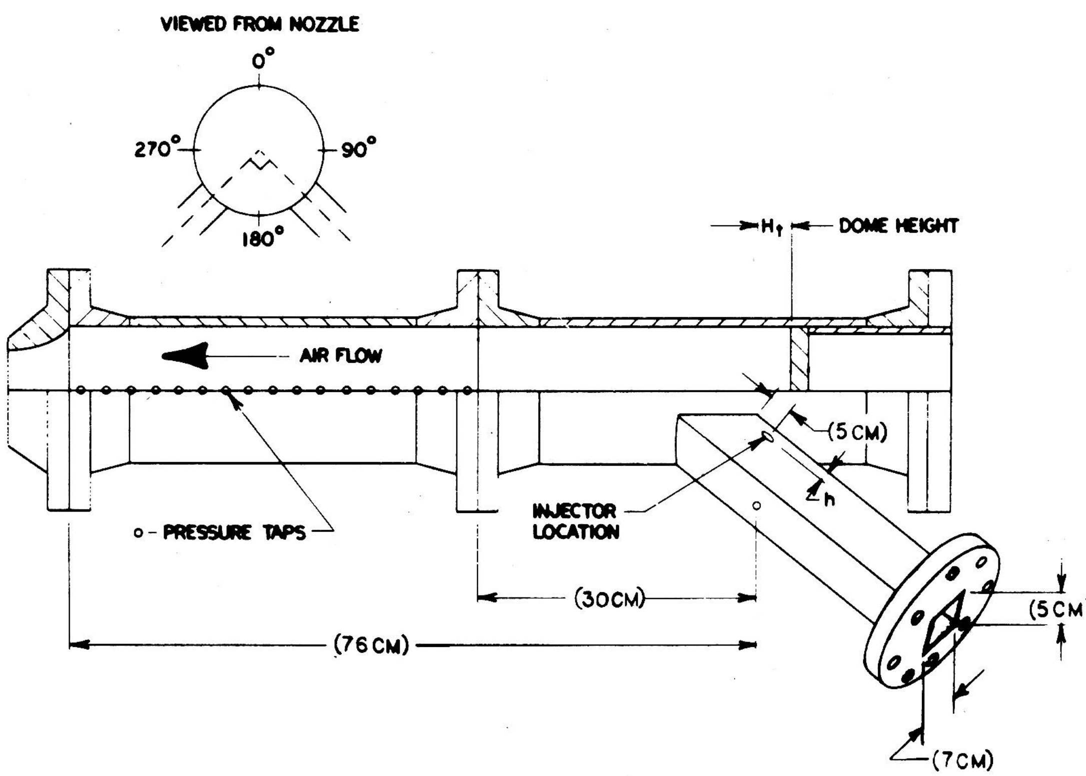

Figure 3.3: Dual ventral inlet combustor from Stull *et al.* [27]

edge of the inlets, and had little effect on combustion efficiency. Air inlet angle also had little effect on combustion efficiency, but 60° was the best. This insensitivity to dome height and inlet angle over the ranges investigated indicated that the general configuration of two inlets 90° apart produced a sufficient recirculation zone for good mixing. However, a modelling study of the same configuration [28] but with gaseous ethylene injected axially from a single 15 mm diameter port in the dome head showed that the combustion efficiency was indeed sensitive to dome height (the best was 50 mm) and to air inlet angle (60° was again the best). Fuel injection position was also important, with an eccentric position 38.1 mm below the centreline between the air inlets being the best. While there were no experimental data to validate the findings, the modelling results showed that injecting the fuel into the dome head appeared to cause the mixing to be more sensitive to geometry than when the fuel was injected into the inlets. Once again, combustion efficiency improved with combustor length.

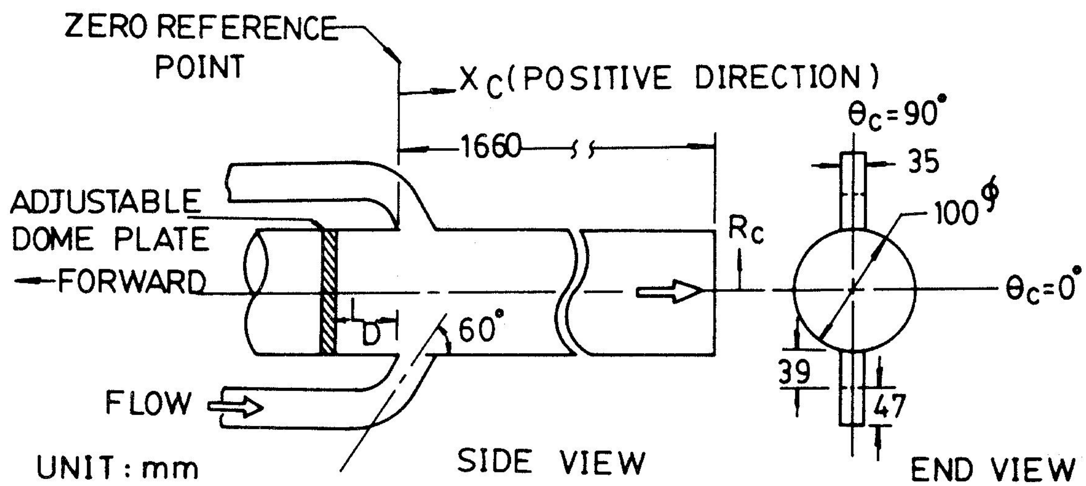

Figure 3.4: Dual opposed inlet combustor from Liou and Wu [29]

Liou and Wu [29] performed a flowfield study on a 100 mm diameter combustor with dual rectangular (35 mm by 47 mm along the main combustor axis) inlets opposed 180° apart and injecting air at 60° (Fig. 3.4). Dome height was fixed at 50 mm. No fuel was injected and the air flow velocity was very low (about 10 m/s calculated). Large recirculation zones were obtained in the head of the combustor. This configuration was only used for gathering Laser Doppler Velocimetry (LDV) data on the flowfield. However, it has since been used to validate modelling work with axial central injection of exhaust from a 50% (by mass) polyester 50% ammonium perchlorate gas generator at 100 m/s, and an air flow velocity of 200 m/s [30]. With these boundary conditions and geometry, good mixing and high combustion temperatures were achieved. More recently, the data were used to validate modelling work by Yen and Ko [31] to investigate the effect of the air injection angle on the flowfield in the combustor. They varied the air injection angle from 30° to 90°, and found that the head-end vortices were stronger at higher angles. There are also weaker recirculation zones downstream of the air inlets whose characteristics are highly dependent on air injection angle. Cold flow pressure losses were insensitive to air injection angle, however. They also concluded that three-dimensional flow structures are different to those in two-dimensional flow, so care must be taken when comparing the two situations.

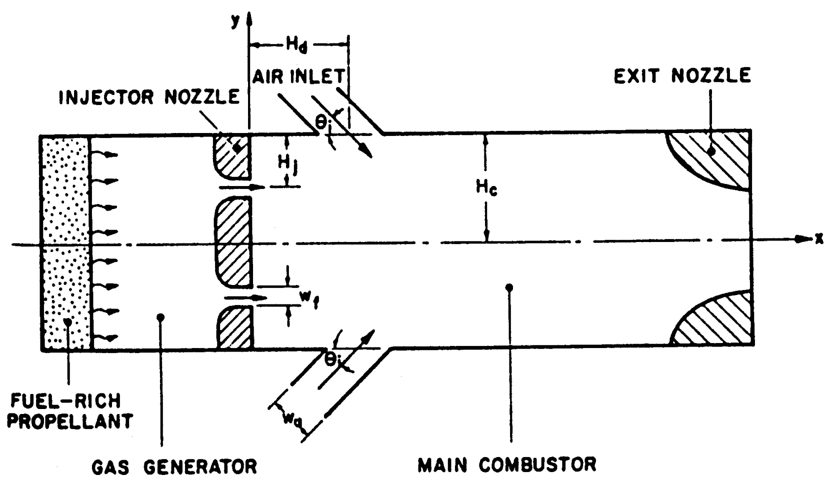

Figure 3.5: Two-dimensional combustor from Chuang *et al.* [32]

Ducted rocket flowfield studies have also taken place at Pennsylvania State University [32, 33] with a two-dimensional configuration of height 127 mm having dual air inlets with an injection angle of 45°, and a dome height of 60.9 mm (Fig. 3.5). Fuel was injected from two ports at one-half the distance between the centreline and the combustor wall, but there was no combustion. Air velocity in the inlet was up to 160 m/s. There were four recirculation zones, two between the fuel ports and one between each fuel port and the wall. The flowfield, including the strengths of the recirculation zones, was highly dependent on the momentum ratios of the injected air and fuel.

A paper from Japan [34] described an investigation of a ramjet with many different inlet configurations (Fig. 3.6). Kerosene was injected directly into the intake ducts. Subscale combustion tests with dual rectangular-inlet configurations showed that stable combustion was obtained only when the inlets were placed 90° apart circumferentially rather than directly opposed at 180°, regardless of whether or not guide vanes were used in the inlet ducts. Full-scale tests were done with configurations of either four single or pairs of circular inlets placed 90° apart circumferentially and injecting air at 90°. The configurations using four pairs of inlets had combustion efficiencies of up to 95%. Unfortunately, dimensions of the hardware were not given in the paper, but air flow rates were up to 15 kg/s.

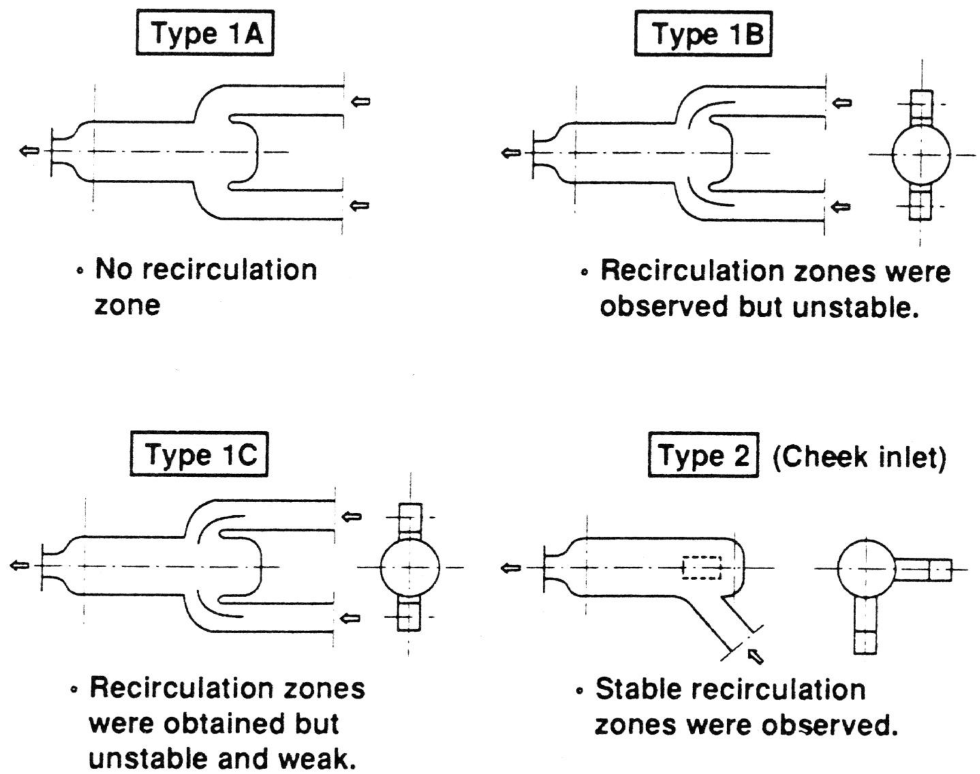

Figure 3.6: Various inlet configurations, from Aoki *et al.* [34]

Tests were done at U.S. Naval Air Warfare Center (NAWC) and TNO-PML [35] with dual circular air inlets spaced 90° apart circumferentially injecting air at 45°. The two experimental setups used the same basic configuration, the one at NAWC being 127 mm in diameter with a dome height of 102 mm injecting gaseous ethylene through a central port at the head end of the combustor (Fig. 3.7), and the other at TNO-PML being 100 mm in diameter with a dome height of 54 mm and injecting exhaust from a GAP-based gas generator propellant, also through a central port (Fig. 3.8). Calculated air injection velocity was 80 m/s (NAWC) or 100 m/s (TNO-

PML), with an air inlet temperature of 650 K and combustor pressure of 0.5 MPa (NAWC) or 0.6 MPa (TNO-PML). This study focused on how the shape of the fuel injector affected combustion efficiency, and with the best injectors, designed to enhance fine-scale mixing, the basic combustor geometry and boundary conditions yielded combustor temperatures that suggest good combustion took place.

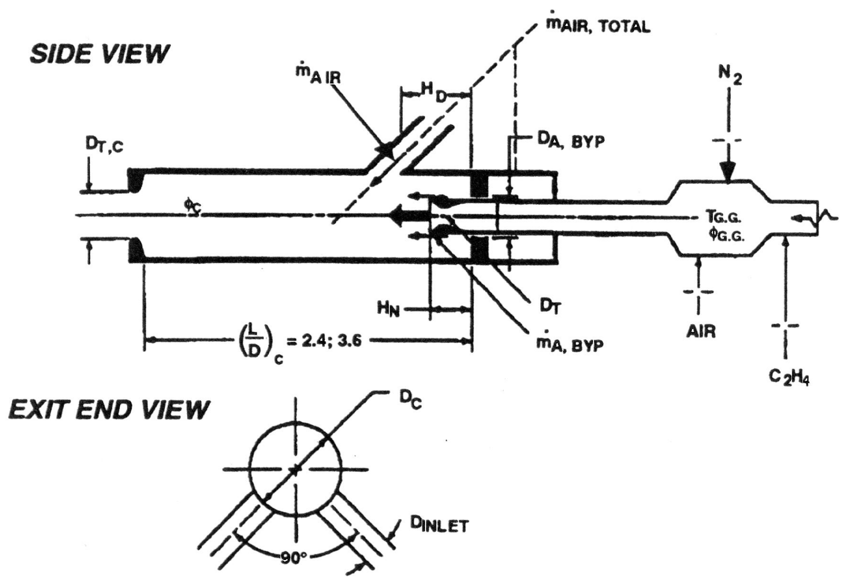

Figure 3.7: NAWC experimental combustor, from Dijkstra *et al.* [35]

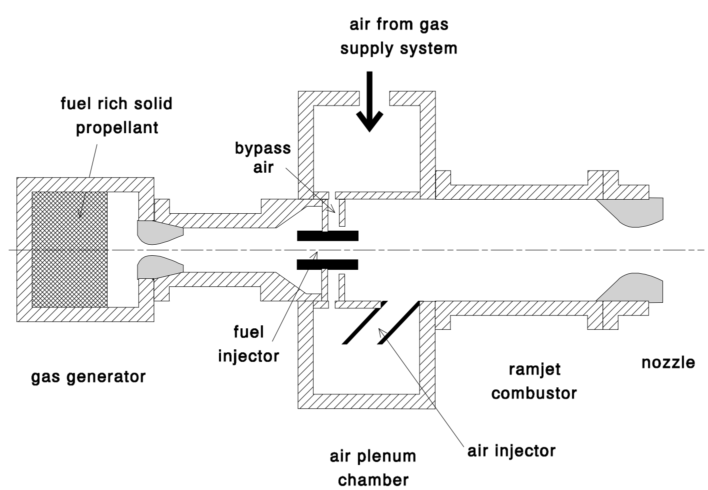

Figure 3.8: TNO-PML experimental combustor, from Dijkstra *et al.* [35]

The Office National d'Études et de Recherches Aérospatiales (ONERA) in France initiated a research project on ramjets in 1995 [36] with the goal of improving combustor design by using validated CFD codes. To validate these codes, they constructed a 100 mm square cross-section ducted rocket combustor with dual opposed inlets, 45° air injection angle, two fuel injection ports 11 mm in diameter on the centreline between the air injectors but each placed laterally 25 mm from the centreline (Fig. 3.9). To date, only non-reacting flow measurements have been done with both cold air flow and water tunnel tests. They found that the intensity of four counter-rotating longitudinal vortices were very important to the mixing, which are analogous to the two counter-rotating vortices seen in a combustor with dual ventral inlets. They found that there was an optimum value for fuel jet momentum; too low and there was not good penetration into the air jets for good mixing, and too high the fuel would shoot through the air jets without mixing.

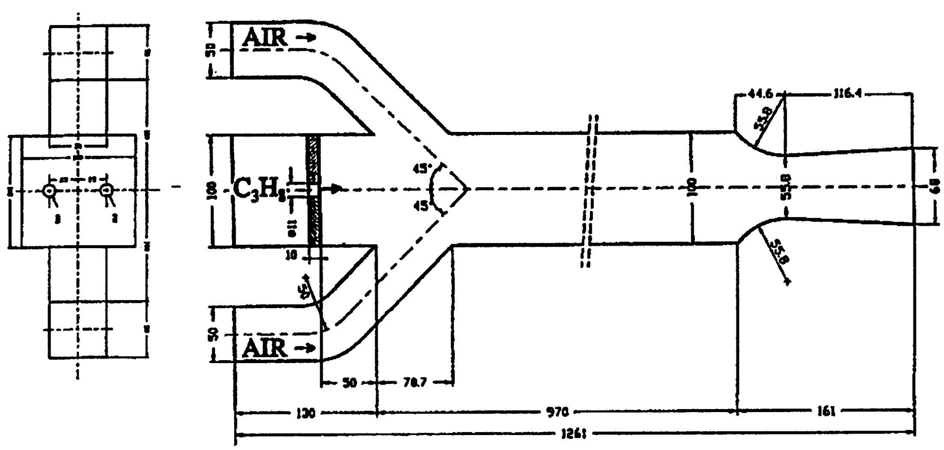

Figure 3.9: Square cross section combustor from Ristori *et al.* [36]

There are also some papers in the open literature that deal specifically with ducted rockets using fuels containing boron. Adding boron to the fuel means a significant increase in performance as long as most of the boron can be burned within the combustor. However, boron fuels are difficult to ignite and burn efficiently, so the mixing of the air and the fuel has to be even more carefully done than with non-boron fuels in order to maximize combustor performance. A research paper by Schadow [37] described the combustion of boron in a two-dimensional (square) side dump configuration of 150 mm height and width. Air was injected through two rectangular slits, one at the top and one at the bottom of the combustor, and was directed toward the central fuel jet at an angle of 45°. The calculated air injection velocity was about 24 m/s, the chamber pressure about 0.2 MPa, and the inlet temperature ambient. Unless the boron was initially at a temperature above 1 950 K, excess gaseous fuel, injected with the boron into the combustor, had to mix properly with the incoming air and burn at high temperature in order to sustain combustion of the boron.

Work done at the Japan Defence Agency [38, 39] used an 83 mm diameter combustor with dual opposed (180° apart) inlets injecting air at an angle of 75° (Fig. 3.10). While not explicitly given in the papers, the dome height looks to be about 25 mm, and with an assumed air inlet diameter of 32 mm, injection velocity would be 140 m/s. Combustion efficiencies were reported to be over 90%.

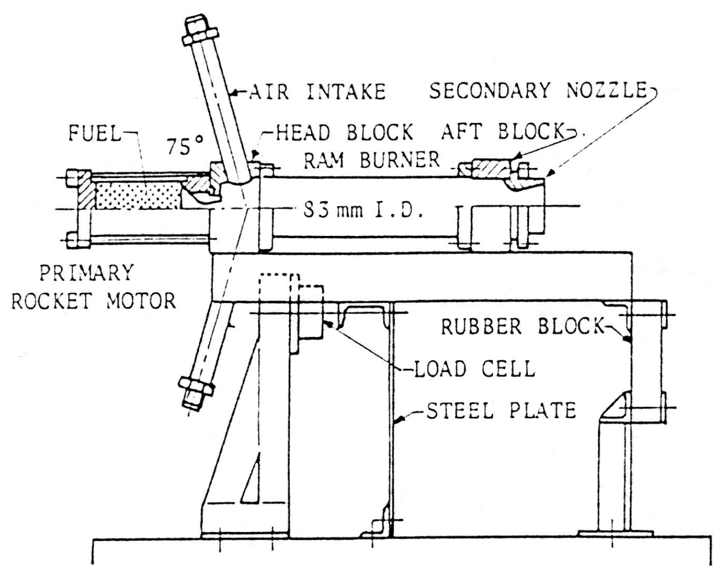

Figure 3.10: Subscale combustor, from Tsujikado *et al.* [39]

Both France and Germany have done extensive development work on boron-fueled ducted rockets. Tests at ONERA in France [40] used both subscale (85 mm internal diameter) and full-scale (168 mm internal diameter) combustors (Fig. 3.11). Configurations of four inlets spaced circumferentially 90° apart were used, with two inlets "shifted" downstream of the others toward the nozzle end of the combustor. Deflectors were used to divide the air flow in each inlet so some would flow toward the head end, while the rest would be injected further downstream. The air was therefore injected at a range of angles for each inlet, from about 45° to 90°. The flow Mach number in the combustors (not the air inlet ports) was very high at about 0.4. Unfortunately, the air inlet port areas are not given so the air injection velocities could not be calculated. Fuel injection was also done with a variety of devices to break up the boron particles effectively and cause efficient mixing with the air. In all cases, good combustor behaviour was obtained and showed that this was a practical configuration for an actual propulsion unit. German work since 1970, described in [41, 42], also dealt with configurations using four sets of air inlets, each set having up to four separate ducts, some of which were shifted toward the nozzle end of the combustor. Air injection angles appeared to be 45° to 60°. The best results had combustion efficiencies of about 95%.

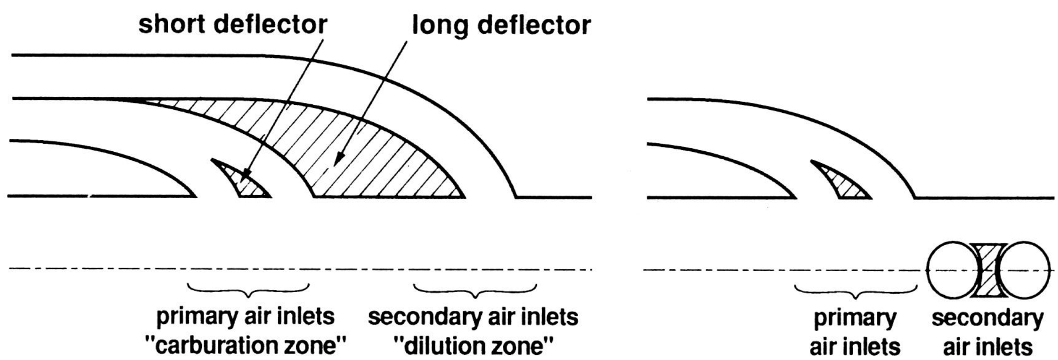

Figure 3.11: Shifted air inlets, from Vigot *et al.* [40]

To summarize the findings, this literature survey showed that many different configurations have been investigated. Air inlet injection angles from 30° to 90° were used, both with and without splitters or guide vanes. Air inlet velocities were up to 200 m/s, with temperatures from ambient up to 800 K and combustor pressures from about 0.2 MPa up to 0.7 MPa. Dome heights were usually from 25% to 100% of the combustor diameter, and for dual inlet systems, more stable recirculation in the dome region was obtained having the intakes spaced 90° apart rather than directly opposed at 180°. Methods of fuel injection varied widely, from axial to radial when injected from the head, to injection in the air inlets themselves. Not only was impingement of the fuel jet against the air jets desirable, but the air/fuel momentum ratio had to be high enough to establish head-end recirculation zones and break up the fuel jet to improve mixing. Mixing at the head end and small-scale flow structures could be quite sensitive to geometry and boundary conditions when the fuel was injected from the head. Computer modelling, flow visualization with water tunnels or wind tunnels, and combustion tests (subscale and full-scale) were all performed to identify the best configurations and maximize combustion efficiency.

3.3 Water Tunnel

The water tunnel, shown schematically in Fig. 3.12, is a closed system that uses a 2 HP pump (Pump 1 in the figure) to circulate the water through the combustor model at flow rates of up to 8 litres/s. Since water is used as the working fluid, Reynolds numbers (based on combustor diameter) obtained in the plexiglass model combustor are high enough (above 40 000) to simulate those in an actual ducted rocket combustor. However, velocities of only 1 m/s in the 100 mm diameter model are sufficient to achieve these Reynolds numbers, and flow phenomena are therefore slow enough to be recorded in real time with a video camera. The model is mounted inside a rectangular tank which holds 560 litres of water. Because the tank is filled with water, distortion of the view of the flow within the combustor model is kept to a minimum. An internal wall dividing the tank in two parts inhibits anything used to seed the flow from contaminating the water in the section surrounding the main part of the combustor.

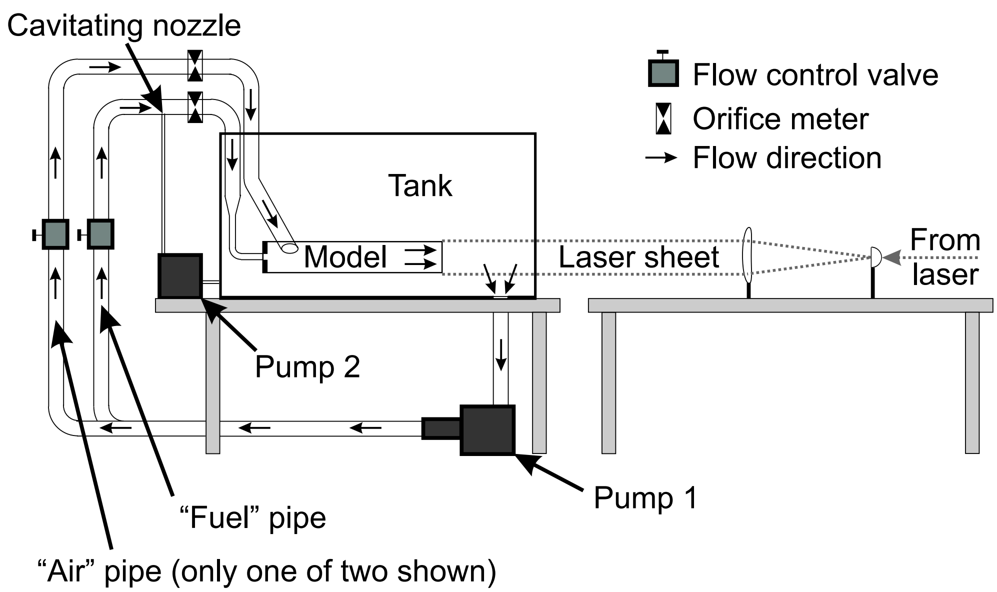

Figure 3.12: Water tunnel and optics setup

The water that simulates the air and the fuel leaves the pump and is split into two air pipes and one fuel pipe, each of which can be controlled individually with a valve. The overall flow rate can also be controlled by a valve. Three sharp-edged orifices in the horizontal upper pipe sections, coupled with differential pressure transducers, were used to measure the flow rates through the air and fuel pipes. Figure 3.13 presents the optical setup used to generate a vertical light sheet so that only the longitudinal centreline plane would be visible. The laser sheet was produced by a 5 W Argon Ion laser, expanded vertically by a cylindrical lens, and then recollimated by a 100 mm spherical lens. By using a mirror, shifting the optical setup to the side of the water tunnel, and viewing the combustor model from the end of the water tunnel, cross-sections of the flowfield could also be seen. Images were recorded with a video camera and transferred to a computer with a frame-grabber.

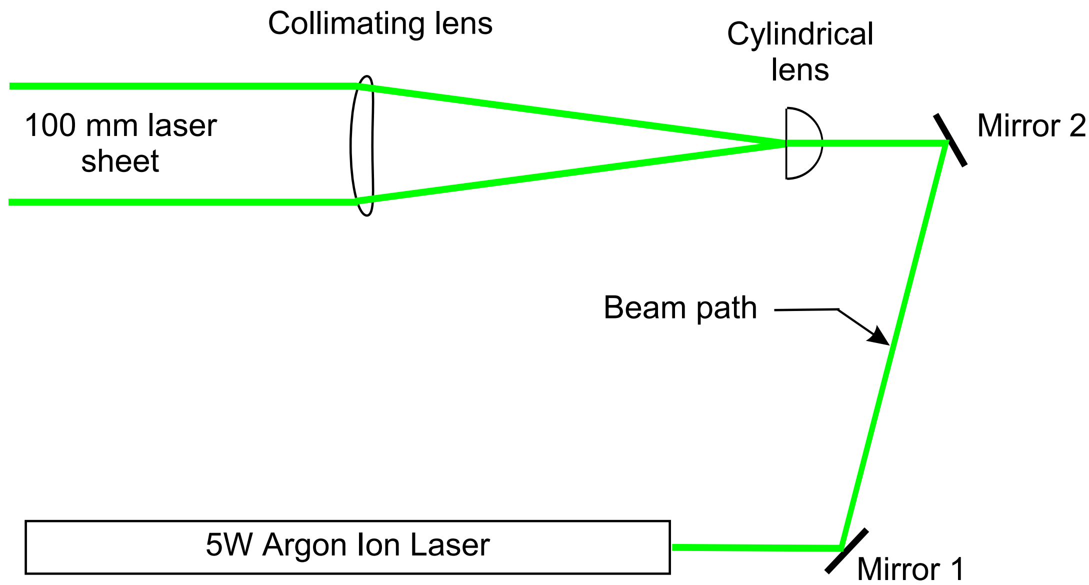

Figure 3.13: Laser sheet optics

Seeding the flow so that the fuel flow could be differentiated from the air flow inside the combustor model proved to be a significant challenge. For simply visualizing the flow within the combustor, 100 μm polystyrene beads were introduced into the flow. Their traces could be easily seen by the naked eye or captured on video tape and appeared to follow the larger flow patterns well. Unfortunately, if they were introduced into either the air or the fuel lines, the other flow would soon become polluted with the beads and could no longer be distinguished. Since the mixing of the air and the fuel was really what was of interest rather than the flow patterns, we had to find a method to keep them separate despite using a closed system. The best choice seemed to be some sort of gas that would rise up after exiting the combustor model and leave the water in the tank. However, if the bubbles were too big, they would not follow the flow very well and would also rise within the combustor since the buoyant forces acting on them were significant. Coloured dyes that could be neutralized once they exited the combustor model were also considered, but nothing suitable was found, and other types of dyes or tracers would quickly pollute the water. Attempts to simply use the 100 μm polystyrene beads and filter them from the fuel flow were not successful, but very fine bubbles were formed in the fuel flow by the flow cavitating within the filter. This phenomenon was then exploited by using a high-pressure water pump (Pump 2 in Fig. 3.12) to inject a small amount of water continuously through a small nozzle into the fuel pipe. The bubbles formed by this method were small enough (on the order of micrometres) to be substantially influenced by the fine-scale turbulence structures in the flow and were therefore much better than larger air bubbles or the beads for visualizing the air/fuel mixing. Since they would slowly rise once exiting the model and most would avoid being recirculated, they were much better suited to this closed system than dyes or similar techniques. They were also much smaller than a pixel in the images taken with the video camera, so the greater the number of bubbles present, the brighter the pixel would be. The intensity of scattered light was therefore closely related to bubble concentration.

Unfortunately, two phenomena meant that for a given concentration of bubbles, the amount of scattered light, and therefore pixel intensity, varied greatly with location. The first phenomenon is how light is scattered off the cavitation bubbles. When viewing the images, one must keep in mind that the bubbles closer to the laser (on the right of the images) will forward-scatter the laser light into the camera, whereas the bubbles toward the head-end of the combustor model (on the left of the images) will back-scatter the laser light. Since the amount of light forward-scattered from a particle can be many times greater than that which is back-scattered, an average bubble on the right of the images will appear brighter than one on the left. The second phenomenon is the fact that the intensity of the laser light in the sheet varies from top to bottom, being strongest at the centre and weakest at the extremities. While we were unable to measure this intensity variation directly, such a measurement at DREV on a similar laser revealed that the intensity of the light near the edges of the sheet was only 14% of that at the centre. This means that bubbles near the centre of the image will appear brighter than those at the edges. Figure 3.14 of an image with constant bubble concentration demonstrates this variation in scattered light intensity with location.

As previously mentioned, distortion of the images due to the round shape of the combustor model and the differences in index of refraction between water, air, and plexiglass, has been kept to a minimum by surrounding the plexiglass model

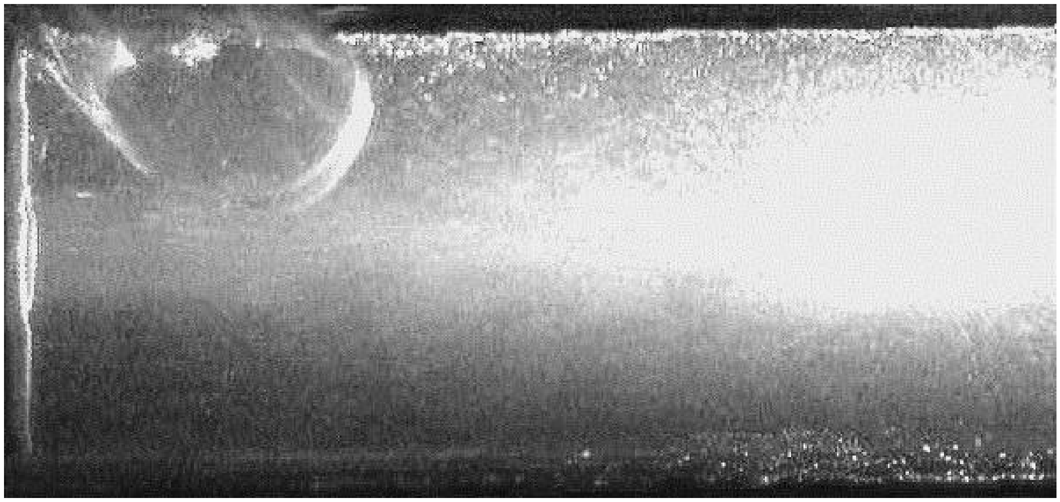

Figure 3.14: Variation in scattered light intensity with location, constant bubble concentration

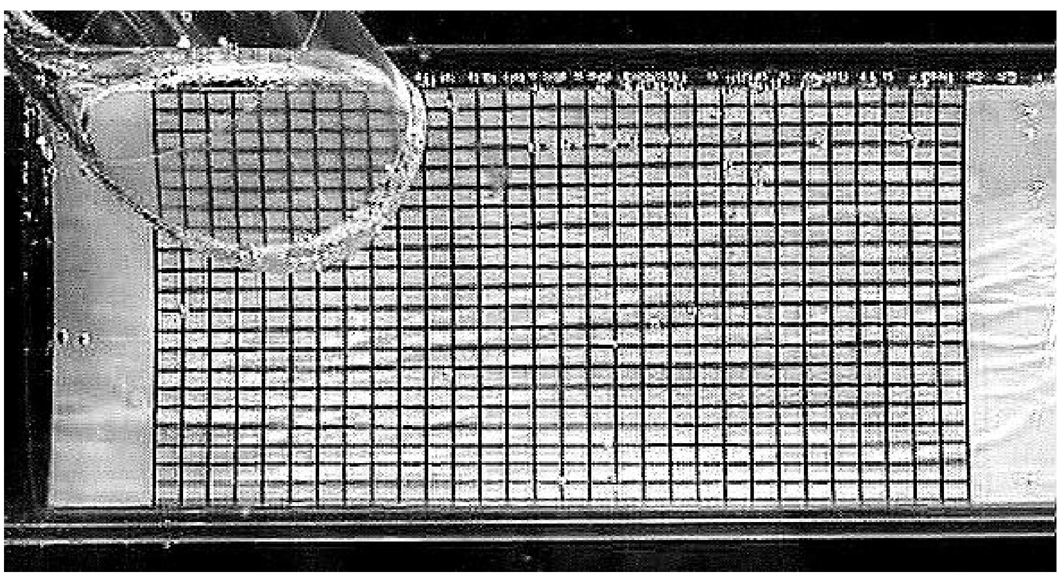

Figure 3.15: Optical distortion of the combustor centreline plane

with the water-filled tank. To demonstrate this a two-dimensional rectangular grid was placed in the centreline of the combustor and an image recorded. As seen in Fig. 3.15, the distortion is small. In fact, the only obvious distortion is where the image is shifted behind the "air" inlet pipe which is at an oblique angle to the camera.

The basic geometry of the water tunnel models was restricted to a combustor with dual inlets spaced 90^o apart circumferentially since this is a favoured configuration for air-launched missiles, and was also one that recurred often in the literature survey. Our geometry differed from a practical missile, however, since it used very long air inlets and main combustor bodies, and had no nozzle. A practical ducted rocket motor would have inlets that hugged the side of the combustor and their ends would face directly forward and be below the missile, and the combustor section would be shorter and have a nozzle at the end. However, our geometry was chosen since it facilitated testing and determining the boundary conditions for the water tunnel testing and CFD modelling. With the addition of a nozzle for combustion tests, it was also easily accommodated in the TNO-PML direct-connect combustion test facility. In fact, apart from the nozzle, the water tunnel and CFD combustor geometries were identical to those used in the direct-connect combustion tests.

Three different air injector and three different fuel injector geometries were tested in the water tunnel and modelled with the CFD at different dome heights (distance from the combustor head to the centre of the air inlets) and air/fuel momentum ratios. (Air/fuel momentum ratio is defined as the product of the air mass flow rate and the air inlet velocity divided by the product of the fuel mass flow rate and the fuel inlet velocity.) Figures 3.16 and 3.17 show schematics of the plexiglass combustor and its inlets. Three different fuel injectors are shown: F0-27 has a centrally-located 27 mm hole, F0-18 has a centrally-located 18 mm hole, and F1-18 has an offset 18 mm hole.

Table 3.2 lists the geometries of the air injectors. Injectors A2, A4, and A6 were used in the water tunnel experiments and the CFD modelling, and later in the combustion tests as well. As previously mentioned, all of the air injector geometries were dual inlet configurations with the inlets spaced 90^o apart circumferentially (see Fig. 3.18).

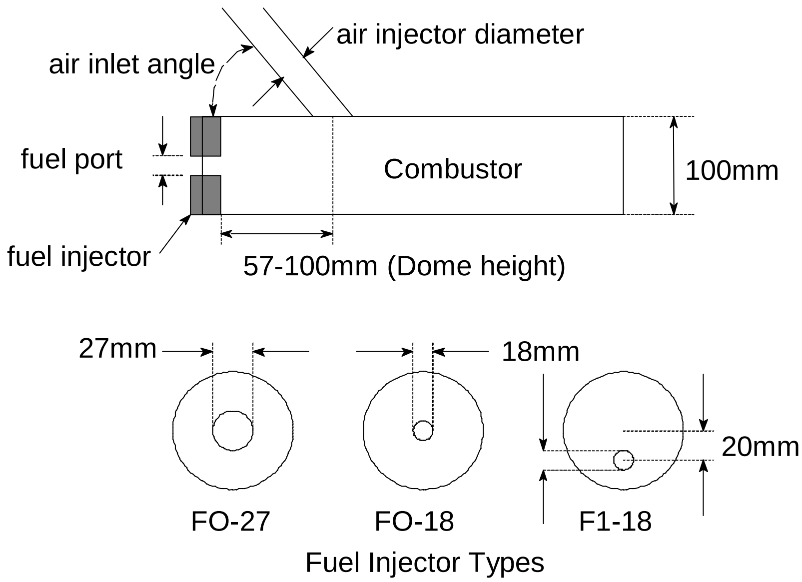

Figure 3.16: Schematic of plexiglass combustor and fuel injectors

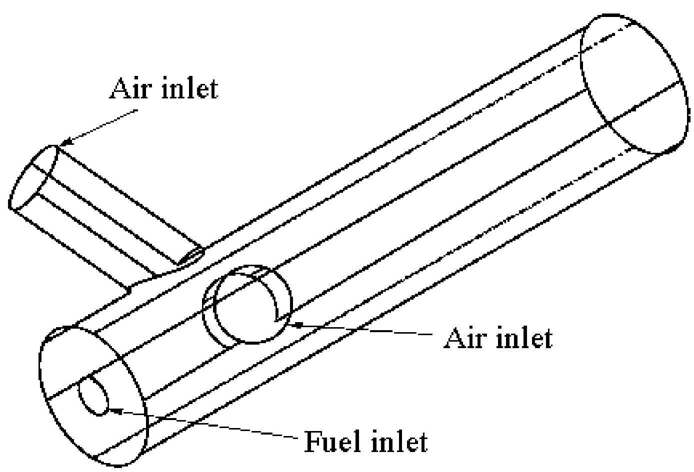

Figure 3.17: Schematic of plexiglass combustor with inlets, isometric view

Table 3.2: Air injector geometries

Model	Shape of air inlet	Air inlet angle	Air inlet diameter
A2	Circular	60º	38.1 mm
A4	Circular	60º	50.8 mm
A6	Circular	90º	50.8 mm

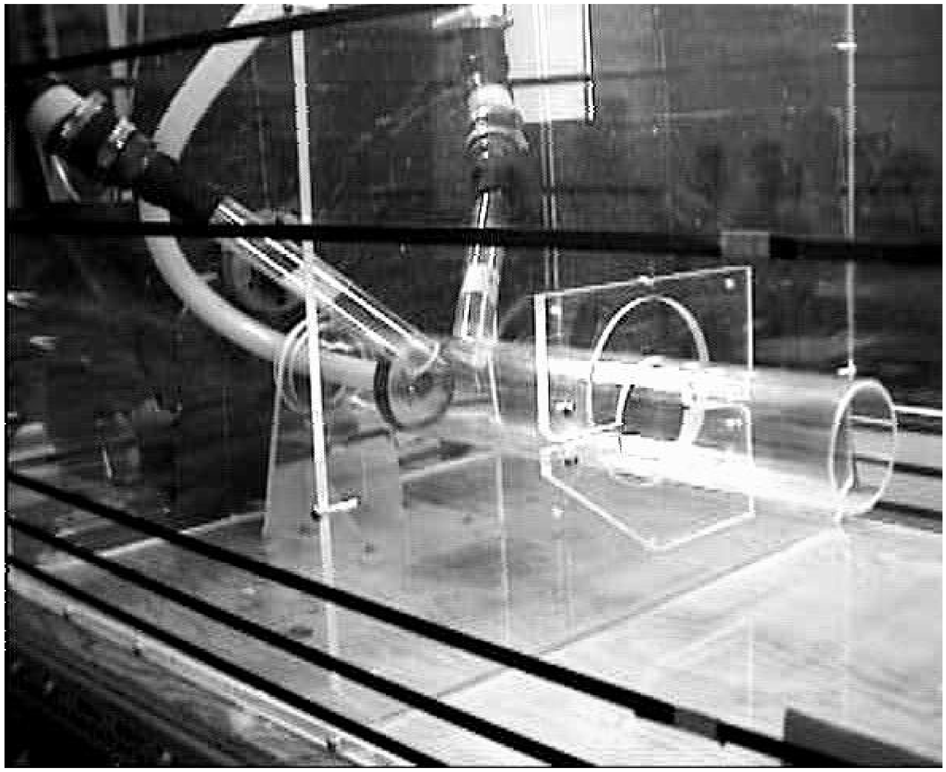

Figure 3.18: Plexiglass model combustor in water tunnel

3.4 Characterization of the Flowfields

Based on the literature survey and previous ducted rocket combustor work carried out at TNO-PML, 12 combinations of geometry and test conditions were chosen to perform the bulk of the water tunnel and CFD work. They were generated from two different air injection angles (60^o and 90^o), two different air injector sizes (38 and 51 mm), two different dome heights (57 and 100 mm measured from head to the centre of the air inlet), three different fuel injectors, and five different air/fuel momentum ratios (3 to 20). Each was tested and modelled at two different combustor Reynolds numbers (approximately 50 000 and 100 000) to make up the 24 possibilities listed in Table 3.3.

3.4.1 Air/Fuel Mixing and Flow Patterns

Good mixing of the air and the fuel in the combustion chamber is a prerequisite for efficient combustor performance. Since mixing occurs on the interface between the air and the fuel, maximizing this interface is desirable. High turbulence levels,

Table 3.3: Configurations for water tunnel experiments and CFD modelling

Test	Air inlet	Air inlet diameter [mm]	Air inlet angle	Fuel inlet	Dome [mm]	Air velocity [m/s]	Fuel velocity [m/s]	Air/fuel mass ratio	Air/fuel momentum ratio	Re combustor
WT1	A2	38.1	60^o	F0-27	57	2.50	2.17	4.59	5.30	98 200
WT2	A2	38.1	60^o	F0-27	57	1.25	1.08	4.59	5.30	49 100
WT3	A2	38.1	60^o	F0-27	57	2.50	1.53	6.50	10.60	93 100
WT4	A2	38.1	60^o	F0-27	57	1.25	0.77	6.50	10.60	46 500
WT5	A2	38.1	60^o	F0-27	57	2.50	1.10	9.07	20.66	89 500
WT6	A2	38.1	60^o	F0-27	57	1.25	0.55	9.07	20.66	44 800
WT7	A4	50.8	60^o	F0-27	57	1.40	2.14	4.64	3.04	97 600
WT8	A4	50.8	60^o	F0-27	57	0.70	1.07	4.64	3.04	48 800
WT9	A4	50.8	60^o	F0-27	57	1.40	1.08	9.21	11.98	89 000
WT10	A4	50.8	60^o	F0-27	57	0.70	0.54	9.21	11.98	44 500
WT11	A4	50.8	60^o	F0-18	57	1.40	2.43	9.19	5.30	89 000
WT12	A4	50.8	60^o	F0-18	57	0.70	1.21	9.19	5.30	44 500
WT13	A4	50.8	60^o	F1-18	57	1.40	2.43	9.19	5.30	89 000
WT14	A4	50.8	60^o	F1-18	57	0.70	1.21	9.19	5.30	44 500
WT15	A4	50.8	60^o	F0-27	100	1.40	2.14	4.64	3.04	97 600
WT16	A4	50.8	60^o	F0-27	100	0.70	1.07	4.64	3.04	48 800
WT17	A4	50.8	60^o	F0-27	100	1.40	1.08	9.21	11.98	89 000
WT18	A4	50.8	60^o	F0-27	100	0.70	0.54	9.21	11.98	44 500
WT19	A6	50.8	90^o	F0-27	57	1.40	2.14	4.64	3.04	97 600
WT20	A6	50.8	90^o	F0-27	57	0.70	1.07	4.64	3.04	48 8006
WT21	A6	50.8	90^o	F0-27	57	1.40	1.08	9.21	11.98	89 000
WT22	A6	50.8	90^o	F0-27	57	0.70	0.54	9.21	11.98	44 500
WT23	A6	50.8	90^o	F0-18	57	1.40	2.43	9.19	5.30	89 000
WT24	A6	50.8	90^o	F0-18	57	0.70	1.21	9.19	5.30	44 500

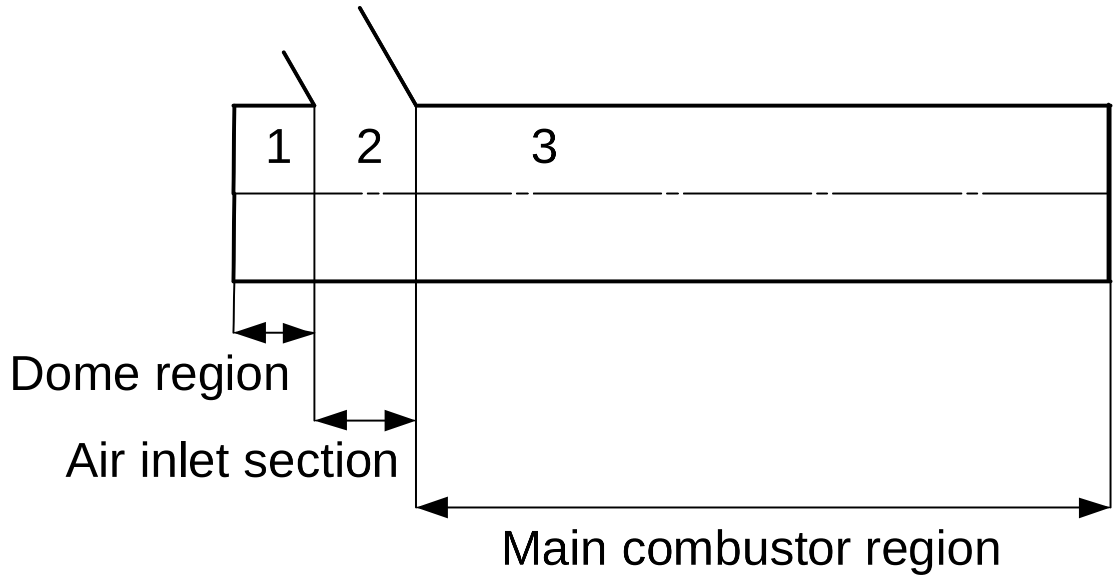

Figure 3.19: Combustion chamber regions

which are associated with high flow velocities, along with well-chosen air/fuel momentum ratios, were necessary for good mixing. To facilitate the description of the mixing, the combustor can be divided in three distinct regions, namely the dome region, the air inlet section, and the main combustor region (Fig. 3.19).

While the exact flow patterns seen from the water tunnel images varied greatly depending on configuration, particularly on air/fuel momentum ratio, two basic flow features appeared to be common. The first, seen in Fig. 3.20, is a pair of longitudinal vortices that are a continuation of the high-speed flow from the air inlets. These structures corkscrew from below the centreline in the air inlet section and continue downstream toward the nozzle. They entrain and transport the fluid from the dome and air inlets regions of the combustor into the main combustor region. They also add swirl to the flow and improve mixing by increasing the interface area between the air and the fuel.

The other basic flow phenomenon is a recirculation zone from the air inlet section into the dome region. Its purpose is to supply air from the air inlet region to the dome region for mixing with the fuel, and its exact shape is dependent on the strength of the fuel jet. At high air/fuel momentum ratios, the recirculation zone appears to fill the entire height of the dome. However, when the fuel jet is moderately strong, this recirculation zone decreases in height and turns back on itself below the fuel jet as shown in Fig. 3.21. A second recirculation zone then forms above the fuel

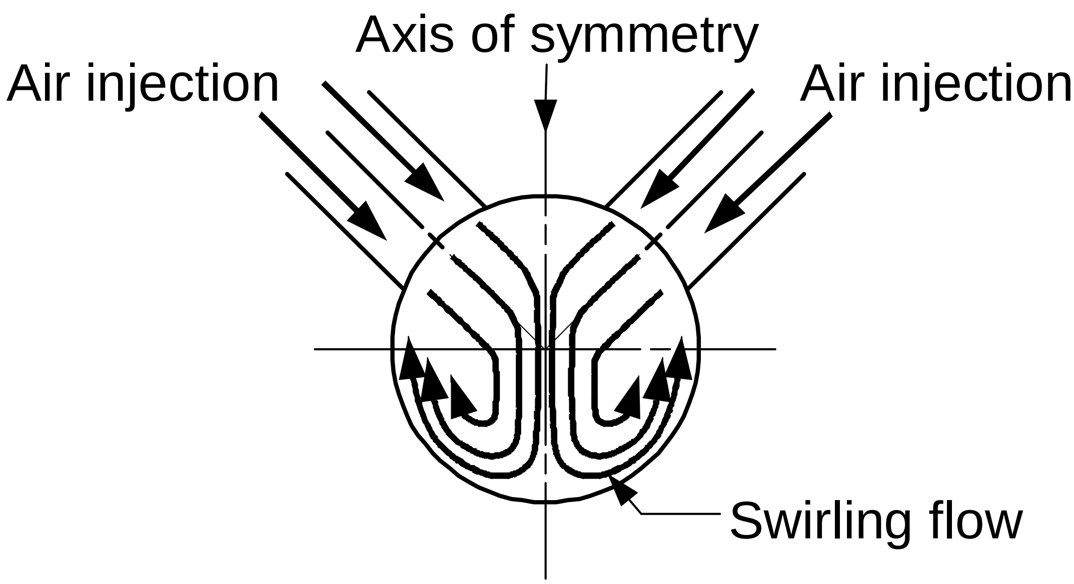

Figure 3.20: Longitudinal vortices (end view)

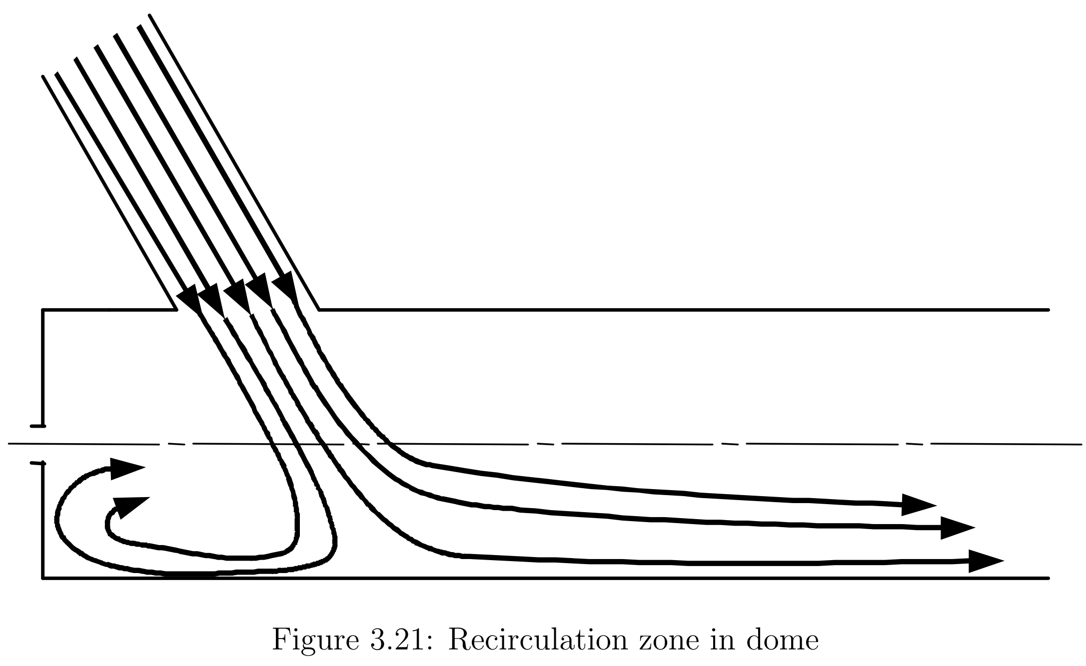

Figure 3.21: Recirculation zone in dome

jet and rotates in the opposite direction. If the fuel jet is stronger still, however, mixing is relatively poor since the fuel jet does not break up in the air inlet section; it continues, relatively intact, into the main combustor region.

Due to the high Reynolds numbers of the flowfields, no dead zones were observed anywhere in the combustor except in a few instances when some bubbles representing the fuel appeared trapped for a time at the extreme upper and lower left of the combustor, above and below the fuel jet. As presented in the next section, however, all configurations demonstrated time-dependent flow and in each instance, the flowfield would eventually change enough to dislodge any trapped fluid and convect it downstream.

3.4.2 Flow Stability

One important advantage of the water tunnel over the CFD modelling was that the unsteady flow phenomena could be observed. The next series of figures show sequences of six images of the flowfield in the combustor of all of the combinations tested, taken at 30 frames per second, but only for the tests at a Reynolds number of approximately 50 000. This lower Reynolds number was chosen since evolution of the fluctuations in the fuel jet is shown more clearly than at the higher Reynolds number because of the lower flow rate. However, one combination will also be shown in the next subsection at the higher Reynolds number to show the lack of evidence of Reynolds number dependence. All images were taken on the longitudinal centreline plane of the combustor where, assuming symmetry in the flows and the geometry, there should be no flow normal to the image. The fuel jet enters from the left, and the circular reflection just above is where the air inlet is attached to the combustor. Due to the nature of the flowfield and the optical effects previously mentioned, the most obvious changes in the flowfield can be seen near the fuel jet so that is where the observations of the stability of the flow will be focused.

Figure 3.22 shows a series of six consecutive images of configuration WT2. As with all the images, the contrast and brightness have been adjusted so that the changing shape of the fuel jet can be more easily seen. The fuel jet appears stable until it meets the air jets. In the first image, the fuel jet is longer than in the next two images; in the fourth and fifth images, the fuel jet is longer once again and the extra length is shed and travels downstream in the sixth image. The structures being shed from the fuel jet disappear quickly from view, and are small compared to those that will be seen for some of the remaining combinations.

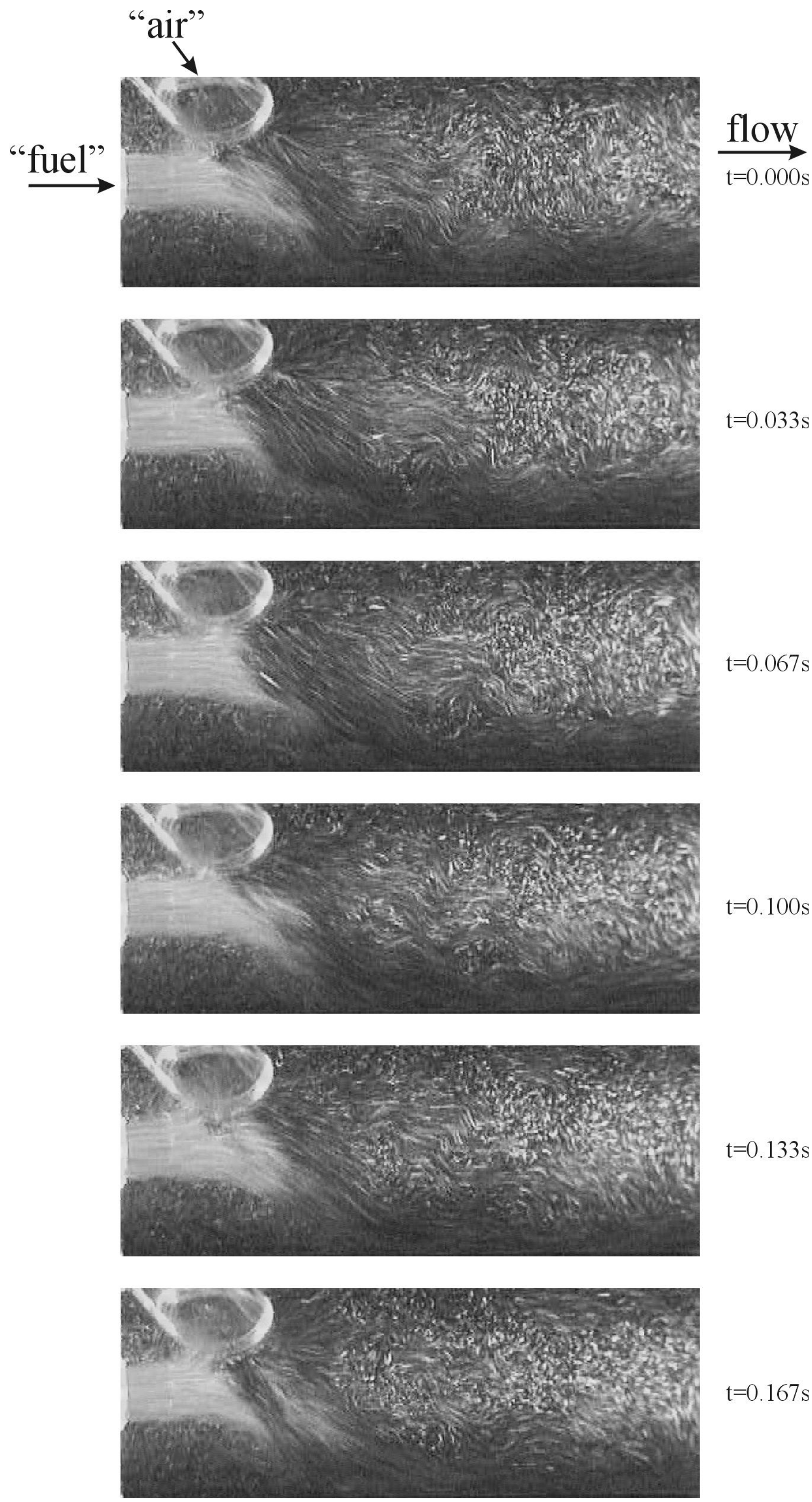

Figure 3.22: Configuration WT2, air injector A2, fuel injector F0-27, air/fuel momentum ratio = 5.3

Figure 3.23 shows configuration WT4 that has a geometry identical to configuration WT2 but has an air/fuel momentum ratio which is twice as high. The air jets are much stronger, and any fluctuations in the shape of the fuel jet are smaller. The lower half of the fuel jet is pulled along somewhat toward the bottom and the exit of the combustor. Figure 3.24 also has a similar geometry, but with even stronger air jets. As with configuration WT4, the shape of the fuel jet remains fairly constant, with only the lower part fluctuating periodically and being carried away by the air jets. These first three configurations with the A2 air injector and F0-27 fuel injector appeared to be the most stable of the combinations tested in the water tunnel, but significant changes in fuel jet size and shape still occurred between the frames as shown.

The next geometry tested used the A4 air injector, which has the same 60° injection angle as the A2 injector but a larger 57 mm inlet diameter rather than a 38 mm inlet. Configuration WT8, shown in Fig. 3.25, has the same air/fuel mass flow ratio as for configuration WT2, but the air velocity and momentum are much lower. The fuel jet is therefore not as abruptly cut off as for configuration WT2, and continues for a distance past the air jets. In the first two frames, the end of the fuel jet sheds itself intermittently, and it remains unstable in the remaining frames. Configuration WT10 shown in Fig. 3.26 has an air/fuel momentum ratio four times as high, and once again the instability of the end of the fuel jet can be seen. The pieces of the fuel jet that break off can be seen to dissipate more quickly than in configuration WT8, however, because of the relatively higher air momentum.

Configuration WT12, shown in Fig. 3.27, uses the same A4 air injector as the previous two configurations, but the F0-18 fuel injector instead. Therefore, for the same air/fuel mass flow ratio, the air/fuel momentum ratio will be lower. The penetration of the fuel jet past the air jets is similar to configuration WT8 that has a similar air/fuel velocity ratio, though the air/fuel mass and momentum ratios are different because the fuel injector sizes differ. The stability of the ends of the fuel jet is similar as well.

Configuration WT14 is presented in Fig. 3.28 and is identical to configuration WT12 except that the port in the fuel injector is placed off centre near the bottom of the combustor. Because it is lower down, the fuel jet impinges against the air jets in a different location than for configurations WT8 and WT12. However, the tip of the fuel jet is still shed with approximately the same frequency, though the size of the fluctuations is smaller than for configurations WT8 and WT12.

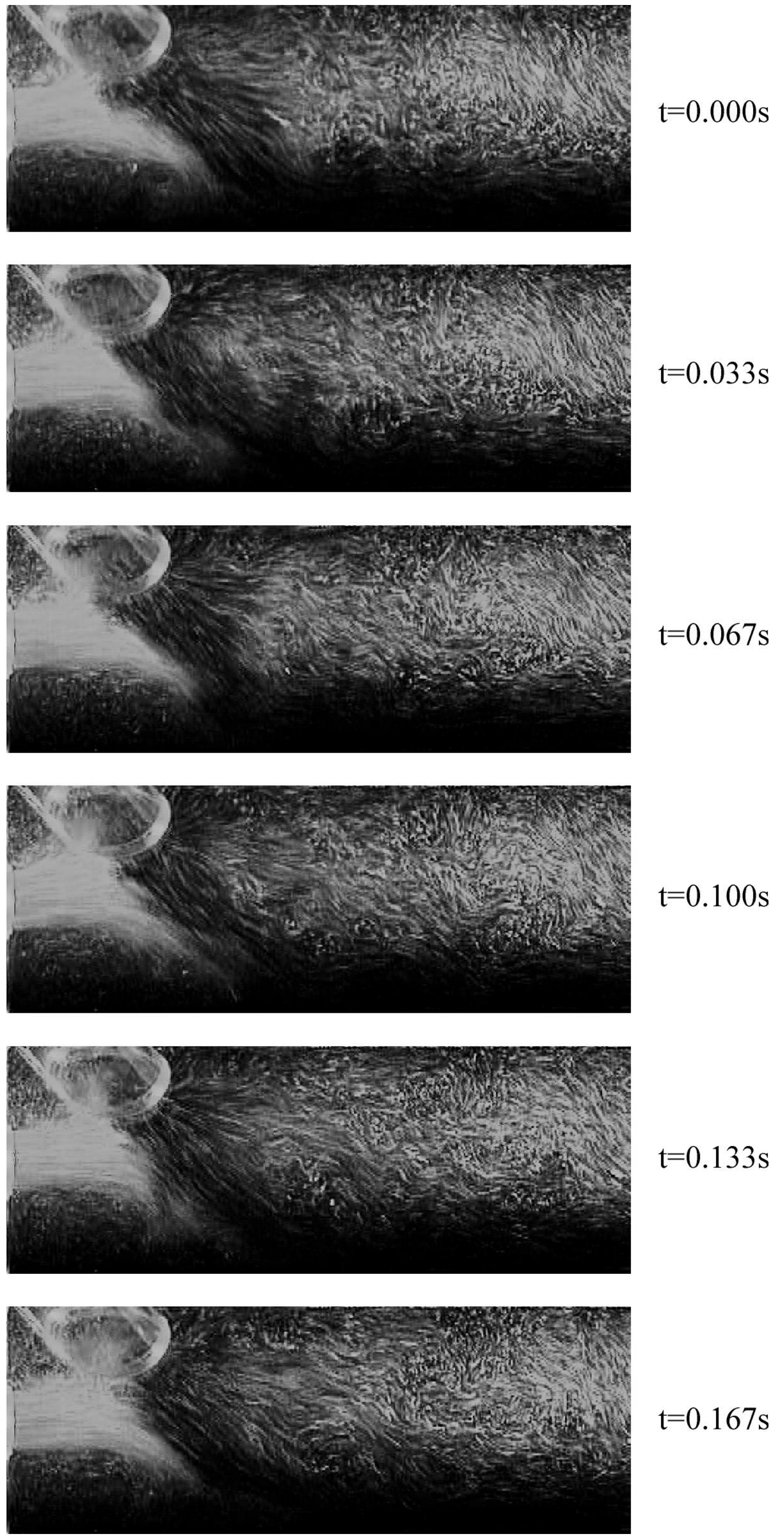

Figure 3.23: Configuration WT4, air injector A2, fuel injector F0-27, air/fuel momentum ratio = 10.6

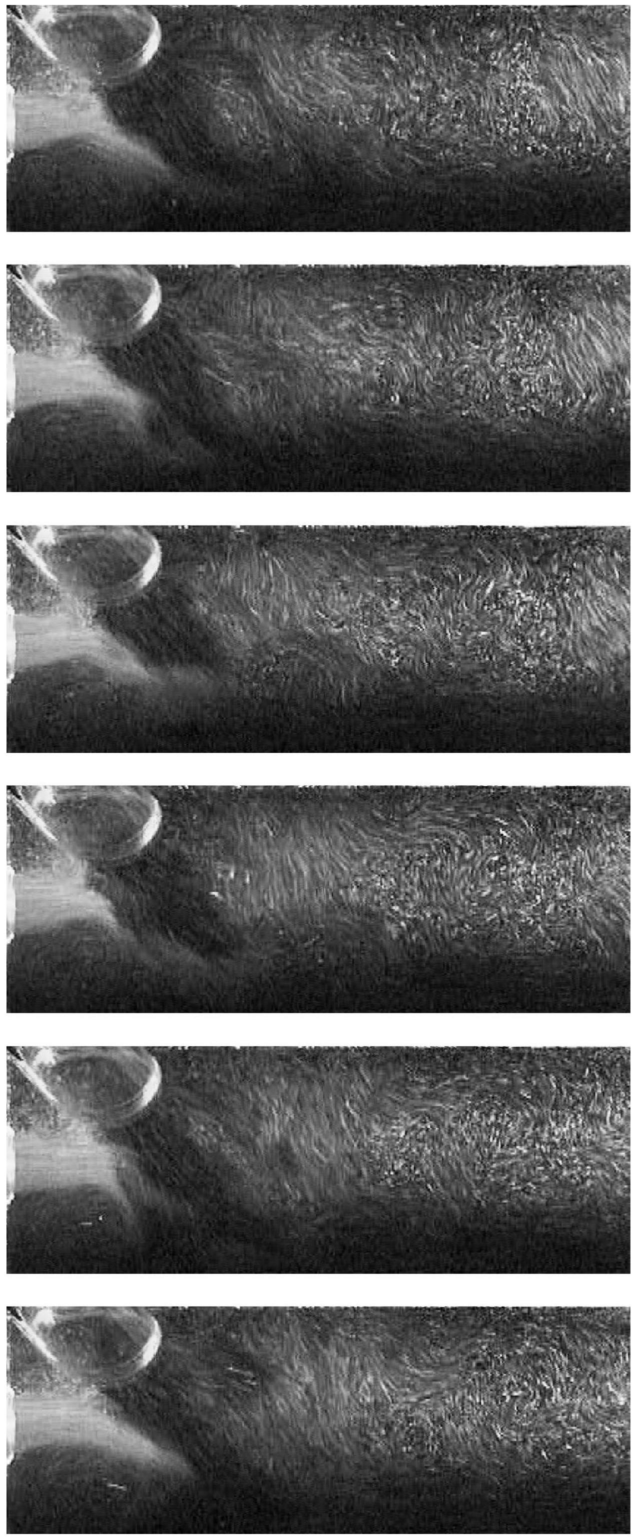

t=0.000s

t=0.033s

t=0.067s

t=0.100s

t=0.133s

t=0.167s

Figure 3.24: Configuration WT6, air injector A2, fuel injector F0-27, air/fuel momentum ratio = 20.66

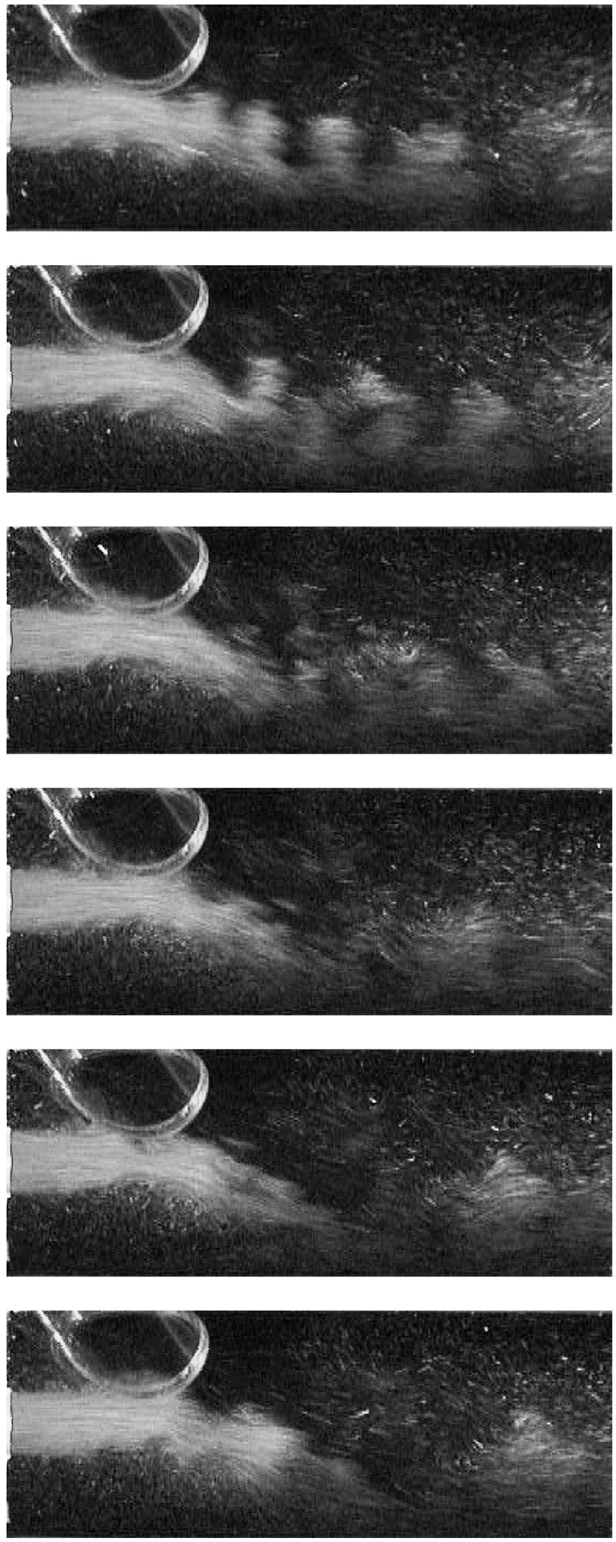

t=0.000s

t=0.033s

t=0.067s

t=0.100s

t=0.133s

t=0.167s

Figure 3.25: Configuration WT8, air injector A4, fuel injector F0-27, air/fuel momentum ratio = 3.04

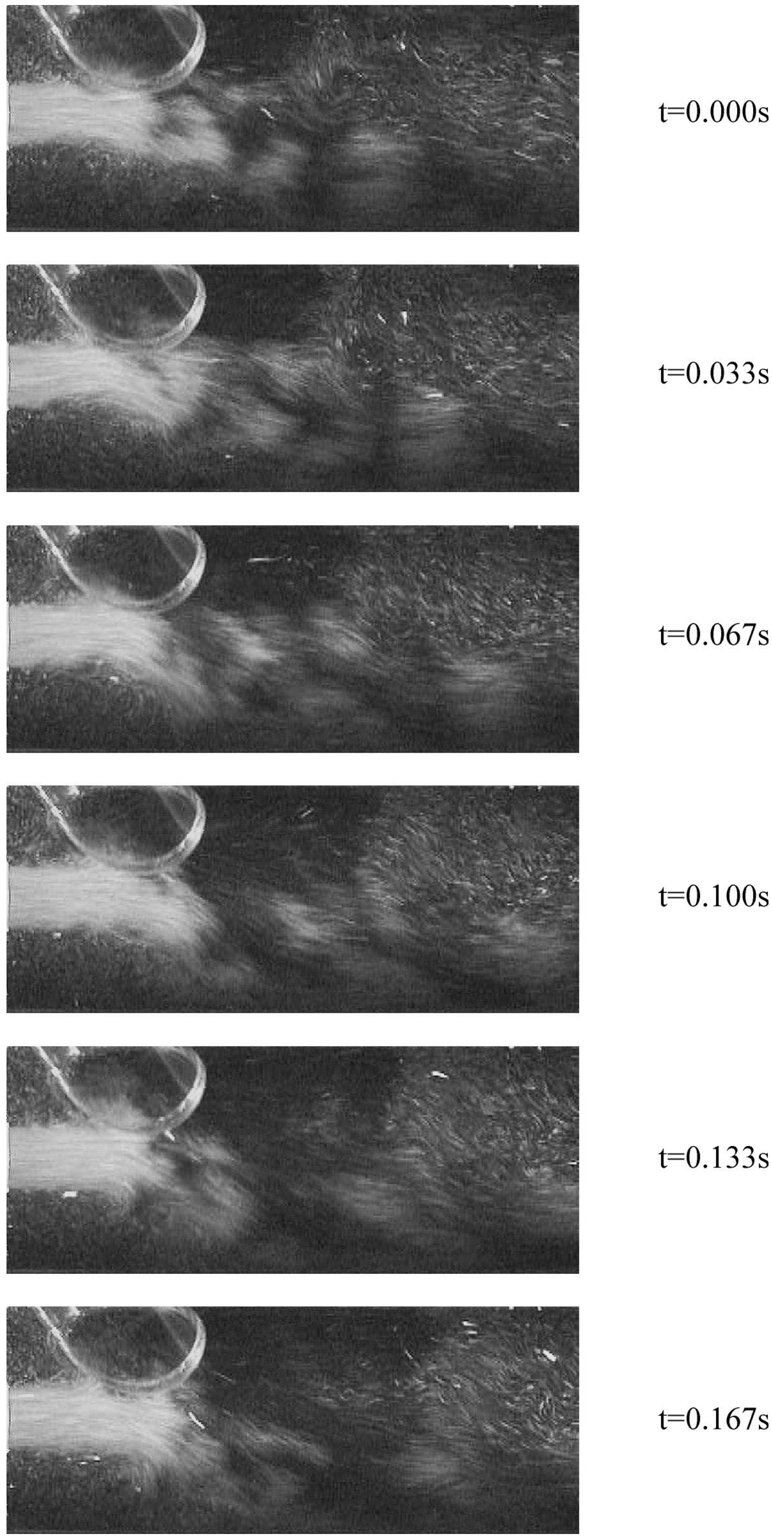

Figure 3.26: Configuration WT10, air injector A4, fuel injector F0-27, air/fuel momentum ratio = 11.98

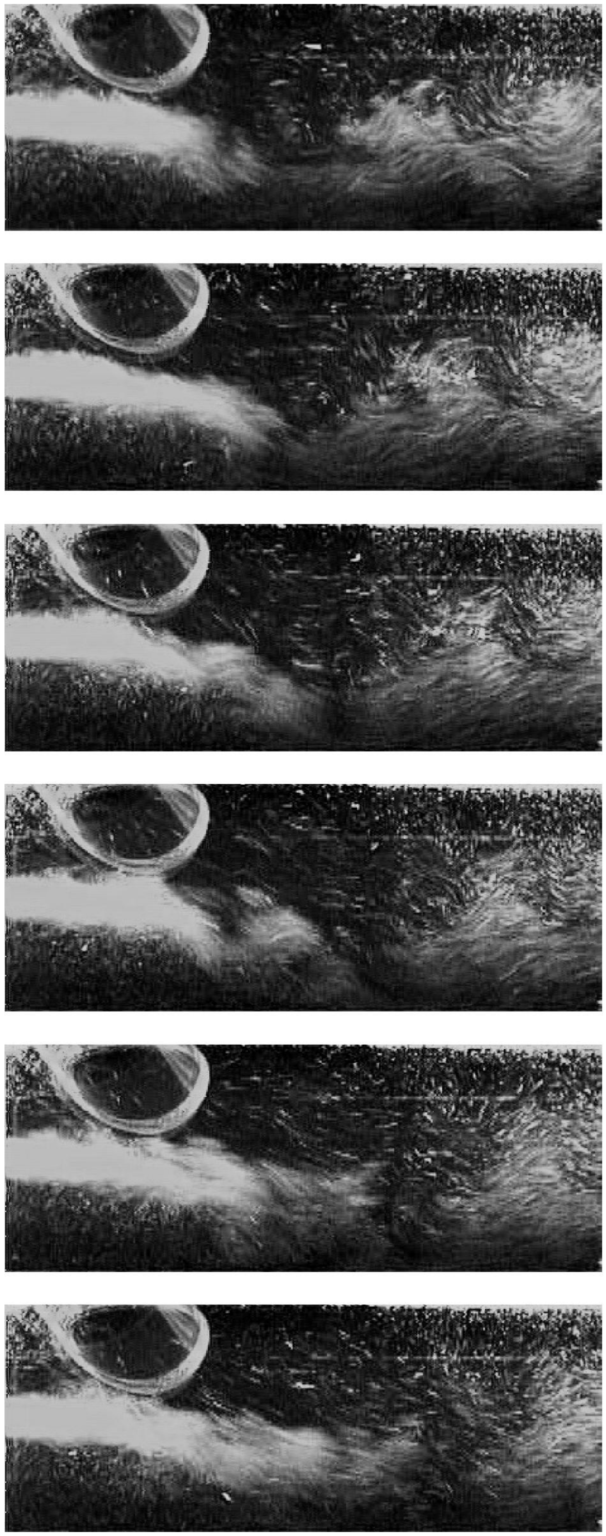

t=0.000s

t=0.033s

t=0.067s

t=0.100s

t=0.133s

t=0.167s

Figure 3.27: Configuration WT12, air injector A4, fuel injector F0-18, air/fuel momentum ratio = 5.3

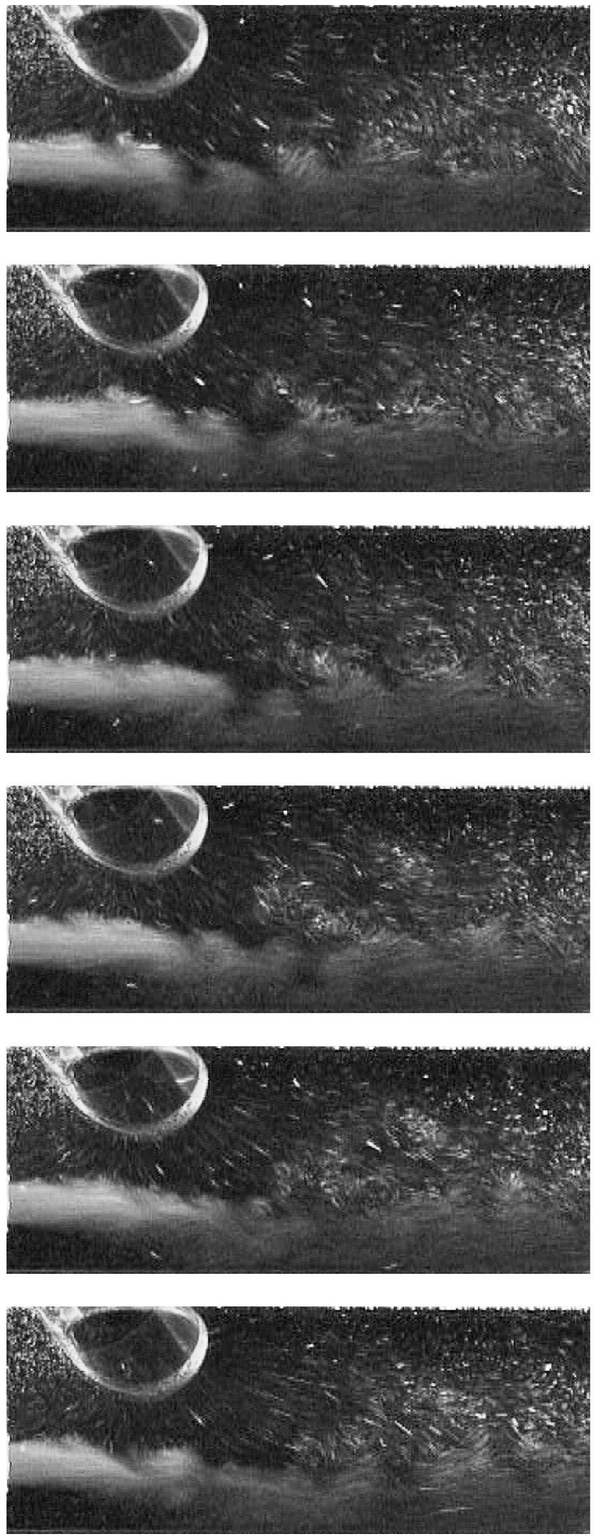
t=0.000s

t=0.033s

t=0.067s

t=0.100s

t=0.133s

t=0.167s

Figure 3.28: Configuration WT14, air injector A4, fuel injector F1-18, air/fuel momentum ratio = 5.3

Figures 3.29 and 3.30 show configurations WT16 and WT18 that are identical to configurations WT8 and WT10, except that they use a dome height of 100 mm rather than 57 mm. Unfortunately these images appear to be brighter, perhaps due to differences in the seeding of the fuel jet. As seen just above where the fuel enters the combustor in configurations WT16 and WT18, there are also some bubbles, larger than the average bubbles used to seed the fuel jet in the other configurations, both stuck to the wall and trapped in the recirculation zone. These not only reflect considerable light into the camera, but provide light to re-illuminate the fuel jet further downstream. As a result the fuel jet is much brighter, even where it may be dilute, and appears to extend well past the air inlets. Despite this, the breaking-up of the fuel jets can still be seen to take place at about the same point relative to the air inlets as for configurations WT8 and WT10.

The remaining three configurations use the A6 air injector which is identical to the A4 injector except for an injection angle of 90°. Figures 3.31 shows the series of images for configuration WT20, and when compared to configuration WT8 (identical except for the air injector angle) the fuel jet can be seen to be more unstable and the size of the flow structures shed from the end of the fuel jet are larger. The upper part of the fuel jet can also be seen to be "cut" by the air jet just at the left-hand-side of the air inlet at 0.067 s and 0.133 s.

Unfortunately, the images shown in Fig. 3.32 indicate that the fuel injector shifted toward the air injector during the test, thus reducing the dome height of 57 mm by a few millimetres. However, the relatively large flow structures seen in Fig. 3.31 can also be seen to shed from the end of the fuel jet, and they dissipate more quickly because of the increased air/fuel momentum ratio.

Configuration WT24, shown in Fig. 3.33, has the same air/fuel mass ratio as configuration WT22 but a lower air/fuel momentum ratio because of the smaller fuel injector. Because of the higher fuel velocity, the fuel jet extends further than in configuration WT22, but the same lack of stability can be seen. Flow structures of similar size break off, however, as in both of the previous two configurations.

All twelve configurations shown in these series of images demonstrate time-dependent flow, with most of the evidence of large-scale fluctuations occurring downstream of where the air and the fuel jets meet. The configurations that exhibited the least frame-to-frame variation in flow structure use the A2 injector and therefore could be considered the most stable. The configurations using the A4 air injector showed more rapid and larger fluctuations in fuel jet shape, so therefore the smaller

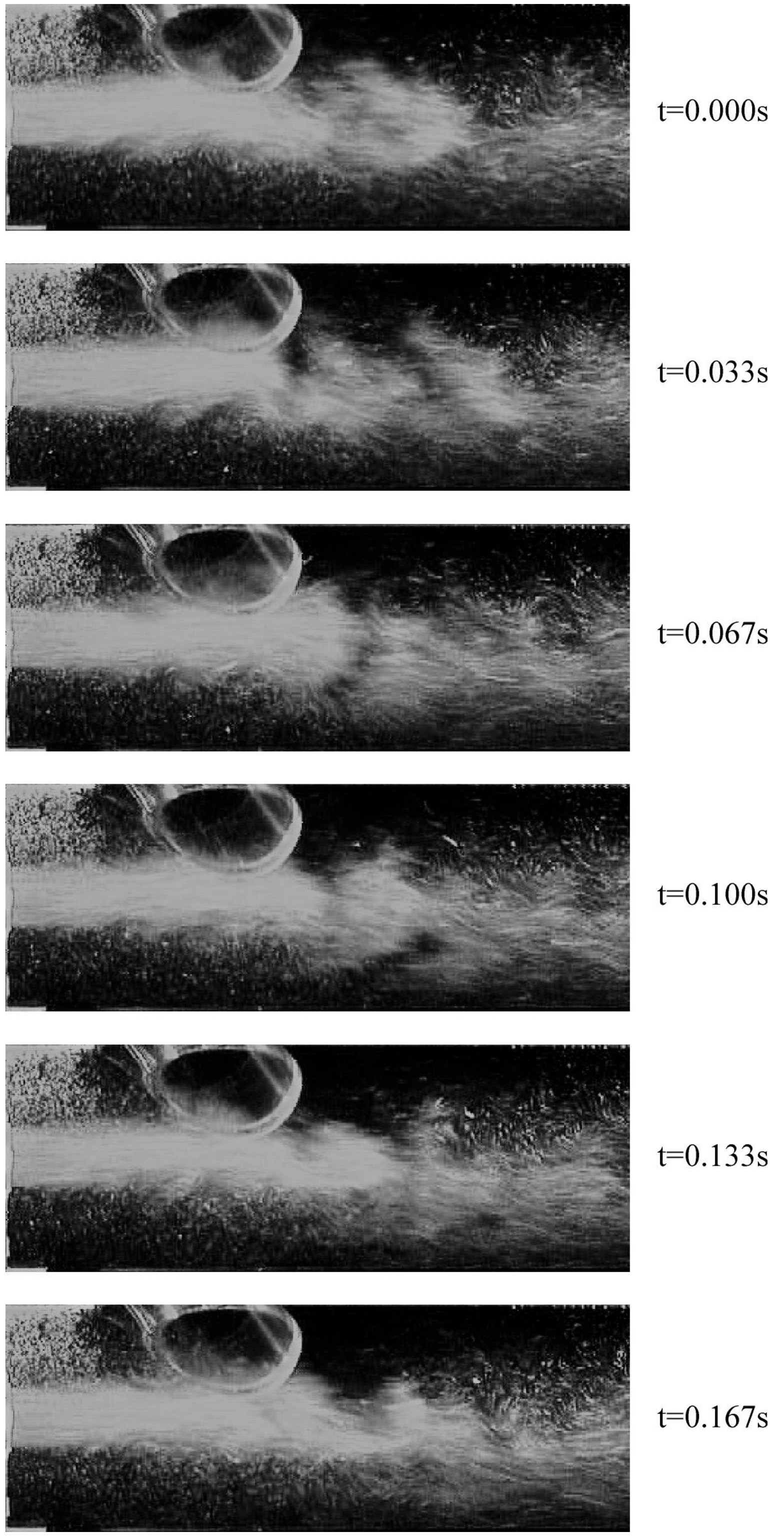

Figure 3.29: Configuration WT16, air injector A4, fuel injector F0-27, air/fuel momentum ratio = 3.04, dome height 100 mm

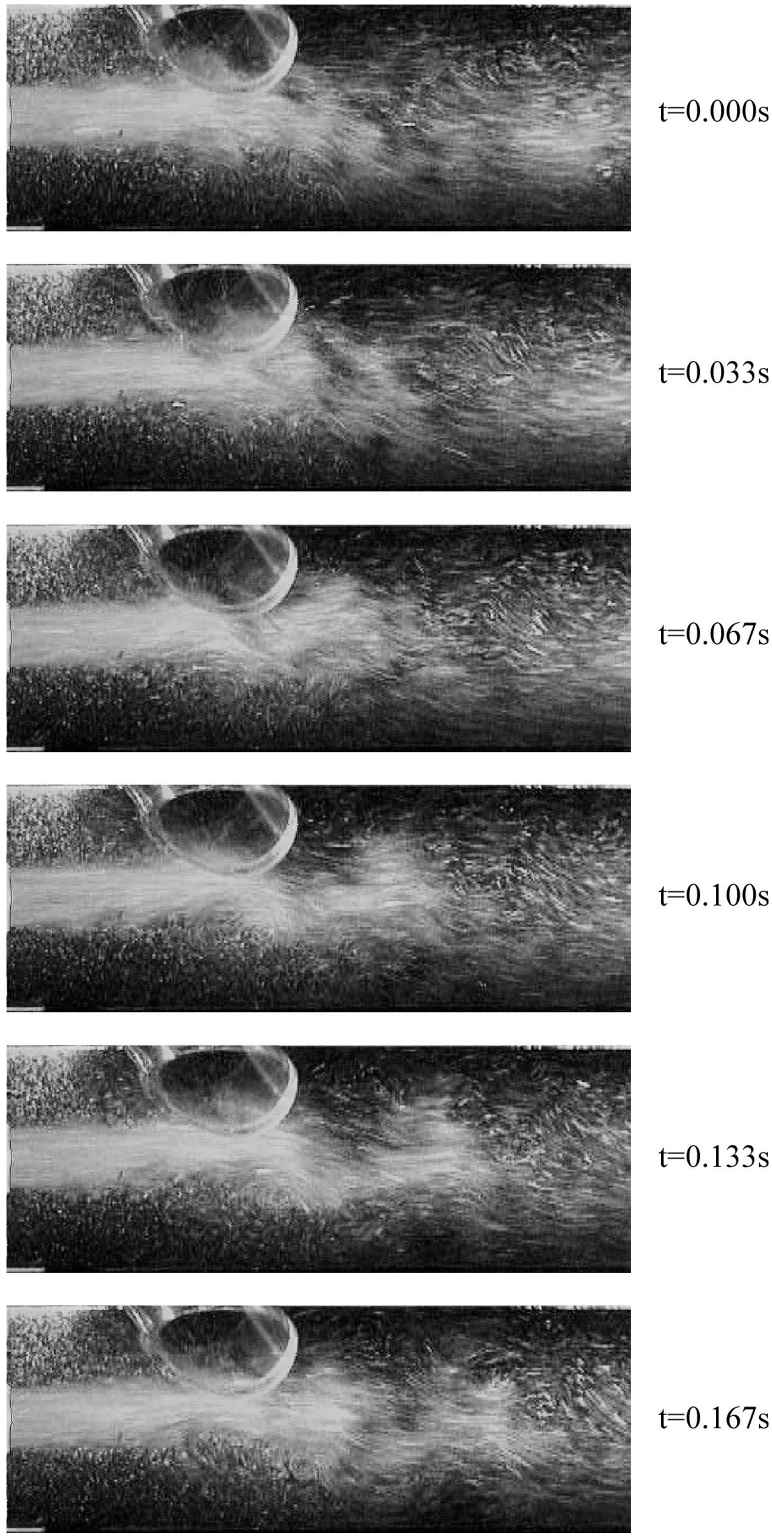

Figure 3.30: Configuration WT18, air injector A4, fuel injector F0-27, air/fuel momentum ratio = 11.98, dome height 100 mm

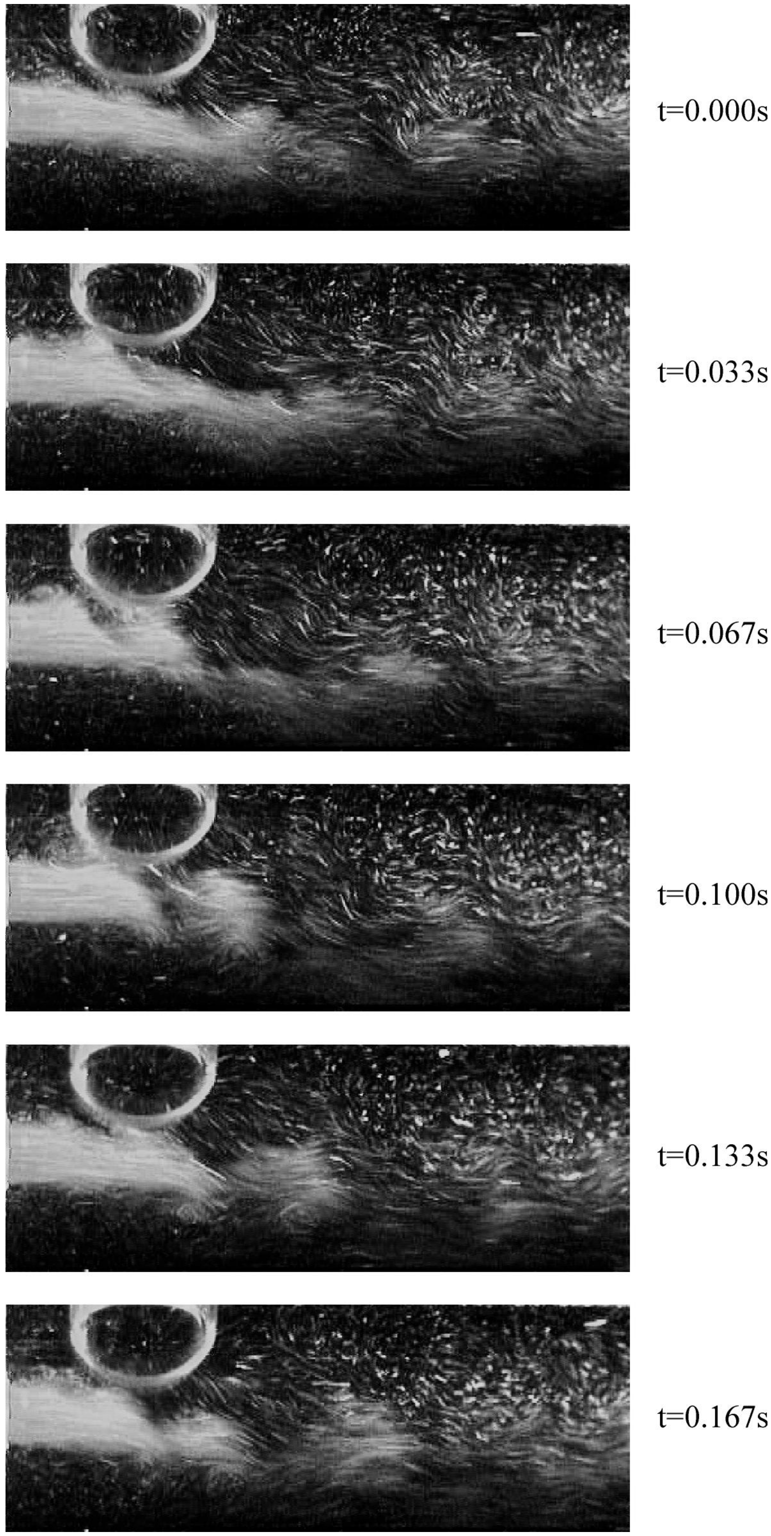

Figure 3.31: Configuration WT20, air injector A6, fuel injector F0-27, air/fuel momentum ratio = 3.04

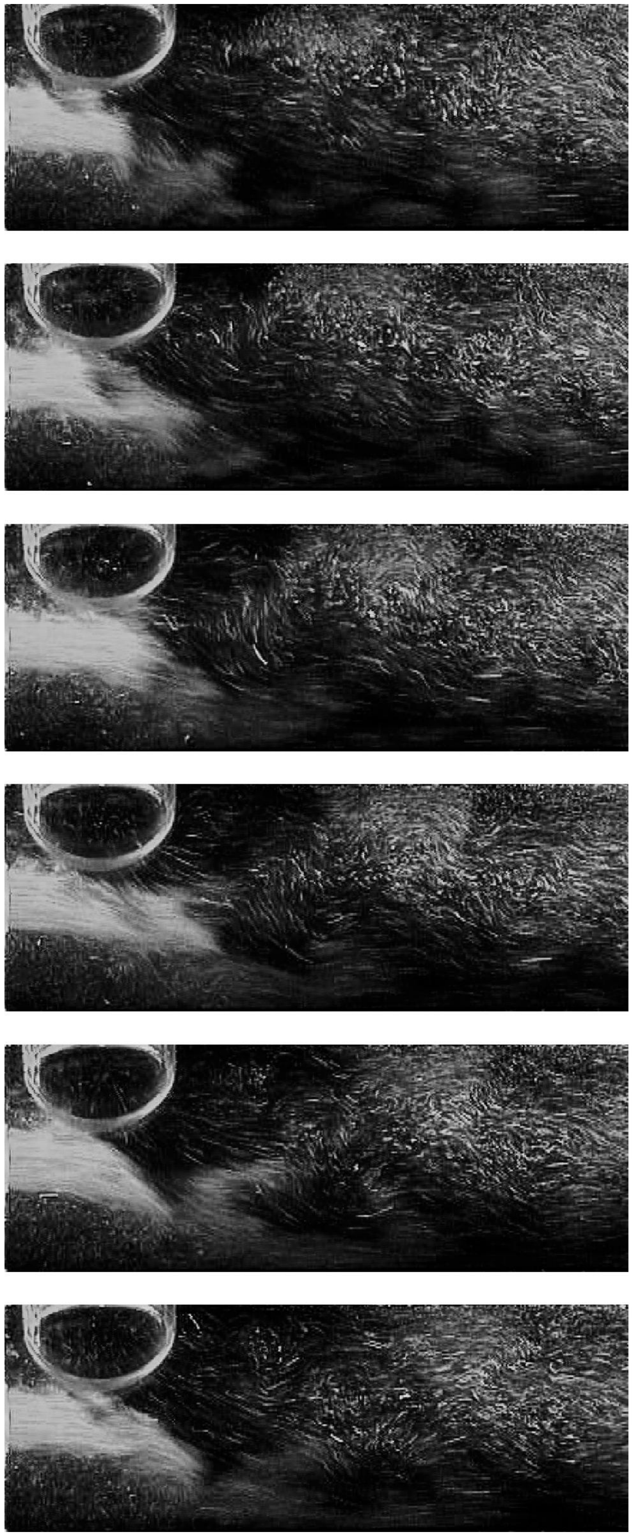

t=0.000s

t=0.033s

t=0.067s

t=0.100s

t=0.133s

t=0.167s

Figure 3.32: Configuration WT22, air injector A6, fuel injector F0-27, air/fuel momentum ratio = 11.98

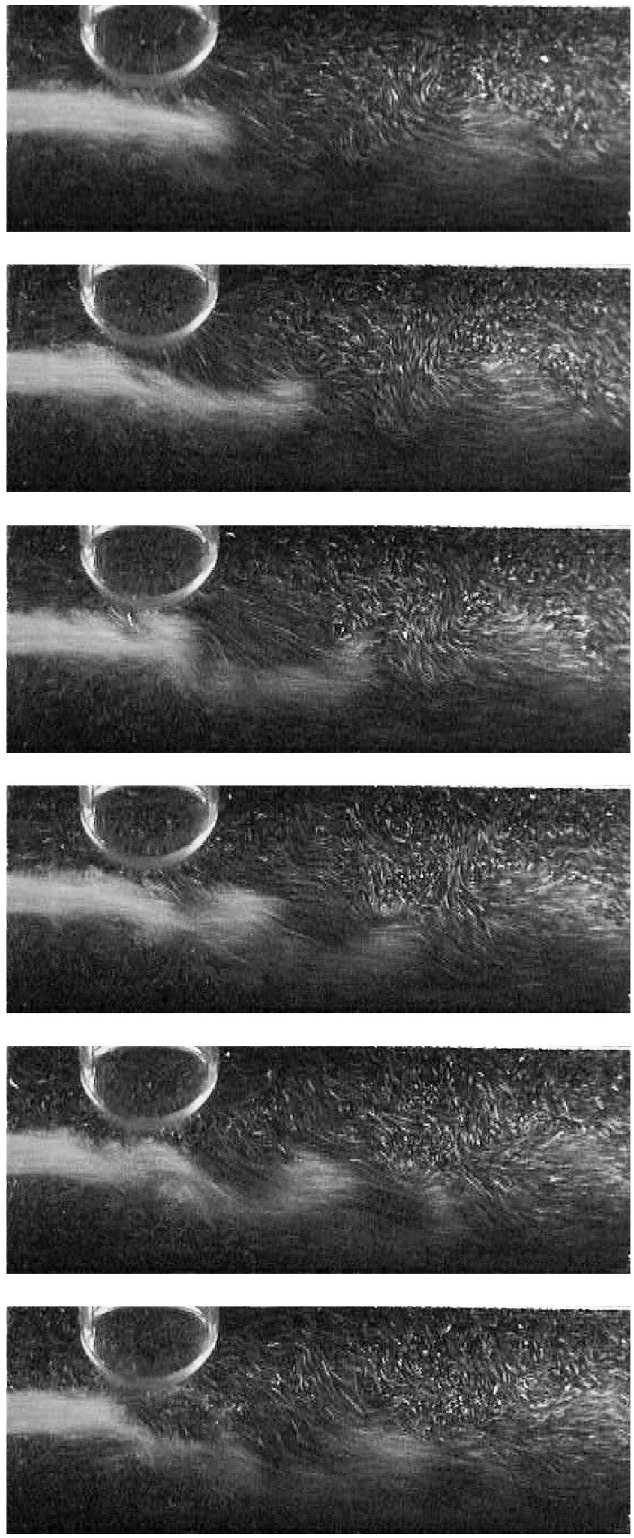

t=0.000s

t=0.033s

t=0.067s

t=0.100s

t=0.133s

t=0.167s

Figure 3.33: Configuration WT24, air injector A6, fuel injector F0-18, air/fuel momentum ratio = 5.3

diameter air injector increased the stability of the fuel jet.

Changing to a smaller diameter fuel injector for a given air/fuel mass ratio lengthened the fuel jet, but the frequency and approximate size of the scale of the fluctuations remained similar. When the location of the inlet for this smaller fuel injector was moved off-centre to the bottom of the combustor, the fluctuations shed with the same frequency as for the other A4 air injector configurations, though the fluctuations were smaller. Increasing the dome height for the A4 air injector, F0-27 fuel injector combinations did not appear to change the location or the frequency of the break-up of the fuel jets. The length of the fluctuations seemed similar, although optical differences in the images made it difficult to compare the overall size of the fluctuations. Therefore, for the configurations examined, dome height and fuel injector size or location did not appear to affect the overall stability of the fuel jet.

The largest variations in the size and shape of the fuel jet occurred for the configurations with the A6 air injector and its 90^o inlet angle. Not only were the size and shape of the fluctuations not as consistent as for the 60^o injectors, but the location of the break-up of the fuel jet varied more, both horizontally and vertically. In addition, the fluid shed from the fuel jet could follow different downstream trajectories as well. Increased air injection angle therefore had an adverse effect on the stability of the fuel jet.

Despite the apparent differences in fuel jet stability, all of the above configurations demonstrated some degree of air/fuel mixing by the time the flow was past the air inlets, though this could not be quantified. The results from the CFD modelling work will give a more quantitative ranking of the configurations, though the effect of fuel jet stability on the air/fuel mixing will not be taken into account. In the absence of a method to quantify the degree of mixing in the water tunnel or time-dependent CFD calculations, however, the only way for us to assess the effect of stability on the mixing would be to do properly-instrumented direct-connect combustion tests in actual combustors[2]. Since no "violently-unstable" behaviour was observed in the water tunnel experiments, all of the above configurations therefore appeared suitable for testing in the direct-connect facility.

[2]Unfortunately, these type of measurements were not available for most of the direct-connect experiments, but recently some have been made for one configuration and are presented in Section 5.6.

3.4.3 Reynolds Number Effects

As previously mentioned, the applicability of the water tunnel results to the flow in an actual combustor in the direct-connect facility using real fuel and air depends on whether or not there is any Reynolds number dependence in the water tunnel flow. If not, then the flowfield observed in the water tunnel should be representative of the much higher Reynolds number flowfield in the actual combustor in the absence of combustion and any compressibility effects. Figure 3.34 shows two series of frames for the same combination of air injector, fuel injector, and air/fuel momentum ratio at two different Reynolds numbers that encompassed the range examined in the water tunnel. Since the rate of seeding into the simulated fuel jet is the same for each configuration, the areas in the flowfield with some fuel present are brighter for the lower Reynolds number configuration. Once this is taken into account, however, along with expected frame-to-frame variation as seen from the previous figures, no evidence of Reynolds number dependence for the size and shape of the fuel jets can be observed. As for fluctuations in the size and shape of the fuel jet, the fuel jet in the higher Reynolds number configuration appears smoother, but this is an effect of having to use the same shutter speed at twice the flow rate. The result is that the flowfield is "averaged" more than for the lower Reynolds number case. The changes in size and shape of the fuel jet are similar in the two cases, but happen at a much faster rate for the higher Reynolds number configuration. The evolution of the shedding was therefore not captured in the images to the same extent as the lower Reynolds number frames. These results were typical of all the combinations.

3.5 Summary of the Water Tunnel Results

Because of the hostile environment inside combustors, measurements of the flowfield are difficult to make. Even in the absence of combustion, speeds are so high that special techniques must be used. However, if geometric and dynamic similarity can be respected, water tunnel visualization can provide important data on the non-reacting flowfield inside combustors, and in this case proved to be an excellent tool to qualitatively visualize the flow in a model ducted rocket combustor.

The water tunnel work began with a literature survey to identify the wide range of geometries and test conditions that have been investigated for solid fuel ducted rocket combustors. This, combined with previous experience on ducted rocket testing at TNO-PML, was used to generate 24 combinations of geometry and test con-

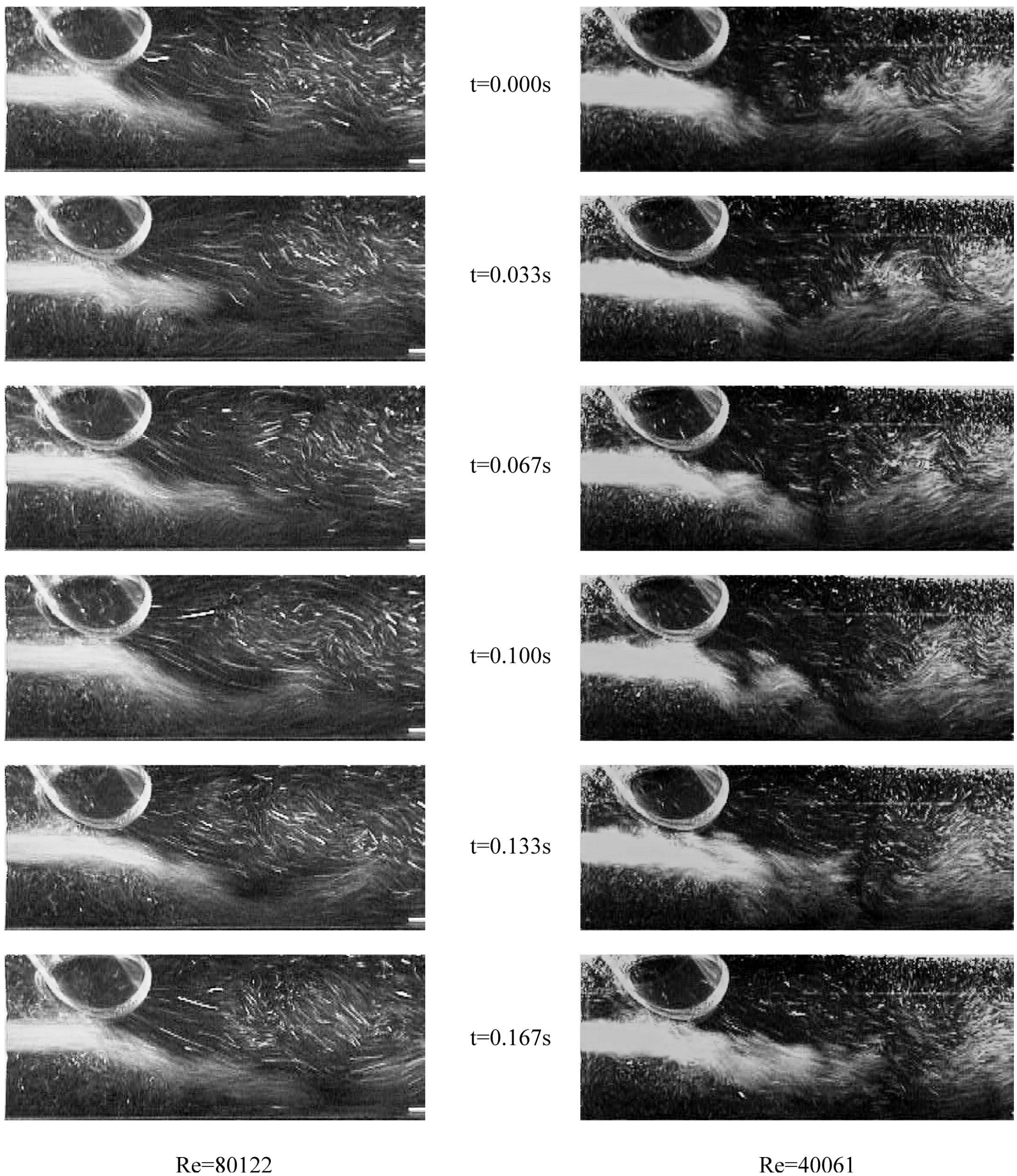

Figure 3.34: Reynolds number dependence, configurations WT11 and WT12, air injector A4, fuel injector F0-18, air/fuel momentum ratio = 5.3

ditions for the water tunnel visualization and the non-reacting CFD modelling to be presented in Chapter 4. The tests on these configurations revealed two basic common flow features, the first being a pair of longitudinal vortices that are a continuation of the high-speed flow from the air inlets. These structures corkscrew from below the centreline in the air inlet section and continue downstream toward the nozzle, transporting the mixture from the dome region of the combustor past the air inlets and to the main combustor region. The second is a recirculation zone from the air inlet section into the dome region, its exact shape being dependent on the geometry and the air/fuel momentum ratios. It supplies air from the air inlet section to the dome region for mixing with the fuel.

The water tunnel also revealed that all configurations tested demonstrated time-dependent flow, with most of the evidence of large-scale fluctuations occurring downstream of where the air and the fuel jets meet. The configurations that exhibited the least variation in flow structure and fuel jet shape used the A2 air injector (38 mm, 60^o) and therefore could be considered the most stable, followed by the A4 air injector (51 mm, 60^o). Configurations with the A6 air injector (51 mm, 90^o) showed the greatest variation in fuel jet shape. Despite the apparent differences in fuel jet stability, all of the configurations demonstrated some degree of air/fuel mixing by the time the flow was past the air inlets, and never displayed "violently-unstable" behaviour. Furthermore, no evidence of Reynolds number dependency was seen for the fuel distribution in the water tunnel experiments.

Chapter 4

NON-REACTING FLOW MODELLING

4.1 FLUENT Code

Computational fluid dynamics (CFD) modelling is based on using various discretized forms of the transport equations for fluid flow, commonly referred to as the Navier-Stokes equations. The original form of these equations is often simplified to facilitate their solution, but still capture the essential features of a flowfield. Their general form for solution in a CFD code in tensor notation is [43]:

$$\underbrace{\frac{\partial}{\partial t}(\rho\phi)}_{accumulation} + \underbrace{\frac{\partial}{\partial x_i}(\rho u_i \phi)}_{convection} = \underbrace{D_\phi}_{diffusion} + \underbrace{S_\phi}_{sources} \tag{4.1}$$

where ϕ is a conserved scalar[1]. Normally these equations include the conservation of mass, momentum, energy, and chemical species.

For the water tunnel, and for the combustion modelling to be shown later, the flow can be assumed to be incompressible, a major but justifiable simplification. Wilcox [44] writes the conservation of mass equation, for incompressible and constant property flow with no body forces, in the following tensor notation:

$$\frac{\partial u_i}{\partial x_i} = 0 \tag{4.2}$$

and for momentum:

$$\rho\frac{\partial u_i}{\partial t} + \rho\frac{\partial}{\partial x_j}(u_j u_i) = -\frac{\partial p}{\partial x_i} + \frac{\partial}{\partial x_j}(2\mu S_{ij}) \tag{4.3}$$

[1] A scalar with no sources nor sinks.

where S_{ij} is the strain rate tensor:

$$S_{ij} = \frac{1}{2}\left(\frac{\partial u_i}{\partial x_j} + \frac{\partial u_j}{\partial x_i}\right) \tag{4.4}$$

In theory, the flow could be solved with only the equations, all time-dependent, presented to this point. To do this, however, the length and time scales characteristic of turbulent flows would have to be resolved, and the spatial and temporal discretization of the governing equations would have to take this into account. As will be evident later, this would mean extremely fine grids of the geometry and time-dependent calculations. With present computers, for a three-dimensional flow such as in the water tunnel, solution of such a problem would not be practical because of the time it would take. Fortunately, by time-averaging the governing equations and using a turbulence model, such a flow can be solved in a reasonable length of time with today's computers.

The governing equations are first transformed by "Reynolds-averaging" or by decomposing the instantaneous variables into time-averaged and fluctuating components and then time-averaging the equations. For instance, the instantaneous velocity becomes:

$$u_i = \bar{u}_i + u_i' \tag{4.5}$$

where $\bar{u}$ is the time-averaged component and u' is the fluctuating component. This expression is substituted for u_i in Eqns. 4.2 and 4.3 and the result is averaged over time. If the fluctuating quantity u_i' is truly random about the mean, then its time average is zero and any term in which it is multiplied by a mean is also zero. However, the product of two fluctuating quantities is not necessarily zero. While the time-averaged mass conservation equation is similar to the instantaneous equation:

$$\frac{\partial \bar{u}_i}{\partial x_i} = 0 \tag{4.6}$$

the time-averaged momentum conservation equation has an extra term which contains the product of two fluctuating quantities $-\rho\overline{u_j' u_i'}$:

$$\rho\frac{\partial \bar{u}_i}{dt} + \rho\bar{u}_j\frac{\partial \bar{u}_i}{\partial x_j} = -\frac{\partial \bar{p}}{\partial x_i} + \frac{\partial}{\partial x_j}\left(2\mu\overline{S_{ij}} - \rho\overline{u_j' u_i'}\right) \tag{4.7}$$

This extra term is called the "Reynolds stresses", and it accounts for the effect of turbulence on the mean flow. The Boussinesq hypothesis relates the Reynolds stresses to the mean velocity gradients,

$$-\rho\overline{u_i'u_j'} = \mu_t \left(\frac{\partial \bar{u}_i}{\partial x_j} + \frac{\partial \bar{u}_j}{\partial x_i}\right) - \frac{2}{3}\delta_{ij}\left(\rho k + \mu_t \frac{\partial \bar{u}_k}{\partial x_k}\right) \tag{4.8}$$

where μ_t is called the turbulent viscosity. For incompressible flow, the term $\frac{\partial \bar{u}_k}{\partial x_k}$ vanishes. The Boussinesq approximation is the basis of many turbulence models, including the widely-used k-ε model. The main assumption with these models is that the turbulence is isotropic. An alternative approach to turbulence modelling, which can take into account any anisotropy of the turbulence, is to solve an additional transport equation for each of the Reynolds stress terms (seven for a three-dimensional problem). The improvement of the predictions with this approach, known as a Reynolds Stress Model (RSM), often does not justify its added complexity and computational time for most problems, however.

The CFD modelling of the water tunnel experiments was carried out using a code known as FLUENT (Versions 4.3 and 4.4) from FLUENT Inc. These versions of FLUENT require a structured grid to discretize the geometry. FLUENT uses what is known as a finite volume formulation. The geometry is divided into discrete finite volume cells, and the generalized equation (Eqn. 4.1) is reduced to a finite-difference form and integrated over the faces of these cells. This finite-difference form of the generalized equation conserves each quantity on a control volume basis [45].

The exact geometries used in the water tunnel, and later in the combustion tests, were modelled as precisely as possible in FLUENT. With a preprocessor called GEOMESH (version 3) also from FLUENT Inc., the geometries were first created within a computer-aided drafting module and nodes placed along the boundaries. Hexahedral cells were then created between the nodes to approximate the geometry. Structured grids of approximately 100 000 hexahedral cells were generated. Of these 100 000 cells, about 50 000 were termed "live" since they were contained within the model geometry and fluid flowed through them. The remainder, termed "dead" cells, were outside the model geometry, had no fluid flowing through them, but were needed to keep the grid structured.

The Reynolds-averaged equations that FLUENT must solve include the overall conservation of mass (continuity) and the conservation of momentum in three directions since the combustor geometry is three-dimensional. In addition, two species conservation equations must be solved, one for the fuel and the other for the air flow. To account for the effect of the turbulence, the Renormalized Group Theory (RNG) model was chosen for the modelling of the water tunnel experiments. It

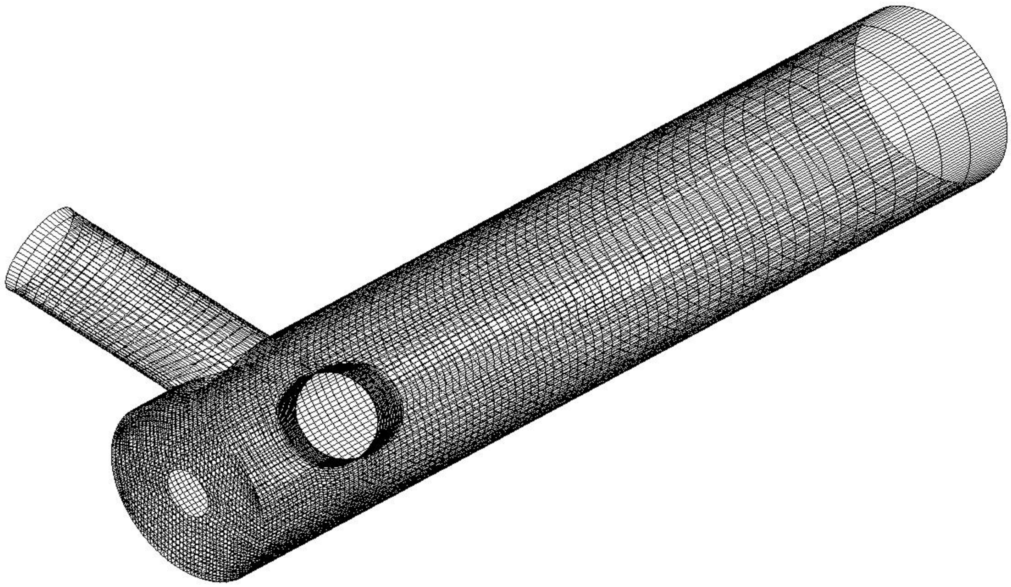

Figure 4.1: Surface mesh of basic combustor geometry

is a modified version of the k-ε model, but it yields superior results for recirculating, swirling flow such as that found in a ducted rocket combustor. The remaining equations in this section describe this model as implemented by FLUENT [46]. As with all two-equation turbulence models, including the k-ε model, the RNG model requires two additional transport equations to be solved for the turbulent kinetic energy k:

$$\rho\frac{\partial k}{dt} + \rho\frac{\partial\left(ku_j\right)}{\partial x_j} = \frac{\partial}{\partial x_i}\left(\alpha_k \mu_{\text{eff}}\frac{\partial k}{\partial x_i}\right) + G_k - \rho\varepsilon \tag{4.9}$$

and its dissipation rate ε:

$$\rho\frac{\partial \varepsilon}{dt} + \frac{\partial\left(\varepsilon u_j\right)}{\partial x_j} = \frac{\partial}{\partial x_i}\left(\alpha_\varepsilon \mu_{\text{eff}}\frac{\partial \varepsilon}{\partial x_i}\right) + C_{1\varepsilon}\frac{\varepsilon}{k}G_k - C_{2\varepsilon}\rho\frac{\varepsilon^2}{k} - R_{\text{RNG}} \tag{4.10}$$

if buoyancy and compressibility are neglected. α_k and α_ε are the inverse effective Prandtl numbers for k and ε, calculated from formulas derived from RNG theory. $C_{1\varepsilon} = 1.42$ and $C_{2\varepsilon} = 1.68$, also derived from RNG theory. G_k is the generation of turbulent kinetic energy from the mean velocity gradients:

$$G_k = \mu_{\text{t}} S^2 \tag{4.11}$$

where S is the modulus of the mean rate-of-strain tensor:

$$S = \sqrt{2S_{ij}S_{ij}} \tag{4.12}$$

and:

$$S_{ij} = \frac{1}{2}\left(\frac{\partial u_i}{\partial x_j} + \frac{\partial u_j}{\partial x_i}\right) \tag{4.13}$$

The term R_{RNG} is the main difference between the standard k-ε and the RNG models:

$$R_{\mathrm{RNG}} = \frac{C_\mu \rho \eta^3 \left(1 - \eta/\eta_0\right)}{1 + \beta\eta^3}\frac{\varepsilon^2}{k} \tag{4.14}$$

where $\beta = 0.012$, $\eta_0 = 4.38$, and $\eta = Sk/\varepsilon$.

The effective viscosity, μ_{eff}, is determined from the following differential equation:

$$d\left(\frac{\rho^2 k}{\sqrt{\varepsilon\mu}}\right) = 1.72\frac{\hat{\nu}}{\sqrt{\hat{\nu}^3 - 1 - C_\nu}}d\hat{\nu} \tag{4.15}$$

where $\hat{\nu} = \mu/\mu_{\mathrm{eff}}$ and $C_\nu \approx 100$. The turbulent viscosity, needed to determine the Reynolds stresses in Eqn. 4.8, is:

$$\mu_{\mathrm{t}} = \rho\, C_\mu \frac{k^2}{\varepsilon} \tag{4.16}$$

where $C_\mu = 0.0845$, derived from RNG theory.

FLUENT also adds an equation to account for swirl on the turbulent viscosity:

$$\mu_{\mathrm{t}} = \mu_{\mathrm{t0}}\, f\left(\alpha_s, \Omega, \frac{k}{\varepsilon}\right) \tag{4.17}$$

where Ω is a characteristic swirl number, α_s is a constant depending on whether or not the flow is mildly swirling or completely dominated by swirl, and μ_{t0} is the turbulent viscosity from Eqn. 4.16 calculated without swirl.

Estimates of the boundary conditions present in the actual water tunnel experiments were used as inputs for modelling with FLUENT. Properties of water at 25°C were used as the working fluid for the air and fuel inlets, and incompressible flow was assumed. Constant velocity inlet profiles at the end of the long inlet tubes were used, along with a turbulence intensity of 10% and a turbulence characteristic length 25% of the inlet diameters.[2]

[2]Unfortunately, converged solutions for a couple of configurations could not be obtained with FLUENT V4.3 or V4.4 with the RNG turbulence model, but were obtained with the k-ε model. However, more recently, the same configurations, including meshes, physical models, and boundary conditions, were modelled with the unstructured version, FLUENT/UNS V4.2, for which converged solutions were obtained with the RNG turbulence model. These results from FLUENT/UNS will therefore be presented.

A very important difference between the water tunnel and the CFD modelling that should be emphasized is that FLUENT, using Reynolds-averaged equations, gives a time-averaged output of the flowfield. While modelling time-dependent flowfields is possible, for our geometries and test conditions it would not be practical given the speed of the computers available to us. With the water tunnel, however, this time-dependence can be seen and the flowfield does indeed vary continuously with time. The water tunnel and CFD results should therefore only be compared with this in mind.

After modelling the water tunnel geometries and configurations, other combustor geometries of possible interest were modelled with FLUENT. While the use of the water tunnel is a technique that is less resource-intensive than experiments in the direct-connect combustion test facility, it still requires models to be constructed, experiments to be carried out, and data to be reduced. With the CFD modelling, a wide range of geometries and test conditions could be evaluated more quickly than with the water tunnel. However, the limitations of CFD modelling, particularly the assumption that the flow is quasi-steady, means that at least some experiments are still essential for validation purposes.

4.2 Comparison of the Predicted Water Tunnel and Direct-connect Combustor Flowfields

With the CFD modelling, further evidence for the applicability of the water tunnel results to an actual combustor flowfield was generated. These calculations were done to confirm that if the air and fuel flows are of different densities, how must the air/fuel mass flow ratio be changed so the flowfields in the water tunnel and the combustion tests are similar. With identical geometry and combustor dimensions, realistic boundary conditions such as temperatures, densities, and velocities were chosen for the actual fuel and air inlet flows in a mass flow ratio that would give the same air/fuel momentum ratio as for the CFD and water tunnel studies. Configuration WT1 was chosen for these calculations, and in the case of the water tunnel, properties of water were used. For the air/fuel flowfield, properties of gas generator exhaust (from a solid fuel of 90% glycidyl azide polymer and 10% carbon by mass) were used for the fuel inlet flow, and properties of vitiated air for the air inlet flow. Both the air/fuel and water tunnel flowfields were assumed to be non-reacting

Table 4.1: Boundary conditions and properties for configuration WT1, water tunnel and air/fuel flowfields

	Water Tunnel	Air/fuel flowfield
Air inlet velocity [m/s]	2.5	222.7
Fuel inlet velocity [m/s]	2.167	324.5
Air inlet density [kg/m^3]	1 000	2.898
Fuel inlet density [kg/m^3]	1 000	1.026
Dynamic Viscosity [kg/m·s]	0.000 9	0.000 025
Air/fuel mass flow ratio	4.59	7.72
Air/fuel momentum ratio	5.30	5.30
Combustor Re	98 198	846 555

and incompressible. Table 4.1 presents the boundary conditions used for the water tunnel and air/fuel flowfield predictions.

As seen, the Reynolds numbers varied by an order of magnitude, but as previously discussed the water tunnel results showed no Re-dependence between approximately 40 000 and 80 000, and should not at values above. The air/fuel mass flow ratios differ greatly, and the velocity ratios somewhat, but the following graphs will indicate that the critical parameter to describe the flowfield is air/fuel momentum ratio. Figure 4.2 shows the mole fraction of fuel for both the water tunnel and the combustion tests on the centreline plane, 57 mm from the head and in the middle of the air inlet section. Here the fuel concentration and velocities vary greatly, and in the case of the combustion tests, density does as well. However, despite all of these differences in the fluid properties, excellent agreement between the calculated water tunnel and combustion test flowfields is shown.

Figure 4.3 shows velocity magnitude normalized by the maximum velocity in the combustor for the two cases. The centres of the flowfields are virtually identical, but some differences exist toward the walls of the combustor. The greatest difference occurs near the top of the combustor where the velocities are very low. However, as seen previously in Fig. 4.2, the effect of this discrepancy on the air/fuel mixture distribution is minor. For the contour plot on the centreline plane in Fig. 4.4, the fuel distributions are virtually identical.

The CFD and the water tunnel images therefore show that the flowfields seen even at the lower Reynolds numbers in the water tunnel should be representative of the flowfield in an actual combustor in the absence of combustion and compressibility

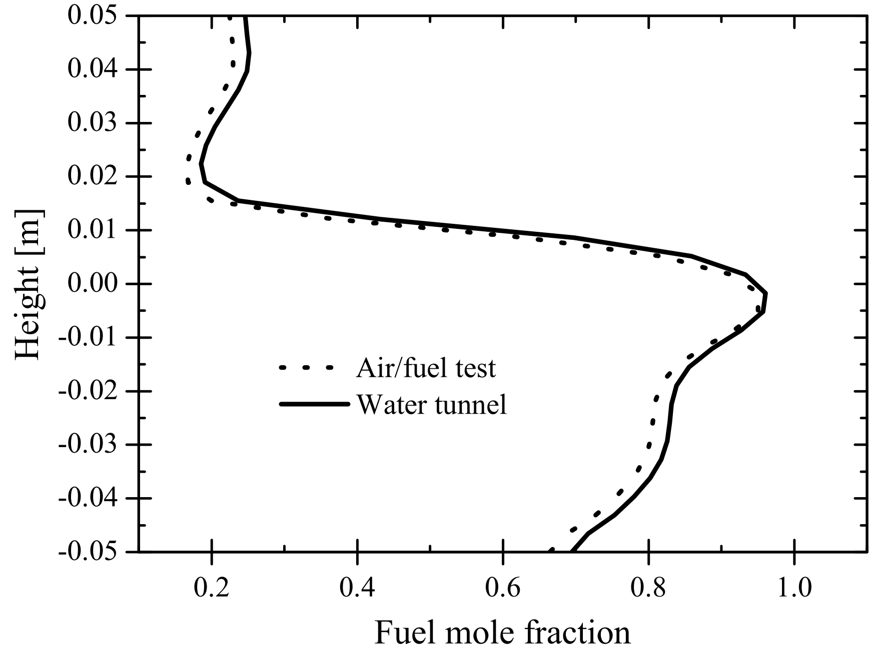

Figure 4.2: Predicted fuel mole fraction on centreline plane at x=0.057 m cross-section

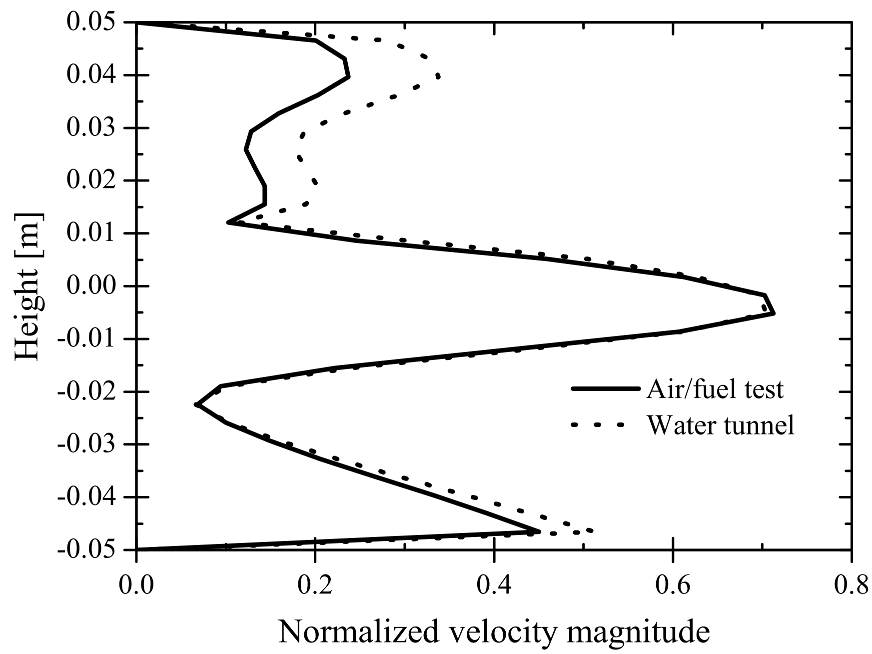

Figure 4.3: Predicted normalized velocity magnitude on centreline plane at x=0.057 m cross-section

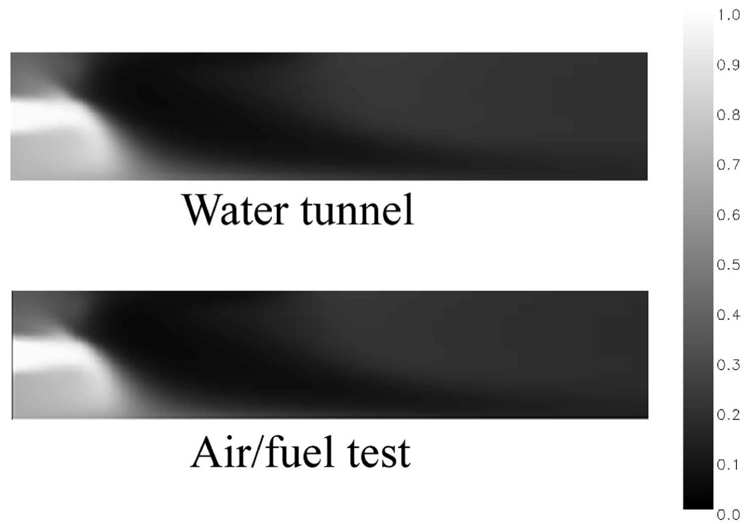

Figure 4.4: Predicted mole fraction of fuel on the centreline plane, legend on right

effects, if the same air/fuel momentum ratio is used. No evidence of Reynolds number dependency was seen in the water tunnel experiments, and any differences in the calculated velocities between the main fuel jet and the wall appeared to have little effect on the fuel distribution.

4.2.1 Water Tunnel and CFD Comparison

To compare the CFD results with the water tunnel images, contour plots of fuel mass fraction on the centreline plane were chosen. As previously mentioned, however, quantitative comparison between the water tunnel images and the CFD calculations is difficult because of the optical effects already explained. The apparent concentration of the simulated fuel in the water tunnel images is therefore not only a function of the number of cavitation bubbles present, but also of how the laser light is scattered from these bubbles and the intensity of the laser light at a particular location. Despite these problems, however, the shape of the fuel jets can justifiably be compared in the CFD and the water tunnel images since the concentration gradients at the edges are fairly sharp. If one takes these limitations into account, the differences between the images away from the fuel jets would certainly be reduced with the appropriate corrections.

Figure 4.5 compares a water tunnel image from configuration WT1 with a contour plot of predicted fuel mass fraction (or volume fraction since the densities of the simulated “air” and “fuel” are assumed to be identical) on the centreline plane from the CFD modelling. The predicted fuel mass (or mole) fraction legend is shown at the left. The areas of highest concentration in the fuel jet are the lightest-coloured areas in the flowfield in both the water tunnel image and CFD modelling, and they represent the fuel jet. The flow from the fuel jet gets turned back toward the head end by the air jets where it is mixed. It is then carried downstream and, seen well in only the CFD plot, reappears as a very dilute mixture at the aft end of the combustor by the longitudinal vortices mentioned in a previous section. There is excellent agreement between the shape of the fuel jets (areas of highest fuel concentration) for the CFD plot and the chosen water tunnel image. However, it must be kept in mind that the shape of the water tunnel fuel jet continually changes with time and can vary significantly, as in Fig. 3.22.

In the water tunnel image, the reflection of where the air inlet connects to the combustor is evident in the top left-hand corner, and forward-scattering from the bubbles on the right-hand side of the image makes the apparent fuel concentration appear higher there. Also, the area of intermediate fuel concentration, seen with the CFD modelling below the fuel jet, cannot be seen on the water tunnel image because the laser sheet intensity is much lower at the top and bottom of the combustor than at the middle. These same effects will be seen in all of the water tunnel and CFD comparisons.

Figure 4.6 shows the results for configuration WT3, which is identical to configuration WT1 except the air/fuel momentum ratio is twice as high. The fuel jet is therefore shorter, and is also turned back toward the head end by the air jets. Since the air/fuel mass ratio is also much higher, the CFD results show that the fuel concentration in the head-end recirculation zone is lower than in configuration WT1.

Configuration WT5, shown in Fig. 4.7, uses the same air and fuel injectors as configurations WT1 and WT3, but the air/fuel momentum ratio is even higher, so the fuel jet is even shorter. Once again, excellent agreement is obtained between the shape of the areas of high fuel concentration in both the CFD results and the water tunnel images. Because of the higher air/fuel mass flow ratio, the fuel in the head end away from the fuel jet is even more dilute.

The next two configurations use the A4 air injector and the F0-27 fuel injector. Figure 4.8 presents configuration WT7 which has the same air/fuel mass flow ratio as configuration WT1, but because of the larger diameter air inlets the air/fuel momentum flow ratio is lower and the fuel jet relatively stronger. The fuel jet extends past the air jets, being only deflected by them somewhat, and is not forced

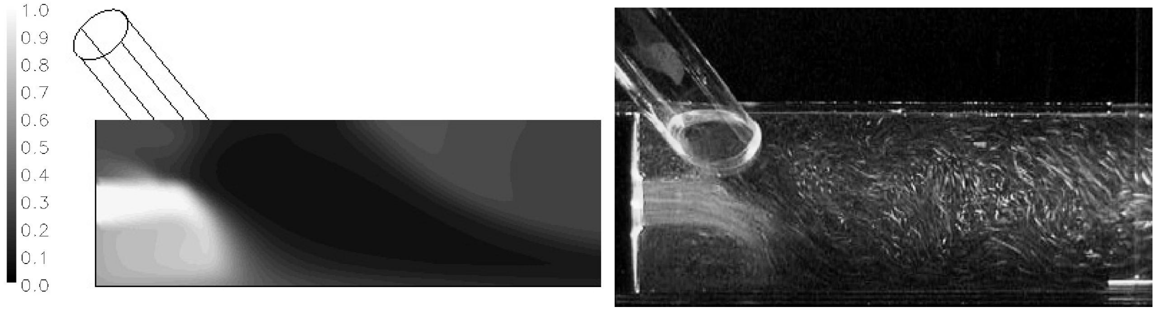

Figure 4.5: CFD prediction versus experimental water tunnel image, configuration WT1, air injector A2, fuel injector F0-27, air/fuel momentum ratio = 5.3 (left CFD, right water tunnel)

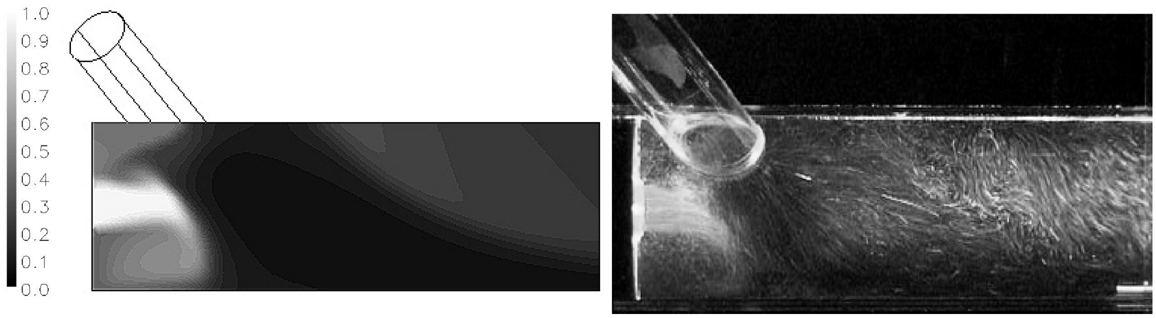

Figure 4.6: CFD prediction versus experimental water tunnel image, configuration WT3, air injector A2, fuel injector F0-27, air/fuel momentum ratio = 10.6 (left CFD, right water tunnel)

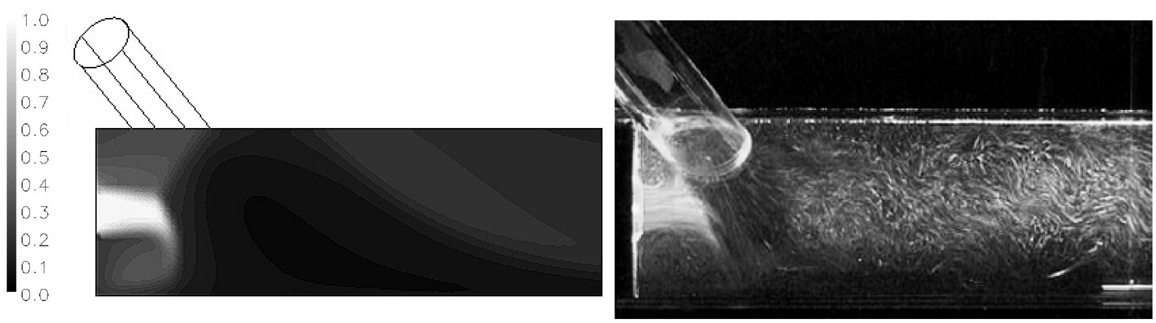

Figure 4.7: CFD prediction versus experimental water tunnel image, configuration WT5, air injector A2, fuel injector F0-27, air/fuel momentum ratio = 20.66 (left CFD, right water tunnel)

back into the head-end region as for the previous configurations. Good agreement for high fuel concentration regions is once again obtained between the CFD and water tunnel results.

Configuration WT9 in Fig. 4.9 has a similar air/fuel mass flow ratio to configuration WT5, but a lower air/fuel momentum ratio because, once again, of the larger air inlets. As such, the air jets are relatively more intense and abruptly cut off the fuel jet and turn it back toward the head end. The CFD results also show a higher fuel concentration in the head end region.

Figure 4.10 shows configuration WT11 which same air injector as configurations WT7 and WT9, but a smaller fuel injector. The fuel jet extends much farther than for configuration WT9 which has the same air/fuel mass flow ratio but a higher air/fuel momentum ratio. In fact, the fuel jet behaves much the same way as in configuration WT7 that has similar air and fuel velocities. Despite being deflected downward somewhat, the fuel jet shoots past the air jets and therefore its dissipation in the head-end region is limited.

For configuration WT13 in Figure 4.11, the fuel inlet port is lowered with respect to configuration WT11, and this has a positive influence on the mixing as can be seen by the area of dilute fuel below the fuel jet. The fuel jet is also cut off more abruptly by the air jets in this position. The same effect can be seen in both the CFD results and the water tunnel image.

The effect of dome height on the flowfield is illustrated in Fig. 4.12. Configuration WT15 is identical to configuration WT7 except for the increased dome height which seems to improve the dispersion of the fuel jet near the air jets. The fuel jet also appears to be deflected more toward the bottom of the combustor than for configuration WT7.

Figure 4.13 presents configuration WT17, the increased dome height version of configuration WT9. The fuel jet is cut off by the air jets and turned back toward the head-end region at the same point relative to the air inlets. In fact, except for the increased dome length that has the effect of lengthening the fuel jet and the dilute fuel regions in the head end, increasing the dome height has no obvious effect at this particular air/fuel momentum ratio. Agreement between the CFD results and the water tunnel image is once again good.

The remaining three configurations use the A6 fuel injector with a 90^o inlet angle. Figure 4.14 presents configuration WT19 which has the same air/fuel momentum and mass flow ratios, and fuel injector as configuration WT7 but uses the A4 air

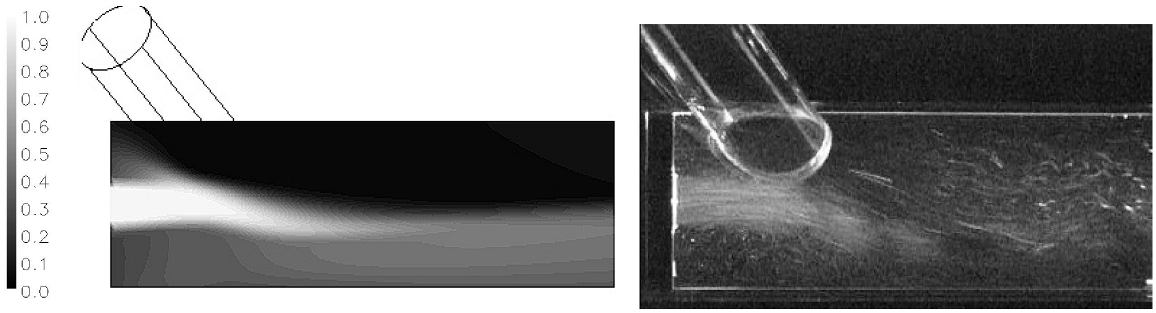

Figure 4.8: CFD prediction versus experimental water tunnel image, configuration WT7, air injector A4, fuel injector F0-27, air/fuel momentum ratio = 3.04 (left CFD, right water tunnel)

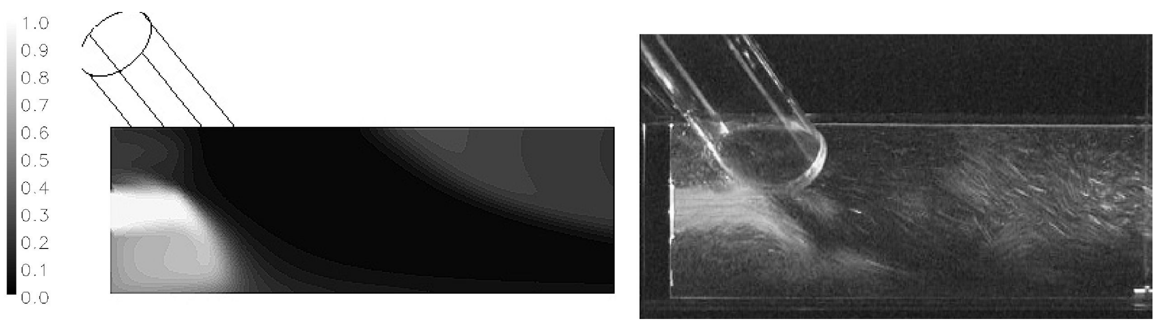

Figure 4.9: CFD prediction versus experimental water tunnel image, configuration WT9, air injector A4, fuel injector F0-27, air/fuel momentum ratio = 11.98 (left CFD, right water tunnel)

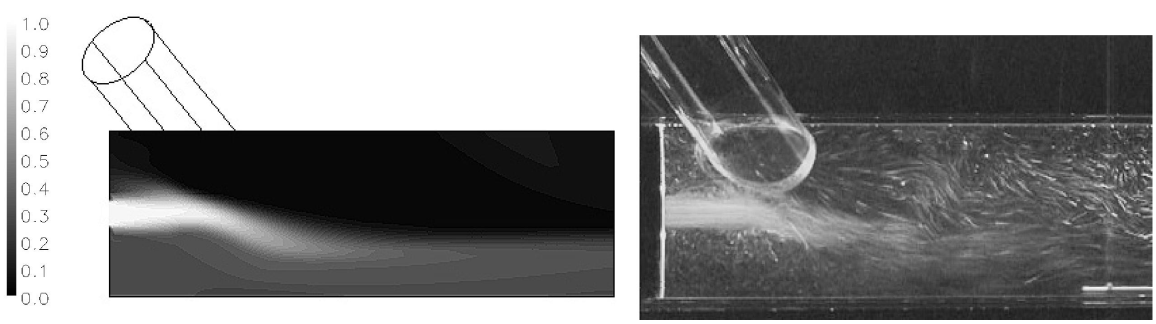

Figure 4.10: CFD prediction versus experimental water tunnel image, configuration WT11, air injector A4, fuel injector F0-18, air/fuel momentum ratio = 5.3 (left CFD, right water tunnel)

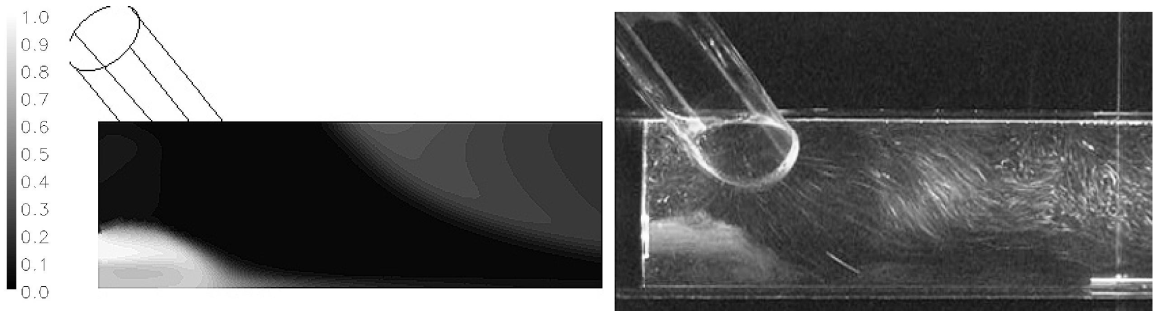

Figure 4.11: CFD prediction versus experimental water tunnel image, configuration WT13, air injector A4, fuel injector F1-18, air/fuel momentum ratio = 5.3 (left CFD, right water tunnel)

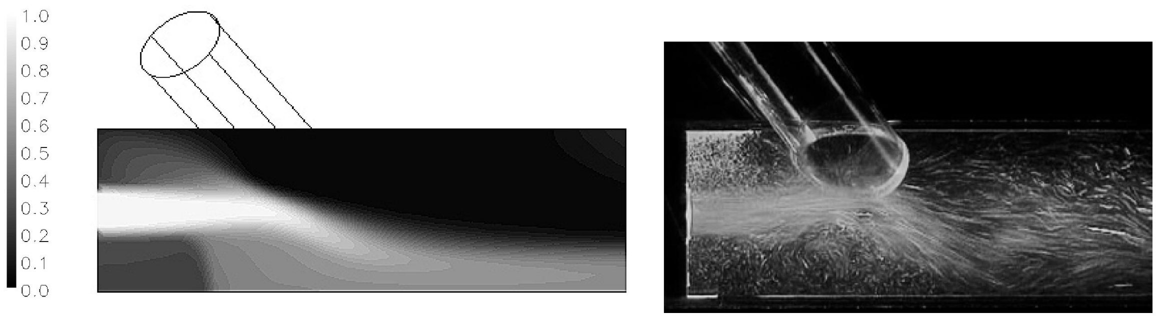

Figure 4.12: CFD prediction versus experimental water tunnel image, configuration WT15, air injector A4, fuel injector F0-27, air/fuel momentum ratio = 3.04, dome height 100 mm (left CFD, right water tunnel)

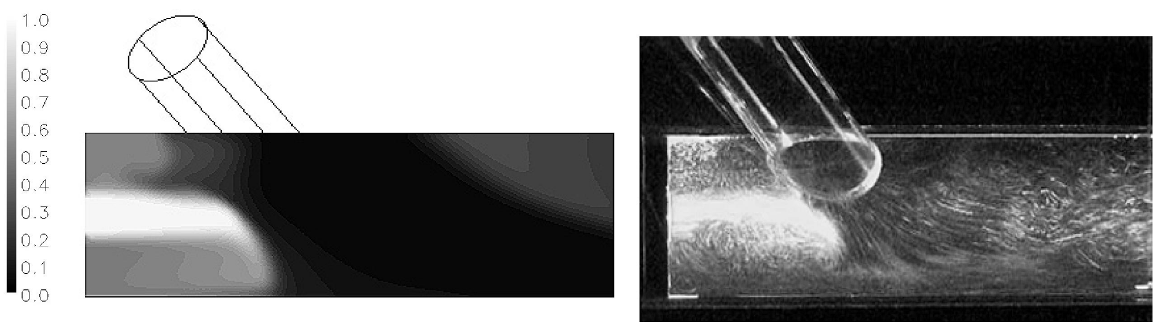

Figure 4.13: CFD prediction versus experimental water tunnel image, configuration WT17, air injector A4, fuel injector F0-27, air/fuel momentum ratio = 11.98, dome height 100 mm (left CFD, right water tunnel)

injector. Because the air jets impinge on the fuel jet at a sharper angle, the fuel jet is shorter than for configuration WT7, and the fuel jet appears to disperse less. However, as will be shown in the next subsection, the fuel jet for configuration WT19 actually disperses more, but away from the centreline plane.

The CFD modelling results for the next two configurations are from FLUENT/UNS since converged solutions could not be obtained using the structured FLUENT solver with the RNG turbulence model. Configuration WT21 in Fig. 4.15 is the same as configuration WT19 except for a lower fuel velocity and therefore higher air/fuel mass and momentum ratios. Unfortunately, the fuel injector shifted during the test by a few millimetres and the dome height is less than 57 mm, but the fuel jet is cut off nonetheless at about the same point relative to the air jets for both the water tunnel image and CFD results. When compared to configuration WT9 which is the same except for the A4 air injector instead of the A6, the steeper air inlet angle once again cuts off the fuel jet more abruptly. Once again, dispersion of the fuel jet appears to be less on the centreline plane.

Figure 4.16 presents configuration WT23. It is the same as configuration WT21, including air/fuel mass flow ratio, except for the use of the F0-18 fuel injector rather than the F0-27 which lowers the air/fuel momentum ratio to 5.3. Because of this, the fuel jet is narrower but longer, extending past the air inlets. Once again, however, the steeper air jets influence the fuel jet to a greater degree than for configuration WT11 which uses the A4 air injector.

For all of the configurations presented, areas of high fuel concentration on the centreline plane in the water tunnel images correspond well to those in the CFD plots, particularly when the frame-to-frame variation in the shape of the fuel is taken into account. Differences in the other regions of the flowfield can be explained by phenomena such as reflections, scattering, and variation in laser intensity, and as such there was no evidence to doubt the accuracy of the CFD modelling results. Therefore, the CFD results will be used to provide a more quantitative comparison between the configurations in the next section, and additional configurations will be modelled as well.

4.2.2 CFD Visualization

Since the centreline contour plots and water tunnel images presented in the last section provide a limited view of the mixing within the combustor, much more extensive visualization and comparison was done with the CFD results at many

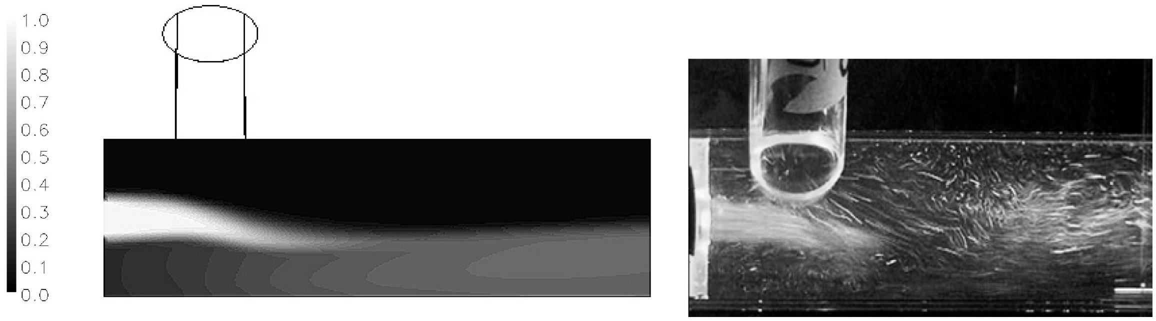

Figure 4.14: CFD prediction versus experimental water tunnel image, configuration WT19, air injector A6, fuel injector F0-27, air/fuel momentum ratio = 3.04 (left CFD, right water tunnel)

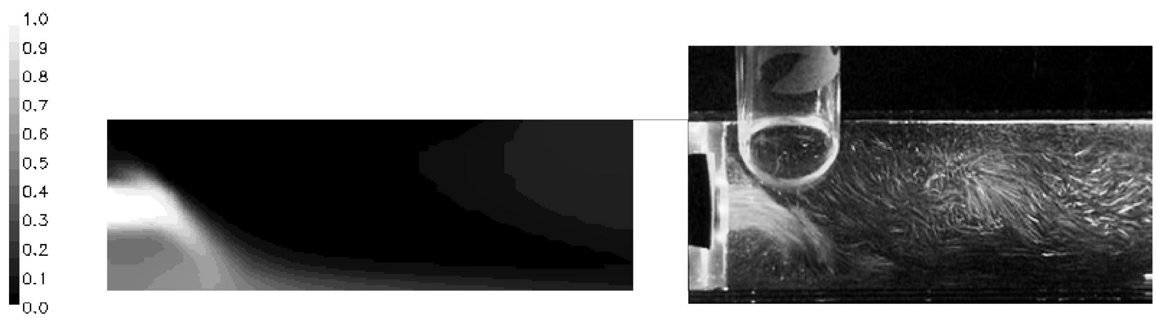

Figure 4.15: CFD prediction versus experimental water tunnel image, configuration WT21, air injector A6, fuel injector F0-27, air/fuel momentum ratio = 11.98 (left CFD, right water tunnel)

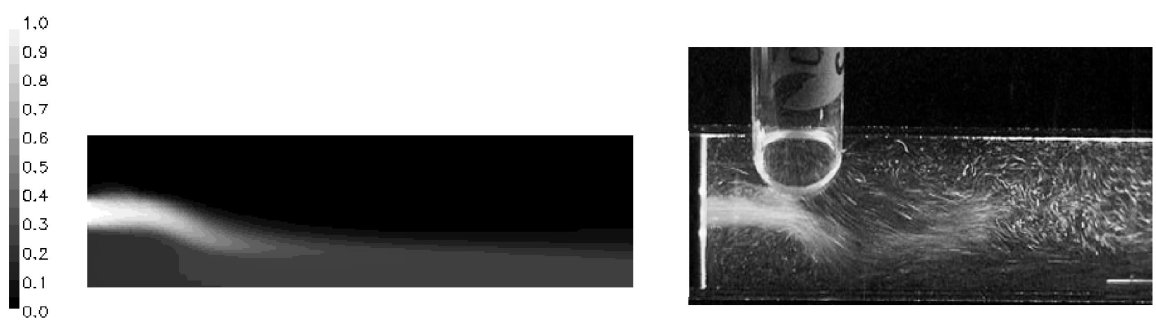

Figure 4.16: CFD prediction versus experimental water tunnel image, configuration WT23, air injector A6, fuel injector F0-18, air/fuel momentum ratio = 5.3 (left CFD, right water tunnel)

different cross-sections. The following figures are all contour plots of fuel mass fraction at cross-sections 50 mm apart. A scale of 0% to 30% was chosen since this better highlighted the differences between the configurations. The fuel rich areas of 30% and above fuel mass fraction are red, and the lean areas are blue.

Configurations WT1, WT3, and WT5 in Figs. 4.17, 4.18, and 4.19 use the A2 air injector with the F0-27 fuel injector. In all three cases, the head-end dome region is fuel rich and well distributed throughout. In the adjacent air injector area there are zones of greatly varying concentration. In this area, the mixture in the dome region appears to be transported by the vortical structures created by the air jets downstream and toward the outside of the combustor. About 250 mm from the air inlets the cross-sections appear to have a uniform fuel mass fraction, except for a small leaner band against the wall. In configuration WT5, with the highest air/fuel mass flow ratios, there is enough air recirculating back toward the head end to dilute the fuel mass fraction almost everywhere there to below 30%.

Figures 4.20, 4.21, and 4.22 present configurations WT7, WT9, and WT11 which all use the A4 air injector. Configuration WT7 has low air/fuel mass flow and momentum ratios and while the fuel jet is deflected by the air jets, it disperses very little and a region of high fuel mass fraction remains near the bottom of the combustor until the exit plane. There are also some very lean areas in the dome region. Configuration WT9 has a lower fuel flow and the flow patterns appear more like those of configurations WT1, WT3, and WT5, though not as well mixed downstream of the air jets. While configuration WT11 has the same air/fuel mass flow ratio as configuration WT9, it uses the F0-18 fuel injector instead so the fuel velocity is higher. Because of this, the fuel jet is relatively strong and the fuel distribution patterns look more like configuration WT7.

Configurations WT13, WT15, and WT17 in Figs. 4.23, 4.24, and 4.25 also all use the A4 air injector. Configuration WT13 is identical to configuration WT11 except the port in the fuel injector has been moved toward the bottom. This has caused the fuel jet to more directly impinge against the air jets and, despite having the same air/fuel momentum ratio as configuration WT11, to be swept toward the outside of the combustor as for configurations WT1, WT3, and WT5. While the fuel jet is somewhat intact near the end of the combustor and causes a rich region in the centre, a change in position of the fuel port has resulted in better mixing, even in the dome region. Configurations WT15 and WT17 are long dome height variants of configurations WT7 and WT9. In configuration WT15, the effect of increasing

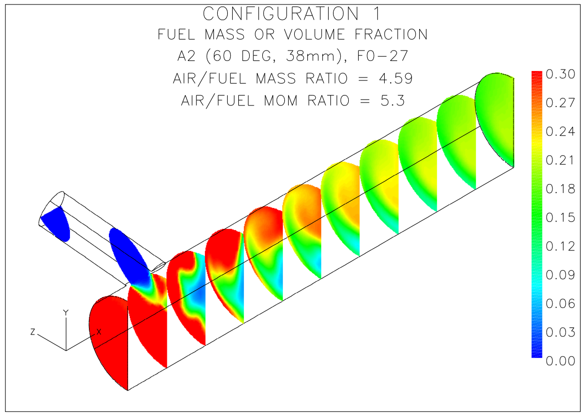

Figure 4.17: Predicted fuel mass fraction, configuration WT1, air injector A2, fuel injector F0-27, air/fuel momentum ratio = 5.3

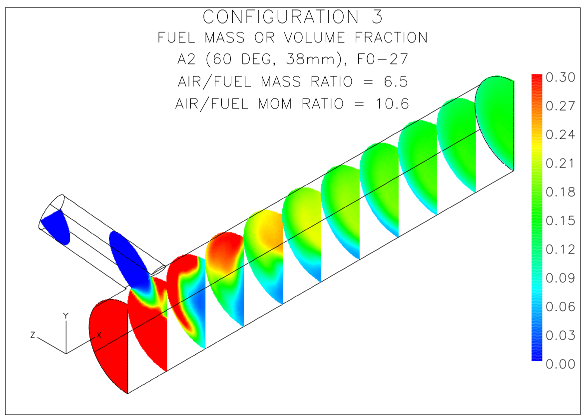

Figure 4.18: Predicted fuel mass fraction, configuration WT3, air injector A2, fuel injector F0-27, air/fuel momentum ratio = 10.6

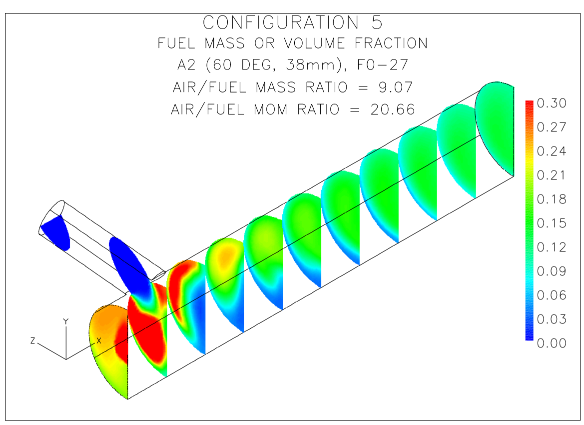

Figure 4.19: Predicted fuel mass fraction, configuration WT5, air injector A2, fuel injector F0-27, air/fuel momentum ratio = 20.66

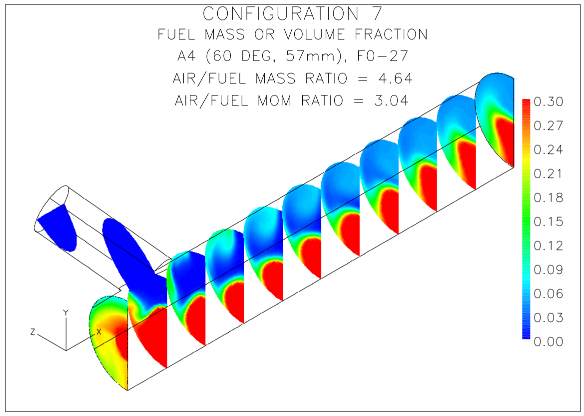

Figure 4.20: Predicted fuel mass fraction, configuration WT7, air injector A4, fuel injector F0-27, air/fuel momentum ratio = 3.04

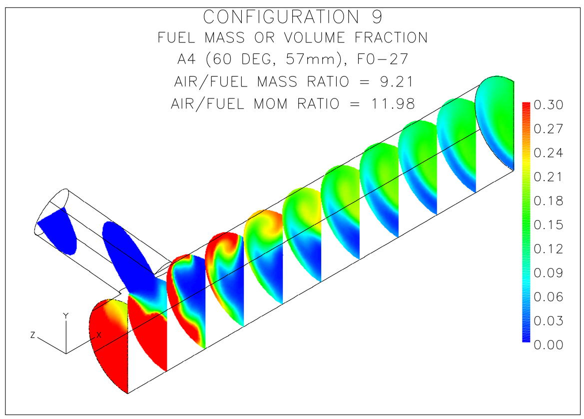

Figure 4.21: Predicted fuel mass fraction, configuration WT9, air injector A4, fuel injector F0-27, air/fuel momentum ratio = 11.98

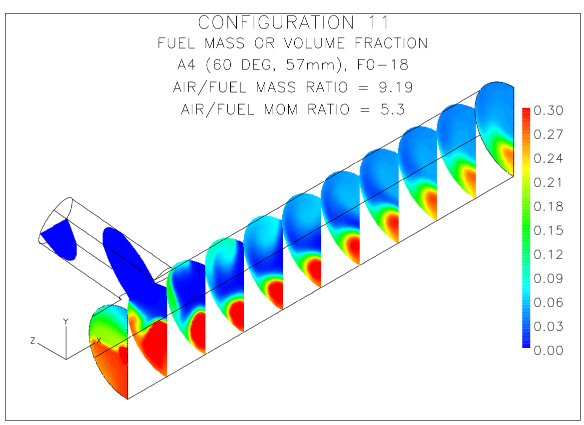

Figure 4.22: Predicted fuel mass fraction, configuration WT11, air injector A4, fuel injector F0-18, air/fuel momentum ratio = 5.3

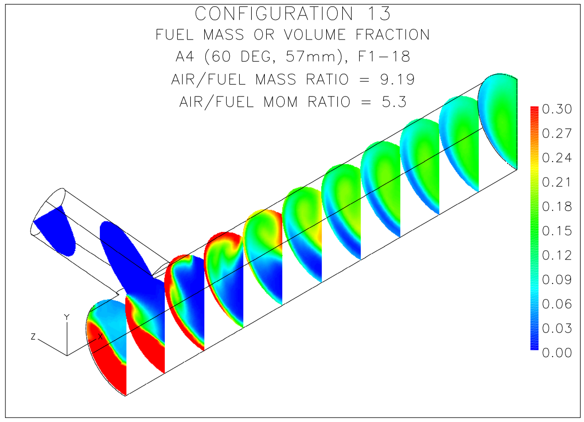

Figure 4.23: Predicted fuel mass fraction, configuration WT13, air injector A4, fuel injector F1-18, air/fuel momentum ratio = 5.3

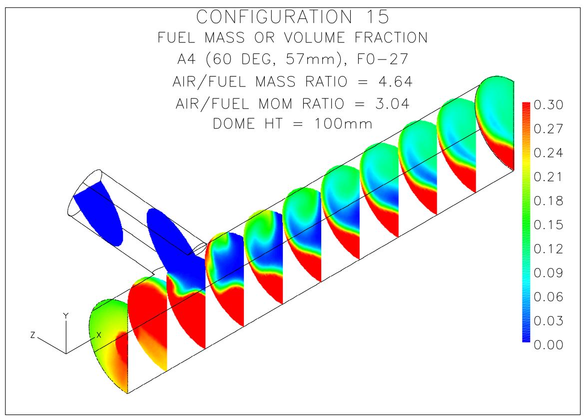

Figure 4.24: Predicted fuel mass fraction, configuration WT15, air injector A4, fuel injector F0-27, air/fuel momentum ratio = 3.04, dome height 100 mm

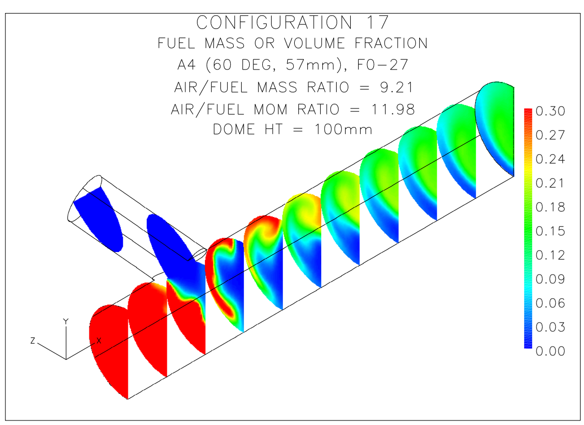

Figure 4.25: Predicted fuel mass fraction, configuration WT17, air injector A4, fuel injector F0-27, air/fuel momentum ratio = 11.98, dome height 100 mm

the dome height has improved the mixing since the fuel jet disperses more before reaching the air jets. The fuel is therefore better distributed in the dome region and around the outside and the top of the combustor in the aft end. For the higher air/fuel momentum case, however, there is very little effect in the fuel distribution due to increasing the dome height.

Figures 4.26, 4.27, and 4.28 show configurations WT19, WT21, and WT23[3], all using the A6 air injector with a 90^o injection angle rather than 60^o. Configuration WT19 is the same as configuration WT7 except for the air injection angle. At this air/fuel momentum ratio, this results in more air in the head-end region, but very little difference elsewhere. Configuration WT21 is analogous to configuration WT9, and likewise more air is present in the dome region. Downstream from the air jets, the fuel-rich mixture from the head end is spread along the combustor wall as for configuration WT9. However, toward the end of the combustor, the mixture becomes more homogeneous, while with configuration WT9 a much leaner area remains near the combustor wall. Configuration WT23 uses the smaller F0-18 fuel injector as does configuration WT11, with the same air/fuel mass flow ratio as configurations WT9 and WT21. The head-end dome region is once again leaner, and the mixture more homogeneous toward the aft end of the combustor. The use of the steeper air injection angle therefore causes more air to recirculate into the dome region, and at the higher air/fuel momentum ratios more homogeneous mixing results at the aft end of the combustor.

Figures 4.29, 4.30, and 4.31 present three configurations that were not tested in the water tunnel. All have an air/fuel mass flow ratio of about 9.2. Configuration WT25 is the same as configuration WT13 except the off-centre F1-18 fuel injector has been rotated 180^o so that the fuel jet is at the top of the combustor near the air inlets (F1-18S means the fuel and air inlets are on the same side). With this placement, however, the fuel jet does not impinge directly on the air jets and rather than being swept to the outside as for configuration WT13, it passes through to the aft end of the combustor near the centreline. The result is that the mixing is not as good near the nozzle exit, but the fuel distribution in the head end is more homogeneous. Configuration WT33 adds a 10X20 mm fence (designated F1-18SF2) across the centre of the fuel injector and better dispersion of the fuel results around the fuel inlet port. Above and below the fence adjacent to the fuel injector the mix-

[3]Configurations WT21 and WT23 were modelled with FLUENT/UNS since convergence with the RNG turbulence model could not be achieved with the structured FLUENT solver.

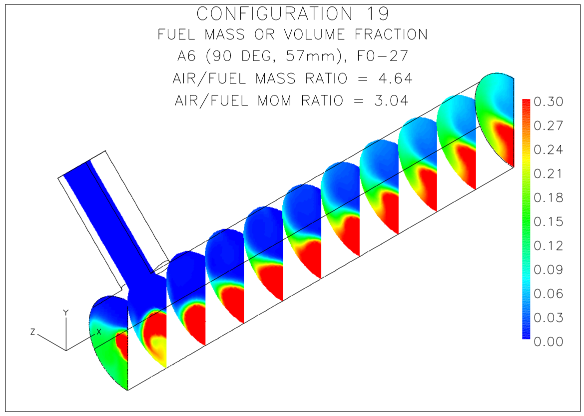

Figure 4.26: Predicted fuel mass fraction, configuration WT19, air injector A6, fuel injector F0-27, air/fuel momentum ratio = 3.04

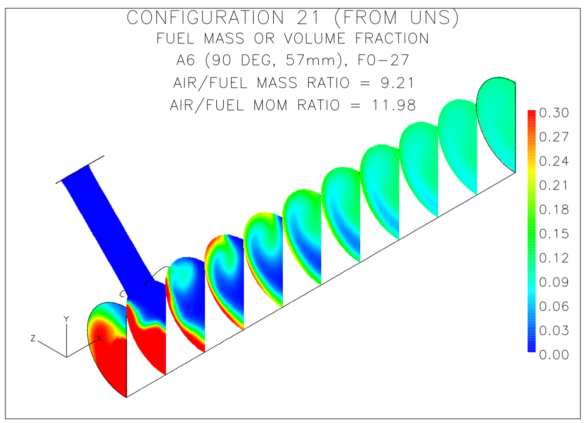

Figure 4.27: Predicted fuel mass fraction, configuration WT21, air injector A6, fuel injector F0-27, air/fuel momentum ratio = 11.98

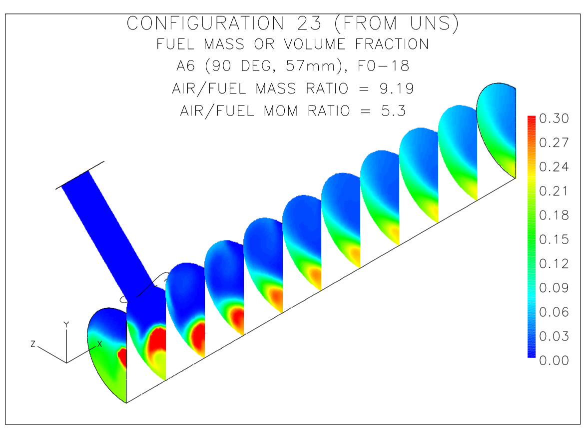

Figure 4.28: Predicted fuel mass fraction, configuration WT23, air injector A6, fuel injector F0-18, air/fuel momentum ratio = 5.3

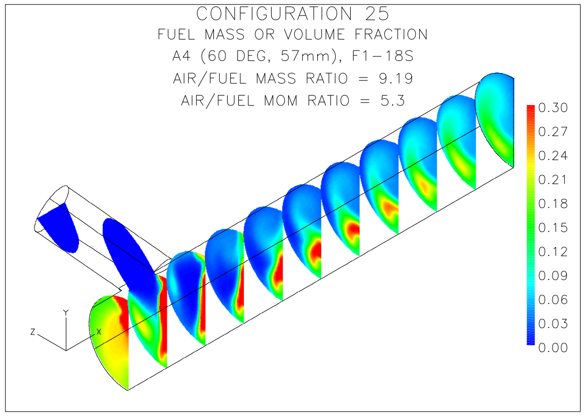

Figure 4.29: Predicted fuel mass fraction, configuration WT25, air injector A4, fuel injector F1-18S, air/fuel momentum ratio = 5.3

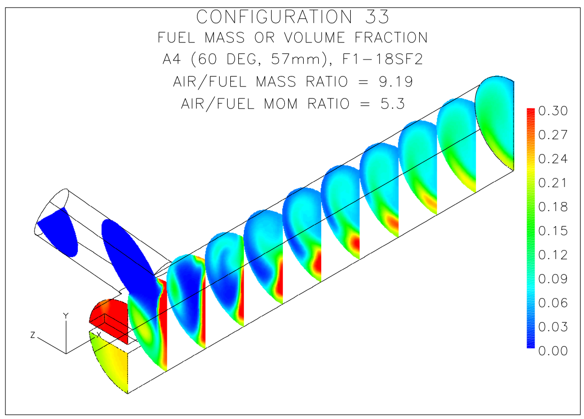

Figure 4.30: Predicted fuel mass fraction, configuration WT33, air injector A4, fuel injector F1-18SF2, air/fuel momentum ratio = 5.3

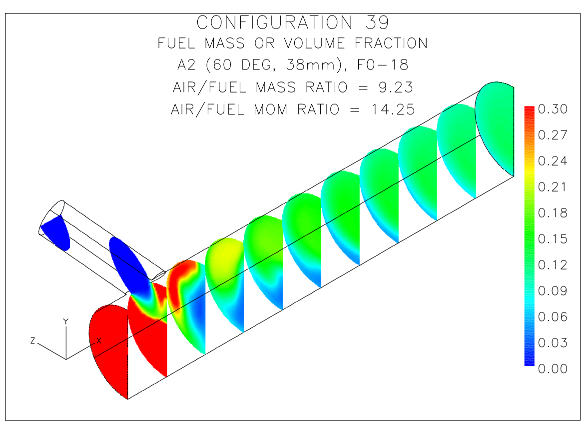

Figure 4.31: Predicted fuel mass fraction, configuration WT39, air injector A2, fuel injector F0-18, air/fuel momentum ratio = 14.25

ture appears almost completely homogeneous. A slightly better fuel distribution at the exit of the combustor also results.

The previous results indicated that high injection velocities promoted better mixing as long as the air/fuel momentum ratio was high enough to prevent the fuel jet from passing through the air inlet section. A combination of the smaller A2 air injector and the F0-18 fuel injectors was therefore modelled in configuration WT39. When compared to configuration WT5, differing by only the fuel injector port diameter (F0-27), the higher fuel injection velocity results in a head-end fuel distribution that is much more homogeneous. This head-end mixture is swept along in a similar way to configuration WT5, and the resulting fuel distribution at the end of the combustor is slightly more uniform.

From the above figures, the configurations likely to give the best and the worst combustion test results can be chosen if this correlates with the homogeneity of the fuel concentration. However, the effect of combustion on the mixing patterns has not been considered, and only results from further CFD reacting flow modelling, and/or experimental results, will determine if this is important. There is no single configuration that has complete mixing throughout, and while fairly homogeneous mixing occurs near the end of the combustor for some configurations, the geometry modelled is unrealistically long for its diameter. To keep the length of the combustor to a minimum with good combustion efficiency, good mixing in the dome region, with some areas of near stoichiometric air/fuel ratio, is likely required.

4.3 Summary of the Non-reacting Flow Results

Non-reacting flow CFD modelling was carried out with the FLUENT code for the same configurations as tested in the water tunnel. For all of the configurations presented, areas of high fuel concentration on the centreline plane in the water tunnel images corresponded well to those in the CFD plots. Differences in the other regions of the flowfield can be explained by phenomena such as reflections, scattering, and variation in laser intensity. With the time-dependency of the water tunnel flowfields taken into account, there is no evidence from the water tunnel tests to discount the accuracy of the CFD.

The fuel mass fraction contour plots of the various cross-sections in the combustor provided a good method of visualizing the homogeneity of the fuel distribution. No single configuration showed complete mixing throughout, but several displayed fairly homogeneous mixing near the end of the combustor. To keep the length of the combustor to a minimum with good combustion efficiency, good mixing in the dome region, with some areas of near stoichiometric air/fuel ratio, is likely required.

Using the same geometry and air/fuel momentum ratio as configuration WT1 but boundary conditions for gas generator exhaust and vitiated air rather than water, only very minor differences in fuel distribution and velocity resulted between the water tunnel and actual air/fuel flowfields. This implies that the air/fuel momentum ratio is the correct parameter to specify the relative amounts of the inlet flows and obtain a similar flowfield between the water tunnel and direct-connect combustors. Furthermore, the flowfields seen at the lower Reynolds numbers in the water tunnel should be representative of the flowfields in an actual combustor, in the absence of combustion.

Chapter 5

DIRECT-CONNECT COMBUSTION EXPERIMENTS

5.1 Simulation of Flight Conditions

The ground testing of airbreathing flight propulsion systems poses special problems, particularly for ramjets which, as explained in the introduction, typically fly at supersonic speeds. The obvious method is to put such a system into a supersonic wind tunnel and test it at the flight speed required. However, wind tunnels capable of supplying air at the freestream temperatures and pressures normally encountered during supersonic flight are few and far between, and are very expensive to operate. Fortunately, if testing of the air intake system is not required, a practical and much more economical alternative exists in the form of direct-connect testing. This means that rather than simulating the static conditions and supersonic speed of the air *upstream* of the air intake, the static conditions and speed of the air *downstream* from the air intake are simulated.

To calculate the static properties and velocity of the air after the intake but upstream of the combustor, the altitude, flight speed, and basic intake geometry must be specified. For these experiments, a flight speed of Mach 2.5 and an altitude of 6 000 m were chosen, along with a two-shock intake system with the air passing through an oblique shock, caused by an intake wedge turning angle of 15.5^o, and then through a normal shock before entering the combustor. The results are shown in Table 5.1, assuming an ideal gas and adiabatic shocks. The static temperature and pressure of the air downstream from the normal shock are much higher than those upstream of the intake, but the velocity is much reduced. Baseline static properties of 0.5 MPa and 600 K, in approximate agreement with the calculated

Table 5.1: Conditions through the air intake system

Property	Station 0 upstream of oblique shock	Station 1 downstream from oblique shock	Station 2 downstream from normal shock
p [Pa]	47 181	119 610	458 484
p_t [Pa]	806 134	743 850	587 273
T [K]	249.15	332.56	522.31
T_t [K]	560.59	560.59	560.59
Mach number	2.5	1.852	0.605
Speed of sound [m/s]	316.4	365.5	458.1
Velocity [m/s]	791.0	676.8	277.3

values downstream from the normal shock, were therefore used for the experimental and CFD modelling results that follow[1].

5.2 TNO-PML Facility

Only a handful of direct-connect combustion test facilities exist in the world that are suitable for testing ducted rocket combustors, and none of these are located in Canada. Fortunately, because the work reported herein was part of a collaboration between Canada and the Netherlands on ducted rocket propulsion, all of the combustion experiments were carried out in the indoor direct-connect facility at TNO-PML [47], unique because the motor firings actually take place inside. A drawing of the building is shown in Fig. 5.1. As explained, the static conditions of the air downstream from the intake system and upstream of the combustor must be simulated, so the stagnation properties of the air for the experiments must be much higher than ambient. This is done by pressurizing and heating the air.

In the TNO-PML facility, the air is pressurized by a compressor and heated in a methane-fuelled burner called a vitiator. Before the experiment, the compressed air is dried to remove excess humidity and is stored in tanks at 20 MPa. During an experiment, the air is released and passes through the vitiator before entering the ducted rocket combustor. Not only is methane supplied to the vitiator, but oxygen to replace that used to burn the methane. This way, the mass fraction of oxygen in

[1]Several experiments were also done at a nominal combustor pressure of 1 MPa to provide data for any dependence of combustor performance on pressure (PD-scaling).

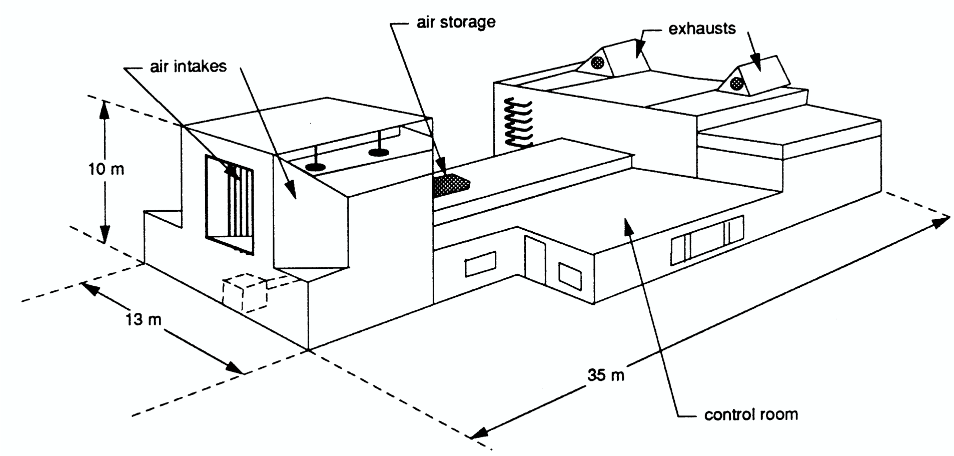

Figure 5.1: Indoor test facility at TNO-PML [47]

the vitiated air is approximately that of ambient air. A schematic of the gas supply system at the TNO-PML facility is presented in Fig. 5.2. As seen, methane and oxygen are also supplied to produce a pilot flame, ignited with a spark plug, which in turn ignites the gases in the vitiator. Nitrogen is used to purge the methane lines after an experiment.

The main drawback of using a vitiator is that the heated air is polluted with combustion products. The two main effects of these combustion products are that they alter the molar mass of the air, and the presence of extra combustion radicals can alter the speed at which chemical reactions take place. While there are methods of producing unpolluted heated air such as pebble beds and electric heaters, in general they are much more expensive to build and operate. Fortunately, for these experiments, the consequences of using vitiated air are not very important. The different molar mass for the air could have an effect on performance determination, but this is minimized since the composition of the vitiated air, not clean air, is used for the calculations. Furthermore, the choice of methane as the vitiator fuel means that as long as all of the methane is burned, the molar mass of the resulting exhaust products is about the same as air and therefore has only a minor effect on performance [48] as compared to clean air. The extra combustion radicals will also have a minimal effect on performance since the main assumption for the CFD modelling to be presented later is that the combustion is controlled by turbulent mixing. This also implies that the chemical reactions are so fast that any change due to the presence of extra radicals will have no effect.

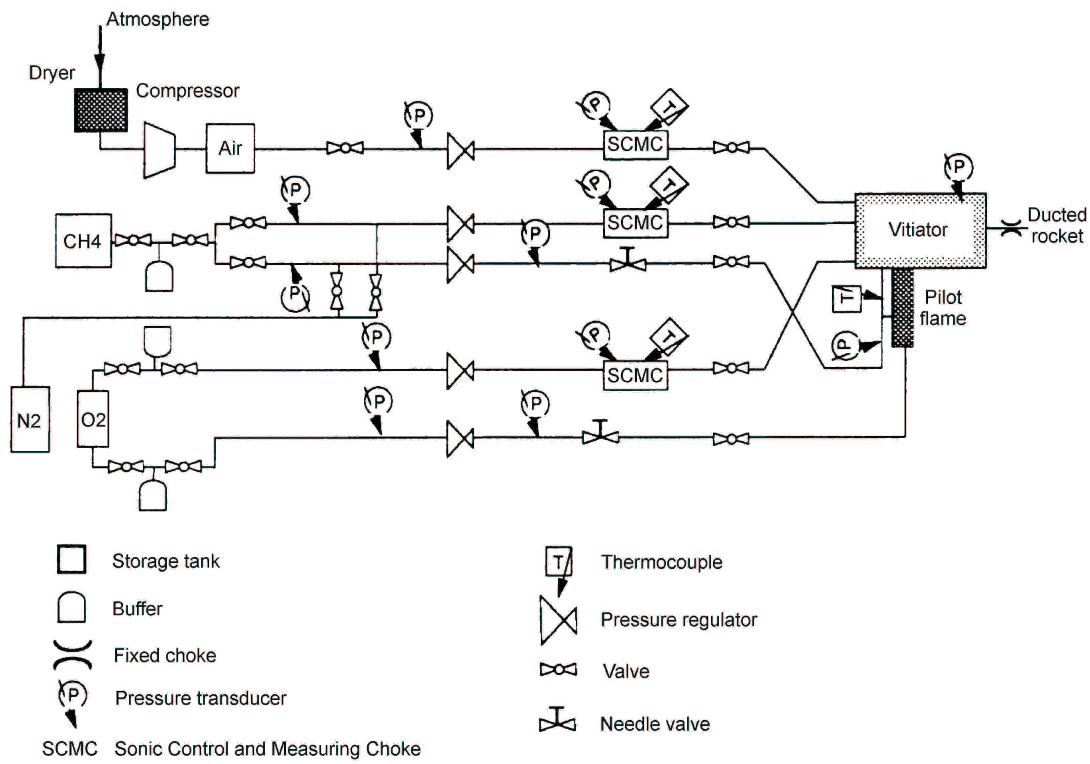

Figure 5.2: Gas supply system [49]

To ensure the correct mass flow rates to produce the desired test conditions at the ducted rocket combustor, the gases supplied to the vitiator all pass through pneumatically-controlled pressure regulators and then through Sonic Control and Measuring Chokes (SCMC). The pintles of the SCMC's (Fig. 5.3) are set before the experiment to give the specified throat area. By monitoring the temperature of the gas just upstream of the choke, only the upstream pressure must be adjusted during the experiment to give a constant mass flow rate through the choke. With the facility set up as shown, the maximum test conditions are a temperature of 900 K and an air mass flow rate of 5 kg/s.

Downstream of the vitiator, the ducted rocket combustor and related hardware are installed. For these experiments, existing ducted rocket hardware used for an earlier test program at TNO-PML [35] was used as much as possible (Fig. 5.4). Several key components can be identified in this diagram. The 100 mm diameter combustor is made up of three sections, the first being the air injector, followed by the two aft sections. The nozzle is attached to the last section. The air injector is surrounded by an air plenum to distribute the air evenly to each of the air inlets. The

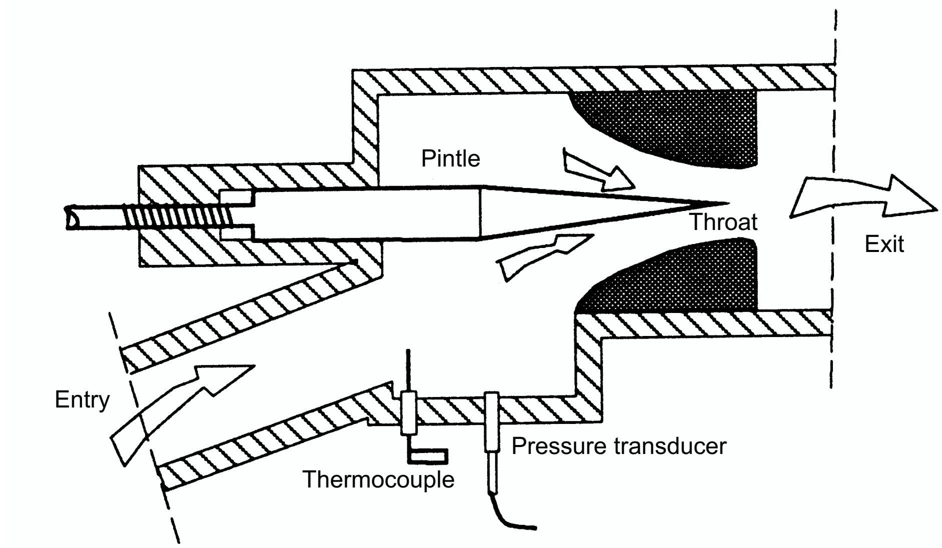

Figure 5.3: Sonic Control and Measuring Choke [47]

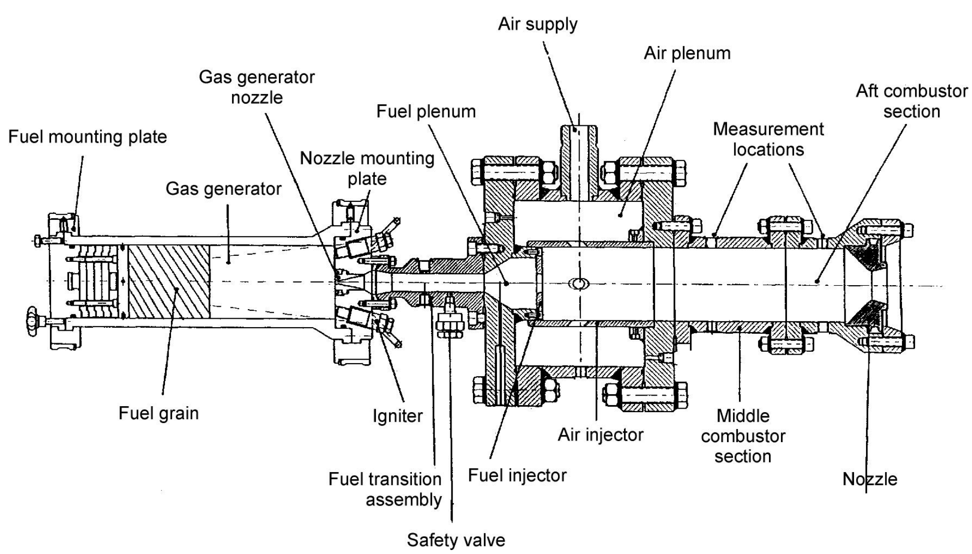

Figure 5.4: Original ducted rocket hardware at TNO-PML [50]

solid fuel grain is housed in the gas generator. Once ignited, the exhaust is expanded through a nozzle into the transition assembly and then into the fuel plenum before it is injected, at subsonic speed, into the combustor.

Since the main reason for doing the combustion tests was to provide validation data for the CFD modelling, the boundary conditions at the air and fuel inlets must be characterized accurately. As part of the work for this thesis, major improvements were proposed and implemented [49] to the air and fuel delivery systems of the original ducted rocket facility so that the characterization of the boundary conditions could be made with much more confidence (Fig. 5.5). For the air delivery, the air plenum was replaced with a much larger one of 0.5 m internal diameter. This meant the air inlet tubes on the air injector could be extended to be more like the plexiglass model shown in Fig. 3.18. This, along with the addition of stainless steel honeycomb at the entrance to each air inlet tube, was to make the initial velocity profile as flat and parallel as possible.

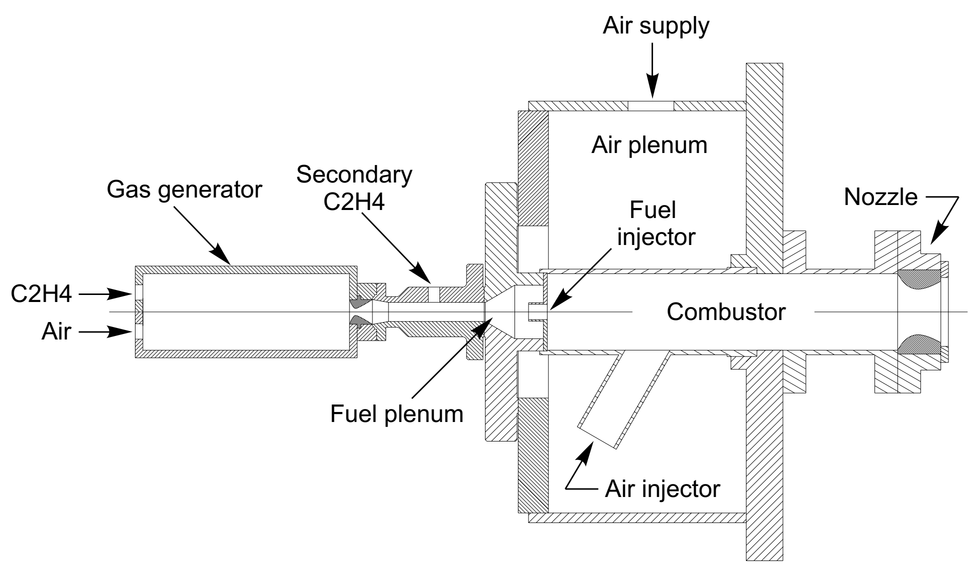

Figure 5.5: Improved ducted rocket hardware

For the fuel delivery system, rather than using a solid fuel for the gas generator, an injection system of air and gaseous ethylene was added. In the right proportions, the calculated equilibrium exhaust properties of the ethylene/air mixture are close to those of the solid ducted rocket fuel mentioned in the introduction and proposed for these tests [51] which contains 90% by mass GAP and 10% carbon. While some tests were eventually done with this solid fuel, the bulk of the experiments, including all of those reported here, were done with the simulated fuel of ethylene and air. This was because, particularly at the early stages of development, the mass flow rates of the solid fuel were difficult to control and steady combustor operation tough to achieve. However, much more consistent results were possible with the gaseous ethylene since its mass flow could be controlled in much the same way as the vitiator gases and the boundary conditions estimated with more confidence.

However, while an actual solid fuel must decompose by itself inside the gas generator once ignited, the mixture of ethylene and air is much too rich to react at the conditions present. About 10% of the ethylene is therefore injected into the head of the gas generator where it reacts with the air in a combustible mixture, and the remainder is injected into the transition assembly where it can react with the hot exhaust from the gas generator. The main assumption here, of critical importance to the CFD modelling to be described later, is that conditions are appropriate to allow the mixture to approach thermochemical equilibrium before being injected into the combustor. Figure 5.6 shows the flow of gases for both the air and fuel delivery systems of the direct-connect facility.

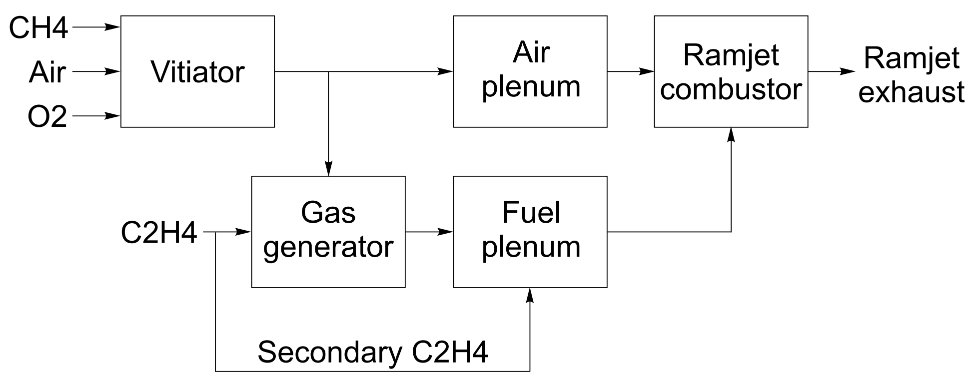

Figure 5.6: Schematic of flows in the direct-connect apparatus

Two other minor modifications were also done. The first was also to the fuel delivery system and involved the addition of an entrance tube to the fuel injector. It extends into the fuel plenum and was added for the same reason as for the extended air tubes, namely to cause the velocity profile of the fuel entering the combustion chamber to be as flat and parallel as possible. The final modification was to remove the aft combustor section and replace it with a shorter section which housed the nozzle. This was done purposely to enhance the importance of mixing closer to the head end of the chamber so that a greater effect on performance could be measured.

The ducted rocket hardware shown in Fig. 5.5 was mounted on a thrust bench (Fig. 5.7) in place of the SFRJ test motor shown. The thrust bench is suspended

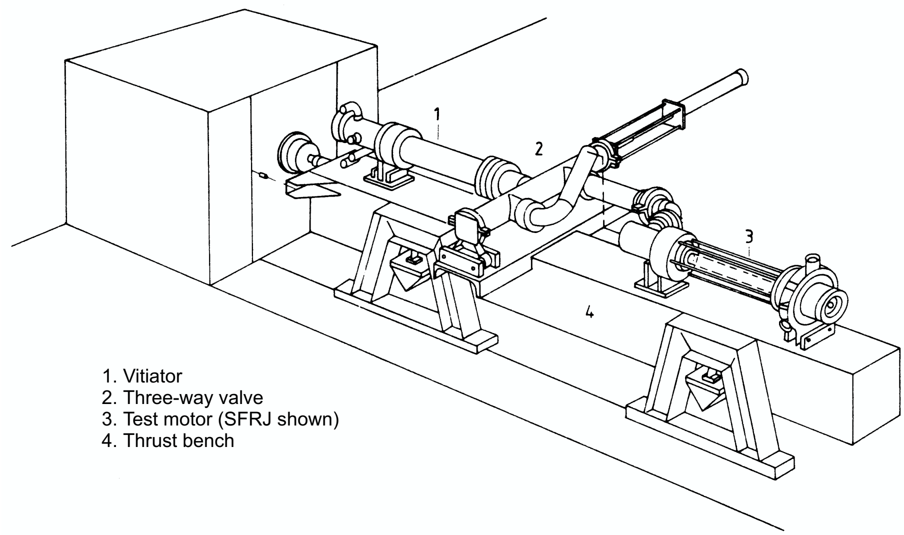

Figure 5.7: Thrust bench [47]

on flexures to allow it to push against a thrust gauge. All supply gases are brought to the vitiator and the gas generator through flexible hoses (not shown). The three-way valve, normally used to divert the air away from the combustor motor before the test to allow the vitiator to come up to operating temperature, was not used for the ducted rocket experiments since the fuel is introduced only on demand. This meant that the vitiated air was instead passed through the air supply system, gas generator, and combustor before the test for 50 s to allow all the hardware to come up to operating temperature.

The actual test setup used for the direct-connect experiments is shown in Fig. 5.8, mounted on the orange thrust bench. The hot air arrives from the vitiator and is conducted to the air plenum through a rigid pipe. The air plenum hides most of the combustor section from view, but the nozzle can be seen. On the upstream side of the air plenum, the gas generator is mounted.

5.3 Calculation of Efficiency

There are several parameters that could be used to characterize experimental combustor performance, including thrust, specific thrust, specific impulse, and overall efficiency. However, none of these was suitable for comparison with the CFD modelling that will be presented later, mainly because the focus of the modelling

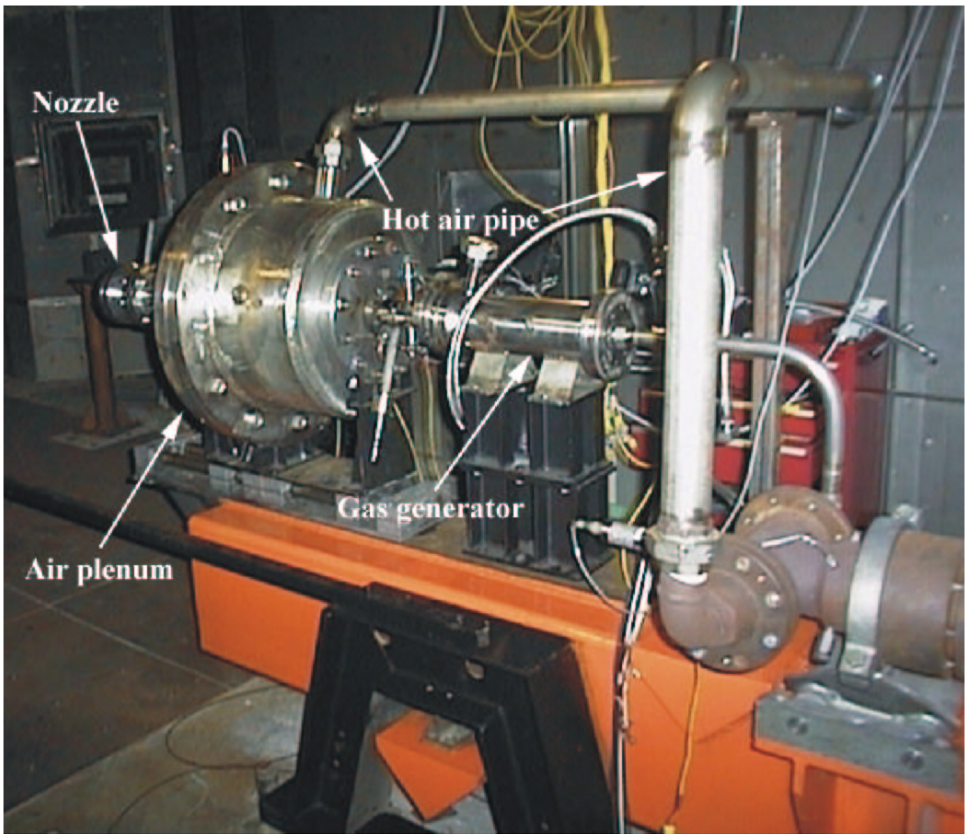

Figure 5.8: Ducted rocket hardware mounted on thrust bench

was only on the combustor and the parameters mentioned also include the effects of other components such as the intake and nozzle. Several ways of calculating combustion efficiency are in use at test facilities around the world to characterize ramjet combustor performance [52], and of these efficiency based on temperature rise in the combustor ($\eta_{\Delta\mathrm{T}}$) was chosen to characterize the direct-connect experiments. It also has the added advantage of varying from 0% to 100% unlike other definitions of efficiency such as that based on characteristic velocity (C^*). It is defined by:

$$\eta_{\Delta\mathrm{T}} = \frac{T_{\mathrm{t4,exp}} - T_{\mathrm{t2}}}{T_{\mathrm{t4,theo}} - T_{\mathrm{t2}}} \tag{5.1}$$

Referring to Fig. 1 in the nomenclature, T_{t2} is the stagnation temperature at the end of the inlet diffuser, $T_{\mathrm{t4,exp}}$ is the experimental stagnation temperature just upstream of the nozzle, and $T_{\mathrm{t4,theo}}$ is the theoretical stagnation temperature just upstream of the nozzle.

Despite the apparent simplicity of Eqn. 5.1, the calculation of $\eta_{\Delta\mathrm{T}}$ includes some complicated steps. While the stagnation temperature at the end of the diffuser T_{t2} can be estimated from thermocouple measurements in the air plenum (for these experiments approximately 600 K), this is much more difficult for the stagnation temperature at the end of the combustor T_{t4}. Not only are the temperatures much higher (perhaps 1 500 K to 2 000 K) and high velocities present, but this measurement must also be averaged over the entire flowfield at the end of the combustor (just upstream of the nozzle). However, several accepted and much more convenient methods exist that estimate this temperature through the use of a thermochemical code such as CET89 [53]. (An example of input and output files for calculations with CET89 is given in Appendix B.) The method chosen is based on measured static pressure and does not explicitly use γ (ratio of specific heats) in the following three equations [52]. First, the measured static pressure in the combustor, $p_{4,\,\mathrm{exp}}$, is used as an estimate of the stagnation pressure in the combustor. This, along with the nozzle entrance-to-throat area ratio and the compositions, temperatures, and mass flow rates of the vitiated air and gas generator exhaust are used as inputs to CET89. The output includes the theoretical stagnation-to-static pressure ratio. With the following equation a much better estimate of the stagnation pressure, $p_{\mathrm{t4,\,exp}}$, is made:

$$p_{\mathrm{t4,\,exp}} = \left(\frac{p_{\mathrm{t4,\,theo}}}{p_{4,\,\mathrm{theo}}}\right) p_{4,\,\mathrm{exp}} \tag{5.2}$$

and CET89 is run again with this and the other inputs previously mentioned. The stagnation-to-static pressure ratio should remain unchanged (if not, the procedure can be repeated) and the theoretical stagnation combustor temperature ($T_{\mathrm{t4,\,theo}}$), the theoretical characteristic velocity (C^*_{theo}), and theoretical gas constant in the combustor ($R_{\mathrm{4,\,theo}}$) are noted. Next, the experimental characteristic velocity is calculated:

$$C^*_{\mathrm{exp}} = \frac{p_{\mathrm{t4,\,exp}}\, A_5 c_{\mathrm{D5}}}{\dot{m}_4} \tag{5.3}$$

where $\dot{m}_4$ is the total mass flow rate through the nozzle. The experimental stagnation temperature in the combustor is:

$$T_{\mathrm{t4,\,exp}} = \left(\frac{T_{\mathrm{t4,\,theo}}\, R_{\mathrm{4,\,theo}}}{C^{*2}_{\mathrm{theo}}} \right) \frac{C^{*2}_{\mathrm{exp}}}{R_{\mathrm{4,\,exp}}} \tag{5.4}$$

For lack of an alternative, the accepted convention [52] is to assume that the experimental gas constant ($R_{\mathrm{4,\,exp}}$) is equal to the value calculated with CET89 ($R_{\mathrm{4,\,theo}}$).

The initial inputs for the above equations come from the measurements made during the direct-connect experiments. There are approximately 30 different transducer measurements taken for a single test, sampled at 1 000 Hz, which include mainly pressures and temperatures. The mass flow rates for the various gases require several of the pressure and temperature measurements, as well as the diameters of the sonic chokes through which they pass. There are also corrections applied for compressibility and van der Waals forces to the mass flow rates. Some of the pressure and temperature values, including those in the air plenum and combustor, are averaged over two or more transducers or thermocouples. For a test, vitiated air flows through the ducted rocket combustor and gas generator for 50 s to allow the temperatures to stabilize. The ethylene flow then starts and continues for 5 s, during which ramjet combustion takes place. After that, the experiment is gradually shut down. The time-averaged values of the temperatures and pressures during this period of ramjet combustion, after the pressure has stabilized inside the combustor and before the ethylene is shut off, are the ones used for the data reduction. Because each test generates a tremendous amount of raw data, including even a single experiment in this thesis as an appendix was not practical. However, more details on reducing the raw data can be found in references [49], [54], and [55]. Furthermore, Appendix C presents the data for direct-connect configuration DC1, including the averaged pressures, temperatures, and mass flow rates that are needed to use the above equations to arrive at a value for combustion efficiency.

5.4 Estimate of Uncertainty

Because the calculation of efficiency based on temperature rise in the combustor is so complicated, the estimation of experimental uncertainty is far from trivial. Several variables are involved, and the uncertainty of each propagates differently through the data reduction equations before it affects the final result. However, as long as the uncertainty of each variable can be estimated, techniques exist to calculate the overall uncertainty of the final result, in this case the efficiency based on temperature rise in the combustor, $\eta_{\Delta \mathrm{T}}$.

A method of how to describe uncertainties in single sample experiments by Kline and McClintock [56] has formed the basis of estimating experimental uncertainties for several years at TNO-PML. This method is also used in general applications [57], and was used in a study specifically on uncertainty analysis in direct-connect ramjet testing [58]. Each equation in the data reduction scheme is a function of n independent variables:

$$f = f\left(x_1, x_2, x_3, \ldots, x_n\right) \tag{5.5}$$

The absolute uncertainty w_f in the function f can be determined from the uncertainties in each of the independent variables:

$$w_f = \sqrt{\left(\frac{\partial f}{\partial x_1} w_{x_1}\right)^2 + \left(\frac{\partial f}{\partial x_2} w_{x_2}\right)^2 + \left(\frac{\partial f}{\partial x_3} w_{x_3}\right)^2 +, \ldots, + \left(\frac{\partial f}{\partial x_n} w_{x_n}\right)^2} \tag{5.6}$$

The uncertainties in the mass flow rates for the gas supply system [54] and other basic measurements [55] for the TNO-PML test facility are given in Table 5.2. They include both precision or random error, and bias or fixed error. They were taken directly or estimated from the manufacturers' data, or calculated using Eqn. 5.6. From these, first the uncertainty of the vitiated air flow rate $\dot{m}_{\mathrm{vitair}}$ was estimated:

$$w_{\dot{m}_{\mathrm{vitair}}} = \sqrt{\left(w_{\dot{m}_{\mathrm{air}}}\right)^2 + \left(w_{\dot{m}_{\mathrm{CH4}}}\right)^2 + \left(w_{\dot{m}_{\mathrm{O2}}}\right)^2} \tag{5.7}$$

and the uncertainty of the total mass flow rate through the combustor calculated:

$$w_{\dot{m}_4} = \sqrt{\left(w_{\dot{m}_{\mathrm{vitair}}}\right)^2 + \left(w_{\dot{m}_{\mathrm{C2H4}}}\right)^2} \tag{5.8}$$

As already mentioned, the calculation of the efficiency based on temperature rise in the combustor, $\eta_{\Delta \mathrm{T}}$, requires the use of a thermochemical equilibrium code such as CET89 to calculate some "theoretical" parameters such as the theoretical stagnation

Table 5.2: Uncertainties in the measured parameters

Quantity	Uncertainty
Air mass flow rate $\dot{m}_{\mathrm{air}}$	2%
Methane mass flow rate $\dot{m}_{\mathrm{CH4}}$	2%
Oxygen mass flow rate $\dot{m}_{\mathrm{O2}}$	2%
Ethylene mass flow rate $\dot{m}_{\mathrm{C2H4}}$	5%
Air plenum temperature T_{t2}	2%
Stagnation pressure in the combustor $p_{\mathrm{t4,\,exp}}$	0.6%
Nozzle area A_5	1.7%
Nozzle discharge coefficient c_{D5}	0%

combustor temperature ($T_{\mathrm{t4,\,theo}}$) and the theoretical characteristic velocity (C^*_{theo}). Since the inputs to these calculations include the parameters listed in Table 5.2, these too have associated uncertainties. Of these parameters, the uncertainty of the oxidizer/fuel ratio O/F ($\dot{m}_{\mathrm{vitair}}/\dot{m}_{\mathrm{C2H4}}$) must first be calculated:

$$w_{\mathrm{O/F}} = O/F\sqrt{\left(\frac{w_{\dot{m}_{\mathrm{vitair}}}}{\dot{m}_{\mathrm{vitair}}}\right)^2 + \left(\frac{w_{\dot{m}_{\mathrm{C2H4}}}}{\dot{m}_{\mathrm{C2H4}}}\right)^2} \tag{5.9}$$

Of all the inputs needed for the CET89 calculations (Section 5.3), O/F has by more than an order of magnitude more influence on $T_{\mathrm{t4,\,theo}}$ and C^*_{theo} than do the others. Since the absolute uncertainty for each output will change for each configuration, values of uncertainty for $T_{\mathrm{t4,\,theo}}$ and C^*_{theo} are shown in Table 5.3 for direct-connect configuration DC1. They were calculated by perturbing O/F by its uncertainty and recording the change in $T_{\mathrm{t4,\,theo}}$ and C^*_{theo}.

Table 5.3: Typical uncertainties for theoretical parameters

Quantity	Uncertainty
$T_{\mathrm{t4,\,theo}}$	2.9%
C^*_{theo}	1.7%

Next, the uncertainty in the experimental characteristic velocity was estimated:

$$w_{C^*_{\mathrm{exp}}} = C^*_{\mathrm{exp}}\sqrt{\left(\frac{w_{p_{\mathrm{t4,\,exp}}}}{p_{\mathrm{t4,\,exp}}}\right)^2 + \left(\frac{w_{A_5}}{A_5}\right)^2 + \left(\frac{w_{c_{\mathrm{D5}}}}{c_{\mathrm{D5}}}\right)^2 + \left(\frac{w_{\dot{m}_4}}{\dot{m}_4}\right)^2} \tag{5.10}$$

where, for these tests, c_{D5} is assumed to be unity and the uncertainty of this is negligible. Next, the uncertainty for the experimental stagnation temperature in the combustor $T_{\mathrm{t4,\,exp}}$ follows:

$$w_{T_{\mathrm{t4,\,exp}}} = T_{\mathrm{t4,\,exp}} \sqrt{\left(\frac{w_{T_{\mathrm{t4,\,theo}}}}{T_{\mathrm{t4,\,theo}}}\right)^2 + \left(\frac{(2) w_{C^*_{\mathrm{exp}}}}{C^*_{\mathrm{exp}}}\right)^2 + \left(\frac{(-2) w_{C^*_{\mathrm{theo}}}}{C^*_{\mathrm{theo}}}\right)^2} \tag{5.11}$$

The uncertainty for the experimental stagnation temperature rise in the combustor is:

$$w_{\Delta T_{\mathrm{exp}}} = \sqrt{\left(w_{T_{\mathrm{t4,\,exp}}}\right)^2 + \left(w_{T_{\mathrm{t2}}}\right)^2} \tag{5.12}$$

and for theoretical stagnation temperature rise in the combustor:

$$w_{\Delta T_{\mathrm{theo}}} = \sqrt{\left(w_{T_{\mathrm{t4,\,theo}}}\right)^2 + \left(w_{T_{\mathrm{t2}}}\right)^2} \tag{5.13}$$

Finally, the uncertainty for efficiency based on stagnation temperature rise in the combustor is:

$$w_{\eta_{\Delta\mathrm{T}}} = \eta_{\Delta\mathrm{T}} \sqrt{\left(\frac{w_{\Delta T_{\mathrm{exp}}}}{\Delta T_{\mathrm{exp}}}\right)^2 + \left(\frac{(-) w_{\Delta T_{\mathrm{theo}}}}{\Delta T_{\mathrm{theo}}}\right)^2} \tag{5.14}$$

Table 5.4 shows values of the uncertainties for the calculated parameters for direct-connect configuration DC1. As seen, the largest uncertainties, before the actual calculation of $\eta_{\Delta\mathrm{T}}$, are associated with the estimation of the experimental temperatures rather than the theoretical ones, so these have the largest impact on the uncertainty of $\eta_{\Delta\mathrm{T}}$. The fact that a difference of two temperatures must be calculated for both the theoretical and experimental temperature rises also magnifies the overall uncertainty. Overall uncertainties for most of the direct-connect configurations were 10-15%[2] of the calculated efficiency, the average being 13%. However, the reproducibility of the experiments was very good, being less than the average experimental uncertainty. Four of the experiments were repeated with the same specified boundary conditions; the actual boundary conditions were then estimated as for the rest of the configurations. The results are shown in Appendix D.

While these values of overall uncertainty may seem high, there were unfortunately no values of uncertainty given in any of the literature cited on direct-connect experiments with which they could be compared. However, the fact that they seem

[2]The uncertainties given here are both positive and negative (ie. 10-15% = ±10-15%).

Table 5.4: Typical uncertainties for calculated parameters

Quantity	Uncertainty
C^*_{exp}	2.6%
$T_{\mathrm{t4,\,exp}}$	6.8%
ΔT_{exp}	10.5%
ΔT_{theo}	3.9%
$\eta_{\Delta\mathrm{T}}$	11.2%

high may well explain this deficiency and why researchers are reluctant to report these values. The only comprehensive description of uncertainty analysis for direct-connect testing found in the literature [58] gave values of overall uncertainty and explained how they were generated, but they used values of uncertainty for the basic measurement parameters reported elsewhere [52]. With these values of uncertainty for the basic measurement parameters and using the method described in Section 5.3 to calculate $\eta_{\Delta\mathrm{T}}$, their estimate of uncertainty appears to be about 5%. However, the uncertainties that they used for almost all of the basic measurement parameters were lower than for these tests. For instance, their uncertainties were 0.9% for $\dot{m}_{\mathrm{air}}$, 0.5% for $\dot{m}_{\mathrm{fuel}}$, 0.8% for T_{t2}, and 0.8% for A_5. Two that were higher were 1% for c_{D5} and 1.2% for $p_{4,\,\mathrm{exp}}$. With these values substituted for the TNO-PML values, the calculated overall uncertainty for $\eta_{\Delta\mathrm{T}}$ is close to that estimated in [58].

5.5 Configurations

The configurations used for the direct-connect experiments and subsequently modelled are presented in Table 5.5. The average fuel and air inlet velocities and the air/fuel momentum ratio are calculated from the experimental pressure and temperature data. Any numbers missing from 1 to 30 were either duplicate tests or used solid fuel. Configuration DC4 is missing because it had a very high uncertainty in the ethylene mass flow rate. As shown, a wide range of geometries, air/fuel momentum and mass flow ratios, and two different combustor pressures were chosen to provide extensive data for validation of the CFD-based method to predict combustor performance.

Table 5.5: Combustor configurations for direct-connect experiments and combustion CFD modelling

Direct Connect Configuration	Water Tunnel Configuration[a]	Air Injector	Fuel Injector	Dome Height [mm]	Air/fuel Momentum Ratio	Air/fuel Mass Ratio	Combustor Static Pressure [MPa]	Fuel Velocity [m/s]	Air Velocity [m/s]
DC1	WT7, WT8	A4	F0-27	57	2.62	7.79	0.396	416	140
DC2	WT9, WT10	A4	F0-27	57	11.73	15.73	0.403	328	245
DC3	WT9, WT10	A4	F0-27	57	8.89	13.84	0.875	282	181
DC6	WT1, WT2	A2	F0-27	57	3.90	7.09	0.411	443	244
DC7	WT5, WT6	A2	F0-27	57	19.43	15.76	0.426	311	384
DC8	WT5, WT6	A2	F0-27	57	17.94	14.96	0.944	239	287
DC9	WT1, WT2	A2	F0-27	57	3.52	6.70	0.845	609	320
DC11	WT11, WT12	A4	F0-18	57	4.87	15.36	0.432	710	225
DC12	WT13, WT14	A4	F1-18	57	4.07	13.96	0.907	600	175
DC13	WT19, WT20	A6	F0-27	57	2.30	7.00	0.44	436	143
DC14	WT21, WT22	A6	F0-27	57	10.80	15.33	0.419	324	229
DC15	WT23, WT24	A6	F0-27	57	5.20	10.66	0.904	358	175
DC16	WT19, WT20	A6	F0-27	57	2.37	7.11	0.8	599	200
DC18	WT15, WT16	A4	F0-27	100	2.13	6.65	0.397	501	160
DC19	WT17, WT18	A4	F0-27	100	10.93	15.35	0.423	317	226
DC20	WT17, WT18	A4	F0-27	100	8.31	13.34	0.882	288	179
DC21	WT15, WT16	A4	F0-27	100	2.76	7.62	0.792	564	205
DC28	WT13, WT14	A4	F1-18	57	4.84	15.32	0.44	692	219
DC29	WT11, WT12	A4	F0-18	57	4.42	14.54	0.923	568	173
DC30	WT25[b]	A4	F1-18S	57	4.29	14.34	0.921	579	173

[a]This is the corresponding water tunnel configuration (same geometry and approximate air/fuel momentum ratio) used in the water tunnel experiments and non-reacting flow CFD modelling presented in Chapters 3 and 4.

[b]This configuration was not tested in the water tunnel, but there are non-reacting flow CFD results.

5.6 High-frequency Pressure Measurements

The combustor pressure data from the direct-connect testing of the configurations shown in Table 5.5 showed some significant oscillations. If these were indeed present in the combustor, they could greatly influence the mixing and combustion. Unfortunately, due to the large number of data channels that had to be sampled during these direct-connect tests, the sampling frequency could only be 1 000 Hz and it was therefore impossible to characterize and identify the source of these oscillations properly. Furthermore, low-frequency-response piezo-resistive transducers were used, better suited to measure the steady pressure in the combustor rather than any rapid fluctuations. Subsequent to these tests, however, an independent data acquisition system was assembled to measure pressure oscillations in the combustor properly, and a few tests carried out. This system included two high-frequency-response piezoelectric pressure transducers, flush mounted to the inner combustor wall and water-cooled to reduce drift due to heating. Their signals were sampled at 80 kHz and filtered to eliminate any 50-cycle noise (the frequency of the electricity in the Netherlands). They were also filtered to eliminate aliasing above 25 kHz.

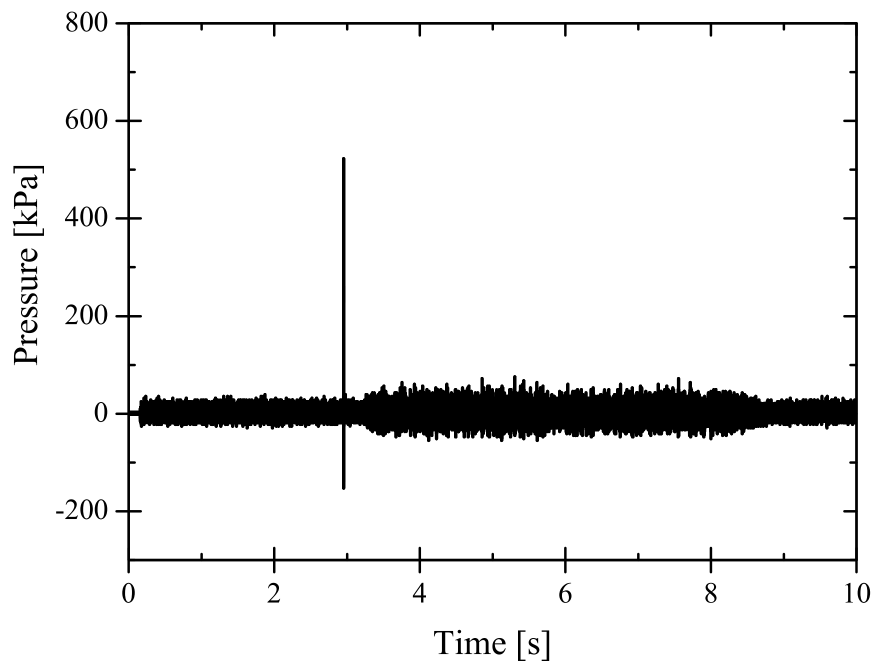

Figure 5.9: Pressure variation versus time

Figure 5.9 shows the magnitude of the pressure oscillations from one of the transducers versus time. The magnitude of the pressure oscillations due to flow noise, about 50 kPa, can be seen before the spike from the ignition of the gas generator that occurs at 3.0 s. Shortly afterwards at about 3.3 s, the fuel-rich exhaust from the gas generator and the vitiated air ignites in the ramjet combustor, and the pressure oscillations are about 100 kPa in magnitude. Given that the average static pressure in the combustor for this test was 0.42 MPa, the magnitude of the pressure oscillations is indeed significant.

While the magnitude of the oscillations obviously changes before and after ignition of the mixture in the ramjet combustor, Fast Fourier Transform (FFT) analysis of the signal was done at one-second intervals to see if the frequencies of the oscillations and the magnitude of each frequency also change. At 2.0 s, before ramjet ignition, Fig. 5.10 shows that there are two significant frequencies at 520 and 2890 Hz. Figure 5.11 shows an FFT at 6.0 s, well after ramjet ignition, and the frequencies and magnitudes have changed significantly. There are dominant frequencies at approximately 250, 800, 920, 1500, 2420, and 4820 Hz, some of which may be harmonics of the others. The magnitude of the lowest frequency component has also doubled with respect to the 520 Hz peak at 2.0 s.

Apart from showing that the combustor pressure oscillations can be significant, these data have demonstrated that the magnitude and frequency of the pressure oscillations change when combustion occurs in the ramjet, and that there is a strong possibility that they are coupled to the combustion processes taking place. The effect of these pressure oscillations on combustor performance has not been considered in the CFD modelling, and therefore may help explain differences between the experimental and predicted results to be presented later. While time-dependent CFD modelling is possible in theory and could take these oscillations into account, this type of modelling would not have been practical for the three-dimensional, turbulent reacting flowfield of interest here.

5.7 Summary of the Direct-connect Experiments

With the same geometries and range of air/fuel momentum ratios as for the water tunnel, several configurations were tested in the TNO-PML direct-connect combustion test facility. Many modifications were made to existing ducted rocket hardware so that the characterization of the boundary conditions, particularly at the air and fuel inlets, could be done with more confidence. These boundary conditions are of critical importance to the CFD modelling.

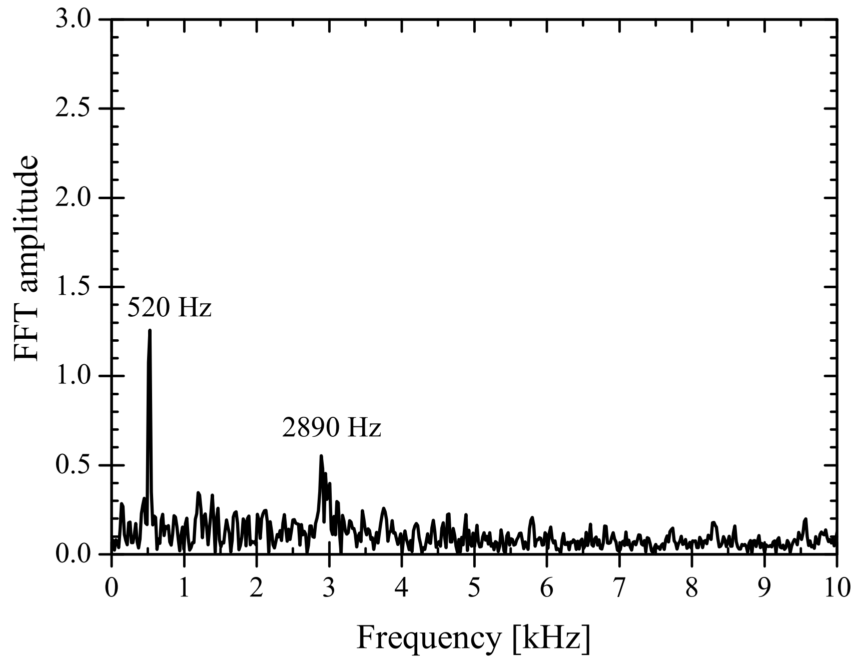

Figure 5.10: FFT amplitude versus frequency at 2.0 seconds

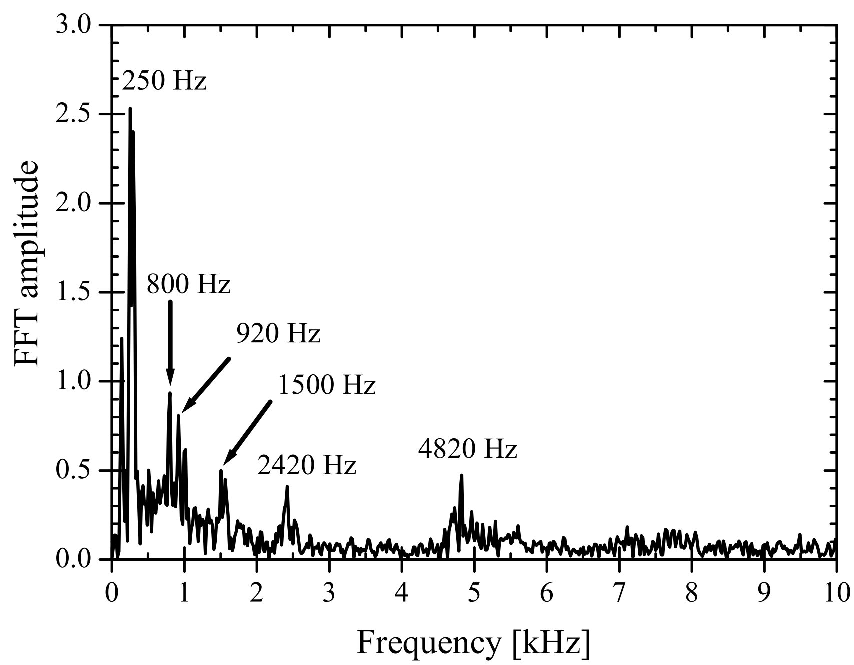

Figure 5.11: FFT amplitude versus frequency at 6.0 seconds

The measure of performance to characterize the results for each of the direct-connect experiments was combustion efficiency based on temperature rise in the combustor. Unlike other definitions of combustion efficiency often reported elsewhere, it varies from 0% to 100%. It is also the best choice to compare with the CFD results because it takes into account the performance of only the combustor and not any other components. A comprehensive assessment to estimate the experimental uncertainty of the combustion efficiency was also carried out. Overall uncertainties for most of the direct-connect configurations were 10-15% of the calculated efficiency, the average being 13%. Unfortunately, very little was found in the literature cited to compare with the values estimated for the experimental uncertainty.

As with the water tunnel, time-dependent processes were expected to take place inside the experimental direct-connect combustors, and they were confirmed with the measurement of significant pressure oscillations. Furthermore, the measurements demonstrated that the magnitude and frequency of the pressure oscillations change when combustion occurs in the ramjet. There is therefore a strong possibility that they are coupled to the combustion processes taking place. The existence of these oscillations and their possible influence on combustor performance must be kept in mind for the reacting flow CFD modelling predictions.

Chapter 6

REACTING FLOW MODELLING

6.1 CFD Modelling of Ramjet Combustors

The work presented in this chapter has been summarized in two papers that are included in Appendix E. The first [59] was presented at the 36th AIAA Joint Propulsion Conference in 2000, and the second [60] was presented at the 37th AIAA Joint Propulsion Conference in 2001.

Until the beginning of the 1980's, the speed of computers was not fast enough to allow CFD modelling of ducted rocket combustors to be practical. Since then, not only has computer technology advanced by orders of magnitude, but CFD codes have improved tremendously as well. Because turbulent mixing is a dominant phenomenon in ducted rocket combustors, all of the previous modelling cited here used the time- averaged Navier-Stokes (N-S) equations.

One of the first of the widely available CFD codes was "TEACH", for Teaching Elliptical Axisymmetric Characteristics Heuristically, developed at Imperial College in London. This was used in 1984 [61] to model an axisymmetric dump combustor with a circumferential air inlet and a fuel consisting of the exhaust from a 50% polyester, 50% ammonium perchlorate (AP) formulation. The turbulence was modelled with a standard k-ε model, the combustion with an infinitely fast one-step global reaction, and the flowfield was considered incompressible. A two-dimensional Cartesian 49X15 grid was employed. The authors claimed qualitative agreement with Schadow's experiments [62].

The experimental combustor presented in Fig. 3.3 was the object of two modelling studies. The first, in 1986, was by Vanka *et al.* [28] who discretized the geometry into an 11X11X24 grid of half the geometry (because of the symmetry plane). Gaseous ethylene injected into the head was a departure from the experimental study, however, which had liquid JP-4 fuel injected into the air inlets. A one-step irreversible reaction with a Probability Density Function (PDF) model to describe the turbulence/chemistry interaction was used. They also used a standard k-ε turbulence model and assumed that the flowfield was incompressible. They had extensive calculated combustion efficiency data versus several parameters and compared them with two data points from [27] for which the agreement was excellent. Unfortunately, neither reference said what type of combustion efficiency was used, nor what the uncertainty was. Furthermore, as already mentioned, the fuels and injection were not even the same in the two cases. The second study by Wu *et al.* [63], reported in 1995, used a finite-volume general-purpose code developed at Los Alamos called KIVA3. The grid had 60 000 nodes, and a modified k-ε turbulence model was used. While KIVA3 can model combustion and two-phase flow, these were ignored in this study, with the work concentrating on the effect of swirlers on the non-reacting, but compressible flowfield.

The next three modelling studies used the dual inlet side dump combustor geometry shown in Fig. 3.4 for which LDV measurements of turbulence intensity and mean velocities exist [29]. All three studies modelled only the isothermal incompressible flowfield in the combustor, the first two by the same research group who did the LDV measurements. The first study [64] in 1988 used a standard k-ε turbulence model and a 40X10X9 grid. The authors claimed results for mean velocities within 15% of the measured values. The second study [65] reported one year later was the same as the first except an Algebraic Reynolds Stress Model (ASM) was used for the turbulence. Results for mean velocities were still generally within 15% of the measured values, but predictions for the vortices in the dome region were improved. This is because the k-ε model assumes isotropic turbulence, while the ASM can handle anisotropic turbulence, albeit with an increase in complexity and computational effort. The third study in 1993, by different researchers, used several grids but found that the 56X20X15 grid was sufficient to minimize the effects of grid size on the main flow structures. They felt that any improvement in the predictions of the ASM over the k-ε model was not worth the extra computational effort, so the k-ε turbulence model was used. Their work showed that structures in three-dimensional combustors were indeed different than those in two-dimensional combustors, and were able to characterize the effects of changing inlet side angle on the flowfield structures.

The two-dimensional combustor in Fig. 3.5 was also the subject of five modelling studies, the first reported in 1989 by a group at Pennsylvania State University who also performed the experiments [66]. They used a k-ε turbulence model, uniform inlet properties, and a two-step global reaction scheme for propane with a modified Eddy Break-Up (EBU) combustion model to account for the turbulence/chemistry interaction. From the vector plots of velocity, the grid appears to be about 30X18, and consists of only the combustor and not the inlets nor the nozzle. The reason given for focusing on a two-dimensional rather than a three-dimensional combustor was that it was beneficial to study the two-dimensional case first. They claim that they were able to reproduce the non-reacting flow structures seen in the Schlieren images from the experiments. From the reacting flow modelling, they were able to calculate the effect of dome height and inlet flow angle on calculated specific impulse. Unfortunately, they do not say how they calculated specific impulse from the computed data. The second study [67], from 1993, used the same CFD model just described, and a grid that may be a few cells more dense. The goal of the study was to determine the effect of air inlet location and equivalence ratio on combustion efficiency and specific impulse. Unfortunately, the method of calculating the performance parameters is not mentioned, nor is the type of combustion efficiency used. A third study [68], also reported in 1993, used a 40X40 Cartesian grid and adjustable implicit/explicit schemes with Taylor/Galerkin methods to deal with widely differing length and time scales. They used a k-ε turbulence model, modified for compressibility, and a two-step global reaction scheme for propane combustion with an EBU model. Results were considered preliminary, and while they appear to have used the same geometry as in Fig. 3.5 with some minor differences, they have done no comparisons with the experimental data.

The group from Pennsylvania State University seems to have used the same basic configuration of their two-dimensional combustor for some modelling work in 1994 [69]. They used a 99X46 mesh for the combustor, but also meshed a curved inlet diffuser. They used a dual time-stepping method [70] to solve the compressible flowfield, and used a low Reynolds number k-ε model to describe the turbulence. For combustion, they assumed a one-step reaction for propane. They were able to demonstrate that the inlet and combustor could be modelled together, but unfortunately did not compare the results with any experimental data.

The authors of the fifth study of this two-dimensional combustor, Chao *et al.* [71], summed up the CFD modelling tools available as of 1995 for design and performance prediction as being far from satisfactory. They said that Direct Numerical Simulation (DNS) calculations would be formidable, so they had to use a turbulence model. Because of anisotropy in the turbulence reported by Liou *et al.* [65], however, they used ASM's as well as the k-ε model. They also modified these to account for compressible turbulence since they questioned the suitability of incompressible turbulence models for compressible jet interactions. They equally questioned the suitability of Cartesian grids because of numerical diffusion, so they opted for a 40X40 adaptive streamline grid. Denser grids were tried, but no significant improvements in predictions resulted. To model the combustion and turbulence/chemistry interaction, they used a clipped Gaussian PDF. Unfortunately, there were no experimental data available to validate their reacting flow predictions, but they were able to compare their non-reacting flow predictions with the available LDV data [32]. Predictions were better with the ASM's than with the k-ε model, particularly when the constants of the ASM's were changed. However, adding an extra term for compressible turbulence to each of the models also improved predictions.

A French research team [72] described another study of a simplified two-dimensional combustor with both CFD modelling and experimental results. The combustor was 70 mm high, 340 mm long, with a dome height of 42.5 mm. The dual opposed inlets were 5 mm wide and injected premixed propane and air at an angle of 90°. An injection velocity of 20 m/s was used for the comparison between modelling and measurements. The modelling was done with a time-dependent finite-volume code, a 53X24 grid, and a standard k-ε turbulence model. For the combustion, a Coherent Flame Model, which is a type of laminar flamelet model, was used. Results for comparison for the non-reacting flow showed reasonable agreement with hot-wire velocity profiles at the head end, but this got worse toward the nozzle end. The authors conceded that the oscillation of the impinging inlet jets was not properly simulated and may account for the lack of agreement. For the reacting flow case, the general pattern of combustion was reproduced, but there the authors said that there was much room for improvement.

Another French paper from 1998 [73] redid the predictions of this simplified combustor with a commercial CFD code called CFD-ACE from CFD-RC which also used a standard k-ε turbulence model and the Coherent Flame Model for combustion. They claimed good qualitative agreement with the measurements, but a comparison of the maximum heat release rate reveals that it is twice as high for the numerical as for the experimental results. This is likely due to use of a one-step irreversible reaction for the Coherent Flame Model rather than allowing many more species and an assumption of thermochemical equilibrium. CFD-ACE was also used to model a coaxial dump combustor configuration [9, 74] which used liquid kerosene as a fuel, sprayed as droplets into the combustor. They meshed from just upstream of the flameholders in the combustor to the end of the nozzle with 120 000 cells. Before comparing the CFD and experimental results, however, they first tuned one of the constants of the combustion model to properly locate the point of maximum heat release for different combustor lengths. After tuning the model, however, it was still not able to reliably predict combustion efficiency for all conditions, but was able to show trends. Predictions ranged from very good to being twice those of the experimental values. While they did identify the type of combustion efficiency used (based on fuel/air ratio) they did not say how this was calculated from the modelling data.

In 1993 Liou *et al.* [75] also reported a study on a small two-dimensional combustor, 30 mm high, with a dome height of 22.5 mm with dual opposed air inlets 15 mm wide and an injection angle of 90°. A 1.6 mm slit in the centre of the head end provided methane fuel. Not only did they perform non-reacting and reacting flow predictions, but they performed LDV measurements on the non-reacting flowfield. Bulk velocity in the combustor was only 23.9 m/s, so the flow was considered incompressible. They used an ASM to model the turbulence as a compromise between the k-ε and RSM. For the combustion, a one-step, finite-rate, irreversible reaction for methane was used with the EBU model to account for the turbulence/chemistry interaction. The solution with the 53X29 grid seemed grid independent. For non-reacting flow, good agreement for reattachment length, velocities, and turbulence parameters were obtained. For reacting flow, predictions for total pressure loss were different from the non-reacting flow predictions and measurements.

Modelling work from the U.K. [76] reported in 1997 was done on a configuration similar to that in Fig. 3.3 but with gaseous fuel injected in the head (there was also a stabilizing fence). The dual ventral inlets injected air at an angle of 45°. They used the FLUENT commercial CFD code, and created a mesh of 90 000 cells that included a portion of the inlets and the combustor. The flow was assumed incompressible, and they used a 16-species adiabatic PDF to model the combustion. The fuel was an unspecified exhaust composition from a solid fuel gas generator. Unfortunately, the calculated temperatures in the combustor were much higher than the experimental values, and they attributed this to specifying gaseous instead of solid carbon in the fuel composition. However, they were able to use the CFD results to see the effects of changing fuel injection methods. Qualitative agreement was also obtained with previous water tunnel results [77].

In 1999 a group at ONERA in France [36] reported work on CFD modelling, water tunnel flow visualization, and LDV measurements on a square cross-section ducted rocket combustor with dual opposed inlets, 100 mm wide and high, and a 45^{o} air injection angle (Fig. 3.9). Propane fuel was injected from two ports of 11 mm diameter in the head, and the dome height varied from 65 mm to 135 mm. Numerical modelling was done with a three-dimensional Navier-Stokes code developed at ONERA, k-ε turbulence model, and a one-step EBU model modified to handle rich flames. Because of the two symmetry planes, they meshed only one quarter of the geometry, 48 260 nodes in the combustor and 9 800 in the air inlet for the combustion model, and 38 625 in the combustor and 20 250 in the air inlet for the non-reacting flows (water and air). The results for the non-reacting flow showed a lower degree of mixing than in the water tunnel visualization. They claimed good general agreement, but axial velocities and fluctuations were underestimated. However, they proposed the use of an ASM to improve these predictions. They presented very limited results for reacting flow that showed a fluctuating mass flow at the nozzle (time-dependent calculations) and one value of mean combustion efficiency. Unfortunately, they have not defined their combustion efficiency or how it was calculated.

The final reference cited here for modelling studies [78] is from 2000. They used an axisymmetric combustor with a nozzle, and used a 240X50 grid with a finite-difference, compressible flow N-S code. They used an "improved" k-ε turbulence model, but only modelled the non-reacting flow. They used the results to determine the effect of injection angles and inlet placement on the flowfield. Unfortunately, there were no experimental data to validate the results.

To sum up the results (Table 6.1), most of the modelling studies considered only the combustor, but a couple also included part of the inlet and/or the nozzle. Grids were generally Cartesian. Flow was often assumed incompressible, except when a nozzle was present or there were very high speeds in the air or fuel inlets. The k-ε model, sometimes with modifications, was usually used to describe the turbulence. Simple hydrocarbon fuels were usually used, and all except one were gaseous. In that one case, liquid kerosene was injected into the flow and the trajectories and

Table 6.1: Previous CFD modelling

Reference	Code	Grid	Turbulence model	Combustion model	Fuel	Experimental data
Chen & Tao [61] 1984	Incompressible, N-S (TEACH)	Axisymmetric 49X15	k-ε	One-step reaction, infinitely fast	Exhaust from 50% polyester, 50% AP	Schadow [62]
Vanka *et al.* [28] 1986	Incompressible N-S	3D, 24X11X11	k-ε	One-step reaction, infinitely fast, PDF	Ethylene	Stull *et al.* [27]
Wu *et al.* [63] 1995	Compressible N-S (KIVA3)	3D, 60 000 cells	Modified k-ε	Non-reacting		Stull *et al.* [27]
Liou *et al.* [64] 1988	Incompressible N-S	3D, 40X10X9	k-ε	Non-reacting		Liou & Wu[29]
Liou & Hwang [65] 1989	Incompressible N-S	3D, 40X10X9	ASM	Non-reacting		Liou & Wu [29]
Yen & Ko [31] 1993	Incompressible N-S	3D, 56X20X15	k-ε	Non-reacting		Liou & Wu [29]
Cherng *et al.* [66] 1989	Compressible N-S	2D, 30X18 (estimated)	Modified k-ε	Two-step finite rate, modified EBU	Propane	Chuang *et al.* [32]
Onn *et al.* [67] 1993	Compressible N-S	2D, 32X18 (estimated)	Modified k-ε	Two-step finite rate, modified EBU	Propane	Chuang *et al.* [32]
Yoon & Chung [68] 1993	Compressible N-S	2D, 40X40	Modified k-ε	Two-step finite rate, EBU	Propane	
Hsieh *et al.* [69] 1994	Compressible N-S, Dual time step	2D, 99X46	Low Re k-ε	One-step finite rate	Propane	
Chao *et al.* [71] 1995	Compressible N-S	2D, 40X40, adaptive	Modified ASM	Adiabatic PDF	Propane	Chuang *et al.* [32]
Montazel *et al.* [72] 1992	Incompressible N-S	2D, 53X24	k-ε	Coherent Flame Model	Propane	Montazel *et al.* [72]
Dufour & Montazel [73] 1998	Compressible N-S (CFD-ACE)	2D	k-ε	Coherent Flame Model	Propane	Montazel *et al.* [72]
Liou *et al.* [75] 1993	Incompressible N-S	2D, 53X29	ASM	One-step finite rate, EBU	Methane	Liou *et al.* [75]
Beasley & Ivey [76] 1997	Incompressible N-S (FLUENT)	3D, 90 000 cells (full geometry)	k-ε	16 gaseous species, adiabatic PDF	Exhaust from unspecified solid fuel	Beasley & Ivey [77]
Dufour & Montazel [73] 1998	Compressible N-S (CFD-ACE)	3D, 120 000 cells (full geometry)	k-ε	Coherent Flame Model	Liquid kerosene (two phase)	Stull *et al.* [9] Craig *et al.* [74]
Ristori *et al.* [36] 1999	Compressible N-S (MSD)	3D, 58 060 cells (1/4 geometry)	k-ε	One-step reaction, modified EBU	Propane	Ristori *et al.* [36]
Zhang *et al.* [78] 2000	Compressible N-S	2D, 240X50	Modified k-ε	Non-reacting		

evaporation of the droplets were modelled. There were no studies that took into account the motion and decomposition of a solid phase, however. A variety of combustion models was used, including one- or two-step global reactions, and some of these accounted for the turbulence/chemistry interaction with an EBU model. Others used newer models like the PDF or laminar flamelet models. The trend was, with time, to use denser grids, the newer combustion models, and commercial CFD codes. As for validation, only a couple of parametric studies were done to establish grid-independence. Any comparison between CFD modelling and experimental results was for the non-reacting flow only, except in a couple of instances where some reacting flow data were available. Unfortunately, none of the reacting flow studies described exactly how combustion efficiency was determined from the CFD results, and usually not even the type of combustion efficiency was noted.

6.2 Onestream PDF Model

As seen in Chapter 4 modelling the flowfield in a ducted rocket combustor is not simple. However, it becomes much more complicated if combustion must be added. The combustion of even the simplest fuels can involve hundreds of individual reactions, so simplifications are absolutely necessary for CFD applications. The simplest combustion models use a single global reaction and may include an Arrhenius-type reaction rate. They neglect, however, one of the biggest challenges to modelling practical combustion problems, which is how to describe the influence of turbulence on the chemical reactions and vice versa. The EBU model, seen in several of the earlier attempts at modelling combustion in a ducted rocket or ramjet, was one of the first widely accepted methods for dealing with the turbulence/chemistry interaction. Basically, this model takes the slower of two rates for each reaction, one calculated from the Arrhenius expression, and the other dependent on the turbulent mixing. Unfortunately, this model relies on some empirical constants which must often be "tuned" for each particular problem. Arrhenius data must also be used, many of which have large uncertainties. Results also depend heavily on exactly which reactions are chosen, so they must be chosen wisely. Normally, better results are obtained with more reactions and chemical species, but one extra transport equation, in addition to the overall conservation of energy, must be solved for each additional species, so computational time will increase accordingly. For a ducted rocket combustor, with the gas generator exhaust being the fuel, the choice of these reactions would be very difficult and, as seen in Table 6.1, has not been attempted with the EBU model.

Fortunately, there is another method which, in combination with the assumption of local thermochemical equilibrium at all but the richest regions, is well suited to modelling a ducted rocket combustor using a solid fuel gas generator. The Probability Density Function (PDF) approach [19] is meant to model turbulent diffusion flames, where the main assumptions are that the reaction rate based on the Arrhenius expression is much faster than that based on the turbulent mixing, and that the Lewis number (Le) is unity (ratio of mass diffusivity to thermal diffusivity, or $Pr/Sc = 1$). Being a turbulent diffusion flame also requires that the fuel and air inlet streams be separate, as they are in the ducted rocket combustor. One of the main advantages of the PDF approach over the EBU model is that regardless of how many species are included in the fuel and oxidizer (air) streams, only two additional transport equations have to be solved, one for the mean mixture fraction, $\bar{f}$, and the other for the variance of the mixture fraction, $\bar{g}$. The mixture fraction is a conserved scalar which varies between 0 and 1. It is defined by:

$$f = \frac{Z_i - Z_{i\mathrm{O}}}{Z_{i\mathrm{F}} - Z_{i\mathrm{O}}} \tag{6.1}$$

where Z_i is the mass fraction of the ith element, and the subscripts O and F denote the values in the oxidizer and fuel inlet streams respectively. The equation for the transport of the mean mixture fraction is:

$$\frac{\partial\left(\rho\bar{f}\right)}{dt} + \frac{\partial\left(\rho\bar{u}_i\bar{f}\right)}{\partial x_i} = \frac{\partial}{\partial x_i}\left(\frac{\mu_\mathrm{t}}{\sigma_t}\frac{\partial\bar{f}}{\partial x_i}\right) + S_m \tag{6.2}$$

where S_m is the transfer of mass from any droplets or particles in the combustor. The transport of the mixture fraction variance is solved from:

$$\frac{\partial\left(\rho\bar{g}\right)}{dt} + \frac{\partial\left(\rho\bar{u}_i\bar{g}\right)}{\partial x_i} = \frac{\partial}{\partial x_i}\left(\frac{\mu_\mathrm{t}}{\sigma_t}\frac{\partial\bar{g}}{x_i}\right) + C_g\mu_\mathrm{t}\left(\frac{\partial\bar{f}}{\partial x_i}\right)^2 - C_d\rho\frac{\varepsilon}{k}\bar{g} \tag{6.3}$$

where $\sigma_t = 0.7$, $C_g = 2.86$, and $C_d = 2.0$ are recommended values [79].

Scalars such as the concentration of each species, the temperature, and the density at any point in the combustor can be determined without solving transport equations for them as long as the mixture fraction is also known at that point. In fact, if the problem can be classified as adiabatic, solution of the equation for the conservation of energy is not even necessary, which not only reduces computational time because of fewer equations, but because of easier convergence of the solution when compared to the EBU model. Exactly how these scalars are related to the mixture fraction is determined by the system chemistry. The simplest of these is the "mixed-is-burned" approach which assumes that there is an infinitely fast and irreversible reaction of the fuel and oxidizer to the products. While computationally fast, this approach neglects any dissociation of the final products and therefore tends to overestimate temperatures. A better approach, and the one used for all of the reacting flow modelling presented here, is to assume that the fuel and oxidizer react infinitely fast, and that the resulting products are in thermochemical equilibrium. Still another approach is the laminar flamelet model which can take into account non-equilibrium effects. Unlike the mixed-is-burned and equilibrium approaches, however, the Arrhenius data for all of the chemical reactions must be known which, as previously mentioned, would be very difficult for a ducted rocket combustor with the gas generator exhaust being the fuel.

While the choice of the system chemistry establishes relationships of how the *instantaneous* values of the scalars are related to f, the calculation of the *time-averaged* values of the scalars requires different relationships to relate them to $\bar{f}$ and take into account the turbulence/chemistry interaction. To calculate the time-averaged species mole fractions and temperature, the following equation is used:

$$\bar{\phi}_i = \int_0^1 p(f)\phi_i(f)df \tag{6.4}$$

where ϕ_i is a species mole fraction or the temperature and is a function of f. The time-averaged density is calculated from:

$$\frac{1}{\bar{\rho}} = \int_0^1 \frac{p(f)}{\rho(f)}df \tag{6.5}$$

The probability density function $p(f)$ is:

$$p(f)\Delta f = \lim_{T\to\infty} \frac{1}{T}\sum_i \tau_i \tag{6.6}$$

where τ_i is the fraction of time that f lies between f and $f + \Delta f$. The shape of the PDF $p(f)$ is extremely important to modelling the turbulence/chemistry interaction, and the β-shaped PDF is thought to best represent experimental observations of turbulent combustion experiments. It is given by:

$$p(f) = \frac{f^{\alpha-1}(1-f)^{\beta-1}}{\int f^{\alpha-1}(1-f)^{\beta-1}df} \tag{6.7}$$

where α is calculated from:

$$\alpha = \bar{f}\left[\frac{\bar{f}(1-\bar{f})}{\bar{g}} - 1\right] \tag{6.8}$$

and β is calculated from:

$$\beta = (1-\bar{f})\left[\frac{\bar{f}(1-\bar{f})}{\bar{g}} - 1\right] \tag{6.9}$$

The shapes of the β-PDF are shown for three combinations of $\bar{f}$ and $\bar{g}$ ($\bar{f} = 0.5$ and $\bar{g} = 0.01$, $\bar{f} = 0.1$ and $\bar{g} = 0.01$, and $\bar{f} = 0.5$ and $\bar{g} = 0.1$) in Fig. 6.1. As shown, the exact shape of the β-PDF is very dependent on the mean mixture fraction and its variance. FLUENT's preprocessor called prePDF (Version 3.1) was used to generate look-up tables for the relevant scalars using 21 discrete points for the mean mixture fraction and 11 discrete points for the variance[1]. The centre point of the distribution was set at $\bar{f} = 0.2$, on the rich side of the stoichiometric value of the mixture fraction ($f_{\text{stoich}} = 0.134$ for a composition equivalent to a solid fuel formulation with 90% GAP and 10% carbon) and equal to the minimum value as recommended [46]. Furthermore, the rich limit was usually set to $f = 0.5$ (less if there was difficulty in calculating the equilibrium composition at that value of f) which means that prePDF would not calculate the equilibrium composition above $f = 0.5$, implying that there was no reaction of the fuel with the oxidizer stream above that limit. This limit was higher than the value recommended [46] of 1.5 to 2 times f_{stoich}, but the FLUENT recommendation is for hydrocarbon fuels in general. For a composition such as the exhaust from a GAP/Carbon gas generator (or its ethylene/air equivalent) which is already partially oxidized and at a temperature on the order of 1 000 K, a higher rich flammability limit was thought reasonable.

With the results of the calculations for the β-PDF's, the look-up tables are constructed for the time-averaged values of the scalars with the use of Eqns. 6.4 and 6.5. The necessary inputs include the species compositions and static temperatures at the oxidizer and fuel inlets, and the static pressure inside the combustor. The list of species that should be included in the calculations includes not only those that are present in the oxidizer and fuel streams, but those expected in significant quantities in the combustor after the two streams have mixed and reacted. An example, representative of all of the direct-connect combustor configurations, is shown in Table 6.2.

[1]While lots of points make for a higher resolution table, the problem will take more calculation time. The number of discrete points used was chosen to give good accuracy within a reasonable calculation time.

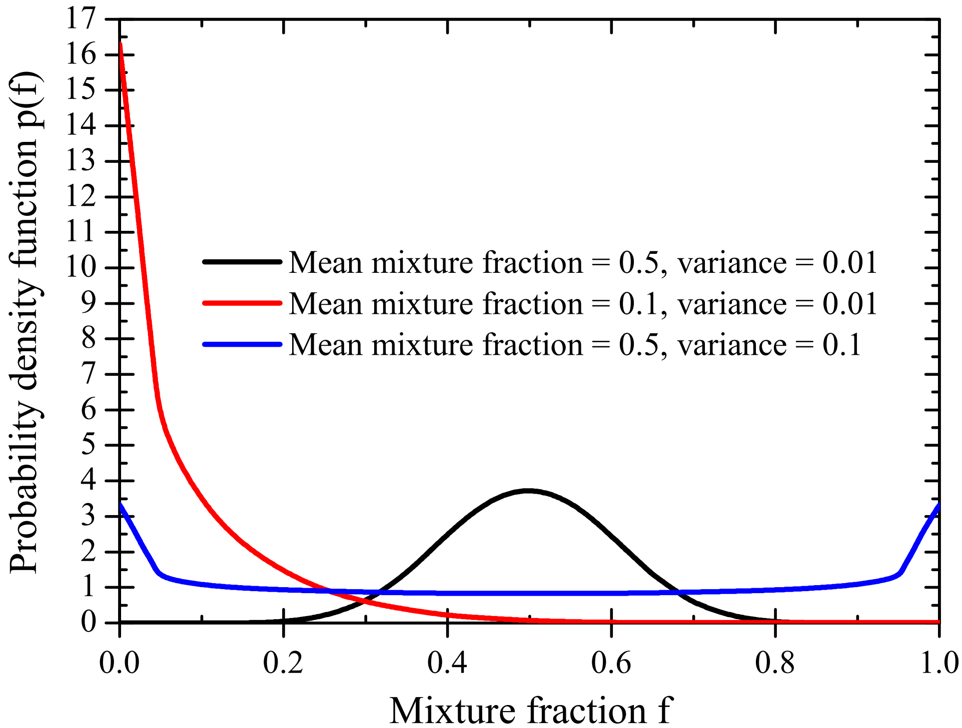

Figure 6.1: Probability Density Function versus mixture fraction, for $\bar{f} = 0.5$ and $\bar{g} = 0.01$, $\bar{f} = 0.1$ and $\bar{g} = 0.01$, and $\bar{f} = 0.5$ and $\bar{g} = 0.1$

Table 6.2: Properties of a reacted ethylene/air mixture, $O/F = 21.6$

Temperature	2 147.42 K
Static pressure	0.5 MPa
Species	Mole fraction
Ar	0.009 85
CO	0.000 78
CO_2	0.102 98
H	0.000 02
HO_2	0.000 01
H_2	0.000 17
H_2O	0.115 24
NO	0.005 93
NO_2	0.000 01
N_2	0.703 33
O	0.000 21
OH	0.002 14
O_2	0.059 32

Calculations were done with the thermochemical equilibrium code CET89 [53] for a mixture at an overall air/ethylene ratio of 21.6 and a combustor pressure of 0.5 MPa. The list of species predicted to be present in amounts greater than 0.1% includes Ar, CO_2, H_2O, NO, N_2, OH, and O_2. In addition, CH_4, CO, HCN, H_2, NH_3, and solid carbon (C(graphite)), were present in the partially-oxidized fuel stream (as to be shown later in Table 6.3), and were also added to the list to make 13 species in all to be considered. While many others are also present, they were predicted to be present in very small quantities and therefore would affect the calculation of overall combustor performance minimally with the PDF combustion models[2].

Since adiabatic conditions are assumed, the time-averaged values of the scalars are a function of mixture fraction only, so the energy equation need not be solved. Examples of this are shown in Figs. 6.2, 6.3, and 6.4.

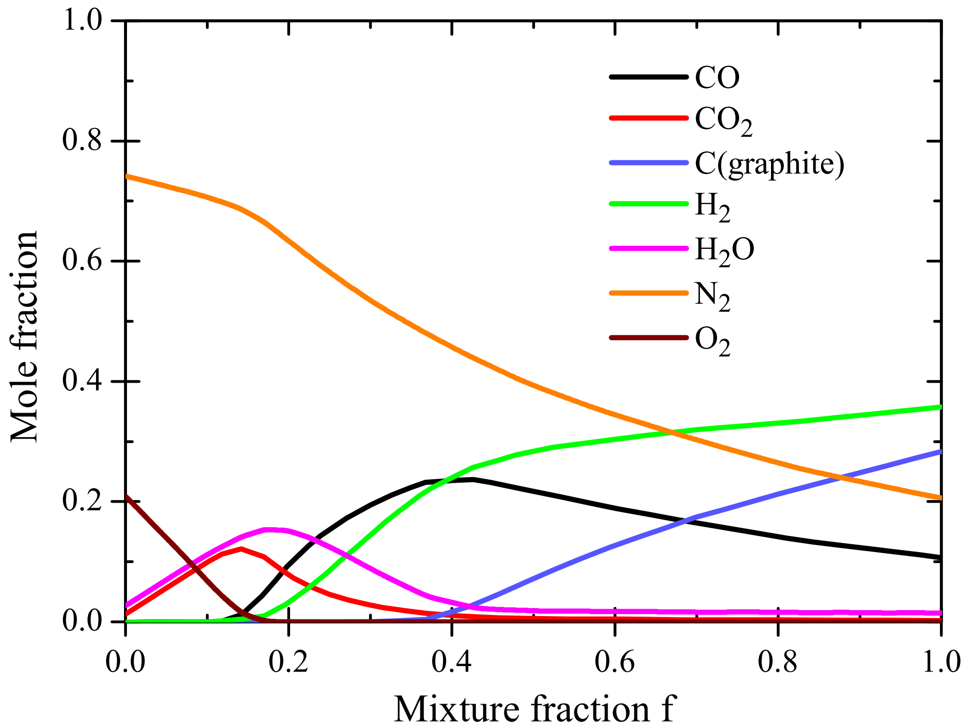

Figure 6.2: Species mole fraction versus mixture fraction (major species only)

[2]However, if a finite-rate chemistry model such as the EBU model were used, these minor species can be critical to the predictions and could not be excluded based solely on their equilibrium quantities.

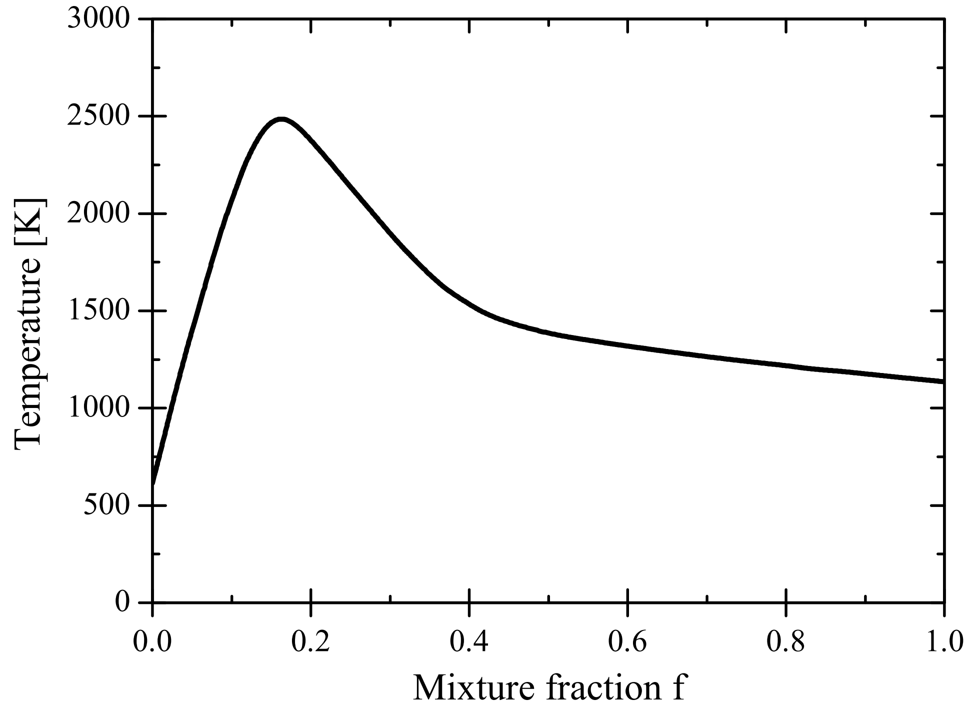

Figure 6.3: Temperature versus mixture fraction

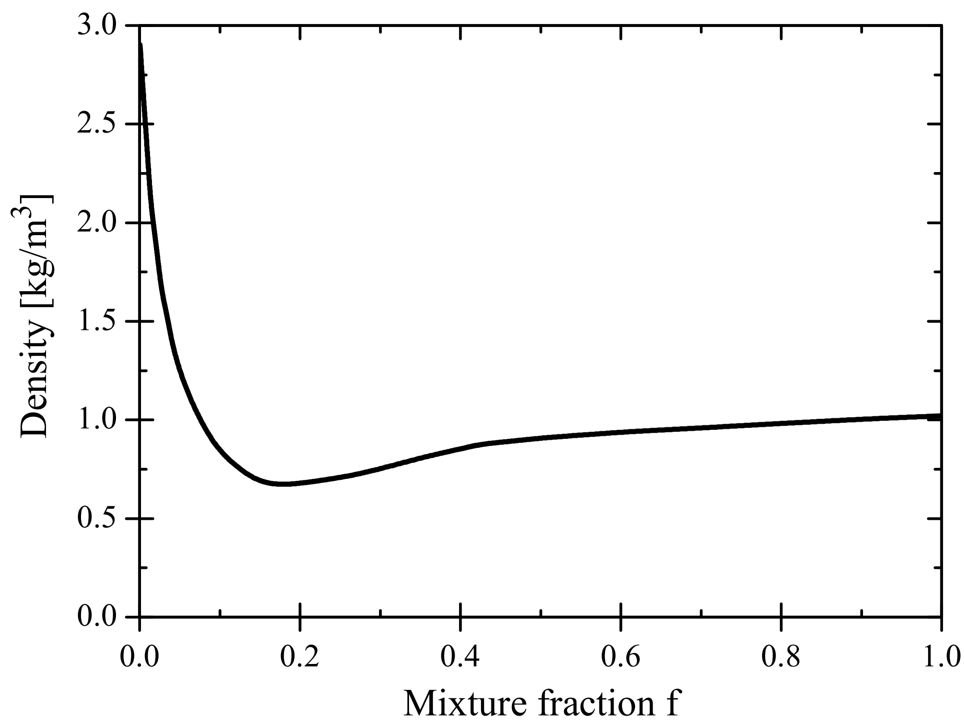

Figure 6.4: Density versus mixture fraction

6.3 Boundary Conditions

As already mentioned in Section 5.2, the direct-connect hardware and experiments were set up in such a way to facilitate the characterization of the boundary conditions for the CFD modelling. For the air inlets, the tubes were lengthened as much as possible within the air plenum and honeycomb installed to straighten the flow and produce a uniform velocity profile at the combustor. Mean velocities at the entrance to the air inlet tubes were calculated from the measured vitiated air mass flow rate and composition, air plenum temperature, and combustor pressure during the direct-connect experiments. While most ramjets with side-mounted inlets have curved inlet ducts, the velocity profiles downstream from these curves depend heavily on the exact geometry. LDV measurements of flow within a plexiglass model of a curved inlet duct [80], also supplied with air from a large chamber, showed a uniform velocity profile in the lengthy (370 mm) horizontal portion of the duct upstream of the curve, but non-uniform downstream from it. A CFD study for a curved inlet diffuser [69] also predicted a uniform velocity profile upstream of the curve in the duct, and non-uniformity downstream from it. Therefore, since the air inlet tubes are straight, the desired uniform velocity profiles can be expected throughout, so this should be a good assumption at the air inlet entrances for the CFD modelling.

Because the air from the vitiator arrives at the air plenum in a small-diameter pipe and is suddenly dumped, its turbulence level was likely high. Since no measurements of the turbulence characteristics of the air entering the inlets could be made, estimates of a turbulence intensity of 10% and a turbulence characteristic length of 25% of the air inlet tube diameter were made for the CFD modelling.

In most of the combustor the Mach number is less than 0.3, so incompressible flow can be justifiably assumed. This is a necessary assumption for the modelling since FLUENT's implementation of the PDF combustion model requires it. While the flow velocities in the air and fuel inlets exceed this Mach number limit for some of the configurations, Spalding [4] states that even flow velocities of up to Mach 0.8 need not be reproduced between a model and a prototype combustor, which implies that they could still be treated as incompressible. However, since the flow had to be assumed incompressible, the nozzle at the end of the combustor was not modelled as for the water tunnel CFD modelling. In fact, exactly the same grids were used.

Characterizing the fuel inlet boundary conditions is much more challenging. As for the air inlets, a constant velocity profile at the fuel inlet was assumed, along with a turbulence intensity of 10% and a turbulence characteristic length 25% of the fuel inlet diameter. For all configurations, measured data from the direct-connect tests, including pressures and temperatures, were used to calculate the measured flow rates for the ethylene and vitiated air. These were then mixed in the gas generator and fuel plenum, allowed to react, and consequently became the gas generator exhaust that was injected through the fuel inlet into the ramjet combustor. As previously mentioned, this ethylene/air mixture was meant to simulate the exhaust from a solid gas generator fuel of 90% GAP and 10% carbon. Table 6.3 shows the equilibrium exhaust compositions, calculated with CET89 [53], of an ethylene/air mixture (1.382 3 air/fuel ratio) and a GAP/Carbon solid fuel expanded from a chamber pressure of 1.175 MPa to the ramjet combustor pressure of 0.5 MPa. Reasonable agreement in the exhaust compositions between the two fuels is achieved, and the densities are within 15% of each other. The critical assumption is that thermochemical equilibrium is reached in the fuel plenum, and continues through the fuel inlet during expansion of the exhaust products. The best way to validate this assumption was to directly sample the gases within the fuel plenum and analyze them with gas chromatography, but unfortunately attempts to do this were not successful. Temperature measurements with thermocouples in the fuel plenum also failed due to high temperatures reached when the ethylene/air mixture was momentarily stoichiometric during start-up. However, exhaust temperature measurements made on small GAP/Carbon solid fuel gas generators [81] suggested that thermochemical equilibrium being reached in the gas generator chamber was a good possibility. If the GAP/Carbon fuel is likely in thermochemical equilibrium within its gas generator, so should be the ethylene/air mixture since it consists of compounds of much lower molar mass and is therefore more reactive. Furthermore, while the sampling and characterization of the gases was not successful for the ethylene/air mixture, a significant proportion of soot was indeed present, as predicted by CET89. Therefore, in the absence of definitive temperature and species measurements of the gas generator exhaust, equilibrium is assumed in the chamber and throughout the expansion to the ramjet combustor. Because of the low pressure ratio, there is little difference between the results for frozen or equilibrium flow during the expansion process.

With the PDF combustion model, any inaccuracy in the exact species composition of the gas generator exhaust should not cause a large error in the energy released by the reactions where the assumption of thermochemical equilibrium holds in the

Table 6.3: Calculated gas generator exhaust properties

	Ethylene/air		GAP/Carbon	
Temperature	1 132.07 K		1 172.54 K	
Density	1.025 5 kg/m^3		1.171 kg/m^3	
Species	Mole fraction	Mass fraction	Mole fraction	Mass fraction
Ar	0.002 87	0.008 28	0.000 00	0.000 00
CH_4	0.024 04	0.027 86	0.013 70	0.015 83
CO	0.106 73	0.215 98	0.109 92	0.221 71
CO_2	0.004 18	0.013 29	0.002 81	0.008 91
HCN	0.000 01	0.000 02	0.000 01	0.000 02
H_2	0.357 60	0.052 08	0.293 90	0.042 66
H_2O	0.015 70	0.020 43	0.009 52	0.012 35
NH_3	0.000 18	0.000 22	0.000 12	0.000 15
N_2	0.205 69	0.416 28	0.178 22	0.359 52
C(graphite)	0.282 98	0.245 55	0.391 78	0.338 86

ramjet combustor in the leaner, hotter regions. However, close to the fuel inlet, the exact species composition profoundly influences the physical properties of the fuel stream. Apart from geometry, the water tunnel experiments and CFD modelling already showed the importance of the momentum ratio of the air and fuel streams on mixing. This was confirmed independently in a more recent study [36] where the size of the fuel injection holes was changed to keep momentum ratio the same between the water tunnel studies and cold-flow experiments using propane fuel injected into air. For the direct-connect experiments, a change in the proportion of solids and/or the overall molar mass of the gases in the exhaust will alter the air/fuel momentum ratio. For example, a small change in the mole fraction of hydrogen, a gas which may be present in significant quantities in the exhaust, can greatly change this momentum ratio since its molar mass is an order of magnitude less than most of the other gases present. A parametric study will be presented in Section 6.4 to show the significance of possible errors in the composition and temperature of the gas generator exhaust, and others such as turbulence intensity, on the calculated temperatures and combustion efficiencies.

6.4 Onestream PDF Results

As seen with the non-reacting flow modelling results, visualization of the output from CFD is a powerful tool to understand the phenomenon inside the combustor. In this section, the results of the fuel distribution and the temperature field in the combustor for each of the direct-connect configurations listed in Table 5.5 will be compared. Before these results are presented, however, the results of a parametric study of the modelling assumptions and approximations will be shown.

6.4.1 Parametric Study

An important part of any CFD modelling study is to estimate the impact of the various assumptions and approximations on the output. With a configuration similar to configuration DC1 as a baseline (Table 6.4), several of the parameters that could be adjusted for the modelling were examined for their impact on the calculated combustion efficiency[3]. The baseline configuration used the RNG turbulence model, onestream PDF combustion model, and inlet boundary conditions of 10% turbulence intensity boundary and a flat velocity profile as previously described. The grid used 56 688 cells (for half the geometry) and adiabatic walls were assumed. Since nitrogen is the predominate species in the combustor, the baseline model used constant values of $1.789\,4 \cdot 10^{-5}$ kg/(m·s) for viscosity and 0.024 1 W/(m·K) for thermal conductivity (nitrogen at 300 K). The use of temperature-dependent polynomials for viscosity and thermal conductivity rather than these constant values was tried but had little effect, primarily because the conditions that render the situation suitable for modelling the combustion with a PDF approach also imply that these transport properties have little influence over the mixing.

As already presented in Eqn. 5.1, the chosen measure of combustor performance is the efficiency based on temperature rise in the combustor:

$$\eta_{\Delta \mathrm{T}} = \frac{T_{\mathrm{t4,exp}} - T_{\mathrm{t2}}}{T_{\mathrm{t4,theo}} - T_{\mathrm{t2}}}$$

For the CFD results, T_{t2} is the air inlet temperature, and $T_{\mathrm{t4,exp}}$ is the mass-averaged stagnation temperature at a given cross-section in the combustor. As for the ex-

[3]The configuration for the parametric study used nominal values of the boundary conditions specified for the direct-connect configuration DC1. Understandably, these nominal values were, in general, not achieved during the experiments. The remainder of the CFD modelling did, however, use values for the boundary conditions derived from the experimental measurements during the direct-connect tests.

Table 6.4: Configuration for parametric study

Air injector	A4
Fuel injector	F0-27
Air inlet velocity [m/s]	127.7
Fuel inlet velocity [m/s]	301.1
Air mass flow rate [kg/s]	1.5
Fuel mass flow rate [kg/s]	0.177
Air/fuel mass flow ratio	8.486
Air/fuel momentum ratio	3.6
Combustor Static Pressure [MPa]	0.5

perimental $\eta_{\Delta \mathrm{T}}$, $T_{\mathrm{t4,theo}}$ is calculated from CET89 using the static pressure in the combustor, the nozzle entrance-to-throat area ratio and the compositions, temperatures, and mass flow rates of the vitiated air and gas generator exhaust as inputs. In the graphs, the value of $\eta_{\Delta \mathrm{T}}$ from the CFD results is given not only at the 458 mm cross-section which represents the length of the combustor in the direct-connect experiments, but also at the 100, 200, 300, 400, and 500 mm cross-sections[4].

The percentage change due to changing one of the parameters is defined by:

$$\%\,change = \left| \frac{\eta_{\Delta \mathrm{T,\,new}} - \eta_{\Delta \mathrm{T,\,baseline}}}{\eta_{\Delta \mathrm{T,\,baseline}}} \right| \cdot 100 \tag{6.10}$$

where $\eta_{\Delta \mathrm{T,\,new}}$ is the new value of the efficiency with the parameter of interest changed. Figure 6.5 shows the effect of the choice of turbulence model on $\eta_{\Delta \mathrm{T}}$. The use of the k-ε turbulence model, not the best choice for this type of flow, increases the calculated efficiency by 17%. The RSM turbulence model has a much smaller impact on calculated efficiency, being about 7% at the 458 mm cross-section, but this model, like the RNG model, is better for this type of flow than the k-ε model.

The next graph, Fig. 6.6, shows that doubling the turbulence length scale has a very small effect on the calculated efficiency. However, the value of turbulence intensity has a profound effect on $\eta_{\Delta \mathrm{T}}$ for this configuration. Changing it to 1% or 20% from baseline 10% changes the magnitude of the calculated combustion efficiency for this configuration by about 25% at the 458 mm cross-section.

To check the grid-independence of a CFD solution, the grid should be refined and any change in the solution noted (Fig. 6.7). If a grid is too coarse, a phe-

[4]The same basic geometries were used in the water tunnel and direct-connect experiments. The grids generated to model the water tunnel combustors, 500 mm in length, were therefore also used to model the direct-connect combustors of 458 mm in length.

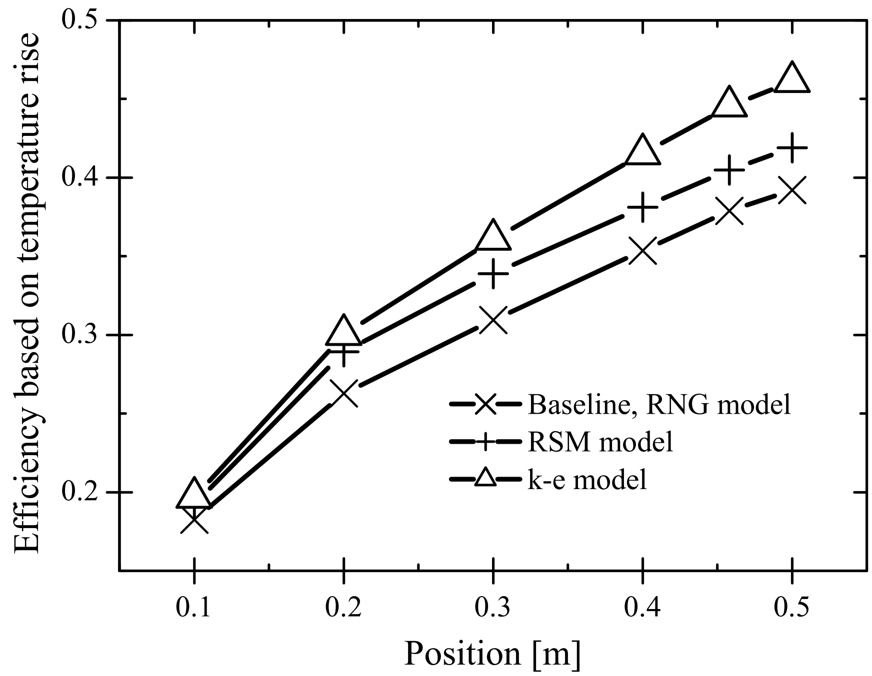

Figure 6.5: Effect of turbulence model on predicted $\eta_{\Delta \mathrm{T}}$

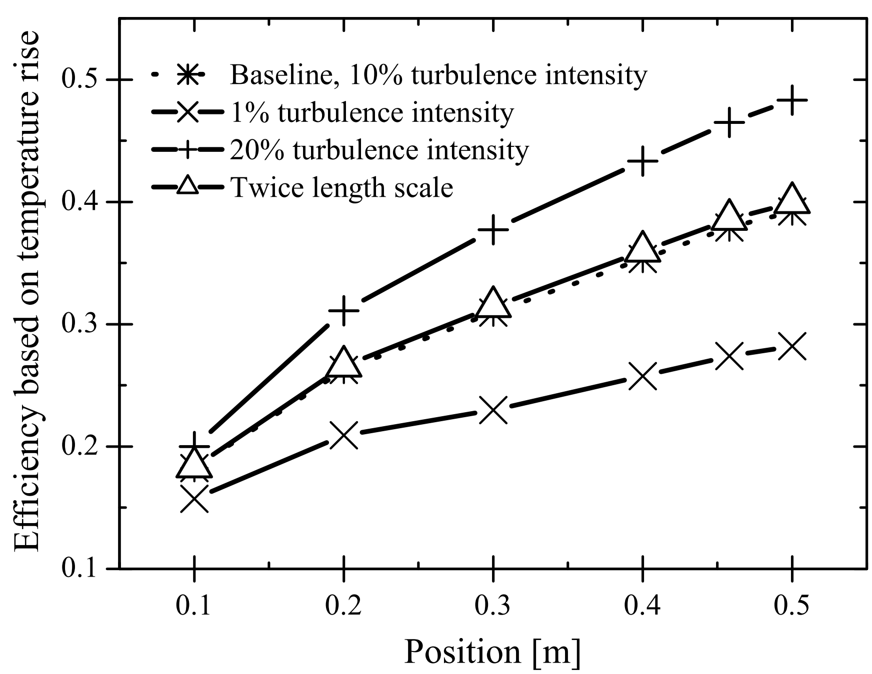

Figure 6.6: Effect of inlet turbulence intensity on predicted $\eta_{\Delta \mathrm{T}}$

nomenon sometimes termed "numerical diffusion" or "artificial viscosity" has the same effect as increasing the diffusion in the flow. Its effect is more pronounced if the flow is not aligned with the grid. Unfortunately, because of the increased calculation time, refining the grid is often not practical. For the configuration in Table 6.4, the grid (for half the geometry) was refined to 147 868 cells (fine grid) and 453 504 cells (doubled grid). The fine grid gave a value for $\eta_{\Delta\mathrm{T}}$ about 7% lower at 458 mm than the baseline, and the doubled grid gave a difference of about 3%, but these percentage changes also changed with position in the combustor, likely due to how aligned the flow was with the grid. (Interestingly, none of the grids shown in Table 6.1 is as refined as the fine grid used here.) Given the much greater effect that the choice of turbulence intensity has on the results, however, meant that the additional effort and calculation time of refining all of the grids would not have been worthwhile. Going to a second order discretization scheme for the equations rather than the baseline first order scheme also affected the results to a similar magnitude, but was positive or negative depending on position in the combustor. This would also increase calculation time significantly, however.

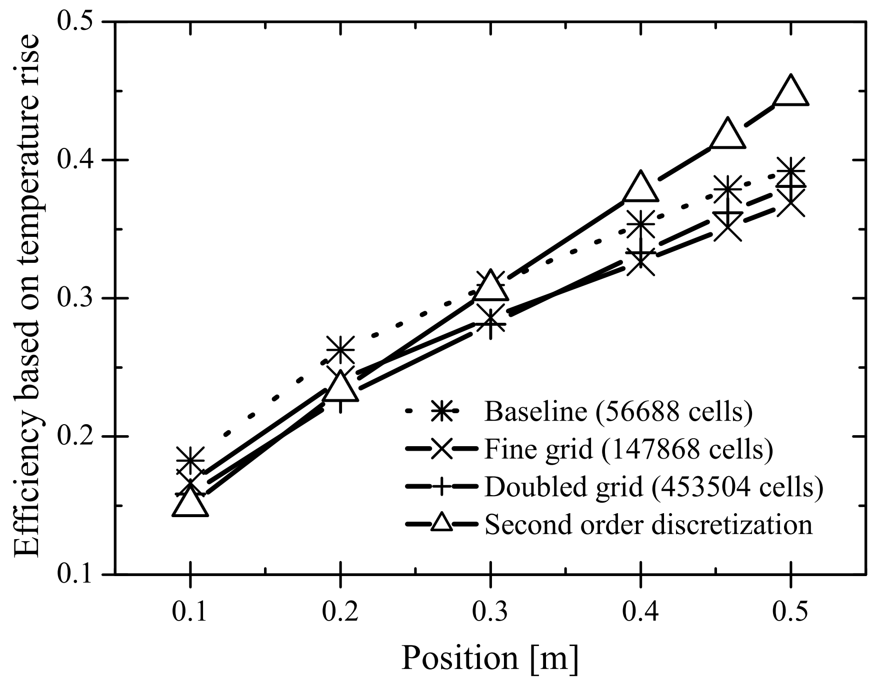

Figure 6.7: Effect of grid size and discretization method on predicted $\eta_{\Delta\mathrm{T}}$

Figure 6.8 shows the effect of how any heat transfer was modelled inside the combustor. First, rather than being adiabatic as for the baseline, the walls of the combustor were assumed to be isothermal at the same temperature as the incoming air at 600 K (a good assumption for most of the combustor which was inside the plenum chamber). Allowing for this heat transfer from the flow lowered calculated combustion efficiency by less than 5%. Adapting the mesh to model the heat transfer through the boundary layer at the wall better had no significant additional effect. Radiation was modelled using a wall emissivity of 0.5, the Weighted-Sum-of-Gray-Gases Model for the gas emissivity, and the Discrete Transfer Radiation Model [46]. No significant effect of radiation on the results was found, as was earlier assumed (see Subsection 2.4.10).

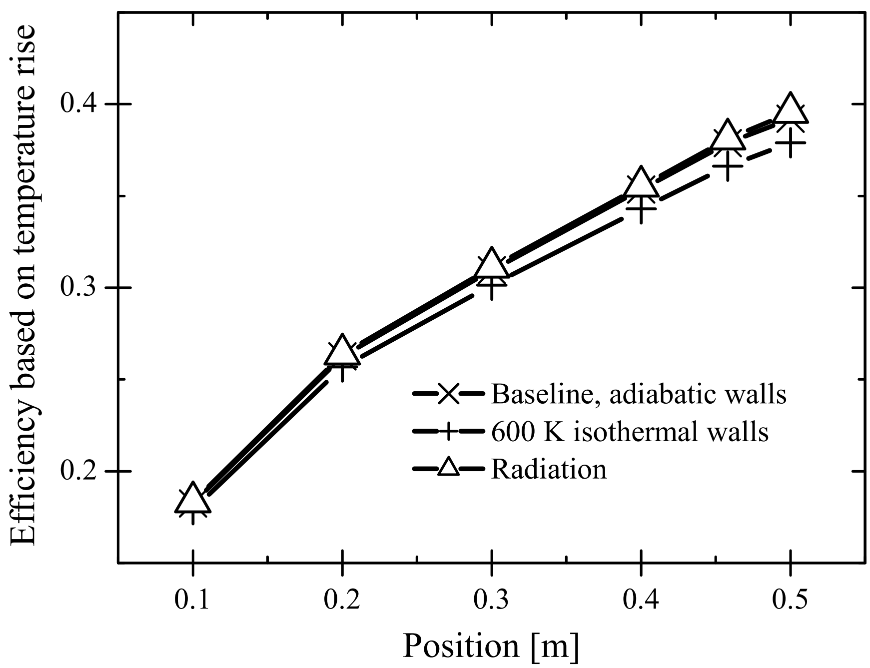

Figure 6.8: Effect of radiation and isothermal walls on predicted $\eta_{\Delta \mathrm{T}}$

To check the effect of errors in fuel (gas generator exhaust) temperature, ethylene mass flow rate and air mass flow rate were each varied by 10%. Figure 6.9 shows that a 4% drop in combustion efficiency resulted from assuming a 10% drop in temperature of the fuel jet, which increases its density and decreases its velocity. Decreasing air mass flow rate also dropped combustion efficiency 5% at 458 mm, but lowering ethylene mass flow rate by 10% increased efficiency by about 7%.

However, none of the changes in the parameters studied had as much effect on $\eta_{\Delta T}$ as varying the turbulence intensity from 1% to 20%. Properly characterizing the inlet turbulence intensities is therefore a priority for improving the accuracy of this CFD modelling.

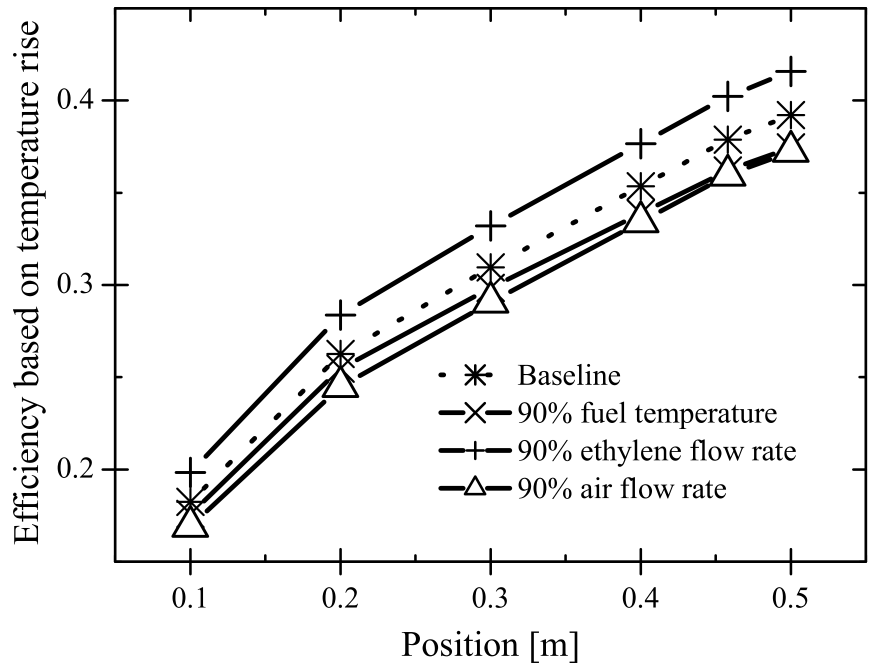

Figure 6.9: Effect of errors in air and fuel mass flow rates and fuel temperature on predicted $\eta_{\Delta T}$

While a parametric study for each configuration was not feasible, two additional configurations, with much higher calculated combustion efficiency, were modelled to see if turbulence intensity would also significantly affect the results. Configurations DC2 and DC19, each with a calculated $\eta_{\Delta T} > 70\%$, were therefore modelled using a turbulence intensity of 1%. These configurations have similar air/fuel momentum ratios and are geometrically identical except that configuration DC19 uses a longer dome height of 100 mm. Since a longer dome height enlarges the recirculation zone to improve the air/fuel mixing, a significant increase in efficiency was expected and was indeed seen in the experimental results. However, no such increase in efficiency is seen in the CFD results (Fig. 6.10). By redoing the CFD modelling for each configuration, but this time specifying inlet boundary conditions of 1% turbulence intensity rather than 10%, a clear difference in combustion efficiency results from an increase in dome height. This is because, at 10% turbulence intensity, the length of the recirculation zone for the shorter dome height is already sufficient for good air/fuel mixing and increasing the dome height provides no additional benefit. At 1% turbulence intensity, however, the benefit of increased dome height and a stronger recirculation zone is obvious with a significant increase in efficiency for the CFD results. This therefore implies that effect of turbulence intensity on the results also varies with each configuration.

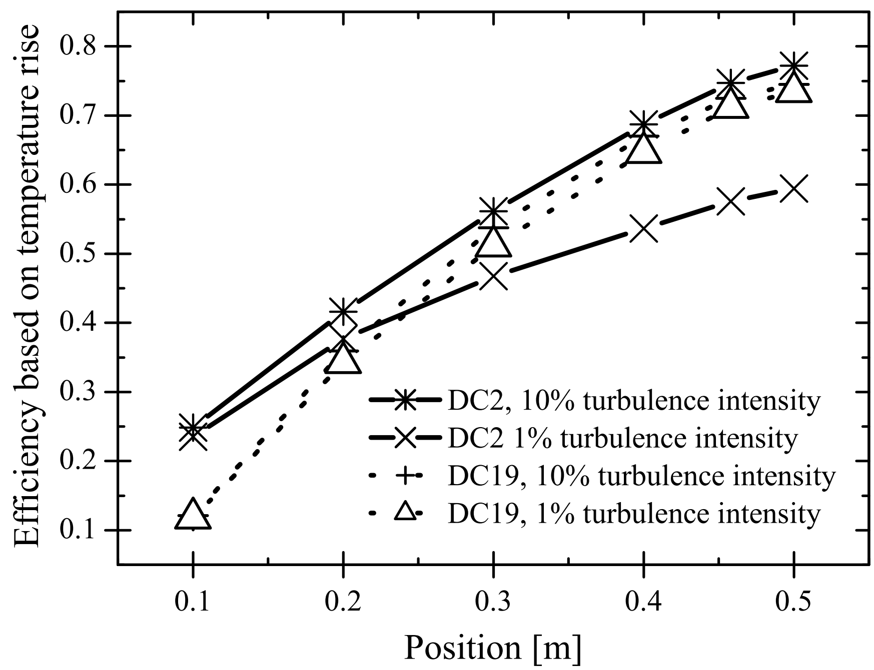

Figure 6.10: Effect of turbulence intensity on predicted $\eta_{\Delta \mathrm{T}}$ for configurations DC2 and DC19

6.4.2 Comparison of Combustor Configurations

As with the water tunnel experiments and non-reacting flow CFD modelling, visualization of results from reacting flow modelling also helps explain why one direct-connect configuration yields a higher combustion efficiency than another. The fuel mixture fraction graphs shown here provide similar information about the mixing in the combustor as the graphs shown in Chapter 4 except the influence of combustion has been included. However, while good mixing is important for good combustor performance, graphs of the temperature distribution in the combustor also provide additional information that the fuel and oxidizer are mixed in the right proportions to maximize the energy release.

The first two graphs deal with 4 configurations with an air/fuel mass flow ratio ≈ 7 and the same fuel injector (F0-27). Figure 6.11 shows the fuel mixture fraction on the centreline plane which, as explained in Section 6.2 for a onestream adiabatic PDF combustion model, determines the composition and temperature of the reacted mixture. Configuration DC6 uses an air injector with smaller inlet tubes than configuration DC1 which, for the same air/fuel mass flow ratio, gives a higher air/fuel momentum ratio and the fuel jet can be seen to be deflected toward the bottom. The consequences of this can be seen better in Fig. 6.12 which shows that the temperature fields are much different. The temperatures are shown, in an isometric view, from the head to the nozzle end of the combustor at 100 mm cross-sections. Near the end of the combustor, configuration DC6 has high temperatures around the circumference of the combustor, while the high temperature for configuration DC1 is in the bottom half of the combustor. Configuration DC13, with 90° air inlet tubes, has a similar fuel mixture fraction and temperature distribution to configuration DC1 with 60° air inlet tubes. Configuration DC18, with a 100 mm dome height, has a longer fuel jet than configuration DC1 but also a similar temperature distribution.

The next group includes 5 configurations that have an air/fuel mass flow ratio of ≈ 15. With the higher air momentum, all of the fuel jets in Fig. 6.13 are deflected toward the lower wall of the combustor. Only configuration DC14 with the 90° tubes shows a large amount of fuel on the centreline plane downstream of the air inlets. However, Fig. 6.14 shows that the other configurations have two strong longitudinal vortices that do not permit high temperatures to exist on the centreline. These 5 configurations also have larger regions of high temperature than do the first four shown in Fig. 6.12 and, as will be shown later, also have higher combustion efficiencies.

Figure 6.15 shows the fuel mixture fraction distribution for 5 configurations with the same approximate air/fuel mass flow ratio of 4 to 5, and the same diameter fuel injector (18 mm) so therefore the same approximate air/fuel momentum ratio. However, the placement of the fuel injector hole changes. Configurations DC11 and DC28 are for a combustor static pressure of approximately 0.45 MPa, and Fig. 6.16 shows that the lower placement results in higher temperatures toward the end of the combustor. Configurations DC12, DC29, and DC30 are for a combustor static pressure of approximately 0.9 MPa and, once again, the lower placement of the fuel jet results in higher combustor temperatures.

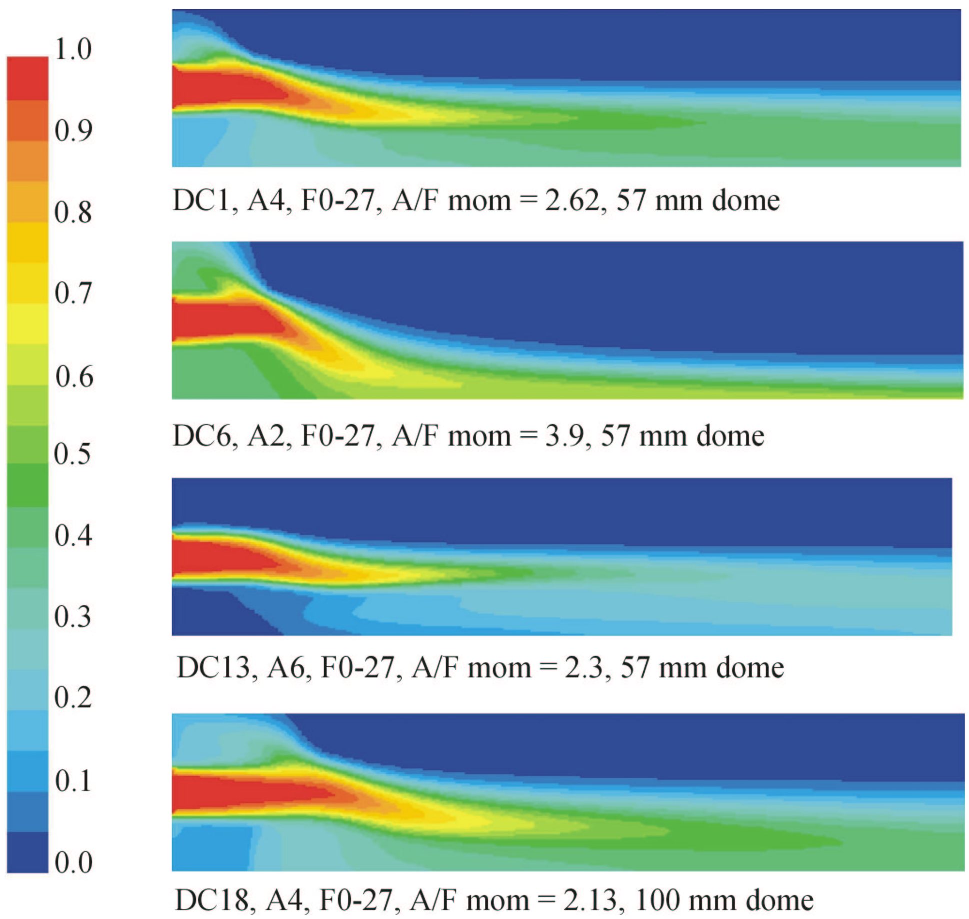

Figure 6.11: Effect of geometry on predicted fuel mixture fraction, similar air/fuel mass ratios (≈ 7), same fuel injector

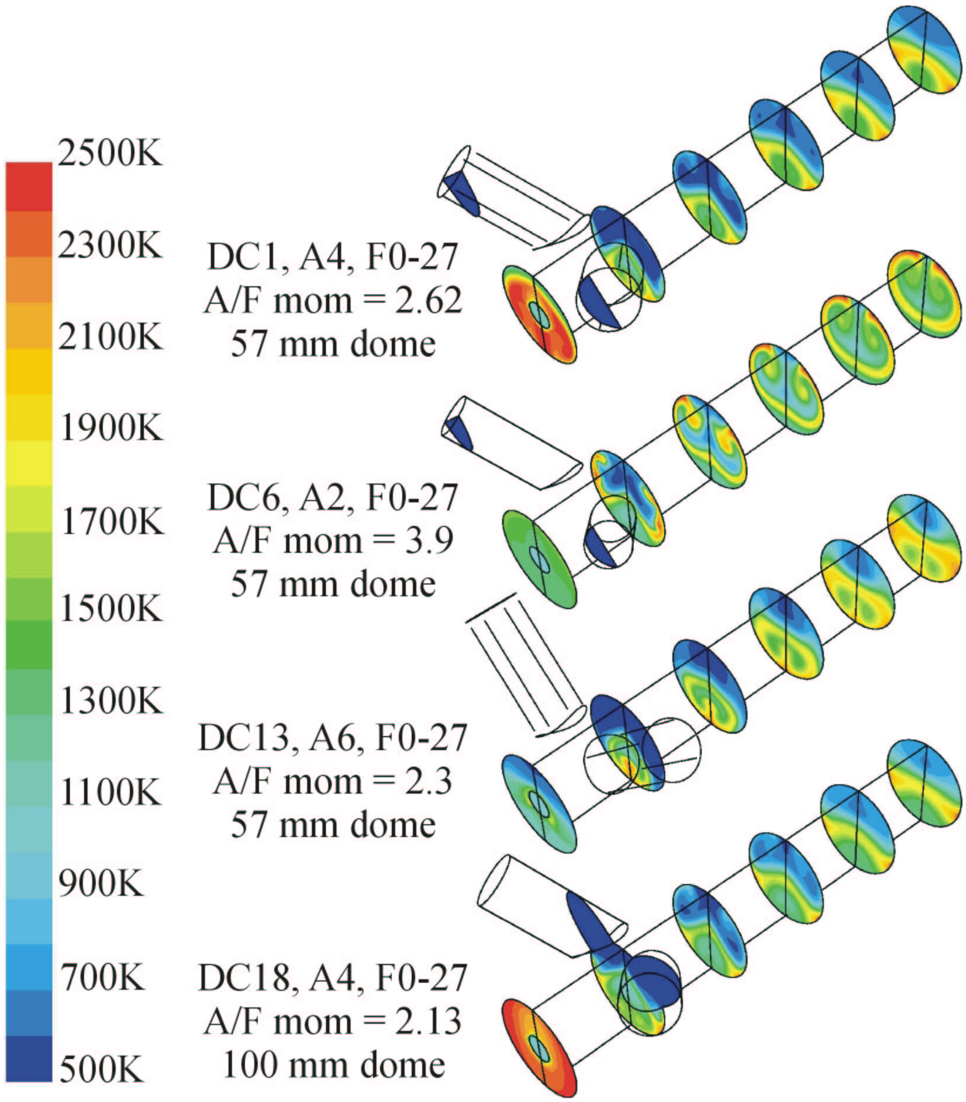

Figure 6.12: Effect of geometry on predicted temperature field, similar air/fuel mass ratios (≈ 7), same fuel injector

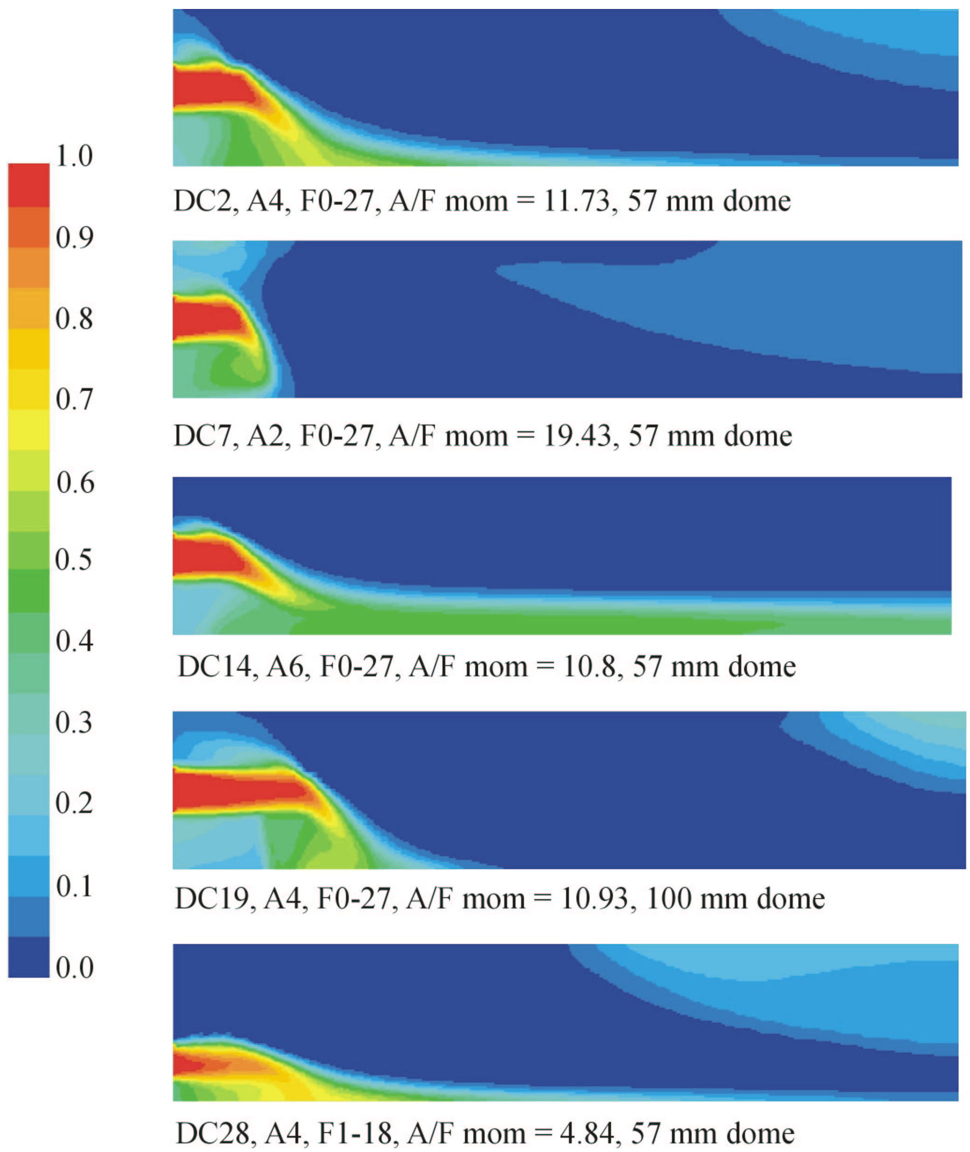

Figure 6.13: Effect of geometry on predicted fuel mixture fraction, similar air/fuel mass ratios (≈ 15)

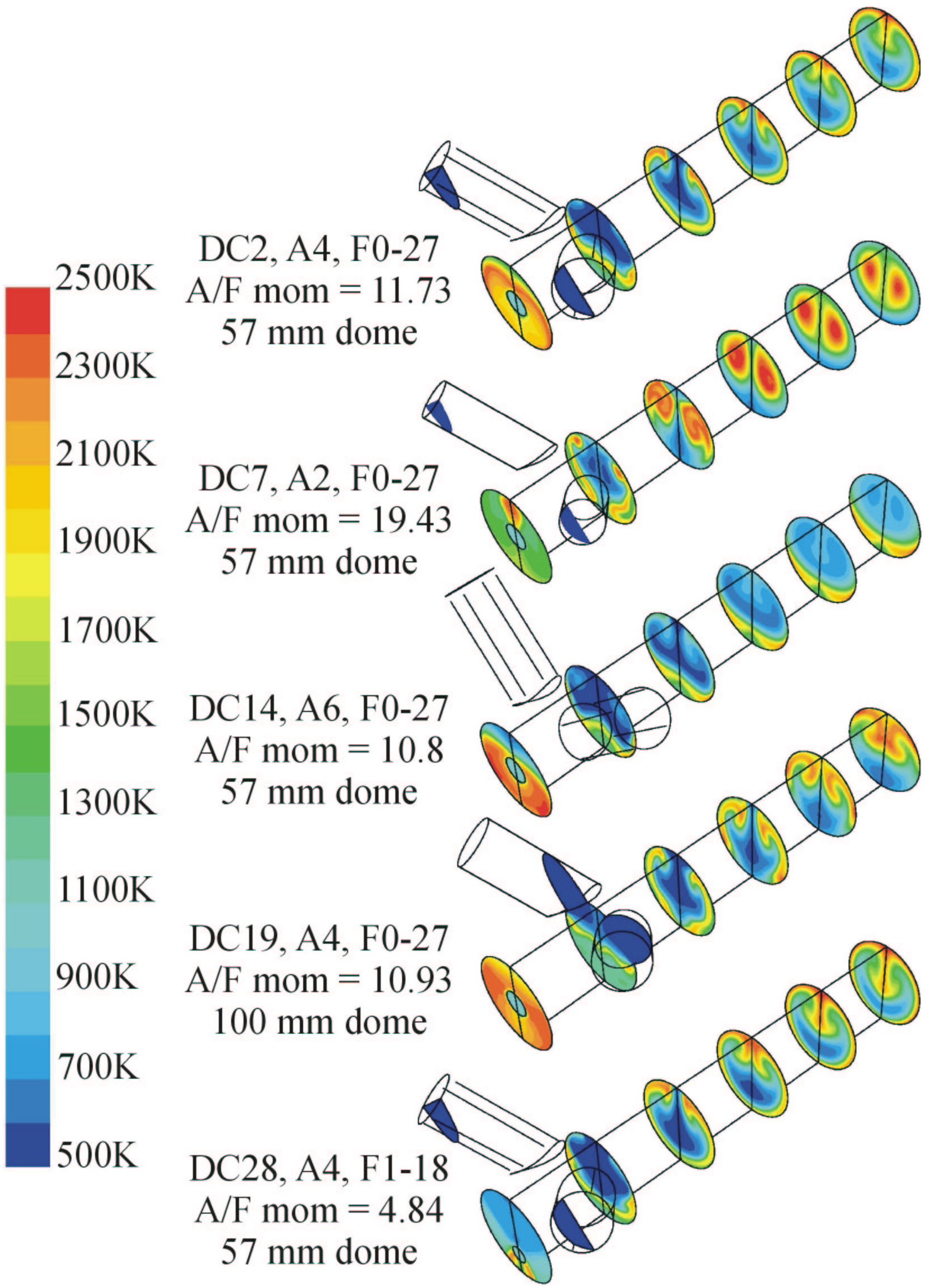

Figure 6.14: Effect of geometry on predicted temperature distribution, similar air/fuel mass ratios (≈ 15)

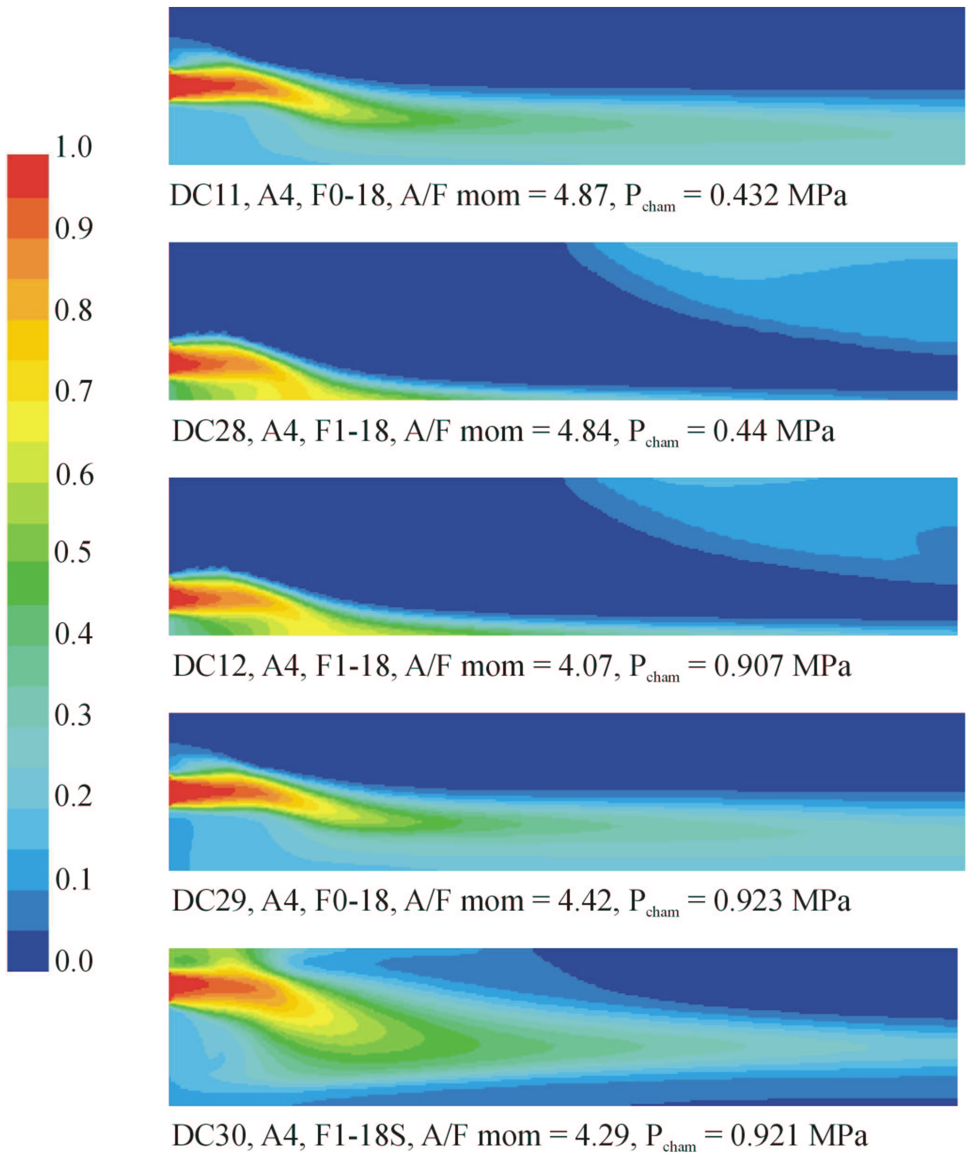

Figure 6.15: Effect of fuel injector placement on predicted fuel mixture fraction, similar air/fuel momentum ratios (≈ 5)

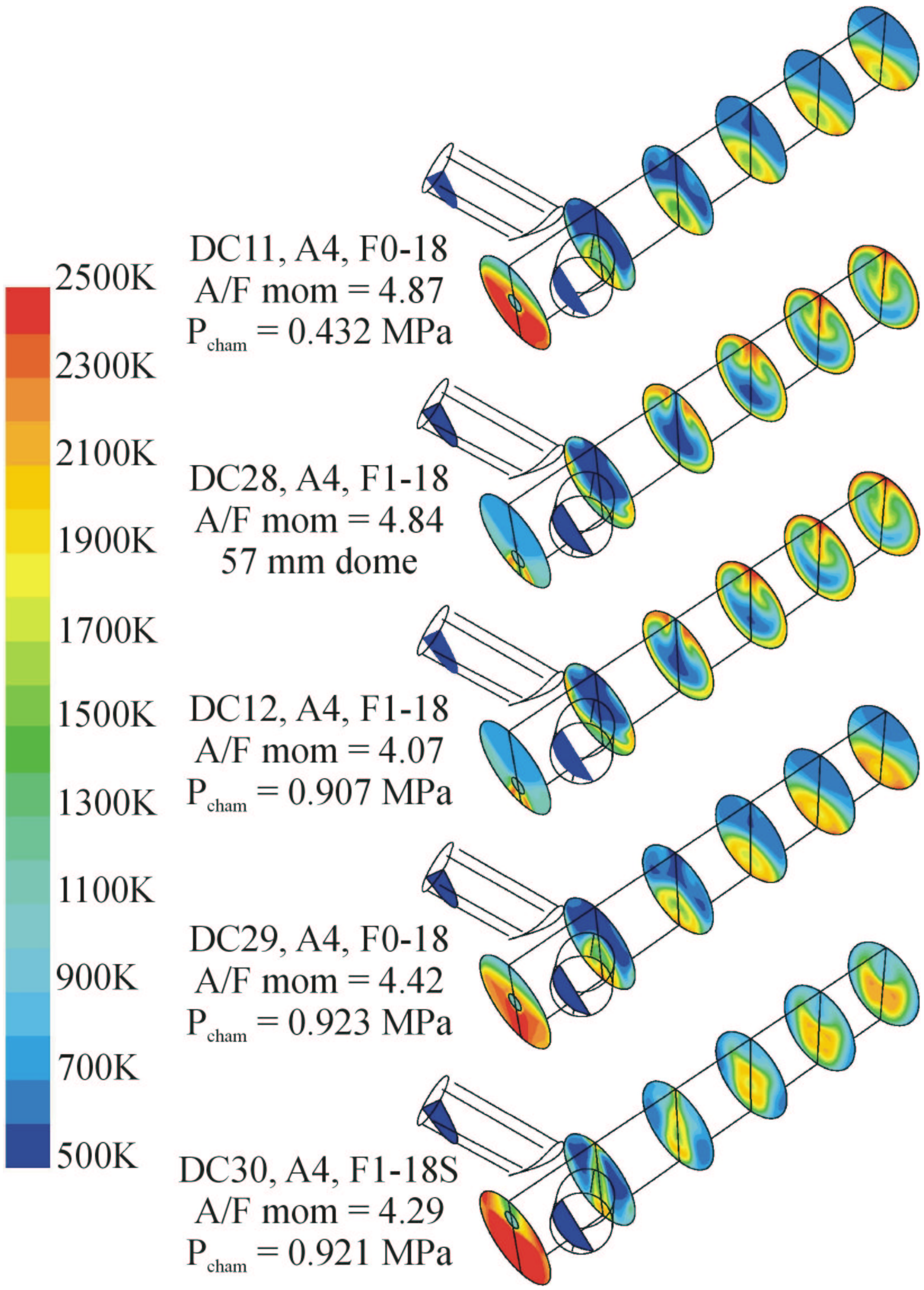

Figure 6.16: Effect of fuel injector placement on predicted temperature distribution, similar air/fuel momentum ratios (≈ 5)

Figure 6.17 shows the effect of changing the size of the fuel injector hole or increasing the dome height of configuration DC3 for a relatively high air/fuel mass flow ratio. For configuration DC12, the fuel jet is narrower but because it is nearer the bottom wall of the combustor, its length is not increased. However, Fig. 6.18 shows that the temperatures have increased toward the end of the combustor. Increasing the dome height understandably lengthens the fuel jet, and also has increased the combustor temperatures in the aft part of the combustor.

The effect of changing the air injector geometry at an air/fuel mass flow ratio of ≈ 7) is shown in Fig. 6.19. Configuration DC9, with the smaller air inlet tubes and the higher air momentum, has a fuel jet that is deflected more toward the bottom of the combustor. The fuel jet for configuration DC16 is about the same length, and configuration DC21 with an increased dome height has a somewhat longer fuel jet. While the differences in the shape of the fuel jet are not large, however, the temperature distributions shown in Fig. 6.20 do vary greatly.

The last two graphs show the effect of changing the air/fuel momentum ratio for two different geometries. Configuration DC8 has a higher air/fuel momentum ratio than configuration DC9, so its fuel jet is much shorter as shown in Fig. 6.21. The temperature fields presented in Fig. 6.22 differ significantly; for the higher air/fuel momentum ratio, the longitudinal vortices dominate the distribution in the combustor and the high temperatures are concentrated away from the combustor walls. For configuration DC9 the higher temperatures stay out near the combustor walls, unlike for configuration DC8. Configuration DC16 has a longer fuel jet than configuration DC15 since its air/fuel momentum ratio is lower, and it has a wider distribution of high temperatures toward the end of the combustor.

These results have shown that for combustion problems, considering only the fuel distribution on the centreline plane can be misleading, and that the three-dimensional temperature field should be examined to decide which configurations may yield superior performance. Since so many parameters can change between configurations despite changing only one feature, general conclusions as to what should be changed to optimize a configuration are difficult to make. The wide range of fuel distributions and temperature fields seen in these results have revealed that each configuration should be modelled to estimate its performance, rather than simply extrapolating from other results.

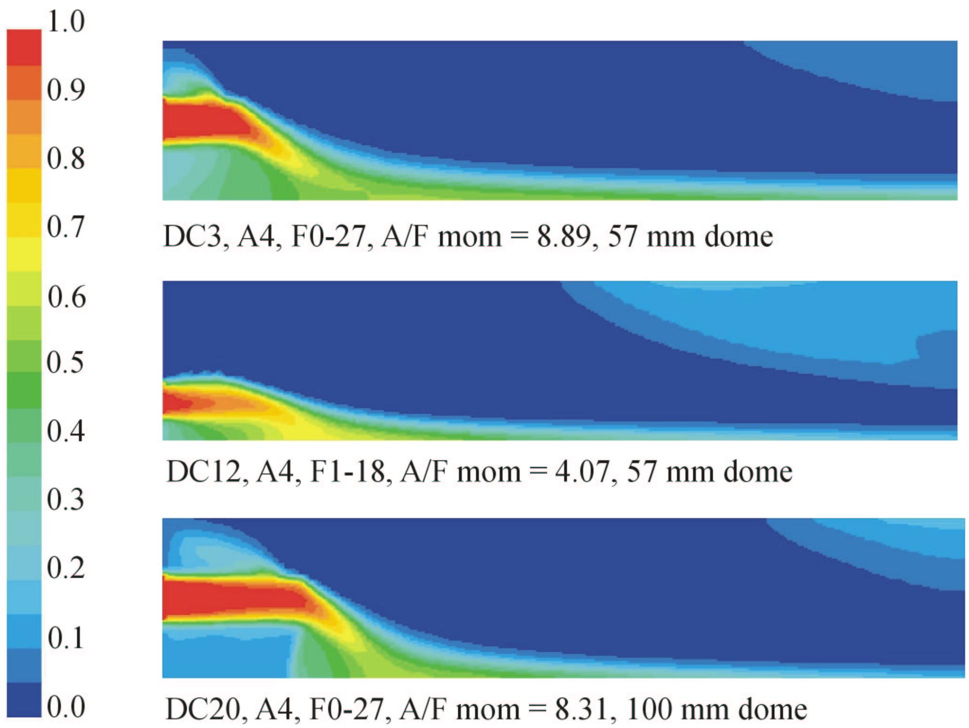

Figure 6.17: Effect of fuel injector and dome height on predicted fuel mixture fraction, similar air/fuel mass ratios (13-14)

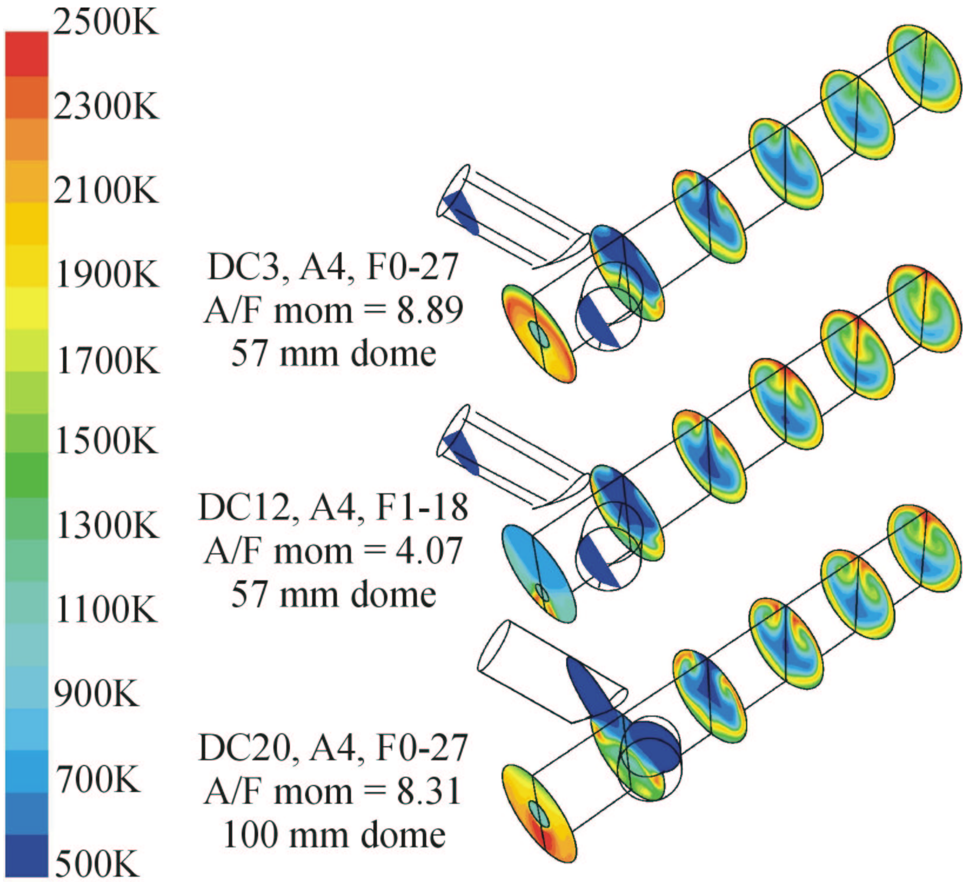

Figure 6.18: Effect of fuel injector and dome height on predicted temperature distribution, similar air/fuel mass ratios (13-14)

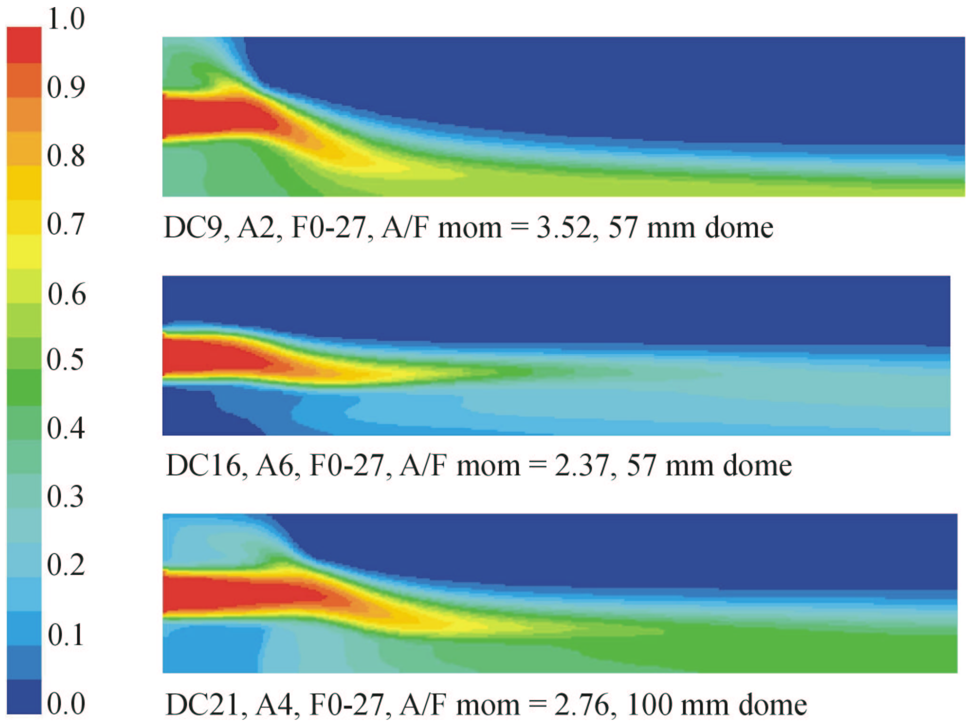

Figure 6.19: Effect of different air injectors on predicted fuel mixture fraction, similar air/fuel mass ratios (≈ 7)

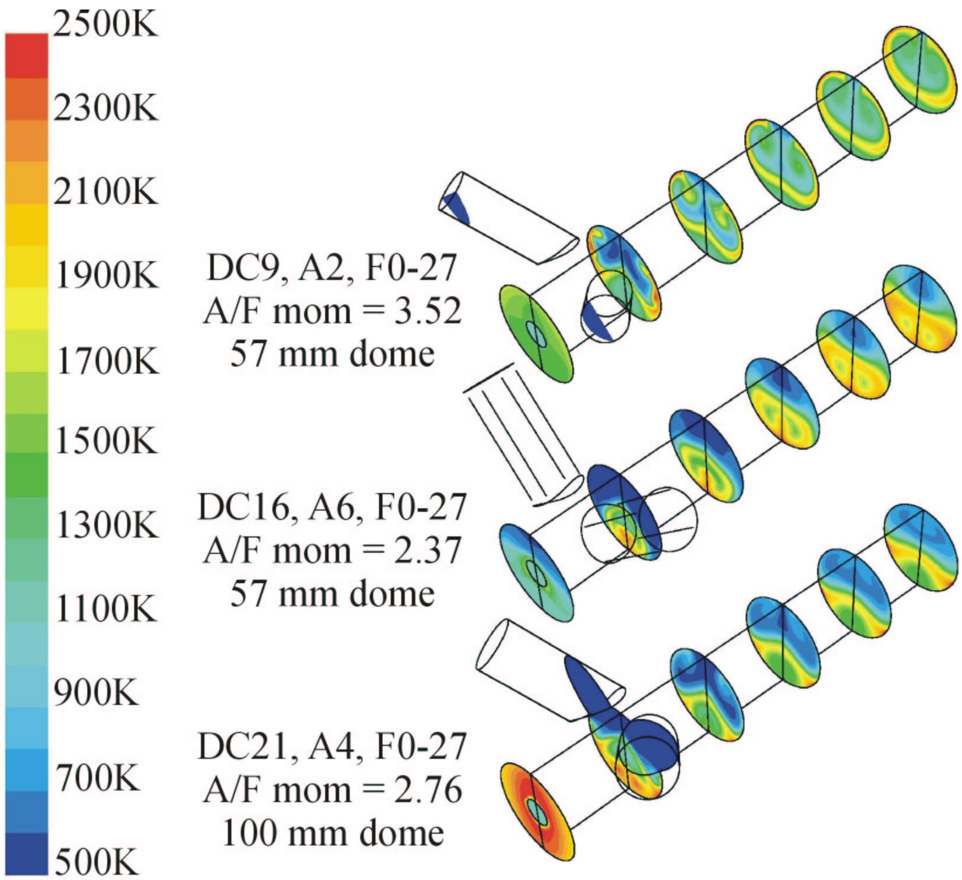

Figure 6.20: Effect of different air injectors on predicted temperature distribution, similar air/fuel mass ratios (≈ 7)

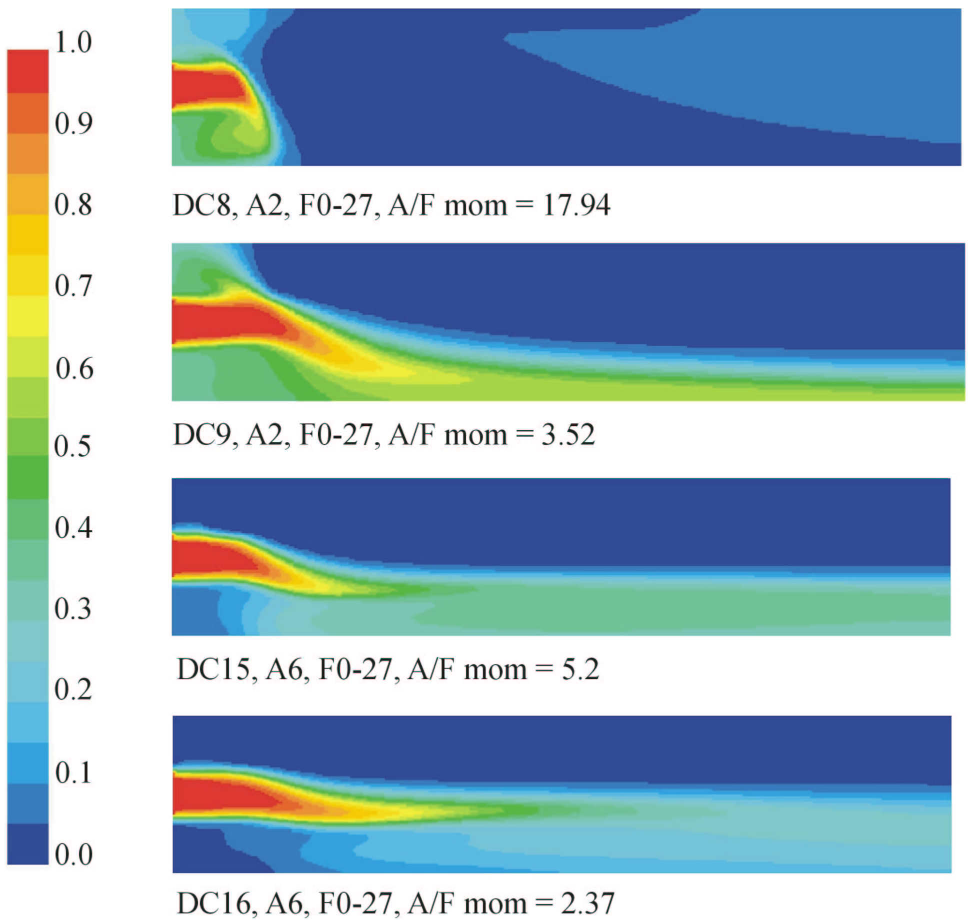

Figure 6.21: Effect of momentum ratio on predicted fuel mixture fraction, two pairs of geometries

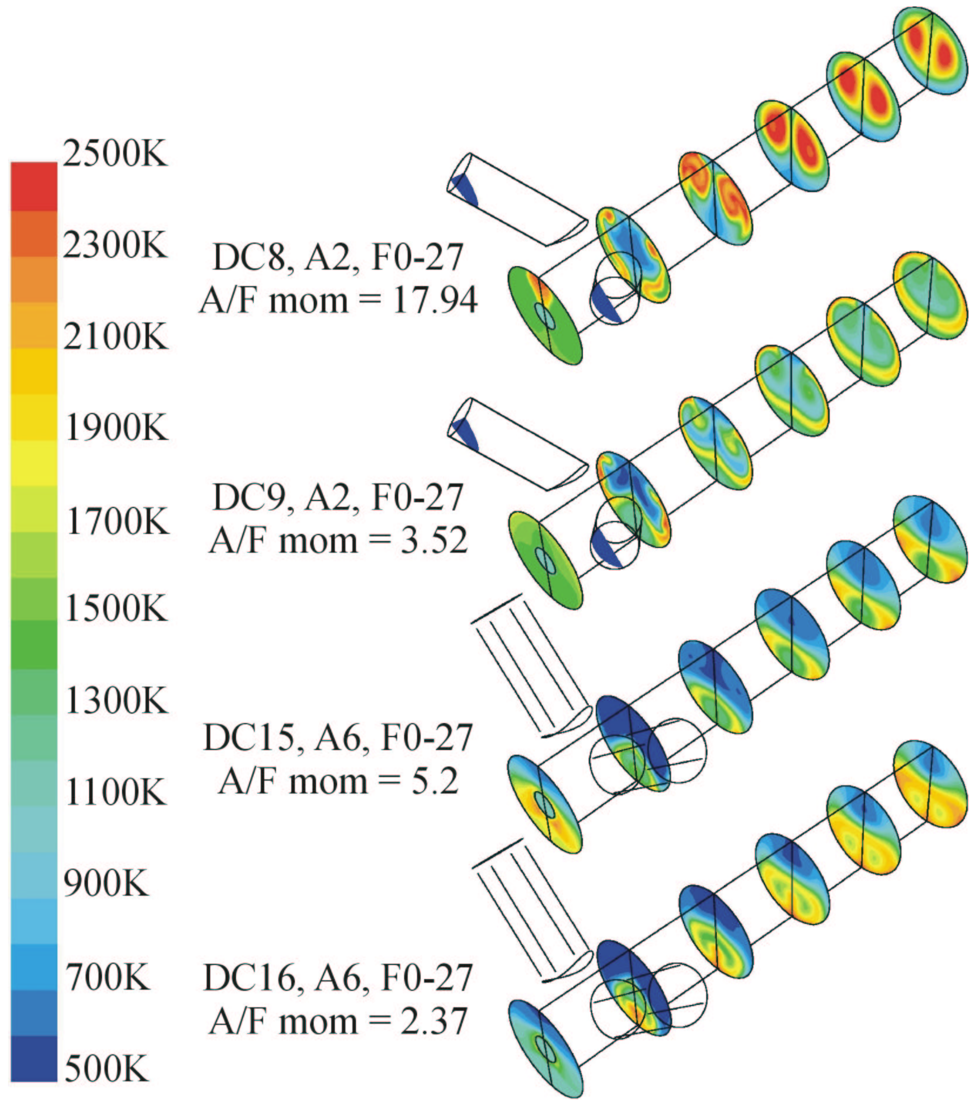

Figure 6.22: Effect of momentum ratio on predicted temperature distribution, two pairs of geometries

6.5 Twostream PDF Model

As previously mentioned, one of the main limitations of the onestream PDF model is that all of the species in the fuel stream are assumed to react instantaneously with the oxidizer stream and come to thermochemical equilibrium as long as the mixture is below the rich limit specified in prePDF for the look-up table. Table 6.3, however, indicates a large proportion of solid carbon in the fuel, and Fig. 6.23 shows a wide range of particle sizes, at least some of which are too large to react quickly in the presence of an oxidizer (calculations will substantiate this later). Brilliant orange-yellow exhaust plumes, a likely indication of soot particles in the exhaust and incomplete combustion, were also observed for some of the configurations during the direct-connect experiments. An obvious way to try to improve the predictions, and one that has not yet been tried according to the references listed in Table 6.1, is therefore to treat the solid particles in the gas generator exhaust separately from the gases present.

To do this, two separate fuel streams must be modelled, one for the gases already present in the gas generator exhaust, and the other for carbon monoxide which is gradually released from carbon particles after they are injected into the combustor. Fortunately, FLUENT has implemented this two mixture fraction or "twostream" modelling approach where there is a primary fuel stream, a primary oxidizer stream, and a secondary stream that can be either fuel or oxidizer [46]. A mixture fraction can be attributed to each one of these streams, and they must add up to unity:

$$f_{\text{fuel}} + f_{\text{sec}} + f_{\text{ox}} = 1 \tag{6.11}$$

The fuel mixture fraction, f_{fuel}, varies between 0 and 1 as for the onestream PDF model, but the secondary mixture fraction obeys:

$$f_{\text{sec}} = p_{\text{sec}} (1 - f_{\text{fuel}}) \tag{6.12}$$

The importance of this equation is the addition of the partial fraction p_{sec} which can vary between 0 and 1 regardless of the value of f_{fuel}, while f_{sec} cannot. To solve the mixture fraction transport equations, Eqns. 6.2 and 6.3 are used for the mean primary fuel mixture fraction and its variance, as for the onestream PDF model. For the secondary stream, Eqn. 6.2 is used to calculate $\bar{f}_{\text{sec}}$, and $\bar{p}_{\text{sec}}$ is found from Eqn. 6.12. Because the mass flow rate of the secondary stream is much smaller than the total mass flow rate, Eqn. 6.3 can be used to calculate the variance of the partial fraction rather than the variance of the secondary mixture fraction since they are not very sensitive to $\bar{f}_{\text{fuel}}$ [46]. In Eqn. 6.3, $\bar{p}_{\text{sec}}$ must replace $\bar{f}$.

For the onestream model, instantaneous values of scalars such as the concentration of each species, the temperature, and the density at any point in the combustor were functions only of the mixture fraction. However, the addition of a secondary stream, as well as a particle model where the solid phase gradually decomposes in the presence of an oxidizer in the surrounding gases, mean that these instantaneous scalars must be functions of the partial fraction and total enthalpy as well:

$$\phi_i = \phi_i\left(f_{\text{fuel}}, p_{\text{sec}}, H\right) \tag{6.13}$$

The addition of an energy equation is therefore required:

$$\frac{\partial}{\partial t}\left(\rho\bar{H}\right) + \frac{\partial}{\partial x_i}\left(\rho u_i \bar{H}\right) = \frac{\partial}{\partial x_i}\left(\frac{k_{\text{t}}}{c_p}\frac{\partial \bar{H}}{\partial x_i}\right) + \tau_{ik}\frac{\partial u_i}{\partial x_k} + S_h \tag{6.14}$$

where S_h accounts for any sources of heat transfer which, neglecting heat transfer to the walls and radiation, includes any heat transfer between the gases and the particles.

To calculate the time-averaged species mole fractions and temperature for a non-adiabatic PDF model with a secondary stream, the following equation is used:

$$\bar{\phi}_i = \int_0^1 \int_0^1 \phi_i\left(f_{\text{fuel}}, p_{\text{sec}}, H\right) p_1(f_{\text{fuel}}) p_2(p_{\text{sec}}) df_{\text{fuel}} dp_{\text{sec}} \tag{6.15}$$

where p_1 and p_2 are both beta-PDF's. The time-averaged density would be:

$$\frac{1}{\bar{\rho}} = \int_0^1 \int_0^1 \frac{p_1(f_{\text{fuel}}) p_2(p_{\text{sec}})}{\rho\left(f_{\text{fuel}}, p_{\text{sec}}, H\right)} df_{\text{fuel}} dp_{\text{sec}} \tag{6.16}$$

For the non-adiabatic PDF model, the FLUENT preprocessor prePDF was used to generate three-dimensional look-up tables for the relevant scalars using 21 discrete points for the mean mixture fraction $\bar{f}_{\text{fuel}}$, 21 discrete points for the mean partial fraction $\bar{p}_{\text{sec}}$, and 31 discrete points for the enthalpy. The centre point of the distribution for $\bar{f}_{\text{fuel}}$ was set at 0.4, on the rich side of the stoichiometric value of the mixture fraction ($f_{\text{fuel,stoich}} \approx 0.2$) for a composition equivalent to a solid fuel formulation with 90% GAP and 10% carbon. The centre point for $\bar{f}_{\text{sec}}$ was set at 0.2, on the rich side of its stoichiometric value ($f_{\text{sec,stoich}} \approx 0.1$) and equal to the minimum value recommended [46]. Furthermore, the rich limit was usually set to $f_{\text{fuel}} = 0.5$ or less if prePDF could not calculate the equilibrium composition at $f_{\text{fuel}} = 0.5$. The secondary rich flammability limit was set at $f_{\mathrm{sec}} = 1.0$. As for the onestream model, these centre points and flammability limits were set richer than that recommended [46] because the fuel was already partially oxidized and at a temperature on the order of 1 000 K. Rich flame stoichiometry was calculated automatically by prePDF rather than being specified.

6.6 Two-phase Flow Model

For the onestream combustion modelling results, the boundary conditions for each experiment were used to generate single fuel stream PDF files. This means that all of the fuel, including both the gaseous and solid phases, was injected into the combustor as a single homogeneous stream. The solid carbon was therefore assumed to react instantaneously, as were the gases, once there was any oxidizer present. However, as will be presented shortly, the carbon in the gas generator exhaust for the direct-connect experiments consists of particles that are of large enough size that they cannot be expected to react instantaneously. This can explain the overestimation of some of the combustion efficiencies to be shown later in Section 6.8. Therefore, by using a two fuel stream PDF, with separate gaseous and solid phase streams, along with a model to describe the flow path and decomposition of the solid carbon, improvement to the estimates of the calculated combustion efficiencies may be possible.

The first step to developing a particle model was to collect and measure some particles during an actual direct-connect combustion experiment. A vacuum bottle was connected to the fuel plenum by a tube, and particles were collected in an in-line filter. The material trapped in this filter was then dispersed in some ethanol using an ultrasonic bath. The particle size distribution from a Malvern Mastersizer 2000, which assumes the particles are spherical, is shown in Fig. 6.23. A wide range of particles was detected, from below 0.1 μm to above 200 μm. For comparison, the results from a sample of effluent from a GAP/Carbon gas generator are also displayed and show that the ethylene/air fuel can also simulate the particle size distribution of the solid fuel exhaust as well.

Soot from typical hydrocarbon/air combustion consists of minute carbon spheres usually less than 60 nm in diameter, which are grouped together as much larger agglomerates that can be as large as several micrometres [82]. However, the ethylene/air mixture used during a direct-connect test cannot be classified as typical

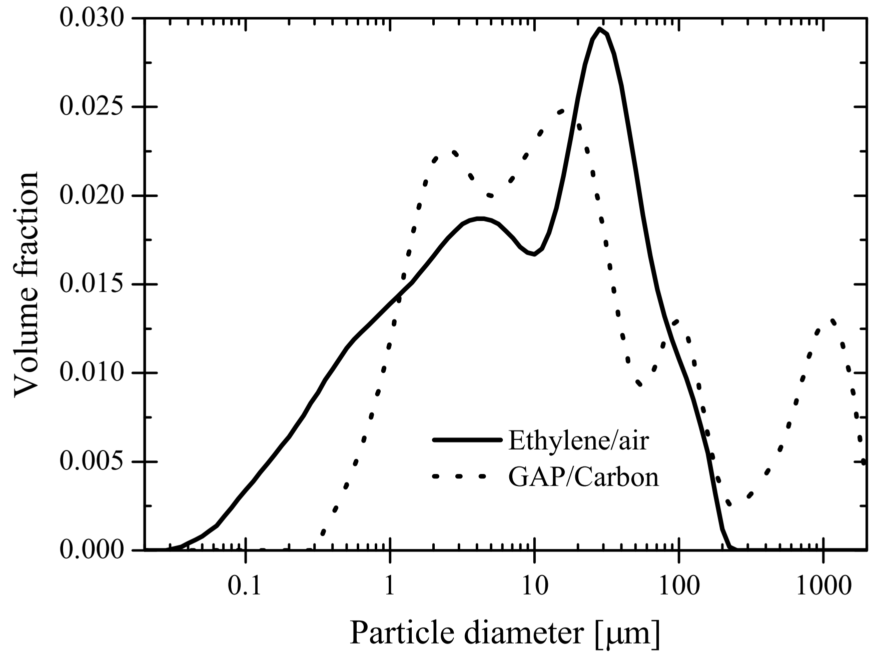

Figure 6.23: Particle sizes of ethylene/air and GAP/Carbon fuels

combustion since it is extremely rich. Nonetheless, a scanning electron microscope (SEM) image (Fig. 6.24) of the solid material collected from the fuel plenum during a direct-connect experiment shows that the majority of the particles present are composed of spheres are about 75 nm in diameter, which is close to that usually reported for soot from typical hydrocarbon/air combustion.

While the trajectories of the particles are closely related to their mass and overall dimensions, their decomposition is a function of their total surface area exposed to the oxidizer. This total surface area is related more to the diameter of the minute spheres that make up the soot particle rather than the overall size of the particle. With the same configuration as for the parametric study (Table 6.4), twostream PDF modelling (with the particle model described below) was carried out for a wide range of particle sizes. The results for the trajectories of these various particle sizes and how much they decompose are shown in Figs. 6.25 and 6.26. To generate these graphs, about 30 particles were injected from the fuel inlet hole. From the side view shown in Fig. 6.25, the trajectories of particles having diameters from 1 nm to 1 μm appear to fill the bottom half of the combustor and abruptly change direction when deflected by the incoming air jets. The 10 and 100 μm particles, however, do not seem to follow the flow as faithfully and take much straighter trajectories toward the end of the combustor. The isometric view in Fig. 6.26 also shows that the ensembles

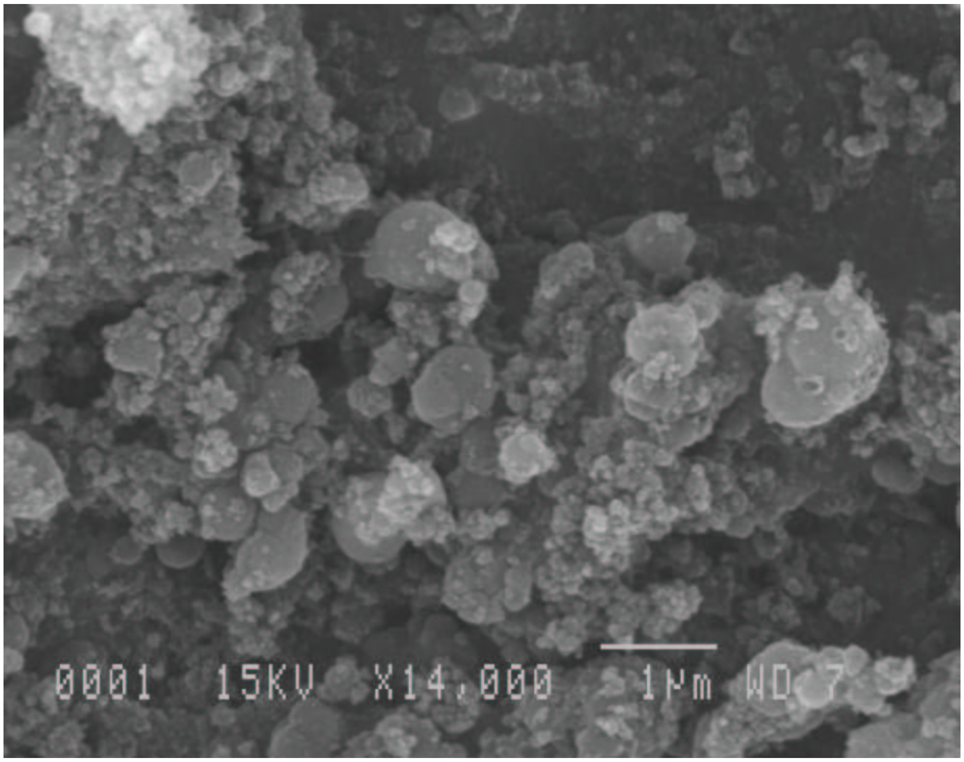

Figure 6.24: SEM picture of particles in the ethylene/air fuel

of trajectories for particles smaller than 10 μm are similar. The particle trajectories are coloured by particle density which changes as the particles decompose, and it can be seen that the smaller the particle is, the faster it decomposes. In fact, for the 1 nm particles, about half decompose completely before reaching the end of the combustor. About 10-20% of the 10 nm particles and less than 5% of the 75 nm particles decompose completely before the end of the combustor. For particle diameters of 1 μm and above, all of the particles leave the combustor before they decompose completely.

The results from Figs. 6.25 and 6.26 therefore imply that the particles from 1 nm to over 1 μm in diameter could be modelled as 75 nm spheres and still be assumed to follow similar paths through the combustor. This assumption may even be valid for larger particles as well. Figure 6.23 shows the existence of many particles with overall diameters of 10 μm and larger, but Fig. 6.24 shows that they were made up of agglomerates of much smaller spheres. Their aerodynamic drag would therefore be much higher than spheres of equivalent overall diameter, so then particles of even several micrometres in diameter could be expected to follow the

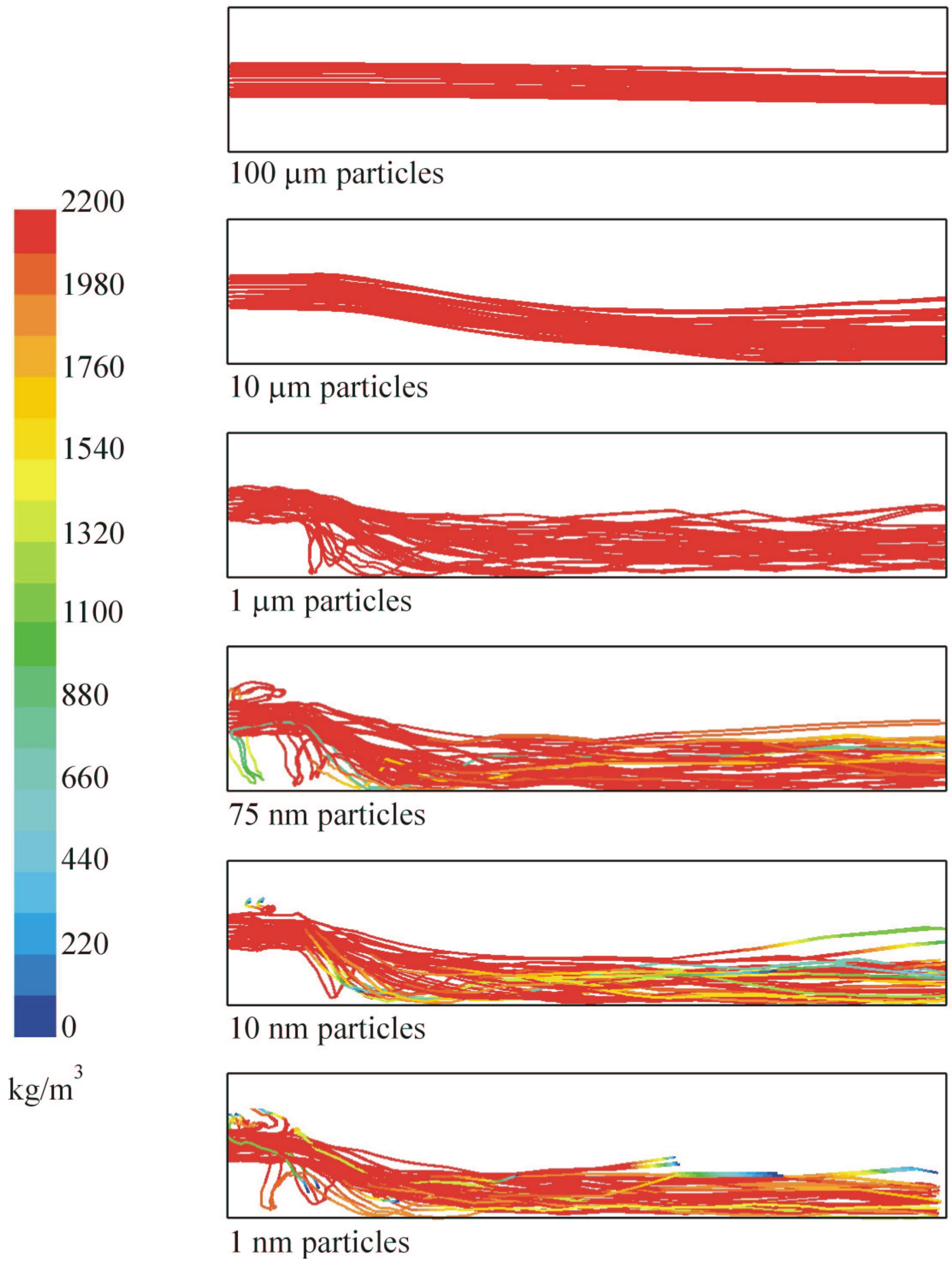

Figure 6.25: Predicted particle trajectories versus diameter, side view, coloured by particle density

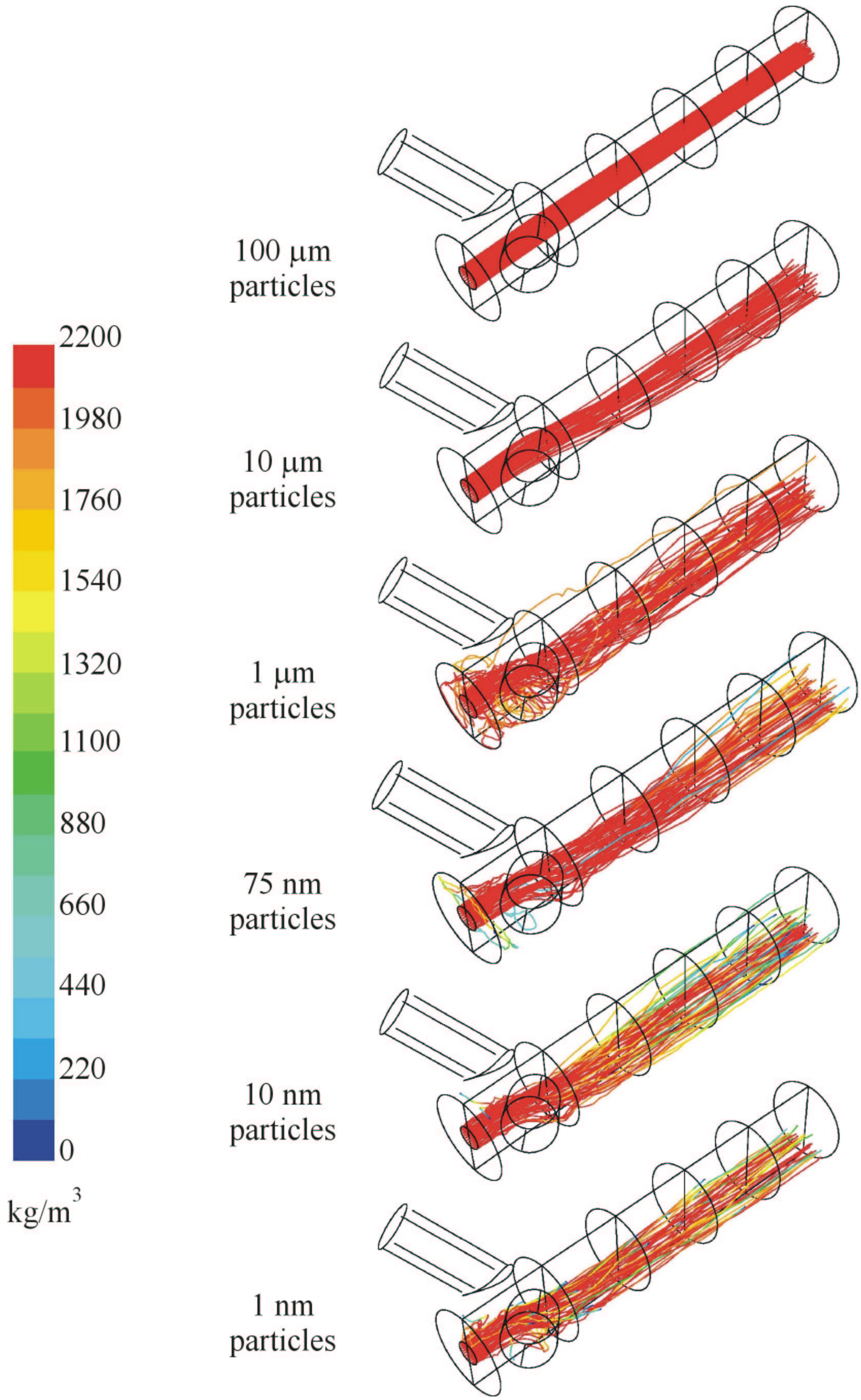

Figure 6.26: Predicted particle trajectories versus diameter, isometric view, coloured by particle density

flow as well as the 1 μm diameter and smaller particles. Furthermore, because they are agglomerates, they likely break up as well. For these reasons, the particles in the flow were assumed to behave as 75 nm diameter solid carbon spheres, for both the trajectory and decomposition models.

To calculate the trajectories of the particles, FLUENT integrates a force balance on each particle. The equation in the x-direction, using a Lagrangian reference frame, is [46]:

$$\frac{du_{\mathrm{p}}}{dt} = F_{\mathrm{D}}(u - u_{\mathrm{p}}) + g_x \frac{(\rho_{\mathrm{p}} - \rho)}{\rho_{\mathrm{p}}} + f_x \tag{6.17}$$

where ρ is the density of the surrounding gas, ρ_{p} and u_{p} are the density and velocity of the particle, g_x and f_x account for the gravitational and other forces in the x-direction, and:

$$F_{\mathrm{D}} = \frac{18\mu}{\rho_{\mathrm{p}} d_{\mathrm{p}}^2} \frac{C_{\mathrm{D}} Re}{24} \tag{6.18}$$

where d_{p} is the diameter of the particle. Here, Re is the relative Reynolds number:

$$Re = \frac{\rho d_{\mathrm{p}} |u_{\mathrm{p}} - u|}{\mu} \tag{6.19}$$

and the drag coefficient C_{D} is for smooth spherical particles over a wide range of Re [83].

To account for the turbulent dispersion of the particles, FLUENT uses a Discrete Random Walk model. The instantaneous gas phase flow velocity u in Eqn. 6.17, as already seen in Eqn. 4.5, is:

$$u = \bar{u} + u' \tag{6.20}$$

Each particle is assumed to interact with a succession of turbulent eddies, each characterized with a turbulent velocity fluctuations (isotropy assumed):

$$u' = v' = w' = \zeta \sqrt{\overline{u'^2}} = \zeta \sqrt{2k/3} \tag{6.21}$$

and a time scale:

$$\tau_e = 2T_{\mathrm{L}} \tag{6.22}$$

where ζ is a normally-distributed random number. For the RNG turbulence model, T_{L} is approximated by:

$$T_{\mathrm{L}} \approx 0.15 \frac{k}{\varepsilon} \tag{6.23}$$

Once one eddy lifetime has been reached, new values for the turbulent fluctuations are calculated with a newly-generated random number.

As the particle travels through the combustor, it is heated or cooled depending on its temperature and that of the surrounding gas. In the absence of radiation, the equation used for the particle heat balance is:

$$m_{\mathrm{p}} c_p \frac{dT_{\mathrm{p}}}{dt} = hA_{\mathrm{p}}(T_\infty - T_{\mathrm{p}}) \tag{6.24}$$

where T_{p} and T_∞ are the temperatures of the particle and the surrounding gas, A_{p} is the surface area of the particle (based on the overall diameter), m_{p} is the mass of the particle, and $c_p = 1\,220$ J/(kg·K) for the solid carbon particles. The convective heat transfer coefficient h is estimated from the Nusselt number Nu:

$$Nu = \frac{hd_{\mathrm{p}}}{k_\infty} = 2.0 + 0.6Re^{1/2}Pr^{1/3} \tag{6.25}$$

where k_∞ and Pr refer to values of the gas phase, and Re is calculated from Eqn. 6.19.

A kinetics/diffusion model in FLUENT [46], with some of the constants modified, was used to describe the decomposition of the carbon particles. The change in mass of the particles is described by:

$$\frac{dm_{\mathrm{p}}}{dt} = -\pi d_{\mathrm{p}}^2 \frac{\rho \bar{R} T m_{\mathrm{ox}}}{M_{\mathrm{ox}}} \frac{R_1 R_2}{R_1 + R_2} \tag{6.26}$$

where T is the temperature of the surrounding gas, $\bar{R}$ is the Universal Gas Constant, m_{ox} and M_{ox} are the mass fraction and the molar mass of the oxidant in the surrounding gas near the particles, and R_1 and R_2 are the diffusion controlled and the surface kinetics controlled rates respectively. The diffusion-controlled decomposition rate is derived from an expression for pulverized coal particles (over a wide range of temperatures) where the particles give off carbon monoxide rather than carbon dioxide [84]:

$$R_1 = C_1 \frac{\left[\left(T_{\mathrm{p}} + T_\infty\right)/2\right]^{0.75}}{d_{\mathrm{p}}} \tag{6.27}$$

where $C_1 = 4.993\,868 \cdot 10^{-12}$ kg/(m·s·Pa·K$^{0.75}$). The kinetics of the surface reaction come from an approximation [85] to the widely-accepted Nagel-Strickland-Constable formula for soot oxidation [86] :

$$R_2 = C_2 \exp\left(-E_{\mathrm{a}}/\bar{R}T_{\mathrm{p}}\right) \tag{6.28}$$

where $C_2 = 1.115\,31 \cdot 10^{-3}$ kg/(m^{2}s·Pa) and $E_\mathrm{a} = 1.425\,37 \cdot 10^8$ J/kmol is the activation energy of the surface reaction. Figure 6.27 shows that this approximation is valid at a wide range of oxygen partial pressures at temperatures below approximately 2 000 K, conditions that are generally present in the ramjet combustor configurations considered here. This approximation is very important since the decomposition of the soot particles is controlled by the surface reaction rate R_2, rather than the diffusion rate R_1, as they become very small. For particles of 75 nm diameter, the decomposition is controlled essentially by the surface reaction rate.

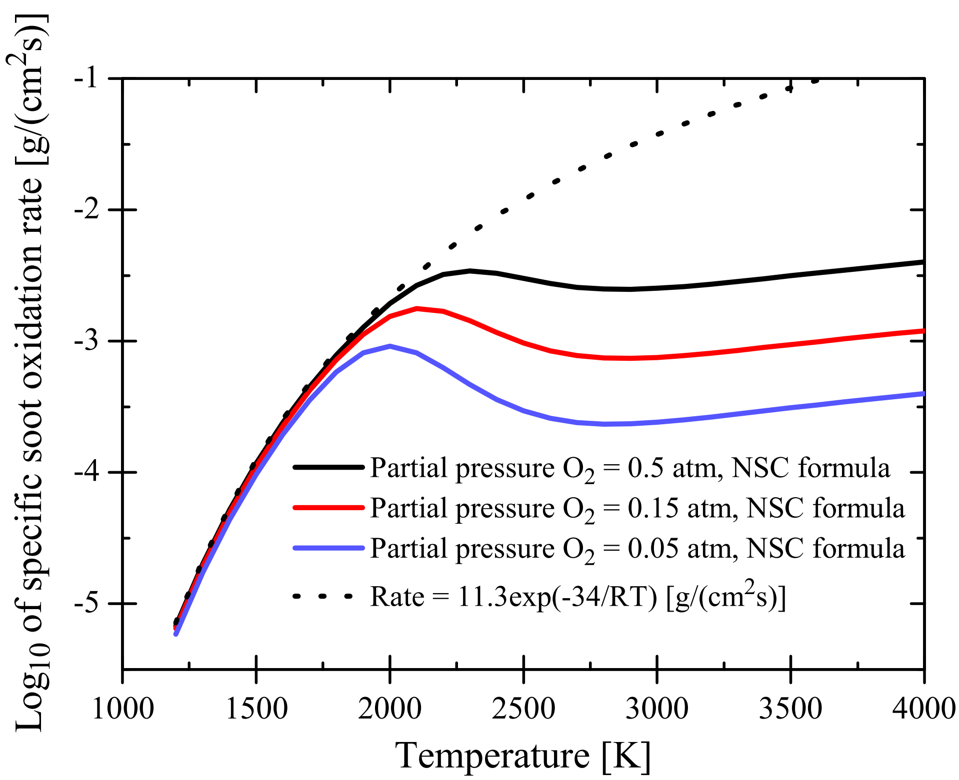

Figure 6.27: Soot oxidation rate versus temperature and oxygen partial pressure, Nagel-Strickland-Constable formula [86] and approximation [85]

When the oxidation of the particles is included, the heat balance equation has an additional term:

$$m_\mathrm{p} c_p \frac{dT_\mathrm{p}}{dt} = h A_\mathrm{p}(T_\infty - T_\mathrm{p}) - f_h \frac{dm_\mathrm{p}}{dt} H_\mathrm{reac} \tag{6.29}$$

where $f_h = 1.0$ for particles giving off carbon monoxide. It is the fraction of the heat of the surface reaction H_reac absorbed by the particle.

Rather than each particle decreasing in diameter as its mass decreases, the diameter remains the same while the density decreases from its initial value of

2 200 kg/m^3. The particle therefore becomes more porous as it decomposes. The continuous phase flowfield and dispersed phase calculations were coupled, meaning that not only did the flowfield affect each particle's trajectory and decomposition, but the particle could affect the flowfield. Mass, momentum, and heat are therefore exchanged between the solid and gas phases as each particle passes through each of the control volumes. Approximately 500 particles had to be injected (spread over the area of the fuel inlet) every ten flowfield iterations to attain a "quasi-steady" state and convergence after several hundred iterations. To find the best number of particles to inject and after how many flowfield iterations to reach convergence without excessive calculation time was a lengthy process of trial and error. After optimizing these calculation parameters, the length of time for a twostream PDF model solution was about an order of magnitude longer than that for a onestream PDF model solution.

6.7 Twostream PDF Results

The next several graphs show the temperature distribution on the centreline plane for each direct-connect configuration modelled with the onestream and twostream PDF's. As will be shown in Section 6.8, the tendency of the onestream PDF model is to overpredict the combustion efficiency. The purpose of the twostream PDF model was to more accurately model the distribution and decomposition of the solid carbon in the gas generator exhaust and hopefully reduce the overprediction of the temperatures. However, as the following graphs will show, the carbon particles, because of their mass, can convect fuel to areas that would otherwise be much leaner. In configuration DC1, the twostream model shows less release of energy right near the head end of the combustor, but further downstream there are higher temperatures on the centreline plane than for the onestream model. For configuration DC2, DC12, and DC28, the temperature distribution around the fuel jet is about the same for the two PDF models. However, there is a higher temperature region near the upper wall at the end of the combustor for the onestream model. A similar region is seen at the aft end of the combustor for configuration DC3 for the onestream model, but the twostream model has greater heat release on the lower centreline plane. The results for the twostream model for configurations DC6 and DC9 show some higher temperatures at the head end, but the heat release on the centreline plane for the rest of the combustor is similar to the onestream model.

The graphs for configurations DC11, DC13, DC14, DC16, DC21, and DC29 are similar at the head end of the combustor, but the twostream model has a higher temperature region near the lower wall on the centreline plane than does the onestream model. Configuration DC15 has a higher heat release for the twostream model all the way along the combustor below the fuel jet. Configuration DC18 has its heat release distributed more evenly right above and below the fuel jet for the twostream model, and also has higher temperatures near the lower combustor wall. The onestream model gives higher temperatures adjacent to the fuel jet for configuration DC20 than does the twostream model, but downstream the temperature distributions are the same for the two models. Configurations DC7, DC8, DC19, and DC30 show only very subtle differences in the temperature distributions for the two models.

Therefore, at least on the centreline plane, the use of the twostream model can indeed change the distribution of temperature, depending on the configuration. Unfortunately, no general conclusion can be made from these graphs that the use of the twostream PDF model lowers the overall temperatures on the combustor and reduces the overprediction of combustion efficiency characteristic of the onestream model. To make that conclusion will require the combustion efficiencies, calculated from the mass-averaged temperatures at the 458 mm cross-section, which will be presented in the next section.

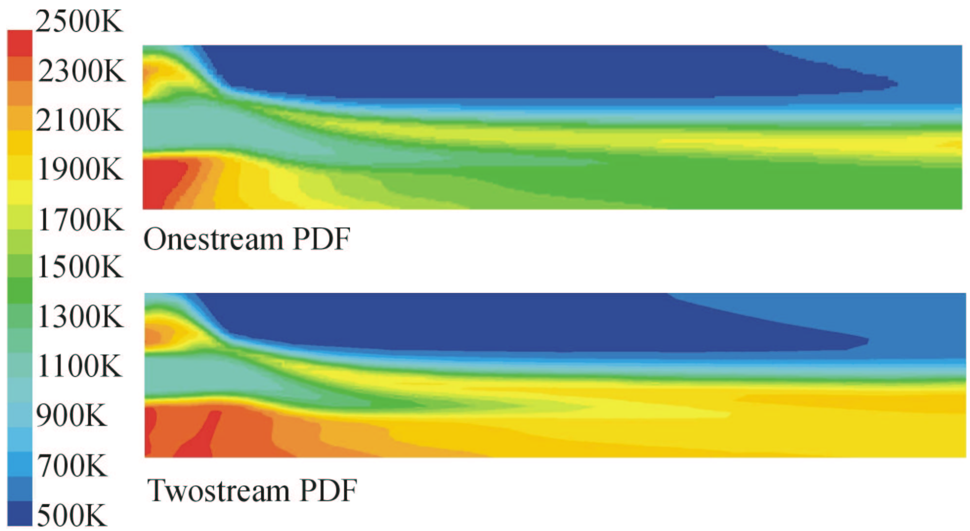

Figure 6.28: Predicted temperature distribution on centreline plane for onestream and twostream PDF models, configuration DC1

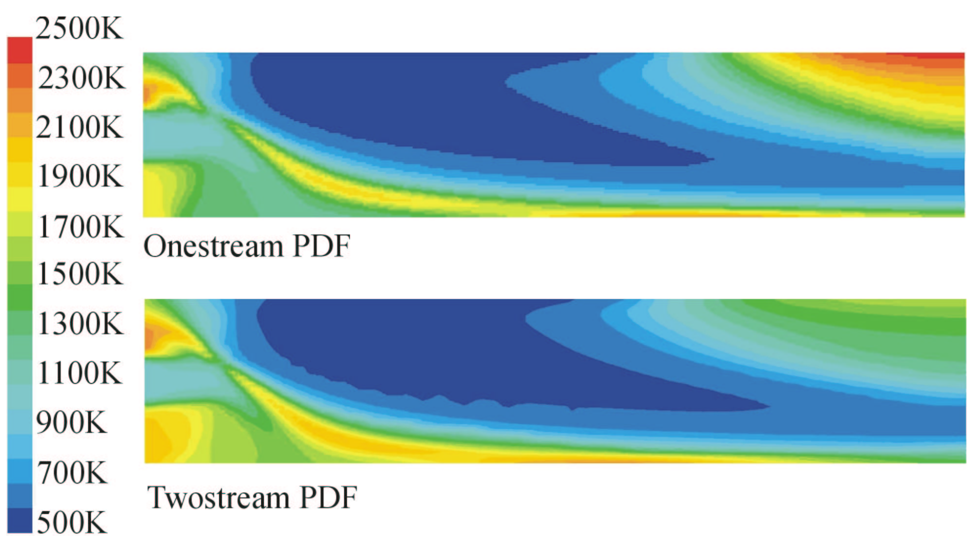

Figure 6.29: Predicted temperature distribution on centreline plane for onestream and twostream PDF models, configuration DC2

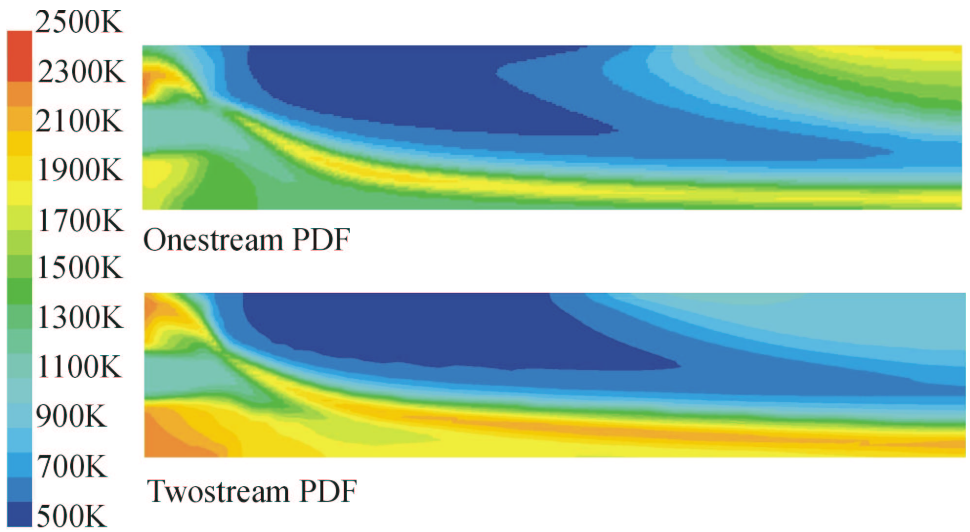

Figure 6.30: Predicted temperature distribution on centreline plane for onestream and twostream PDF models, configuration DC3

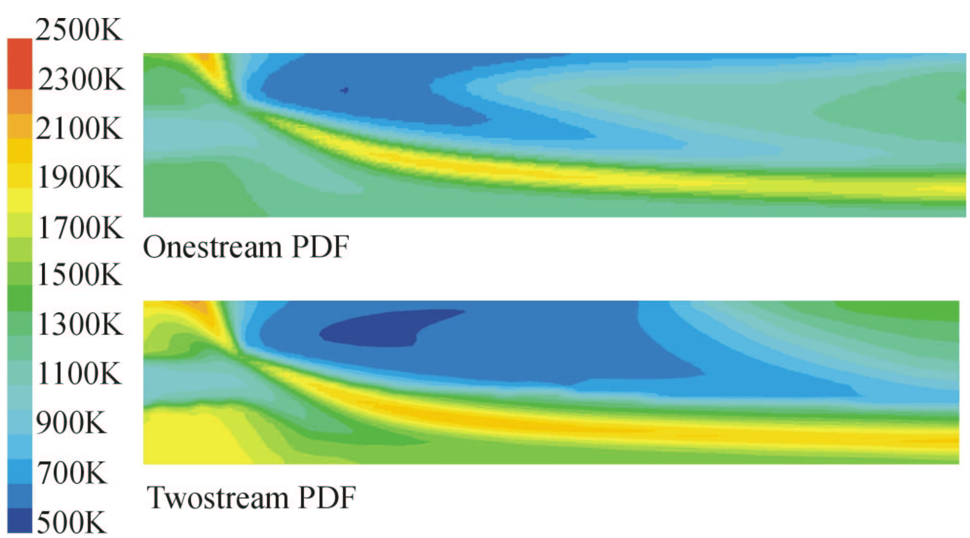

Figure 6.31: Predicted temperature distribution on centreline plane for onestream and twostream PDF models, configuration DC6

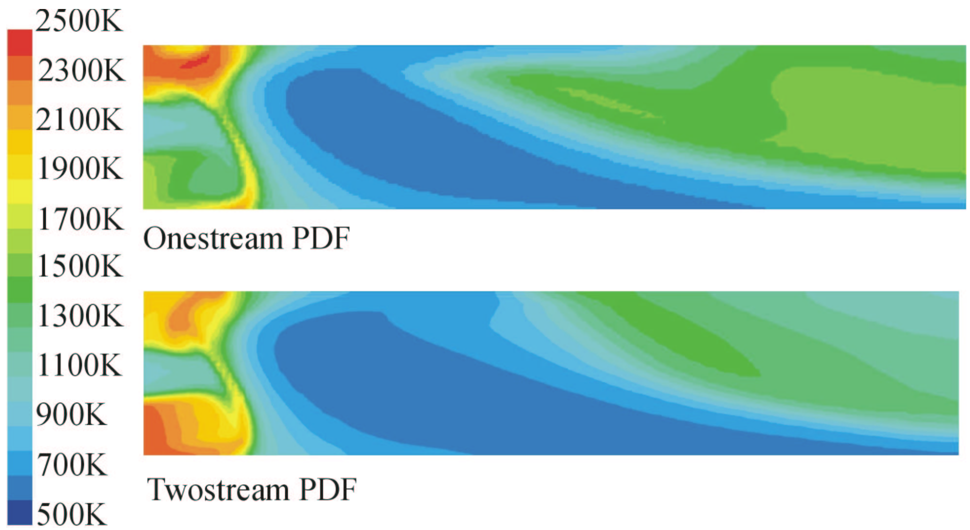

Figure 6.32: Predicted temperature distribution on centreline plane for onestream and twostream PDF models, configuration DC7

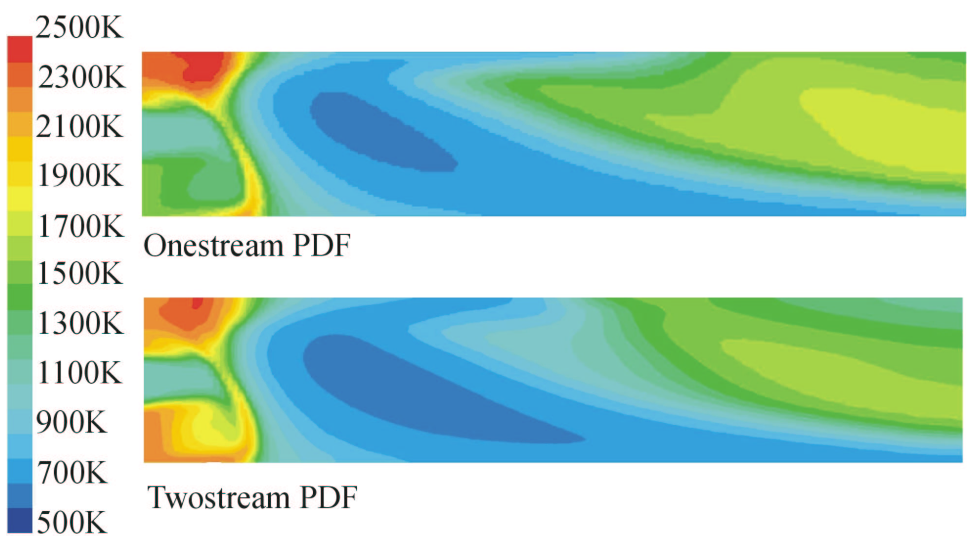

Figure 6.33: Predicted temperature distribution on centreline plane for onestream and twostream PDF models, configuration DC8

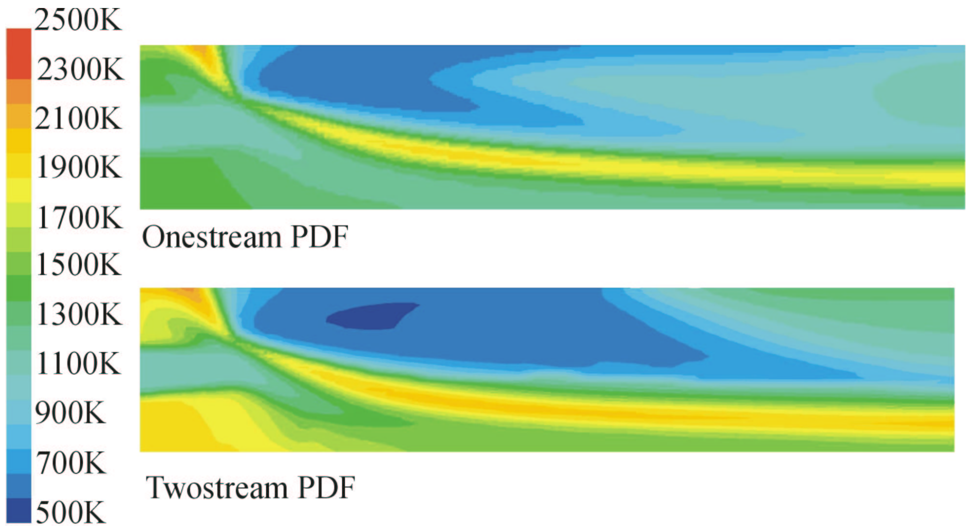

Figure 6.34: Predicted temperature distribution on centreline plane for onestream and twostream PDF models, configuration DC9

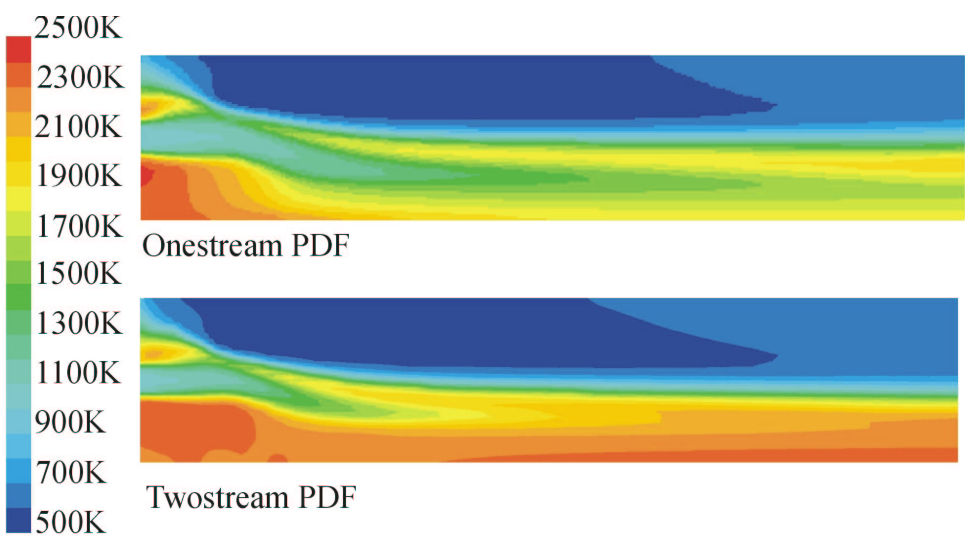

Figure 6.35: Predicted temperature distribution on centreline plane for onestream and twostream PDF models, configuration DC11

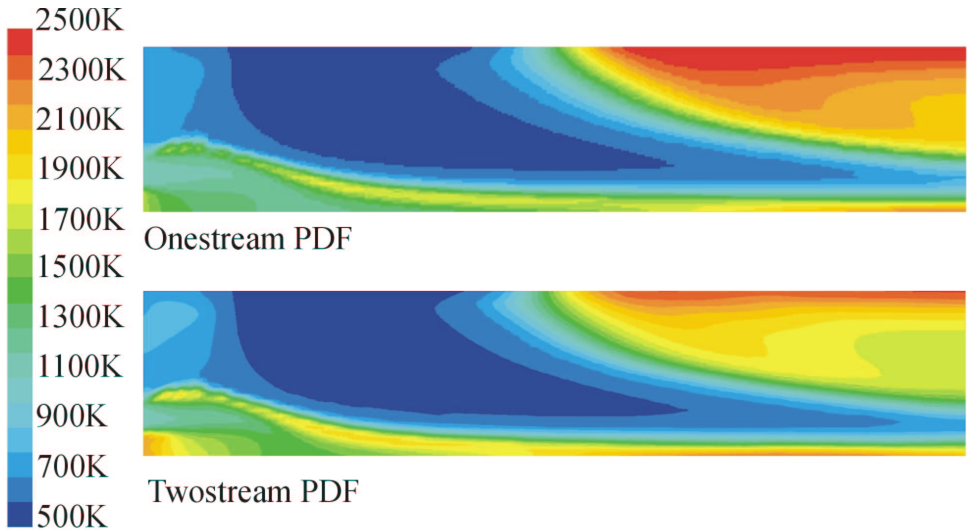

Figure 6.36: Predicted temperature distribution on centreline plane for onestream and twostream PDF models, configuration DC12

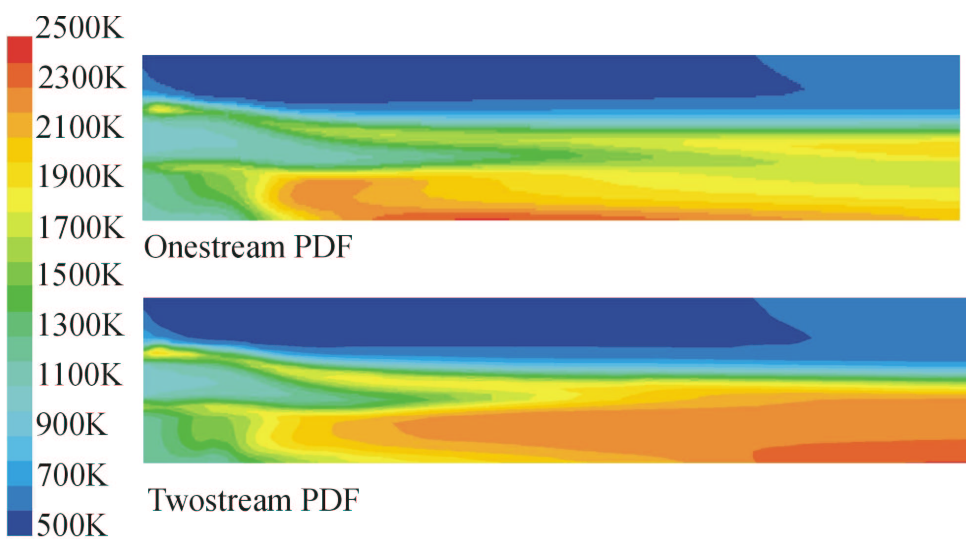

Figure 6.37: Predicted temperature distribution on centreline plane for onestream and twostream PDF models, configuration DC13

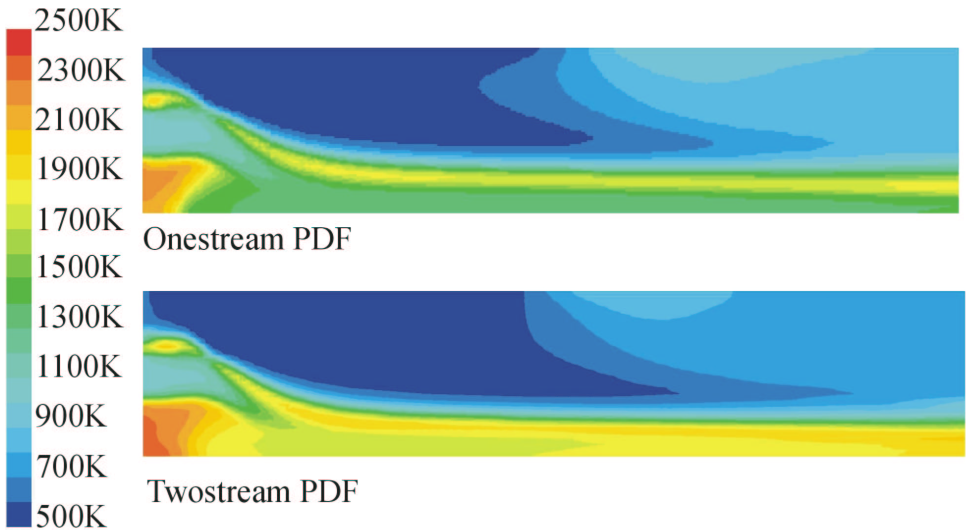

Figure 6.38: Predicted temperature distribution on centreline plane for onestream and twostream PDF models, configuration DC14

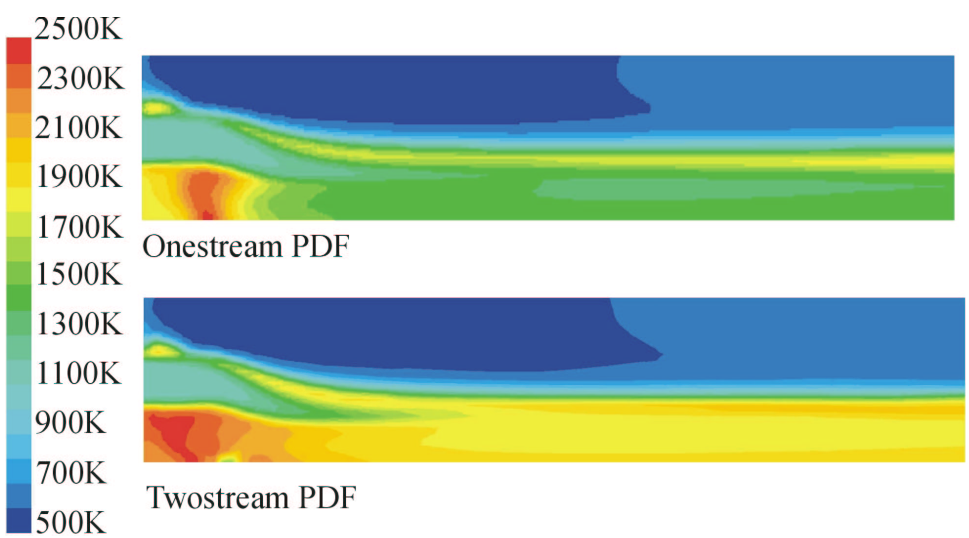

Figure 6.39: Predicted temperature distribution on centreline plane for onestream and twostream PDF models, configuration DC15

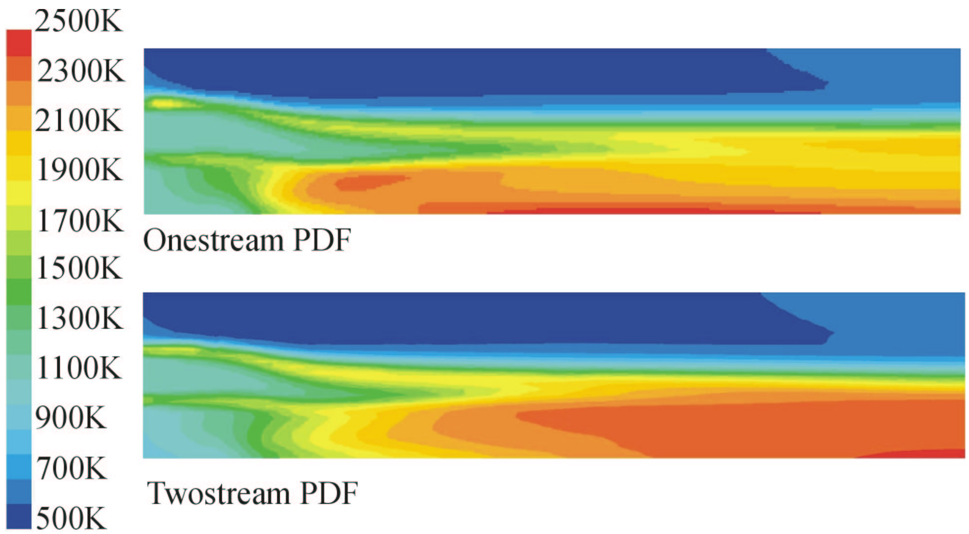

Figure 6.40: Predicted temperature distribution on centreline plane for onestream and twostream PDF models, configuration DC16

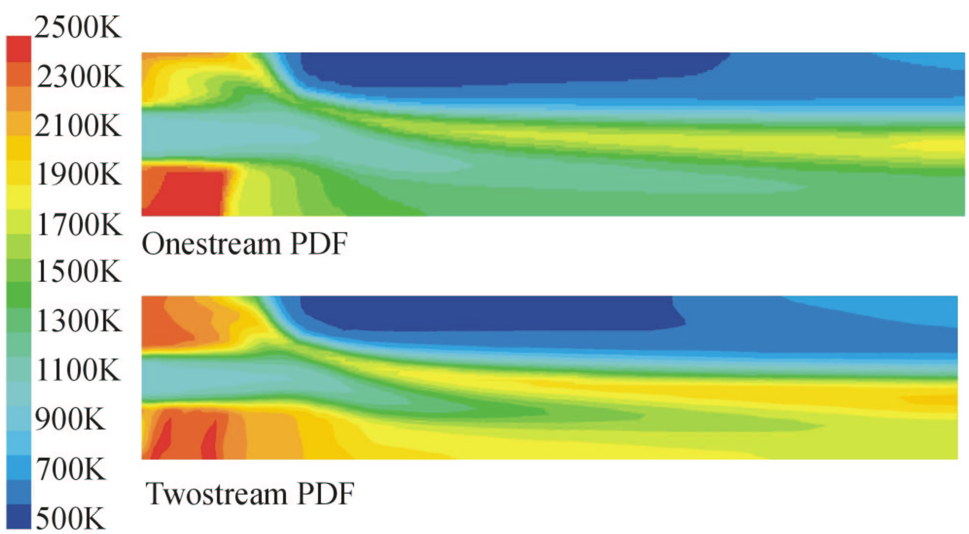

Figure 6.41: Predicted temperature distribution on centreline plane for onestream and twostream PDF models, configuration DC18

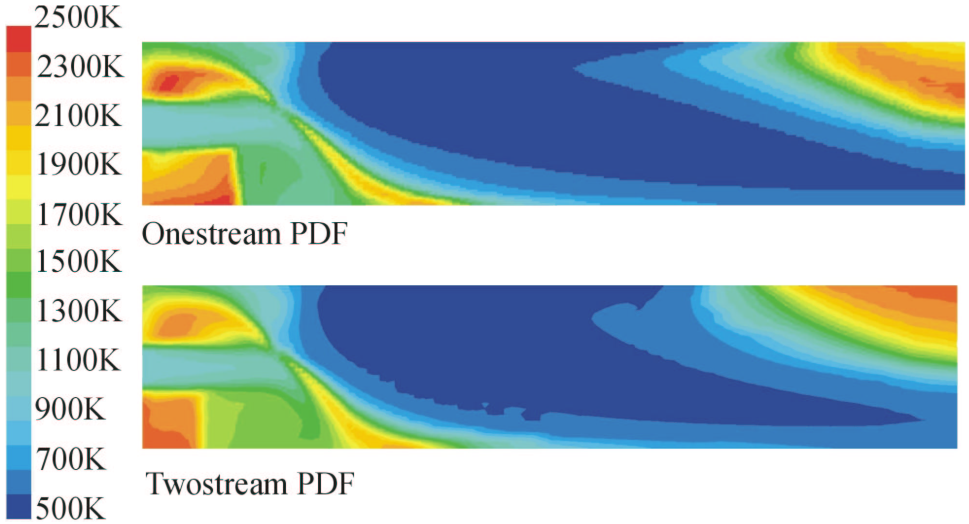

Figure 6.42: Predicted temperature distribution on centreline plane for onestream and twostream PDF models, configuration DC19

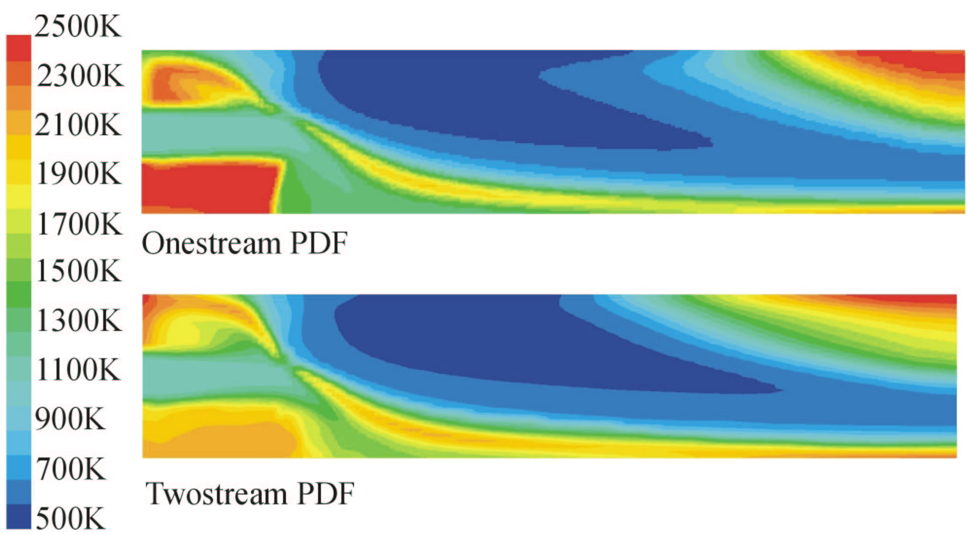

Figure 6.43: Predicted temperature distribution on centreline plane for onestream and twostream PDF models, configuration DC20

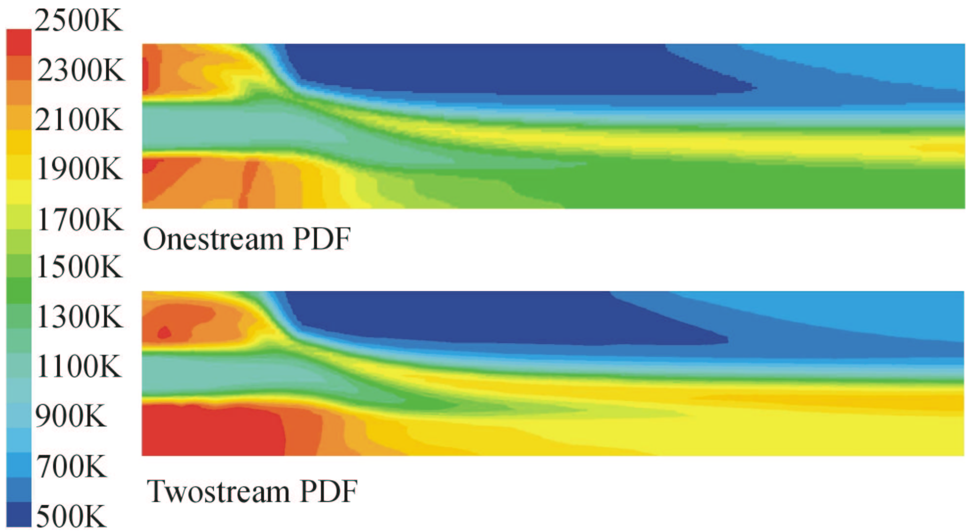

Figure 6.44: Predicted temperature distribution on centreline plane for onestream and twostream PDF models, configuration DC21

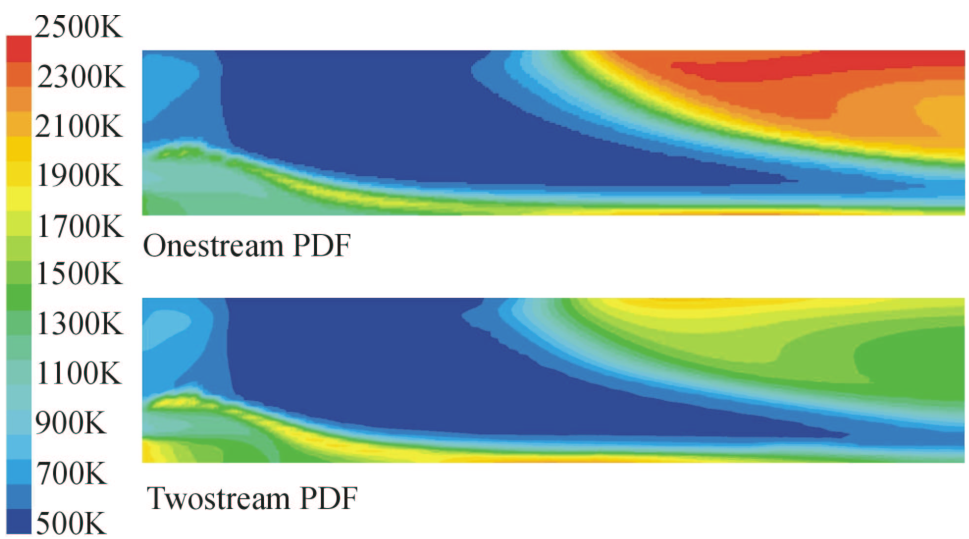

Figure 6.45: Predicted temperature distribution on centreline plane for onestream and twostream PDF models, configuration DC28

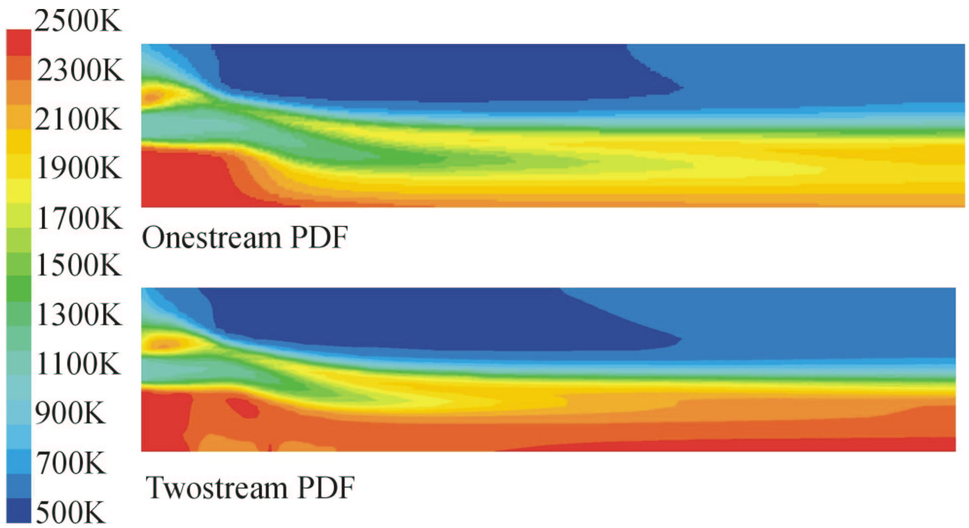

Figure 6.46: Predicted temperature distribution on centreline plane for onestream and twostream PDF models, configuration DC29

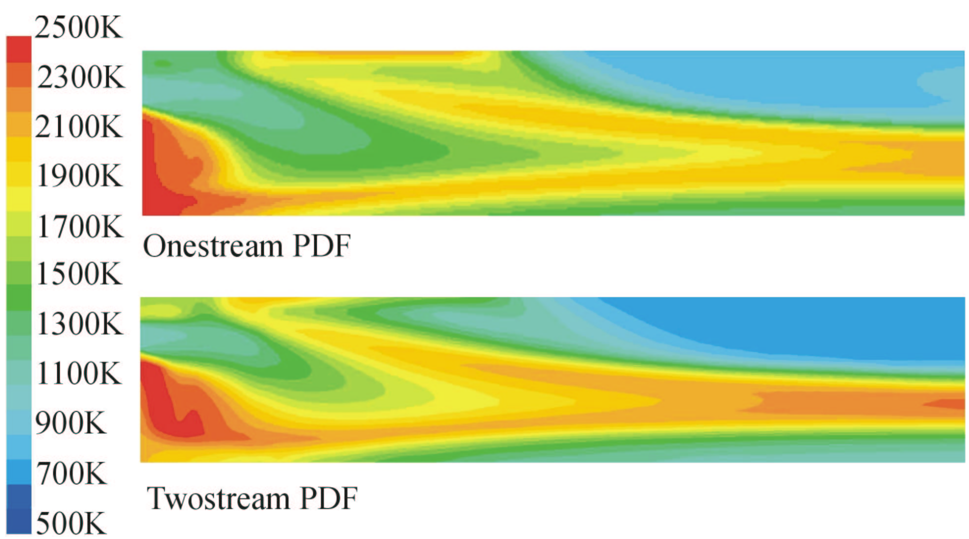

Figure 6.47: Predicted temperature distribution on centreline plane for onestream and twostream PDF models, configuration DC30

6.8 Comparison of the CFD and Direct-connect Results

Using the methods already described in Sections 5.3 and 6.4, the combustion efficiencies based on temperature rise in the combustor for the direct-connect experiments and the CFD results are presented in Fig. 6.48 for each of the direct-connect configurations. Results for both the onestream and twostream PDF models, calculated from the mass-averaged temperature at the 458 mm cross-section, are given. As shown, while some results with the onestream PDF were close to the experimental results, on the average their calculated combustion efficiencies were overestimated. Predictions are significantly improved, however, with twostream PDF model, for most of the configurations. Another important observation is that exactly half of the twostream results are higher than the experimental, values and half are lower. This is of interest because, as previously shown in the parametric study in Section 6.4, the turbulence intensity can have a significant effect on the combustion efficiency. If a poor value was chosen for this boundary condition, the results would be consistently higher or lower than the experimental efficiencies; this does not appear to be the case in this instance.

While there still seem to be some large differences for some of the twostream PDF predictions and the experimental results, the average difference between the CFD predictions and experimental results is almost the same as the average experimental uncertainty. Table 6.5 presents the numerical values of the combustion efficiencies presented in Fig. 6.48, along with the percent differences between the predictions and the experimental efficiencies for both the onestream and twostream models, and the experimental uncertainties for each configuration calculated as described in Section 5.4. The average difference between the onestream PDF and the experimental results is 26.8% (where the percent difference is defined by Eqn. 6.10). However, for the twostream PDF results, with separate streams for the gaseous and solid phases of the gas generator exhaust, this difference is significantly lower at 15.6%. This is almost the same as the average experimental uncertainty at 13.1%.

The average differences between the onestream and twostream predictions and the experimental results give an indication of the validity of the modelling, but a much more statistically-rigorous analysis was developed specifically for this work [87] to better support the conclusions. It will be summarized here. If this work had dealt with a single combustor configuration, the validity of the modelling could

Table 6.5: Combustion efficiencies for direct-connect experiments and CFD modelling

Direct Connect Config	Air Inj	Fuel Inj	Dome Height [mm]	Air/fuel Momentum Ratio	Experimental Efficiency	Experimental Uncertainty	Onestream PDF Efficiency	Onestream PDF Difference	Twostream PDF Efficiency	Twostream PDF Difference
DC1	A4	F0-27	57	3.19	0.61	11%	0.37	40%	0.36	42%
DC2	A4	F0-27	57	11.73	0.48	16%	0.75	56%	0.51	7%
DC3	A4	F0-27	57	8.89	0.40	15.7%	0.59	46%	0.40	0.4%
DC6	A2	F0-27	57	3.90	0.37	10%	0.51	37%	0.40	8%
DC7	A2	F0-27	57	19.43	0.64	14%	0.87	36%	0.55	13%
DC8	A2	F0-27	57	17.94	0.70	13%	0.89	28%	0.79	13%
DC9	A2	F0-27	57	3.52	0.44	10%	0.47	6%	0.39	13%
DC11	A4	F0-18	57	4.87	0.64	13%	0.54	16%	0.47	26%
DC12	A4	F1-18	57	4.07	0.50	14%	0.76	52%	0.61	23%
DC13	A6	F0-27	57	2.30	0.41	9%	0.44	8%	0.44	8%
DC14	A6	F0-27	57	10.80	0.57	14%	0.57	0.3%	0.45	21%
DC15	A6	F0-27	57	5.20	0.27	16%	0.36	36%	0.34	26%
DC16	A6	F0-27	57	2.37	0.43	12%	0.49	14%	0.48	10%
DC18	A4	F0-27	100	2.13	0.28	11%	0.33	16%	0.32	14%
DC19	A4	F0-27	100	10.93	0.61	14%	0.73	20%	0.51	15%
DC20	A4	F0-27	100	8.31	0.40	15%	0.57	44%	0.43	7%
DC21	A4	F0-27	100	2.76	0.49	12%	0.35	28%	0.35	29%
DC28	A4	F1-18	57	4.84	0.69	13%	0.84	21%	0.56	20%
DC29	A4	F0-18	57	4.42	0.59	14%	0.57	4%	0.52	12%
DC30	A4	F1-18S	57	4.29	0.56	14%	0.73	30%	0.60	6%

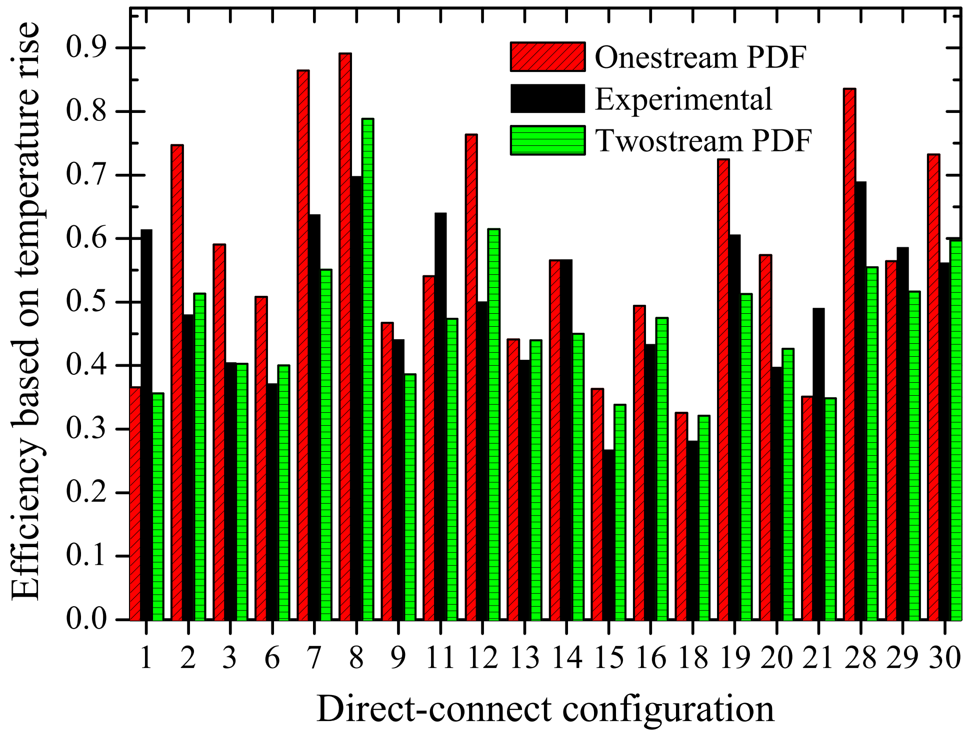

Figure 6.48: Results for the calculated efficiencies from the experiments and CFD modelling

have been assessed by simply performing several experiments, estimating a mean and standard deviation for the combustion efficiency, and comparing this to both the onestream and twostream predictions. While a wide range of geometries and test conditions was tested in the direct-connect facility, this also meant that since the number of tests was limited, only one test could usually be carried out for each configuration. On a case-by-case basis, judging the validity of a prediction is difficult for any single configuration, and the conclusion can vary greatly with each case, with some underpredicted and others overpredicted to different degrees. However, if all of the configurations can be taken together and compared, a better assessment of the validity of the modelling can be done.

To do this, a non-parametric analysis was developed to examine the residual errors. The residual error for each configuration is defined as the difference between the experimental observation and the prediction. The analysis is termed "non-parametric" because the details of the model, in this case the CFD prediction methodology, are not specified. This is in contrast to multiple regression techniques [88] in which a theoretical model, often a linear or higher order equation involving the dependent variables, is proposed and regression procedures used to calibrate it and determine its goodness-of-fit to the experimental data. From the extensive developments that have taken place for multiple regression, several techniques have been modified specifically for this non-parametric analysis of the residual errors for the values of combustion efficiency between the predictions and experiments.

Three procedures were carried out on the residuals, the first being to construct a linearized normal probability graph to determine whether or not they follow a normal distribution with a mean of zero and a constant variance. The purpose of this is to verify that the residuals are influenced solely by random effects. If this is true, the points should lie approximately on a straight line on the graph, and be randomly scattered about this line with the same proportion of points above and below the zero residual value (i.e. equally distributed). If the residuals follow a non-random pattern, this may indicate that the variance is a function of the experimental value, or that the modelling is inadequate.

The linearized normal probability graph can also be used to identify outliers. The second procedure carried out on the residuals, which transforms the residuals into standardized and studentized residuals, provides a formal statistical procedure, based on the statistics of extreme observations, for the identification of potential outliers. Figure 6.49 plots the normal standard deviate versus the residual for each configuration. Both the onestream and twostream results can be approximated by straight lines, but the onestream residuals do not meet the requirements of zero mean (not passing through intersection of the horizontal and vertical zero lines) and constant variance (values of the residuals mostly negative and therefore not randomly distributed). Because these requirements were not met, the second procedure was unable to identify any outliers. However, an obvious outlier was identified for the twostream residuals (configuration DC1), as well as a possible one (configuration DC11). With these two outliers removed, the linear fit of the twostream residuals passes almost right through the intersection of the zero lines, and the residuals are almost equally distributed about this intersection. The twostream residuals therefore appear to meet the requirements of zero mean and constant variance.

The third and final procedure carried out on the residuals quantifies the validity of the two modelling methodologies. The proposed coefficient of model adequacy

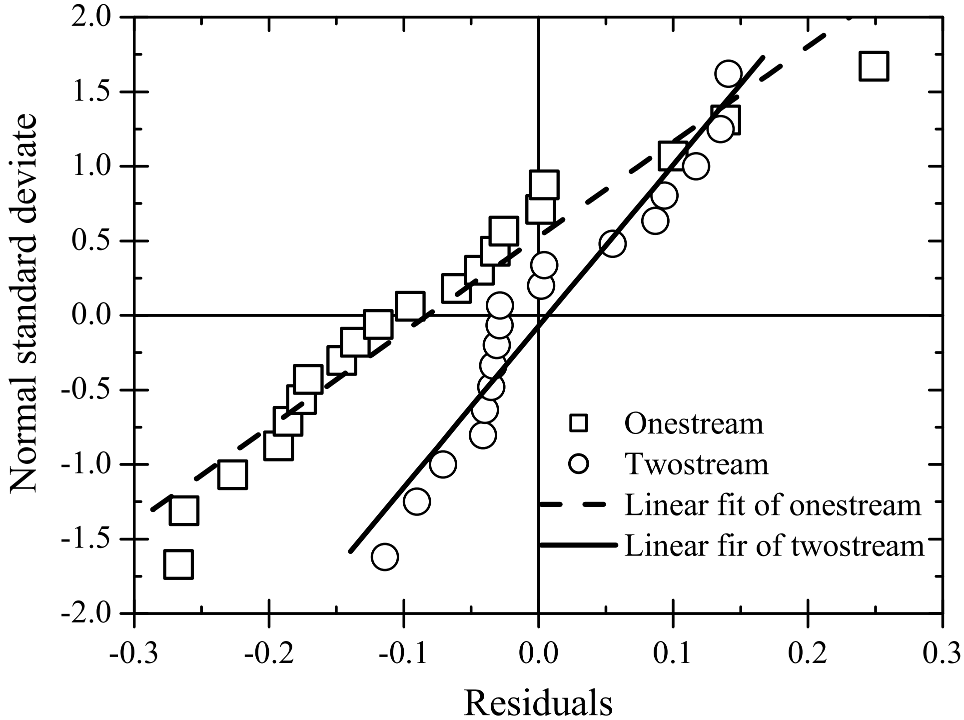

Figure 6.49: Normal probability graph of the residuals

M_{A} is defined by:

$$M_{\mathrm{A}} = 1 - \frac{\sum_{i=1}^{N} (y_i - \hat{y}_i)^2}{\sum_{i=1}^{N} y_i^2} \tag{6.30}$$

where y is the experimental value and $\hat{y}$ is the prediction. If $M_{\mathrm{A}} = 1$, the correlation between the predictions and the experiment results is perfect, while if $M_{\mathrm{A}} = 0$, the magnitude of the residual errors equals the magnitude of the experimental results. For the onestream PDF model, $M_{\mathrm{A}} = 0.91$ which is interpreted to mean that the model explains 91% of the variability in predicting the experimental values. For the twostream PDF model, however, M_{A} improves to 0.98. This is interpreted to mean that the twostream model can explain 98% of the variability in predicting the experimental results. Based on this, for the configurations described herein, the twostream PDF model can predict, within a good degree of accuracy, the performance of a ducted rocket combustor.

6.9 Summary of the Reacting Flow Results

A literature survey of ramjet combustor modelling to date revealed that there were no studies that took into account the the motion of solid particles and their decomposition. Any comparison between CFD modelling and experimental results was for the non-reacting flow only, except in a couple of instances where some reacting flow data were available. Unfortunately, none of the reacting flow studies described exactly how combustion efficiency was determined from the CFD results, and usually not even the type of combustion efficiency was noted for either the experimental or CFD results.

An equilibrium-chemistry Probability Density Function model was chosen to model the reacting flow in the ducted rocket combustor. It is well-suited for turbulent diffusion flames where the combustion is controlled by turbulent mixing rather than the kinetics of the chemical reactions, and the fuel and air inlet streams are separate. One of the main advantages of the PDF model over other combustion models is that regardless of how many species are included, in this case thirteen, for a problem with a single air and a single fuel stream (onestream PDF) only two additional transport equations have to be solved. Below a rich limit, the air/fuel mixture is assumed to be at equilibrium at any point within the combustor, and the turbulence/chemistry interaction is also taken into account.

A parametric study was carried out to determine the consequences of any errors in the estimates of the boundary conditions or how the combustor was modelled. No significant effects were seen when heat transfer from the walls, radiation, temperature-dependent transport properties, or a doubled turbulence length scale were included in the CFD model. Refining the grid, using the RSM turbulence model, using second order discretization, or applying a 10% variation in fuel (gas generator exhaust) temperature, ethylene mass flow rate, or air mass flow rate all had effects of less than 7%. Using the k-ε turbulence model changed the combustion efficiency at 458 mm by 17%, but this turbulence model does not perform well in this type of flow. However, none of the changes in the parameters studied had as much influence as the 25% change in $\eta_{\Delta \mathrm{T}}$ from varying the turbulence intensity from 1% to 20%. Further calculations on two other configurations, though, revealed that the effect of changing turbulence intensity could vary with each configuration.

Next, the onestream PDF model was used to model the direct-connect combustors using boundary conditions calculated with data from the actual experiments.

The results have shown that for combustion problems, considering only the fuel distribution on the centreline plane can be misleading, and that the three-dimensional temperature field should also be examined to decide which configurations may yield superior performance. Since so many parameters can change between configurations despite changing only one feature, general conclusions as to what should be changed to optimize a configuration are difficult to make. The wide range of fuel distributions and temperature fields seen in these results has revealed that each configuration should be modelled to estimate its performance, rather than simply extrapolating from other results.

When compared to the direct-connect experiments, the onestream PDF model tended to overestimate the combustion efficiency. A likely cause of this was that all of the gas generator exhaust, including both the gaseous and solid phases, was injected into the combustor as a single homogeneous stream and assumed to react instantaneously once there was any oxidizer present. To improve the predictions, a twostream PDF model, with separate gaseous and solid phase streams, was used. Based on experiments carried out to characterize the gas generator exhaust, the solid stream was assumed to consist of 75 nm diameter carbon spheres which gradually decomposed into carbon monoxide, controlled mainly by surface oxidation, as they flowed through the combustor. Graphs of the temperature distribution on the centreline plane were compared with the onestream PDF results and they showed that the carbon particles, because of their mass, could convect fuel to areas that would otherwise be much leaner and, depending on the configuration, noticeably change the temperature field. Predictions with the twostream PDF model improved significantly to an average difference of 16% with the experimental results, or about the same as the experimental uncertainty. For the onestream PDF model, this difference was 27%. A rigorous non-parametric statistical analysis was also carried out and a proposed measure of model adequacy showed that the twostream PDF model can explain 98% of the variability in predicting the experimental results. Therefore, for the configurations described herein, the twostream PDF model can predict, within a good degree of accuracy, the performance of a ducted rocket combustor.

Chapter 7

CONCLUSIONS AND RECOMMENDATIONS

7.1 Conclusions

Limited resources meant that only one type of gas generator fuel and one size of combustor (100 mm diameter) were used to generate experimental data from the direct-connect tests. As such, some aspects of the CFD-based performance prediction method, particularly the model for decomposition of solid carbon particles, are not generally applicable to all ducted rocket combustors. However, the methodology used toward the development of this model is certainly relevant to the development of prediction methods for ducted rocket combustors in general, and also demonstrates how the applicability of the experimental results and predictions can be extended.

7.1.1 Similarity and the Dimensionless Parameters

Five of the ten dimensionless parameters important for reacting flow in combustors were identified as relevant to ducted rockets with unchoked, subsonic fuel jets. Along with dimensionally-accurate models of combustor geometry, the air/fuel momentum ratio and the inlet turbulence parameters, these five dimensionless parameters must be applied to ensure that geometric, dynamic, thermal, and compositional similarity will be respected as closely as possible. They are Damköhler's first dimensionless ratio, Damköhler's third dimensionless ratio, the Reynolds number, the Prandtl number, and the ratio of specific heats. The Mach number and the ratio of kinetic energy to internal energy must be added in the case of a choked fuel jet with supersonic flow.

7.1.2 Water Tunnel Results

The water tunnel proved to be an excellent tool to qualitatively visualize the flow in a model ducted rocket combustor. Two basic flow features were frequently observed, one being a pair of longitudinal vortices that corkscrew from the air inlet section toward the nozzle, and the other being a recirculation zone in the dome region. The water tunnel also revealed that all configurations demonstrated time-dependent flow, and in particular large-scale fluctuations resulting from an interaction of the air and fuel jets. No evidence of Reynolds number dependency was seen for the fuel distribution in the water tunnel experiments.

7.1.3 Non-reacting Flow Results

Non-reacting flow CFD modelling, using the FLUENT code with the RNG turbulence model, was carried out on the same configurations as tested in the water tunnel. Areas of high fuel concentration from the water tunnel images corresponded well with those in the CFD plots. With the time-dependency of the water tunnel flowfields taken into account, there was no evidence to discount the accuracy of the CFD modelling.

CFD predictions were also carried out for the same geometry and air/fuel momentum ratio but with boundary conditions for gas generator exhaust and vitiated air rather than water. Only very minor differences in fuel distribution and normalized velocity profiles resulted between the predictions for the water tunnel and actual air/fuel flowfields. The air/fuel momentum ratio is therefore the correct parameter to specify the relative amounts of the inlet flows, and the flowfields seen at the lower Reynolds numbers in the water tunnel should be representative of the flowfields in an actual combustor, in the absence of combustion.

7.1.4 Direct-connect Experiments

The modifications to existing ducted rocket hardware at the TNO-PML direct-connect combustion test facility allowed the characterization of the boundary conditions, of critical importance to the CFD modelling, to be done with more confidence. The combustion efficiency based on temperature rise in the combustor was the best output parameter to compare with the CFD results since it takes into account the performance of only the combustor. A comprehensive assessment estimated the average experimental uncertainty of the combustion efficiency to be 13%.

The existence of time-dependent processes in the experimental direct-connect combustors were confirmed with the measurement of significant pressure oscillations. There is a strong possibility that they are coupled to the combustion processes taking place. These pressure oscillations may influence combustor performance and must be kept in mind for the reacting flow CFD modelling predictions.

7.1.5 Reacting Flow Results

An equilibrium-chemistry Probability Density Function approach was used to model the reacting flow in the ducted rocket combustor since it could properly account for many of the important phenomena, including the turbulence/chemistry interaction and a large number of chemical species, while being computationally efficient. Two variations of the PDF model were used, the first termed "onestream" for which the fuel was treated as a single stream, and the second termed "twostream" for which the fuel was divided into separate gaseous and solid streams.

With the onestream model, a parametric study revealed that changing the value of the turbulence intensity to 1% or 20% from 10% had a profound effect on the predicted combustion efficiency. Lesser effects occurred with the choice of the k-ε or RSM turbulence models, refining the grid, using second order discretization, or applying 10% variations in the fuel temperature, ethylene mass flow rate, or air mass flow rate. No significant effects were seen when heat transfer from the walls, radiation, temperature-dependent transport properties, or a doubled turbulence length scale were included in the CFD model. Further calculations on two other configurations, though, revealed that the effect of changing turbulence intensity could vary with each configuration.

The onestream PDF model was also used to model the direct-connect combustors using boundary conditions calculated with data from the actual experiments. The output revealed that considering only the fuel distribution on the centreline plane can be a misleading indication of combustor performance, and that graphs of three-dimensional temperature fields should also be examined. General conclusions as to what should be changed to optimize a configuration are difficult to make because changing one input parameter often alters several others. The wide range of fuel distributions and temperature fields seen in these results has therefore revealed that each configuration should be modelled to estimate its performance, rather than simply extrapolating from other results.

When compared to the direct-connect experiments, the onestream PDF model tended to overestimate the combustion efficiency, with an average difference of 27%. To improve the predictions, a twostream PDF model, with separate gaseous and solid phase streams, was used. Based on characterization of the gas generator exhaust, the solid stream was injected as 75 nm diameter carbon spheres that decomposed into carbon monoxide due to surface oxidation. Because of their mass, these particles could convect fuel to areas in the combustor that would otherwise be much leaner. The twostream PDF model improved the predictions significantly, with an average difference of 16% with the experimental results, or nearly the same as the experimental uncertainty. A rigorous non-parametric statistical analysis was also carried out and a proposed measure of model adequacy showed that the twostream PDF model can explain 98% of the variability in predicting the experimental results.

Based on this, for the configurations described herein, the twostream PDF model can predict, within a good degree of accuracy, the performance of a ducted rocket combustor.

7.2 Summary of Contributions

Through a careful examination of the governing equations and experimental measurements, a method based on CFD was developed to predict the performance of a ducted rocket combustor. Along with a twostream PDF approach, it uses a two-phase flow and carbon decomposition model that properly accounts for all the components in the gas generator exhaust, including the solid particles, on the combustion. Most importantly, this method has also been validated over a wide range of geometries and test conditions. In particular, the significant contributions that improve the current understanding of combustion in a ducted rocket are:

- Application and validation of a twostream PDF combustion model, a two-phase flow model, and a particle decomposition model for a solid fuel ducted rocket combustor.

- Identification of the dimensionless parameters and other factors important to respecting geometric, dynamic, thermal, and compositional similarity for modelling ducted rocket combustors.

- Characterization of the gas generator exhaust to provide data on how the solid particles should be modelled.

- Comprehensive assessment of experimental uncertainty for the direct-connect experiments and a thorough description of how combustion efficiency was calculated.

- Properly-instrumented high-frequency pressure measurements taken during direct-connect experiments that confirm the presence of significant oscillations that are likely coupled to the combustion.

- Investigation of the flow and combustion in a wide range of ducted rocket configurations using a water tunnel, non-reacting and reacting flow CFD, and direct-connect combustion experiments.

This work has been presented and defended in several fora. A list of publications and three of the most significant papers are included in Appendix E.

7.3 Recommendations for Future Work

To improve the current understanding of combustion in a ducted rocket even further, the following recommendations are made:

- As inputs to a CFD model, the characterization of the inlet boundary conditions, particularly the inlet turbulence intensities and the gas generator exhaust, should be improved.

- The experimental uncertainty of direct-connect combustor experiments should be reduced.

- While not necessary for the ducted rocket configurations investigated for this thesis, CFD models that take into account compressible flow, while at the same time using as sophisticated combustion model as the PDF model, should be developed since, in general, ducted rockets have compressible, supersonic fuel jets.

- PD-scaling for ducted rockets should be validated with experiments on combustors of different diameters.

- Now that it exists and has been extensively validated over a wide range of geometries and test conditions, this methodology should be used to help design a high-efficiency ducted rocket combustor.

Bibliography

[1] Needham, J., "Gunpowder as the Fourth Power, East and West", Hong Kong University Press, Hong Kong, 1985.

[2] Hill, P.G. and Peterson, C.R., *Mechanics and Thermodynamics of Propulsion*, Second Edition, Addison-Wesley Publishing Company, Reading, Massachusetts, U.S., 1992.

[3] Wittenberg, H., "Some Fundamentals on the Performance of Ramjets with Subsonic and Supersonic Combustion", Delft University Press, Delft, The Netherlands, 2000.

[4] Spalding, D.B., "The Art of Partial Modeling", in *Ninth Symposium on Combustion*, pp 833-843, Academic Press, London, U.K., 1963.

[5] Stewart, D.G., "Scaling of Gas Turbine Combustion Systems", in *Selected Combustion Problems - II: Transport Phenomena; Ignition, Altitude Behaviour and Scaling of Aeroengines*, pp 384-413, Butterworths Scientific Publications, London, U.K., 1956.

[6] Lefebvre, A.H., and Halls, G.A., "Some Experiences in Combustion Scaling", in *Advanced Aeroengine Testing*, pp 177-204, Pergamon Press, London, U.K., 1959.

[7] Stewart, D.G. and Quigg, G.C., "Similarity and Scale Effects in Ramjet Combustors", in *Ninth Symposium on Combustion*, pp 907-922, Academic Press, London, U.K., 1963.

[8] Hottel, H.C., Williams, G.C., Jensen, W.P., Tobey, A.C., and Burrage, P.M.R., "Modeling Studies of Baffle-Type Combustors", in *Ninth Symposium on Combustion*, pp 923-935, Academic Press, London, U.K., 1963.

[9] Stull, F.D., Craig, R.R., and Hojnacki, J.T., "Dump Combustor Parametric Investigation", Air Force Aero Propulsion Laboratory Report AFAPL-TR-74-90, Wright Patterson AFB, Ohio, U.S., November 1974.

[10] Ben-Arosh, R. and Gany, A., "Similarity and Scale Effects in Solid-Fuel Ramjet Combustors", Journal of Propulsion and Power, Vol. 8, No. 3, pp 615-623, May-June 1992.

[11] Pulsonetti, M.V. and Stalker, R.J., "Scaling in a Scramjet Combustor", Queensland University, Saint Lucia, Australia, January 1995.

[12] Rosner, D.E., *Transport Processes in Chemically Reacting Flow Systems*, Chapter 7, Butterworths Publishers, Stoneham, Massachusetts, U.S., 1986.

[13] Streeter, V.L. and Wylie, E.B., *Fluid Mechanics*, Seventh Edition, pp 156-181, McGraw-Hill, New York, U.S., 1979.

[14] Weller, A.E., "Similarities in Combustion, A Review", in *Selected Combustion Problems - II: Transport Phenomena; Ignition, Altitude Behaviour and Scaling of Aeroengines*, pp 371-383, Butterworths Scientific Publications, London, U.K., 1956.

[15] Damköhler, G., "Einflüsse der Strömung, Diffusion und des Wärmeüberganges auf die Leistung von Reaktionsöfen", Z. Elektrochem., Vol. 42, pp 846-862, 1936.

[16] Penner, S.S., "Similarity Analysis For Chemical Reactors and the Scaling of Liquid Fuel Rocket Engines", in *Combustion Researches and Reviews*, 1955, pp 140-162, Butterworths Scientific Publications, London, U.K., 1955.

[17] Way, S., "Combustion in the Turbojet Engine", in *Selected Combustion Problems - II: Transport Phenomena; Ignition, Altitude Behaviour and Scaling of Aeroengines*, pp 296-327, Butterworths Scientific Publications, London, U.K., 1956.

[18] von Kármán, T., Sorbonne Lectures, Paris, France, 1952-1953.

[19] Kuo, K.K., *Principles of Combustion*, John Wiley and Sons, Toronto, Canada, 1986.

[20] Schlichting, H., *Boundary Layer Theory*, Seventh Edition, Chap. III, McGraw-Hill, New York, U.S., 1979.

[21] Hebrard, P., Lavergne, G., Torgue, A., Bismes, F., and Heid, G. "Prédiction des Performances en Combustion de Stato-réacteurs et Stato-fusées par Expérimentations Isothermes et Modélisations", Paper No. 37, *Airbreathing Propulsion for Missiles and Projectiles*, AGARD-CP-526, 79th AGARD PEP Symposium, Villepreux, France, 1992.

[22] Brophy, C.M. and Hawk, C.W., "A Flow Visualization Facility for Ducted Rocket Engine Mixing Studies", AIAA paper AIAA-95-2934, AIAA/ASME/SAE/ASEE 31st Joint Propulsion Conference, San Diego, California, U.S., 10-12 July 1995.

[23] Zetterström, K-A., Sjöblom, B., and Jarnmo, A., "Solid Ducted Rocket Engine Combustor Tests", ISABE paper 83-7001, 6th International Symposium on Air Breathing Engines, Paris, France, 1983.

[24] Stowe, R.A., De Champlain, A., Mayer, A.E.H.J., and Niemeijer, S.F., "Modelling and Flow Visualization of Mixing in a Ducted Rocket Combustor", AIAA paper AIAA-98-3768, AIAA/ASME/SAE/ASEE 34th Joint Propulsion Conference, Cleveland, Ohio, U.S., 13-15 July 1998.

[25] Clark, W.H., "Experimental Investigation of Pressure Oscillations in a Side Dump Ramjet Combustor", Journal of Spacecraft and Rockets, Vol. 19, No. 1, pp 47-53, January-February 1982.

[26] Choudhury, P.R., "Characteristics of a Side Dump Gas Generator Ramjet", AIAA paper AIAA-82-1258, AIAA/SAE/ASME 18th Joint Propulsion Conference, Cleveland, Ohio, U.S., 21-23 June 1982.

[27] Stull, F.D., Craig, R.R., Streby, G.D., and Vanka, S.P., "Investigation of a Dual Inlet Side Dump Combustor Using Liquid Fuel Injection", AIAA paper AIAA-83-0420, AIAA 21st Aerospace Sciences Meeting, Reno, Nevada, U.S., 10-13 January 1983.

[28] Vanka, S.P., Craig, R.R., and Stull, F.D., "Mixing, Chemical Reaction, and Flowfield Development in Ducted Rockets", Journal of Propulsion and Power, Vol. 2, No. 4, pp 331-338, July-August 1986.

[29] Liou, T-M. and Wu, S-M., "Flowfield in a Dual-Inlet Side-Dump Combustor", Journal of Propulsion and Power, Vol. 4, No. 1, pp 53-60, January-February 1988.

[30] Hwang, Y.H. and Hung, Y.H., "Turbulent transport phenomena in three-dimensional side-dump ramjet combustors", International Journal of Heat and Mass Transfer, Vol. 32, No. 11, pp 2113-2125, 1989.

[31] Yen, R-H. and Ko, T-H., "Effects of Side-Inlet Angle in a Three-Dimensional Side-Dump Combustor", Journal of Propulsion and Power, Vol. 9, No. 5, pp 686-693, September-October 1993.

[32] Chuang, C.L., Cherng, D.L., Hsieh, W.H., Settles, G.S., and Kuo, K.K., "Study of Flowfield Structure in a Simulated Solid-Propellant Ducted Rocket Motor", AIAA paper AIAA-89-0011, AIAA 27th Aerospace Sciences Meeting, Reno, Nevada, U.S., 9-12 January 1989.

[33] Hsieh, W.H., Chuang, C.L., Yang, A.S., Cherng, D.L., Yang, V., and Kuo, K.K., "Measurement of Flowfield in a Simulated Ducted Rocket Combustor Using Laser Doppler Velocimetry", AIAA paper AIAA-89-2789, AIAA/ASME/SAE/ASEE 25th Joint Propulsion Conference, Monterey, California, U.S., 10-13 July 1989.

[34] Aoki, S., Sakata, K, Sato, T., Horiuchi, Y., and Kubota, K., "Experimental Investigation of Side Dump Type Combustors For Integral Rocket Ramjets", ISABE paper 91-7110, 10th International Symposium on Air Breathing Engines, Nottingham, U.K., 1991.

[35] Dijkstra, F., Mayer, A.E.H.J., Smith, R.A., Wilson, K.J., and Schadow, K.C., "Ducted Rocket Combustion Experiments at Low Gas Generator Combustion Temperatures", AIAA paper AIAA-95-2415, AIAA/ASME/SAE/ASEE 31st Joint Propulsion Conference, San Diego, California, U.S., 10-12 July 1995.

[36] Ristori, A., Heid, G., Cochet, A., and Lavergne, G., "Experimental and Numerical Study of Turbulent Flow Inside a Dual Inlet Research Ducted Rocket Combustor", ISABE paper 99-7182, 14th International Symposium on Air Breathing Engines, Florence, Italy, 1999.

[37] Schadow, K.C., "Boron Combustion Characteristics in Ducted Rockets", Combustion Science and Technology, Vol. 5, pp 107-117, 1972.

[38] Tsujikado, N., "An Experimental Study on Configuration of a Secondary Combustion Chamber for a Ram-Rocket", ISABE paper 83-7000, 6th International Symposium of Air Breathing Engines, Paris, France, 1983.

[39] Tsujikado, N., Kashikawa, I., Harada, T., and Dohke, K., "Static Firing Tests of Experimental Ram-Rocket with Highly Boron Loaded Solid Propellant Type Fuels", ISABE paper 87-7028, 8th International Symposium on Air Breathing Engines, Cincinnati, Ohio, U.S., 1987.

[40] Vigot, C., Cochet, A., and Guin, C., "Combustion Behaviour of Boron-Based Solid Propellants in a Ducted Rocket", in *Combustion of Boron-based Solid Propellants and Fuels*, pp 386-401, CRC Press, Boca Raton, Florida, U.S., 1993.

[41] Besser, H-L., "Development Testing of Throttleable Ducted Rockets", Paper No.6 in *Airbreathing Propulsion for Missiles and Projectiles*, AGARD-CP-526, 79th AGARD PEP Symposium, Villepreux, France, 1992.

[42] Besser, H-L. and Strecker, R., "Overview of Boron Ducted Rocket Development During the Last Two Decades", in *Combustion of Boron-based Solid Propellants and Fuels*, pp 133-178, CRC Press, Boca Raton, Florida, U.S., 1993.

[43] *FLUENT User's Guide, Version 4.2*, Fluent Inc., Lebanon, N.H., U.S., 1993.

[44] Wilcox, D.C., *Turbulence Modeling for CFD*, KNI Inc., Anaheim, California, U.S., 1998.

[45] Patankar, S.V., *Numerical Heat Transfer and Fluid Flow*, Hemisphere Publishing Company, Washington, D.C., U.S., 1980.

[46] *FLUENT 5 User's Guide*, Fluent Inc., Lebanon, New Hampshire, U.S., July 1998.

[47] Dijkstra, F. and Wijchers, T., "Experimental Facilities for Solid Fuel Combustion Research", Proceedings of the Symposium on High Speed Airbreathing

Propulsion: The Solid Fuel Combustion Chamber and Beyond, Delft University of Technology, The Netherlands, 7 June 1991.

[48] Mayer, A.E.H.J. and Korting, P.A.O.G., "Effect of Vitiated Air on Ramjet Performance", Technical Report 1991-66, TNO Prins Maurits Laboratory, The Netherlands, 1991.

[49] Mayer, A.E.H.J. and Stowe, R.A., "Results of the IRRDP Ducted Rocket Combustor Experiments", Integral Rocket Ramjet Demonstration Program Report IRRDP-TNO-TRP-0101 (1), TNO Prins Maurits Laboratory, The Netherlands, 2001.

[50] Dijkstra, F., "Description and Operation of a Scale Ducted Rocket Test Facility", Technical Report IRR TF TS 01 01 002(1), TNO Prins Maurits Laboratory, The Netherlands, 4 January 1993.

[51] Dijkstra, F., "Conceptual Design of a Ducted Rocket Combustor", Thesis A2R-P21, Delft University of Technology, Faculty of Aerospace Engineering, The Netherlands, 23 July 1993.

[52] Advisory Group for Aerospace Research and Development, "Experimental and Analytical Methods for the Determination of Connected-Pipe Ramjet and Ducted Rocket Internal Performance", AGARD Report AGARD-AR-323, Propulsion and Energetics Panel Working Group 22, 1994.

[53] McBride, B.J., "CET89 – Chemical Equilibrium with Transport Properties", NASA Lewis Research Center, Cleveland, Ohio, U.S., 1989.

[54] Nuhn, L.P.W., "Evaluatie van de TNO-PML/FAE-Dut Testfacility Een vaste Brandstof Verbrandingskamer met by-pass als uitvoeringsvorm", Thesis EA2-P14, Delft University of Technology, The Netherlands, October 1991.

[55] Mayer, A.E.H.J., "Effect van metaaltoevoegingen op de brandstofprestaties van HTPB", Thesis EA2-P16, Delft University of Technology, The Netherlands, August 1992.

[56] Kline, S.J. and McClintock, F.A., "Describing Uncertainties in Single-Sample Experiments", Mechanical Engineering, Vol. 75, pp 3-8, January 1953.

[57] Holman, J.P., *Experimental Methods for Engineers*, Chapter 3, Fourth Edition, McGraw-Hill Book Company, New York, U.S., 1984.

[58] Blevins, J.A. and Coleman, H.W., "Uncertainty Assessment of Ramjet Performance Determination in Connected-Pipe Testing", AIAA paper AIAA-95-3074, AIAA/ASME/SAE/ASEE 31st Joint Propulsion Conference, San Diego, California, U.S., 10-12 July 1995.

[59] Stowe, R.A., De Champlain, A., and Mayer, A.E.H.J., "Modelling Combustor Performance of a Ducted Rocket", AIAA paper AIAA-2000-3728, AIAA/ASME/SAE/ASEE 36th Joint Propulsion Conference, Huntsville, Alabama, U.S., 17-19 July 2000.

[60] Stowe, R.A., Dubois, C., Harris, P.G., Mayer, A.E.H.J., De Champlain, A., and Ringuette, S., "Two Phase Flow Combustion Modelling of a Ducted Rocket", AIAA paper AIAA-2001-3461, accepted for the AIAA/ASME/SAE/ASEE 37th Joint Propulsion Conference, Salt Lake City, Utah, U.S., 8-11 July 2001.

[61] Chen, L. and Tao, C.C., "Study on the Side-Inlet Dump Combustor of Solid Ducted Rocket with Reacting Flow", AIAA paper AIAA-84-1378, AIAA/ASME/SAE 20th Joint Propulsion Conference, Cincinnati, Ohio, U.S., 11-13 June 1984.

[62] Schadow, K.C., "Experimental Investigation of Boron Combustion in Air-Augmented Rockets", AIAA Journal, Vol. 7, No. 10, pp 1870-1876, October 1969.

[63] Wu, P.K., Chen, M.H., Chen, T.H., and Nejad, A.S., "Flowfields in a Side-Inlet Ducted Ramrocket with/without Swirler", AIAA paper AIAA-95-2478, AIAA/ASME/SAE/ASEE 31st Joint Propulsion Conference, San Diego, California, U.S., 10-12 July 1995.

[64] Liou, T.M., Hwang, Y.H. and Hung, Y.H., "Computational Study of Flow Field in Side Inlet Ramjet Combustors", AIAA paper AIAA-88-3010, AIAA/ASME/SAE/ASEE 24th Joint Propulsion Conference, Boston, Massachusetts, U.S., 11-14 July 1988.

[65] Liou, T.M. and Hwang, Y.H., "Calculation of Flowfields in Side-Inlet Ramjet Combustors with an Algebraic Reynolds Stress Model", Journal of Propulsion and Power, Vol. 5, No. 6, November-December 1989.

[66] Cherng, D.L., Yang, V., and Kuo, K.K., "Numerical Study of Turbulent Reaction Flows in Solid-Propellant Ducted Rocket Combustors", Journal of Propulsion and Power, Vol. 5, No. 6, pp 678-685, November-December 1989.

[67] Onn, S.C., Chiang, H.J., Hwang, H.C., Wei, J.K., and Cherng, D.L., "Optimization of Operation Conditions and Configurations for Solid-Propellant Ducted Rocket Combustors", AIAA paper AIAA-93-1855, AIAA/SAE/ASME/ASEE 29th Joint Propulsion Conference, Monterey, California, U.S., 28-30 June 1993.

[68] Yoon, W.S. and Chung, T.J., "Numerical Simulations of Airbreathing Combustion at All Speed Regimes", AIAA paper AIAA-93-1972, AIAA/SAE/ASME/ASEE 29th Joint Propulsion Conference, Monterey, California, U.S., 28-30 June 1993.

[69] Hsieh, S.Y., Yang, V., Cherng, D.L., and Yang, H.T., "A Unified Flow Analysis of Ramjet Propulsion Systems", AIAA paper AIAA-94-3326, AIAA/ASME/SAE/ASEE 30th Joint Propulsion Conference, Indianapolis, Indiana, U.S., 27-29 June 1994.

[70] Withington, J.P., Shuen, J.S., and Yang, V., "A Time Accurate Implicit Method for Chemically Reacting Flows at All Mach Numbers", AIAA paper AIAA-91-0581, AIAA/ASME/SAE/ASEE 27th Joint Propulsion Conference, Sacramento, California, U.S., 24-26 June 1991.

[71] Chao, Y.C., Chou, W.F., and Liu, S.S., "Computation of Turbulent Reacting Flow in a Solid-Propellant Ducted Rocket", Journal of Propulsion and Power, Vol. 11, No. 3, May-June 1995.

[72] Montazel, X., Samaniego, J.M., Lacas, F., Poinsot, T., and Candel, S., "Turbulent Combustion Modelling in a Side Dump Ramjet Combustor", AIAA paper AIAA-92-3599, AIAA/ASME/SAE/ASEE 28th Joint Propulsion Conference, Nashville, Tennessee, U.S., 6-8 July 1992.

[73] Dufour, E. and Montazel, X., “Numerical Simulation of Direct Connect Liquid- Fueled Ramjet Tests”, AIAA paper AIAA-98-3769, AIAA/SAE/ASME/ASEE 34th Joint Propulsion Conference, Cleveland, Ohio, U.S., 12-15 July 1998.

[74] Craig, R.R., Drewry, J.D., and Stull, F.D., “Coaxial Dump Combustor Investigation”, AIAA paper AIAA-78-1107, AIAA/SAE 14th Joint Propulsion Conference, Las Vegas, Nevada, U.S., 25-27 July 1978.

[75] Liou, T-M., Chen, L., and Wu, S-M., “Effects of momentum ratio on turbulent non-reacting and reacting flows in a ducted rocket combustor”, International Journal of Heat and Mass Transfer, Vol. 36, No. 10, pp 2589-2599, July 1993.

[76] Beasley, J.H. and Ivey, M.S., “CFD Modelling of a Ramrocket Combustor”, 22nd Meeting of The Technical Cooperation Program, Technical Panel WTP-4, Energetic Materials and Propulsion Technology Workshop, U.K., 14-18 April 1997.

[77] Beasley, J.H. and Ivey, M.S., “Some Results from Flow Modelling of a Ramrocket Combustor”, 20th Meeting of The Technical Cooperation Program, Technical Panel WTP-4, Propulsion Technology Workshop, U.S., 24 April to 02 May 1995.

[78] Zhang, W., Fang, D.Y., and Xia, Z.X., “Numerical Study of Turbulent Flows in Unchoked Solid Ducted Rocket Combustor”, AIAA paper AIAA-2000-3729, AIAA/ASME/SAE/ASEE 36th Joint Propulsion Conference, Huntsville, Alabama, U.S., 17-19 July 2000.

[79] Jones, W.P. and Whitelaw, J.H., “Calculation Methods for Reacting Turbulent Flows: A Review”, Combustion and Flame, Vol. 48, pp 1-26, 1982.

[80] Liou, T.M. and Liao, C.C., “Flows in a Curved Combustor Inlet With and Without a Guide Vane”, Journal of Propulsion and Power, Vol. 11, No. 3, May-June 1995.

[81] Stowe, R.A., Dubois, C., Smithson, T., and De Champlain, A., ”Preliminary Exhaust Characterization of a GAP/Carbon Ducted Rocket Fuel”, 24th Meeting of The Technical Cooperation Program, Technical Panel WPN/TP-4 Workshop, NSWC, Indian Head, Maryland, U.S., 15-16 April 1999.

[82] Faeth, G.M. and Köylü, Ü.Ö., "Soot Morphology and Optical Properties in Nonpremixed Turbulent Flame Environments", Combustion Science and Technology, Vol. 108, pp. 207-229, 1995.

[83] Morsi, S.A. and Alexander, A.J., "An Investigation of Particle Trajectories in Two-Phase Flow Systems", Journal of Fluid Mechanics, Vol. 55, No. 2, pp. 193-208, 1972.

[84] Field, M.A., "Rate of Combustion of Size-Graded Fractions of Char from a Low Rank Coal between 1200K - 2000K", Combustion and Flame, Vol. 13, pp. 237-252, 1969.

[85] Glassman, I., *Combustion*, Second Edition, Academic Press, Orlando, Florida, U.S., 1987.

[86] Nagel, J., Strickland-Constable, R.F., "Oxidation of Carbon Between 1000-2000°C", Proceedings of the Fifth Conference on Carbon, London, U.K., 1962.

[87] Margetson, J. and Stowe, R.A., "Analysis of Experimental Observations and Theoretical Predictions for a Ducted Rocket Application Using Non-parametric Error Diagnostic Procedures", DREV Technical Note, to be published 2001.

[88] Walpole, R.E. and Myres, R.H., *Probability and Statistics for Engineers and Scientists*, Macmillan Publishing Company, New York, U.S., 1993.

Appendix A

"PD-SCALING" OF COMBUSTORS

Preserving the most relevant of the dimensionless parameters, already presented in Chapter 2, between subscale and full-size gas turbine combustors has often been attempted using what is known as "PD-scaling", "P" being the static pressure in the combustor and "D" being a representative linear dimension such as the diameter. For this technique, geometric similarity and inlet temperatures, flow velocities, fuel properties, and air/fuel ratio must be maintained between the model and the full-size combustor. Then only the static pressure is changed in inverse proportion to the linear scale [5]:

$$p_{\mathrm{m}} d_{\mathrm{m}} = p_{\mathrm{p}} d_{\mathrm{p}} \tag{A.1}$$

This means that a half-scale combustor should be operated at twice the pressure in order to approach dynamic, thermal, and compositional similarity. For gas turbines, however, there are three main factors that can limit the success of PD-scaling. The first is that scaling the fuel injection is quite difficult since the dimensions of the injector cannot be scaled linearly with the rest of the combustor if the spray pattern, momentum, and atomization are to be scaled correctly to yield the right fuel distribution in the combustor [5, 17]. The second factor is that heat losses, if significant compared to the heat generated by the combustion, do not scale linearly in the combustor. While the convective processes inside the combustor can be scaled correctly [5], neither convective processes outside the combustor (such as external aerodynamic heating) nor radiative processes can [8].

The third factor deals with the overall order of the chemical reactions in the combustor. In terms of the progress of reaction ε, the rate of reaction is [19]:

$$\frac{\partial \varepsilon}{\partial t} \propto A e^{\frac{-E_\mathrm{a}}{RT}} \varepsilon^n p^{n-1} \tag{A.2}$$

which shows that the reaction rate has a pressure dependence of $n-1$ where n is the reaction order. From the laminar flame theory of Mallard and Le Chatelier as described in [19], the laminar flame speed can be expressed as:

$$S_\mathrm{L} = \sqrt{\left(\frac{k}{\rho c_p}\right) \frac{T_\mathrm{f} - T_\mathrm{ign}}{T_\mathrm{ign} - T_\mathrm{u}} \left(\frac{\partial \varepsilon}{\partial t}\right)} \propto \sqrt{\frac{1}{\rho} p^{n-1}} \propto \sqrt{p^{n-2}} \tag{A.3}$$

assuming that the temperatures are constant and the thermal conductivity and specific heats are functions of temperature only. The temperatures T_u, T_ign, and T_f denote the temperature of the unreacted mixture, the ignition temperature, and the flame temperature of the fully reacted mixture respectively. Since most chemical reactions are classified as second order (and therefore their reaction rates are directly proportional to pressure) the laminar flame speed for a system whose overall reaction order is 2 will not show any pressure dependence. As for turbulent flame speed, which is more relevant to combustors in which turbulent flow dominates, correlations of turbulent flame speed with laminar flame speed [6] show that turbulent flame speed is a function of the laminar flame speed and either the Reynolds number or the turbulent flow velocities. In a PD-scaled system with velocities and Reynolds number constant, turbulent and laminar flame velocities will therefore be constant and similarity will be respected for an overall reaction order of 2. Unfortunately, for the combustion of many hydrocarbon fuels the reaction schemes are very complex and include reactions that are not second order. Lefebvre and Halls [6] also noted that in practical combustion systems the *true* reaction order may be influenced by Reynolds number effects to yield an *apparent* reaction order. The apparent reaction scheme is therefore often not second order, but somewhat less, typically 1.3 to 1.6 [12]. In these cases, flame speeds will decrease with increasing pressure.

For gas turbine combustors, Lefebvre and Halls [6] reported that when aerodynamic, chemical, and fuel spray scaling requirements have been respected, PD-scaling as proposed by Stewart [5] had resulted in excellent similarity between model and prototype (full-size) combustors. They also said that the consequences of not maintaining geometric similarity of the fuel injector are probably minor since modern fuel injectors are designed to give adequate fuel atomization and distribution over a wide range of operating conditions. As for heat transfer, Stewart [5] stated that convective processes are much more important than radiative processes, especially when distillate fuels are used. Since convective processes inside the combustion chamber scale correctly for PD-scaling, neglecting radiation should have a minor effect on the success of the results. The factor concerning apparent reaction order may be of more consequence, but this can be treated as follows. Way [17] proposed the following scaling scheme to take into account the pressure dependence of reaction orders (n) other than 2:

$$\frac{p_{\mathrm{m}}^{n-1} d_{\mathrm{m}}}{v_{\mathrm{m}}} = \frac{p_{\mathrm{p}}^{n-1} d_{\mathrm{p}}}{v_{\mathrm{p}}} \tag{A.4}$$

which reduces to PD-scaling for second order reactions and the same flow velocities in the model and the prototype. He also showed that the inverse of the quantity in the scaling scheme is proportional to the *loading intensity* (which is also the inverse of Damköhler's first dimensionless ratio):

$$\left(\frac{p^{n-1}d}{v}\right)^{-1} = \frac{v}{p^{n-1}d} = \frac{vpd^2}{d^3p^n} \propto \frac{\mathit{energy\ input}}{\mathit{unit\ time} \cdot \mathit{unit\ volume} \cdot \mathit{pressure}^n} \propto Dam^{-1} \tag{A.5}$$

and that combustor efficiency can be correlated with this and the Reynolds number. Building on this, Lefebvre and Halls [6] assume that n is actually the true reaction order (not the apparent one) but that it is combined with a factor a which is related to the Reynolds number. This yields a pressure dependence of $0.5n/(1-a)$ so the correlating group for $n = 2$ is:

$$\frac{(pd)^{\frac{a}{1-a}}}{v} \tag{A.6}$$

This means that even if the effects of having an apparent reaction order other than 2 are significant, PD-scaling can still be applied as long as the performance data are correlated using the above group. Based on reported past experience, PD-scaling can be successfully applied to gas turbine combustors even if similarity for the fuel injectors, heat transfer, and apparent reaction order is not strictly respected.

In the case of afterburners and liquid fuel ramjets (LFRJ), both of which are mechanically simpler than gas turbine combustors, Lefebvre and Halls [6] concluded that PD-scaling has proven highly successful. For afterburners, they found that smaller model combustors always run with cooler metal temperatures because the overall heat transfer, particularly radiation, is not scaled correctly with PD-scaling.

Stewart and Quig [7] confirmed the successful application of PD-scaling to LFRJ's and also showed that suspected problems due to fuel distribution had only minor effects on combustor performance. Hottel *et al.* [8] also studied scaling in LRFJ's and recommended that scaling can be based on the loading intensity (inverse of Damköhler's first dimensionless ratio) with a reaction order $n = 2$ as long as the Reynolds number based on the combustor diameter is greater than 24 000. However, they found that for this to be successful, factors such as heat losses through the burner walls, turbulence variations due to very low pressure operation (less than 0.02 MPa), and acoustic instabilities, all of which can affect the apparent reaction order but do not scale correctly with PD-scaling, must have little consequence. Stull *et al.* [9] performed a scaling study on liquid fuel ramjet dump-type combustors with different diameters and found that with $PD = constant$, similar combustion efficiencies were obtained except for the cases where heat losses were significant. Solid fuel ramjets (SFRJ) have also been the object of a scaling study. Ben-Arosh and Gany [10] tested over 40 small-scale SFRJ combustors with an approximately constant value of the product of combustor pressure and port (inside combustor) diameter. They found that performance correlated as expected with port diameter.

In the case of ducted rocket combustors, PD-scaling should also be applicable. The problem of scaling fuel distribution, as present in liquid fuel combustors, should be minimal if geometric similarity is maintained for the fuel injection and the processes concerning the combustion of any solid particles can be scaled correctly (or have little effect). As for heat losses, normally a ducted rocket combustor would be insulated on the inside, but for our experiments this will not be the case, so heat losses through the combustor wall will occur. While PD-scaling will scale the convective heat transfer correctly for geometrically-similar combustors, heat losses due to convection and radiation outside the combustor will not, in general, be scaled correctly. If the heat losses are significant, the inner wall temperature of the combustor will be different between the model and the prototype, and thermal similarity will not be maintained (which will affect dynamic and compositional similarity as well). The importance of these heat losses should therefore be determined. The last concern is whether or not the global reaction rate is second order. If it is not exactly second order, then as suggested by Way [17] the pressure could be changed in the model to compensate so the combustor performance would scale correctly. However, a better approach until the exact reaction order is known is to maintain PD-scaling and, if there is evidence later to suggest that the global reaction rate is not second order, then correlate the performance data with a modified parameter. The best way to determine the global reaction order would be to test at a different geometric scale. However, if this is not possible, a comprehensive study into the combustion processes, including solid particle effects, should be done to estimate the global reaction order.

Appendix B

SAMPLE INPUT AND OUTPUT FILES FOR CET89

These are the input and output files for a sample calculation of combustion efficiency based on temperature rise in the combustor with CET89. The configuration is DC1, the same one used for the sample calculation in Appendix C.

cet89.in Input File

```
REACTANTS
REACTANTS
C 2.0    H 4.0                      00       100.00           289.00 F
N 2.                                00        71.92607111     G 523.20 O
H 2.     O 1.                       00        1.586562157     G 523.20 O
C 1.     O 2.                       00        1.939131525     G 523.20 O
O 2.                                00        23.11639571     G 523.20 O
AR1.                                00        1.431839504     G 523.20 O

THERMO         THERMOCHEMICAL DATA
TRANSPORT      PROPERTY COEFFICIENTS
NAMELISTS
```

rkinpt.dat Input File

```
.TRUE.    EQL      .TRUE.
.FALSE.   FROZ     .TRUE.
2.0525 0.00  0.00  0.00  0.00  0.00  0.00  0.00  0.00  0.00    SUBAR  1:10
0.00  0.00  0.00                                              SUBAR 11:13
0.00  0.00  0.00  0.00  0.00  0.00  0.00  0.00  0.00  0.00    SUPAR  1:10
0.00  0.00  0.00                                              SUPAR 11:13
0.00  0.00  0.00  0.00  0.00  0.00  0.00  0.00  0.00  0.00    PCP  1:10
0.00  0.00  0.00  0.00  0.00  0.00  0.00  0.00  0.00  0.00      PCP 11:20
0.00  0.00                                                      PCP 21:22
3800.     TCEST     3800.
1         NFZ       1
.FALSE.   FAC      .FALSE.
1332.     MA        1332.
1.58      ACAT      0.0
.FALSE.   DEBUGF   .FALSE.
```

inpt2.dat Input File

```
1         KASE      1
0.00  0.00  0.00  0.00  0.00  0.00  0.00  0.00  0.00  0.00        T  1:10
0.00  0.00  0.00  0.00  0.00  0.00  0.00  0.00  0.00  0.00        T 11:20
0.00  0.00  0.00  0.00  0.00  0.00                                T 21:26
4.57E5 0.00  0.00  0.00  0.00  0.00  0.00  0.00  0.00  0.00        P  1:10
0.00  0.00  0.00  0.00  0.00  0.00  0.00  0.00  0.00  0.00        P 11:20
0.00  0.00  0.00  0.00  0.00  0.00                                P 21:26
.FALSE.   PSIA     .FALSE.
.FALSE.   MMHG     .FALSE.
.TRUE.    NSQM     .FALSE.
0.00  0.00  0.00  0.00  0.00  0.00  0.00  0.00  0.00  0.00        V  1:10
0.00  0.00  0.00  0.00  0.00  0.00  0.00  0.00  0.00  0.00        V 11:20
0.00  0.00  0.00  0.00  0.00  0.00                                V 21:26
0.00  0.00  0.00  0.00  0.00  0.00  0.00  0.00  0.00  0.00      RHO  1:10
0.00  0.00  0.00  0.00  0.00  0.00  0.00  0.00  0.00  0.00      RHO 11:20
0.00  0.00  0.00  0.00  0.00  0.00                              RHO 21:26
.FALSE.   ERATIO   .FALSE.
.TRUE.    OF       .TRUE.
.FALSE.   FPCT     .FALSE.
.FALSE.   FA       .FALSE.
21.1881  -1.0   -1.0   -1.0   -1.0   -1.0   -1.0   -1.0   -1.0   -1.0   MIX
1:10
-1.0    -1.0   -1.0   -1.0   -1.0   -1.0   -1.0   -1.0   -1.0   -1.0   MIX 11:20
-1.0    -1.0   -1.0   -1.0   -1.0   -1.0                              MIX 21:26
.FALSE.   TP       .FALSE.
.FALSE.   HP       .FALSE.
.FALSE.   SP       .FALSE.
.FALSE.   TV       .FALSE.
.FALSE.   UV       .FALSE.
.FALSE.   SV       .FALSE.
.TRUE.    RKT      .FALSE.
.FALSE.   SHOCK    .FALSE.
.FALSE.   DETN     .FALSE.
0.D0      TRACE     0.D0
1.D30     SO        1.D30
1.D30     SO        1.D30
.FALSE.   IONS     .FALSE.
0         IDEBUG    0
.FALSE.   PHI      .FALSE.
.TRUE.    SIUNIT   .FALSE.
.FALSE.   INHG     .FALSE.
.FALSE.   TRNSPT   .FALSE.
.99995D0  TRPACC    .99995D0
.FALSE.   NODATA   .FALSE.
1.D30     U         1.D30
1.D30     H         1.D30
```

cet89.out Output File

```
1
 REACTANTS
 C   2.0000  H   4.0000      0.0000      0.0000  00  0.0000  100.000000
0.00       289.000     F
 N   2.0000      0.0000      0.0000      0.0000  00  0.0000   71.926003  0
0.07  G    523.200     O
 H   2.0000  O   1.0000      0.0000      0.0000  00  0.0000    1.586500  6
0.02  G    523.200     O
 C   1.0000  O   2.0000      0.0000      0.0000  00  0.0000    1.939100  3
0.02  G    523.200     O
 O   2.0000      0.0000      0.0000      0.0000  00  0.0000   23.115999  3
0.10  G    523.200     O
 AR  1.0000      0.0000      0.0000      0.0000  00  0.0000    1.431800  3
0.10  G    523.200     O


 THERMO         THERMOCHEMICAL DATA
 TRANSPORT      PROPERTY COEFFICIENTS
 NAMELISTS
0   ***INPT2***
OKASE =        1   IDEBUG =  0   TRACE = 0.00000D+00   IONS = F   SIUNIT = T
OTP = F   HP = F   SP = F   TV = F   UV = F   SV = F   RKT = T   SHOCK = F
DETN = F
OTRNSPT = F   TRPACC = 0.999950E+00   NODATA = F
OOF = T   FA = F   FPCT = F   ERATIO = F   PHI = F
OSO = 0.10000001E+31   U = 0.00000000E+00   H = 0.00000000E+00
OP =   0.45700E+06
OT =   0.00000E+00
OMIX = 0.21188E+02
OSPECIES BEING CONSIDERED IN THIS SYSTEM
  L 5/66  AR              J 3/78  C                J12/67  CH
J12/72  CH2             J 3/61  CH2O
  J 6/69  CH3             J 3/61  CH4              J 6/69  CN
J 6/66  CNN             J12/70  CN2
  J 9/65  CO              J 9/65  CO2              J12/69  C2
J 3/67  C2H             J 3/61  C2H2
  L 4/80  C2H4            L 2/80  C2H6             J 3/67  C2N
J 3/61  C2N2            J 9/66  C2O
  J12/69  C3              J 6/68  C3O2             J12/69  C4
J 3/61  C4N2            J12/69  C5
  J 3/77  H               L12/69  HCN              J12/70  HCO
J12/70  HNCO            J 3/63  HNO
  J 6/63  HNO2            J 6/63  HNO3             J 9/78  HO2
J 3/77  H2              J12/65  H2N2
  J 3/79  H2O             L 6/80  H2O2             J 3/77  N
J12/70  NCO             J 6/77  NH
  J 6/77  NH2             J 6/77  NH3              J 6/63  NO
J 9/64  NO2             J12/64  NO3
  J 3/77  N2              J12/65  N2H4             J12/64  N2O
J 9/64  N2O4            J12/64  N2O5
  J12/70  N3              J 3/77  O                J 6/77  OH
J 3/77  O2              J 6/61  O3
  J 3/78  C(GR)           L 3/81  H2O(S)           J 3/79  H2O(L)
0   ***RKTINP***
OEQL = T   FROZ = F   NFZ =  1   TCEST =  3800.000   FAC = F   MA =
0.13320000E+04   ACAT = 0.15800000E+01   DEBUGF = F
OPCP =
OSUBAR = 0.20525000E+01
OSUPAR =
OOF =  21.188101
                            EFFECTIVE FUEL         EFFECTIVE OXIDANT
MIXTURE
 ENTHALPY                       HPP(2)                  HPP(1)
HSUBO
```

```
 (KG-MOL)(DEG K)/KG         0.22253583E+03          -0.18653619E+02          -
0.77834027E+01
0KG-FORM.WT./KG               BOP(I,2)                BOP(I,1)
B0(I)
 C                          0.71291692E-01           0.44060905E-03
0.36338109E-02
 H                          0.14258338E+00           0.17612932E-02
0.81080325E-02
 N                          0.00000000E+00           0.51351303E-01
0.49036941E-01
 O                          0.00000000E+00           0.16209992E-01
0.15479421E-01
 AR                         0.00000000E+00           0.35841807E-03
0.34226445E-03
0POINT ITN   T      C               H               N               O
AR
   1   15 2120.84  -24.766         -13.460         -12.986         -15.159
-24.478
 PC/PT= 1.791252   T =  2120.84
   2    3 1895.28  -27.221         -14.277         -13.086         -15.239
-24.821
 PC/PT= 1.802240   T =  1895.28
   2    2 1892.98  -27.249         -14.287         -13.087         -15.240
-24.824
 PC/PT= 1.802331   T =  1892.98
   2    1 1892.96  -27.249         -14.287         -13.087         -15.240
-24.824
   3    2 2102.64  -24.944         -13.519         -12.994         -15.165
-24.505
   3    2 2099.01  -24.979         -13.531         -12.996         -15.166
-24.511
   3    2 2098.58  -24.984         -13.532         -12.996         -15.167
-24.511
   3    1 2098.58  -24.984         -13.532         -12.996         -15.167
-24.511
1                        THEORETICAL ROCKET PERFORMANCE ASSUMING EQUILIBRIUM
COMPOSITION DURING EXPANSION

                                                FROM INFINITE AREA COMBUSTOR
0PINF =    66.3 PSIA
 CASE NO.       1
                                                                              WT
FRACTION    ENERGY   STATE   TEMP
          CHEMICAL FORMULA
(SEE NOTE)    KJ/KG-MOL        DEG K
 FUEL    C  2.00000   H  4.00000
1.000000    51907.211        289.00
 OXIDANT N  2.00000
0.719264     6599.144   G    523.20
 OXIDANT H  2.00000   O  1.00000
0.015865  -234072.422   G    523.20
 OXIDANT C  1.00000   O  2.00000
0.019391  -384161.844   G    523.20
 OXIDANT O  2.00000
0.231161     6809.268   G    523.20
 OXIDANT AR 1.00000
0.014318     4677.952   G    523.20
0               O/F= 21.1881    PERCENT FUEL=   4.5069    EQUIVALENCE RATIO=
0.7314    PHI= 0.6986
0                 CHAMBER   THROAT     EXIT
 PINF/P            1.0000   1.8023   1.0580
 P, MPA           0.45700  0.25356  0.43196
 T, DEG K         2120.84  1892.96  2098.58
 RHO, KG/CU M    7.4767-1 4.6511-1 7.1428-1
 H, KJ/KG         -64.715  -405.13  -98.978
 U, KJ/KG         -675.94  -950.29  -703.73
```

```
 G, KJ/KG        -19025.8 -17328.9 -18861.0
 S, KJ/(KG)(K)     8.9404   8.9404   8.9404

 M, MOL WT         28.850   28.870   28.853
 (DLV/DLP)T      -1.00039 -1.00010 -1.00035
 (DLV/DLT)P        1.0126   1.0038   1.0113
 CP, KJ/(KG)(K)    1.5643   1.4557   1.5509
 GAMMA (S)         1.2323   1.2488   1.2341
 SON VEL,M/SEC      867.9    825.1    863.9
 MACH NUMBER        0.000    1.000    0.303

OPERFORMANCE PARAMETERS

 AE/AT                      1.0000   2.0525
 CSTAR, M/SEC                 1191     1191
 CF                          0.693    0.220
 IVAC, M/SEC                1485.8   2572.0
 ISP, M/SEC                  825.1    261.8


OMOLE FRACTIONS

 AR               0.00987  0.00988  0.00988
 CO               0.00069  0.00014  0.00060
 CO2              0.10414  0.10477  0.10424
 H                0.00002  0.00000  0.00002
 H2               0.00016  0.00004  0.00014
 H2O              0.11582  0.11663  0.11593
 NO               0.00546  0.00298  0.00518
 NO2              0.00001  0.00000  0.00001
 N2               0.70461  0.70636  0.70483
 O                0.00018  0.00004  0.00016
 OH               0.00194  0.00075  0.00179
 O2               0.05709  0.05840  0.05723
OADDITIONAL PRODUCTS WHICH WERE CONSIDERED BUT WHOSE MOLE FRACTIONS WERE LESS
THAN  0.50000E-05 FOR ALL ASSIGNED CONDITIONS

  C                CH               CH2              CH2O             CH3
CH4              CN
  CNN              CN2              C2               C2H              C2H2
C2H4             C2H6
  C2N              C2N2             C2O              C3               C3O2
C4               C4N2
  C5               HCN              HCO              HNCO             HNO
HNO2             HNO3
  HO2              H2N2             H2O2             N                NCO
NH               NH2
  NH3              NO3              N2H4             N2O              N2O4
N2O5             N3
  O3               C(GR)            H2O(S)           H2O(L)
ONOTE. WEIGHT FRACTION OF FUEL IN TOTAL FUELS AND OF OXIDANT IN TOTAL OXIDANTS
1
```

Appendix C

SAMPLE CALCULATION

To calculate the combustion efficiency, the raw data measured from each direct-connect experiments are averaged. This table includes the data reduced from this voluminous raw data, mainly from pressure and temperature measurements, for direct-connect configuration DC1. From this reduced data, the combustion efficiency is calculated with the equations given in Chapter 5, and these results are also given. The boundary conditions for the CFD modelling also came from these data. The predicted temperatures and combustion efficiencies from the onestream and twostream PDF models are therefore presented as well. Figure C.1 shows a schematic of the gas flows and the location of the chokes mentioned in the table.

Parameter	Value	Units
Configuration	DC1	
Equivalent water tunnel configuration	WT7, WT8	
Vitiated air flow into air plenum (choke C2)	1 561	g/s
Total vitiated air flow (chokes C1+C2)	1 665	g/s
Total mass flow through fuel plenum (chokes C1+C3+C4)	182.6	g/s
Total ethylene flow (C3+C4)	78.6	g/s
Vitiated air flow through gas generator (choke C1)	104.1	g/s
Ethylene temperature	289	K
Oxidizer/fuel ratio in fuel plenum	1.325	
Gas generator pressure	1.047	MPa
Static pressure in combustor	0.432	MPa
Stagnation temperature in air inlets	523	K
Static temperature in air inlets	516	K
Oxidizer/fuel ratio in combustor	8.545	
Fuel injector diameter	27	mm
Calculated fuel velocity	354	m/s
Air injector diameter	50.8	mm
Calculated air velocity	132	m/s

Fuel momentum (mass flow rate · velocity)	64.6	kg·m/s^2
Air momentum	206.2	kg·m/s^2
Air/fuel momentum ratio	3.19	Ratio
Air injector	A4	
Fuel injector diameter	F0-27	
Overall air/ethylene ratio in combustor (not the same as the oxidizer/fuel ratio in the combustor)	21.19	
Theoretical combustor temperature ($T_{\mathrm{t4,theo}}$)	2 121	K
Theoretical characteristic velocity (C^*_{theo})	1 191	m/s
Combustor length	458	mm
Combustor dome	57	mm
Theoretical molar mass in combustor	28.85	g/g-mol
Stagnation pressure in combustor (p_{t4})	0.457	MPa
Total mass flow rate through combustor ($\dot{m}_4$)	1 743	g/s
Diameter of combustor nozzle throat	69.8	mm
Combustor nozzle discharge coefficient	1.0	
Experimental combustor stagnation temperature ($T_{\mathrm{t4,exp}}$)	1 505	K
Experimental characteristic velocity (C^*_{exp})	1 003	m/s
Vitiated air composition		
N_2 mole fraction	0.742 51	
O_2 mole fraction	0.208 91	
H_2O mole fraction	0.025 47	
CO_2 mole fraction	0.012 74	
Ar mole fraction	0.010 37	
Total	1	
Molar mass of the vitiated air	28.92	g/g-mol
Density of the vitiated air	2.914	kg/m^3
Gas generator exhaust composition		
Ar mole fraction	0.002 79	
CH_4 mole fraction	0.025 2	
CO mole fraction	0.100 31	
CO_2 mole fraction	0.004 49	
HCN mole fraction	0.000 01	
H_2 mole fraction	0.358 19	
H_2O mole fraction	0.016 85	
NH_3 mole fraction	0.000 18	
N_2 mole fraction	0.199 72	
C(graphite) mole fraction	0.292 26	
Sum of mole fractions	1	
Density of gases and solids	0.902	kg/m^3

Mass fraction of solids in the gas generator exhaust	0.257	
Mass fraction of gases in the gas generator exhaust	0.743	
Static temperature of the gas generator exhaust at the combustor fuel inlet	1 112	K
Mole fractions of gases only		
Ar mole fraction	0.003 94	
CH_4 mole fraction	0.035 61	
CO mole fraction	0.141 73	
CO_2 mole fraction	0.006 34	
HCN mole fraction	0.000 01	
H_2 mole fraction	0.506 10	
H_2O mole fraction	0.023 81	
NH_3 mole fraction	0.000 25	
N_2 mole fraction	0.282 19	
Sum of mole fractions	1	
Onestream PDF Results		
100 mm	796	K
200 mm	918	K
300 mm	993	K
400 mm	1 065	K
458 mm	1 107	K
500 mm	1 129	K
Twostream PDF Results		
100 mm	788	K
200 mm	916	K
300 mm	990	K
400 mm	1 056	K
458 mm	1 092	K
500 mm	1 113	K
Combustion efficiencies based on temperature rise in the combustor		
Experimental combustion efficiency	61%	
Onestream PDF combustion efficiency at 458 mm	37%	
Twostream PDF combustion efficiency at 458 mm	36%	

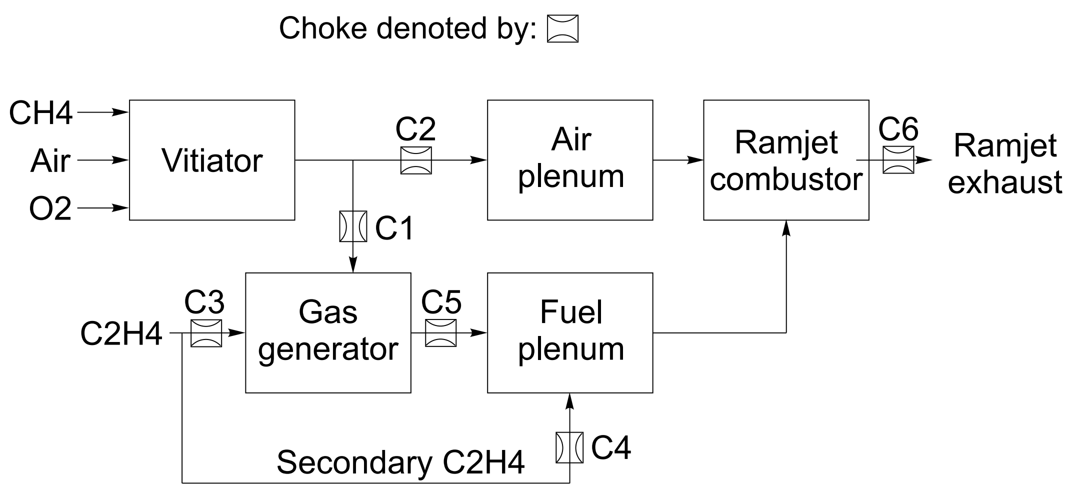

Figure C.1: Placement of the gas chokes

Appendix D

REPRODUCIBILITY OF THE EXPERIMENTS

Four of the direct-connect configurations were tested twice to determine how reproducible the experiments were. The experimental results are presented in Table D.1. Configuration DC5 is a repeat of configuration DC2, configuration DC10 is a repeat of configuration DC7, configuration DC17 is a repeat of configuration DC14, and configuration DC22 is a repeat of configuration DC19. For each configuration, since the input parameters vary slightly for each of the two experiments, so do the outputs.

Table D.1: Combustion efficiencies for repeat tests

Direct Connect Config	Air Inj	Fuel Inj	Dome Height [mm]	Air/fuel Momentum Ratio	Experimental Efficiency	Experimental Uncertainty
DC2	A4	F0-27	57	11.73	0.48	16%
DC5	A4	F0-27	57	11.59	0.50	16%
DC7	A2	F0-27	57	19.43	0.64	14%
DC10	A2	F0-27	57	19.07	0.66	14%
DC14	A6	F0-27	57	10.80	0.57	14%
DC17	A6	F0-27	57	11.07	0.59	14%
DC19	A4	F0-27	100	10.93	0.61	14%
DC22	A4	F0-27	100	11.14	0.65	13%

Appendix E

PUBLICATIONS

The following is a list of publications and presentations based on the work done for this thesis. Three of the publications are also included in their entirety.

1. Dubois, C., Stowe, R.A., Farinaccio, R., and Lessard, P., "Development of a New GAP-Based Propellant for Airbreathing Propulsion", TTCP WTP-4 Technical Workshop - Airbreathing Propulsion, April 10, 1997, Fort Halstead, U.K.

2. Stowe, R.A, "Scaling in a Ducted Rocket Combustor, IRRDP-DREV-TN-9602(1)", DREV TM-9733, February 1998, UNCLASSIFIED.

3. Couture, F., Stowe, R.A., De Champlain, A., et Oumejjoud, K., "Étude de la quantification du mélange air-carburant dans une statofusée à l'aide d'un tunnel à eau", 66e Congrès de l'Acfas (l'Association canadienne-française pour l'avancement des sciences), Université Laval, Québec, Canada, 11-15 mai 1998.

4. Stowe, R.A., Couture, F., et De Champlain, A., "FLUENT Modelling and Water Tunnel Visualization of a Ducted Rocket Combustor", 1998 FLUENT Users' Group Meeting, Burlington, Vermont, U.S., 16 June 1998.

5. Stowe, R.A., De Champlain, A., Mayer, A.E.H.J., and Niemeijer, S.F., "Modelling and Flow Visualization of Mixing in a Ducted Rocket Combustor", AIAA paper AIAA-98-3768, AIAA/ASME/SAE/ASEE 34th Joint Propulsion Conference, Cleveland, Ohio, U.S., 13-15 July 1998.

6. Stowe, R.A., De Champlain, A., Mayer, A.E.H.J., and Niemeijer, S.F., "Modelling and Water Tunnel Visualization of Air/Fuel Mixing in a Ducted Rocket Combustor", IRRDP-DREV/TNO-TN-9707(1), DREV-TM-9828, February 1999, UNCLASSIFIED.

7. Stowe, R.A., Dubois, C., Smithson, T., and De Champlain, A., "Preliminary Exhaust Characterization of a GAP/Carbon Ducted Rocket Fuel", 24th Meeting of The Technical Cooperation Program, Technical Panel WPN/TP-4 Workshop, NSWC, Indian Head, Maryland, U.S., 15-16 April 1999.

8. Jeffries, M.A. and Stowe, R.A., “Improved Image Correction Technique for Visualization of the Air/Fuel Mixing in a Ducted Rocket Combustor”, DREV TM 1999 220, March 2000, UNCLASSIFIED.

9. Mayer, A.E.H.J. and Stowe, R.A., “Experimental Study Into Mixing in a Solid Fuel Ducted Rocket Combustion Chamber”, AIAA paper AIAA-2000-3346, AIAA/ASME/SAE/ASEE 36th Joint Propulsion Conference, Huntsville, Alabama, U.S., 17-19 July 2000.

10. Stowe, R.A., De Champlain, A., and Mayer, A.E.H.J., “Modelling Combustor Performance of a Ducted Rocket”, AIAA paper AIAA-2000-3728, AIAA/ASME/SAE/ASEE 36th Joint Propulsion Conference, Huntsville, Alabama, U.S., 17-19 July 2000.

11. Mayer, A.E.H.J. and Stowe, R.A., “Results of the IRRDP Ducted Rocket Combustor Experiments”, Integral Rocket Ramjet Demonstration Program Report IRRDP-TNO-TRP-0101 (1), TNO Prins Maurits Laboratory, The Netherlands, 2001.

12. Stowe, R.A. and De Champlain, A., “CFD Modelling of Ramjet Combustors”, Meeting of The Technical Cooperation Program, Technical Panel WPN/TP-4 Workshop, 21st Century Propulsion Systems, Fort Halstead, U.K., 26-27 April 2001.

13. Jeffries, M.A., Stowe, R.A., and Farinaccio, R., “Air/Fuel Mixing in a Ducted Rocket Combustor”, 9th Annual Conference of the CFD Society of Canada, Paper 37, Waterloo, Ontario, Canada, May 27-29, 2001.

14. Stowe, R.A., Dubois, C., Harris, P.G., Mayer, A.E.H.J., De Champlain, A., and Ringuette, S., “Two Phase Flow Combustion Modelling of a Ducted Rocket”, AIAA paper AIAA-2001-3461, accepted for the AIAA/ASME/SAE/ASEE 37th Joint Propulsion Conference, Salt Lake City, Utah, U.S., 8-11 July 2001.

15. Ringuette, S., Dubois, C., and Stowe, R.A., “On the Optimization of GAP-Based Ducted Rocket Fuels from Gas Generator Exhaust Characterization”, accepted for publication in the Journal of Propellants, Explosives, Pyrotechnics.

16. Margetson, J. and Stowe, R.A., “Analysis of Experimental Observations and Theoretical Predictions for a Ducted Rocket Application Using Non-parametric Error Diagnostic Procedures”, DREV Technical Note, to be published 2001.

MODELLING AND FLOW VISUALIZATION OF MIXING IN A DUCTED ROCKET COMBUSTOR

R.A. Stowe*, Defence Research Establishment Valcartier, Québec, Canada
A. DeChamplain†, Université Laval, Québec, Canada
A.E.H.J. Mayer‡, TNO Prins Maurits Laboratory, The Netherlands
S.F. Niemeijer§, Hogere Technische School, Haarlem, The Netherlands

ABSTRACT

Under a co-operative program, the Defence Research Establishment Valcartier (DREV) and Université Laval in Canada and the TNO Prins Maurits Laboratory (TNO-PML) and HTS Haarlem in the Netherlands have studied the use of a ducted rocket for missile propulsion. To maximize the benefit of the experimental combustion tests on scale-model combustors, the effect of geometry and flow conditions on the mixing of the air and the fuel was first examined. A literature survey was performed to identify a likely range of geometries and boundary conditions for testing, followed by flow visualization and computational fluid dynamic (CFD) modelling of air/fuel mixing within a water tunnel at flow conditions geometrically and dynamically similar to those expected during the combustion experiments. Since the CFD modelling compared well with the water tunnel visualization, further geometries were modelled to determine which would likely have good mixing and therefore give high efficiency in combustion tests. High air and fuel inlet velocities were generally associated with good mixing, but only at high enough air/fuel momentum ratio. Additional CFD modelling using boundary conditions expected in the combustion experiments confirmed that air/fuel momentum ratio was a critical parameter to describe the flowfield in the combustor.

INTRODUCTION

The Defence Research Establishment Valcartier (DREV) and Université Laval in Canada and the TNO Prins Maurits Laboratory (TNO-PML) and HTS Haarlem in the Netherlands have undertaken a collaborative activity to study the use of a ducted rocket for missile propulsion. This type of motor has several advantages over solid fuel rocket motors including increased range, higher speed, and throttleability, but only a limited increase in complexity. In the ramjet combustor, fuel-rich exhaust from the gas generator is mixed with air from the inlets, burns, and is accelerated through the nozzle to provide thrust. This aspect of the overall ducted rocket propulsion system formed a major part of this collaboration, and involved performing experiments at TNO's direct-connect combustion test facility to determine combustor performance. However, since a limited number of combustion tests could be carried out, a test matrix was carefully designed so that only configurations that would likely exhibit a high

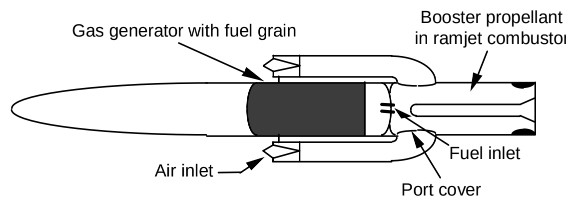

Figure 1 - Ducted rocket missile

degree of air/fuel mixing, and therefore could be expected to demonstrate good combustion efficiency, were tested. The possibilities were further narrowed by restricting the basic geometry to a combustor with dual inlets spaced 90^{o} apart circumferentially since this is a favoured configuration for air-launched missiles. The geometries, as Fig. 2 shows, also used very long air inlets and main combustor bodies that would not be practical on a missile motor, but facilitated testing and determining the boundary conditions for the water tunnel testing and CFD modelling. A practical ducted rocket motor would have inlets that hugged the side of the combustor and their ends would face directly forward, as shown in Fig. 1. During flight, the dual inlets would normally be below the missile as well. This paper describes the literature survey, water tunnel visualization, and CFD modelling that were performed to study the mixing of the air and fuel within the combustor and to choose the test matrix.

* Scientist, Propulsion Group, Member AIAA
† Associate Professor, Mechanical Engineering
‡ Propulsion Engineer, Rocket Technology Group
§ Student, Aeronautical Engineering

	Dia of combustor [mm]	Re in combustor	Air intakes	Type	Injection angles [deg]	Dome height	Fuel injection type	Stag. pressure [MPa]	Stag. temperature [K]
Clark 1980 [Ref. 1]	196.85	1850917	2	Circular 162 deg opposed	60	0.5 est.	In inlets	0.639	610
Choudhury 1982 [Ref. 2]	89	No T,P data	4	Circular, cantable	45,70	0.6-4.0	Radial central	No T,P data	No T,P data
Zetterstrom 1983 [Ref. 3]	100	1158833	4	Circular	60	0.75 est.	In inlets	0.714	704
Stull 1983 [Ref. 4]	150	4472945	2	Rectangular ventral	30,45,60	0.4-0.9	In inlets	0.248	571
Cherng 1989 [Ref. 5]	127	843322	2	Opposed 2D	45	0.48	2 off-centre ports, 2D	0.199	286
TNO 1995 [Ref. 6]	100	216065	2	Circular ventral	45	0.7	Central nozzle protruding 30mm	0.617	655
NAWC 1995 [Ref. 6]	127	259752	2	Circular ventral	45	0.96	Central nozzle protruding 51mm	0.508	653
Schadow 1972 [Ref. 7]	150	273001	2	Opposed rectangular slits	45	0-neg	Central nozzle	0.201	298
Japan 1987 [Ref. 8]	83	460207	2	Opposed	75	0.5 est.	Central nozzle	0.464	460
ONERA 1993 [Ref. 9]	85	1108057	4	Circular, shifted, deflectors	45-90	0.5 est.	Various	NA	NA
ONERA 1993 [Ref. 9]	168	1760239	4	Circular, shifted, deflectors	45-90	0.5 est.	Various	NA	NA

Table I - Previous experiments

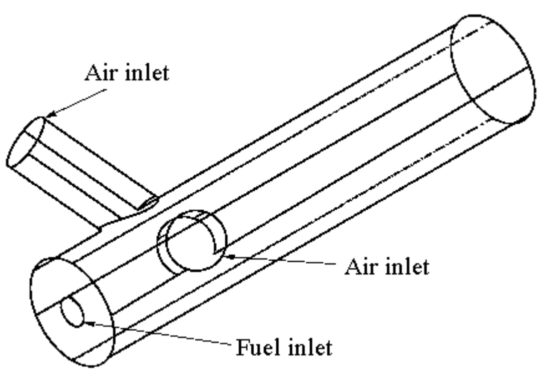

Figure 2 - Basic geometry

Literature survey

The purpose of the literature survey was to find out which geometries and test conditions had already been investigated by other researchers. Test conditions were noted, and additional data calculated, such as air and fuel velocities, Reynolds numbers (Re), and stagnation properties to describe more completely the flow within the combustors. Apart from the geometries and test conditions, the papers were also examined for additional parameters that described the flow, such as air/fuel velocity, momentum, and mass flow ratios.

The literature survey showed that many different configurations have been investigated. Air inlet injection angles from 30^o to 90^o were used, both with and without splitters or guide vanes. Air inlet velocities were up to 200 m/s, with temperatures from ambient up to 800 K and combustor pressures from about 0.2 MPa up to 0.7 MPa. Dome heights were usually from 25% to 100% of the combustor diameter and, for dual inlet systems, more stable recirculation in the dome region was obtained with the intakes positioned 90^o apart rather than directly opposed at 180^o. Methods of fuel injection varied widely, from axial to radial when injected from the head, to injection in the air inlets themselves. Impingement of the fuel jet against the air jets was desirable to better break up the fuel jet and improve mixing. The mixing and the small scale flow structures in the dome region of the combustor were found to be quite sensitive to geometry and boundary conditions when the fuel was injected from the head, so this was kept in mind during our own mixing studies. The literature survey also revealed that computer modelling, flow visualization with water tunnels or wind tunnels, and combustion tests (subscale and full scale) were all performed to identify the best configurations and maximize combustion efficiency.

Water tunnel visualization

After the literature survey, a water tunnel was used to visualize the non-reacting flow and air/fuel mixing within 100mm diameter model combustors at 24 combinations of geometry and test conditions. The use of a water tunnel is an accepted method to visualize flowfields within combustors, and has also been used specifically for ducted rocket combustors [3, 10, and 11]. DREV's water tunnel is basically a 560 litre plexiglass tank in which a plexiglass model of a ducted rocket combustor is installed. The tank is filled with water to minimize refraction effects. A 2HP motor pumps water through the "fuel" and "air" inlets of the combustor - this

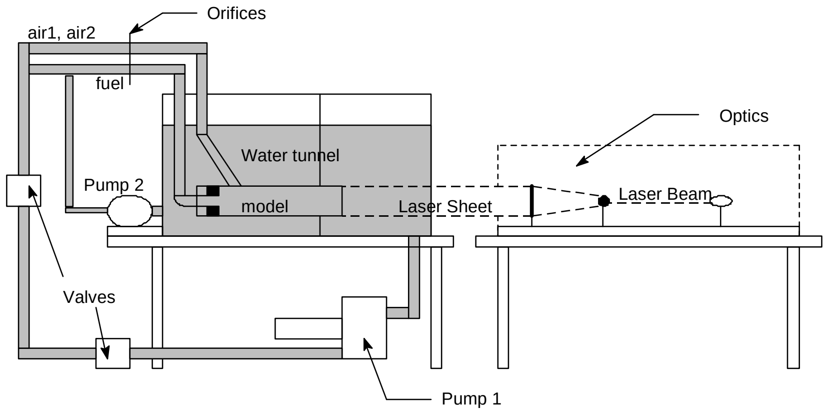

Figure 3 - Water tunnel and optics setup

water simulates both the fuel and the air flowing through an actual combustor. Differential pressure gauges across sharp-edged orifices measure the flow through the air and fuel inlets. The main advantage of a water tunnel for flow visualization is that the Reynolds numbers achieved for a 1 m/s water velocity in the main part of the combustor were on the order of 10^5 and therefore representative of the flow in a typical ducted rocket combustor. Apart from Reynolds numbers and geometry, the ratio of the fuel and air momentum through their respective inlets was used to describe the flow. Momentum was defined as the product of the mass flow rate and the velocity at the inlet.

Several combustor models were built and tested at various flow conditions. To visualize the velocities within the combustor, the water was first seeded with 100 micron polystyrene spheres which, since they were of approximately the same density as water, could follow the flow quite well. A laser sheet was created with a 5W argon-ion laser to illuminate the planes of interest (both longitudinal and cross-sectional). With the proper shutter speed, the streaks of the particles could

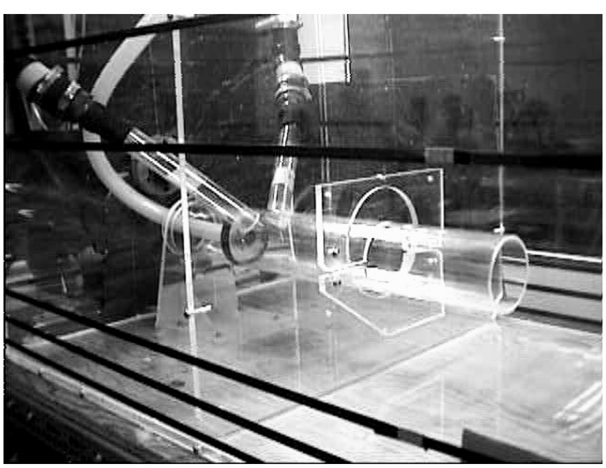

Figure 4 - Plexiglass water tunnel model and piping

be recorded with a digital video camera and compared to the velocity field on a vector plot from the CFD modelling. While this technique revealed the large-scale flow structures quite well, the fine-scale turbulence, very important for the air/fuel mixing, was not resolved. Therefore, since air/fuel mixing was of greater interest than the velocity field, the visualization focused on this instead. A method was found to seed the water simulating the fuel flow with very fine bubbles to distinguish it from the water that was simulating the air. These bubbles came from forcing water from a second low-volume but higher-pressure pump through a cavitation nozzle upstream of the fuel flow meter. Since the vast majority of these bubbles were just a few microns in diameter and barely buoyant, they appeared to behave much more like an injected dye than the much larger polystyrene spheres and would therefore be more representative of actual air/fuel mixing.

CFD modelling

Computational fluid dynamics (CFD) modelling of the water tunnel experiments was carried out using a code known as FLUENT (Version 4.4). Geometries were modelled as precisely as possible, and structured grids of approximately 100,000 hexahedral cells, including dead cells, were generated. Constant velocity inlet profiles at the end of the long inlet tubes were assumed, along with a turbulence intensity of 10% and a turbulence characteristic length 25% of the inlet diameters. The Renormalized Group Theory (RNG) turbulence model was used for the results presented in this paper. Properties of water at 25°C were used for the working fluid, and incompressible flow was assumed. An important difference between the water tunnel and the CFD modelling is that FLUENT, being a quasi-steady modelling code, gives a time-averaged output of the flowfield, whereas the experimental water tunnel flowfields are unsteady and change continuously with time.

FLUENT was also used to model other combustor geometries of possible interest. While the use of the water tunnel is a technique that is less resource-intensive than experiments in the direct-connect combustion test facility, it still requires models to be constructed, experiments to be carried out, and data to be reduced. With the CFD modelling, a wide range of geometries and test conditions could be evaluated more quickly than with the water tunnel. However, the limitations of CFD modelling, particularly the assumption that the flow is quasi-steady, means that at least some experiments are still essential for validation purposes.

RESULTS

In all, 12 combinations of two different air injection angles (60^o and 90^o), two different air injector sizes (38 and 51mm), two different dome heights (57 and 100mm measured from head to the centre of the air inlet), three different fuel injectors, and five different air/fuel momentum ratios (3 to 20) were tested in the water tunnel and modelled with FLUENT. Each of these was also tested and modelled at two different combustor Reynolds numbers (approximately 40000 and 80000), but no Re-dependency was ever observed.

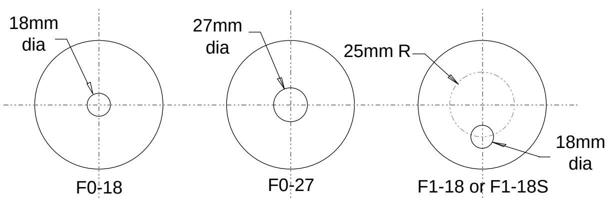

Figure 5 - Fuel injectors

Air/fuel mixing and flow patterns

Good mixing of the air and the fuel in the combustion chamber is a prerequisite for efficient combustor performance. Since mixing occurs on the interface between the air and the fuel, maximizing this interface is desirable. High turbulence levels, which are associated with high flow velocities, along with well-chosen air/fuel momentum ratios, were necessary for good mixing. To facilitate the description of the mixing, the combustor can be divided in three distinct regions, namely the dome region, the air inlet section, and the main combustor region (Fig. 6).

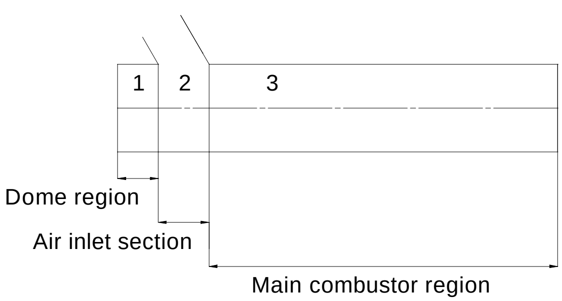

Figure 6 - Combustion chamber regions

While the exact flow patterns seen from the water tunnel images varied greatly depending on configuration, particularly on air/fuel momentum ratio, two basic flow features appeared to be common. The first, seen in Fig. 7, is a pair of longitudinal vortical structures that are a continuation of the high-speed flow from the air inlets. These structures corkscrew from below the centreline in the air inlet section and continue downstream toward the nozzle. They entrain and transport the mixture from the dome region of the combustor past the air inlets and to the main combustor region. They also add “swirl” to the flow and improve mixing by increasing the interface area between the air and the fuel.

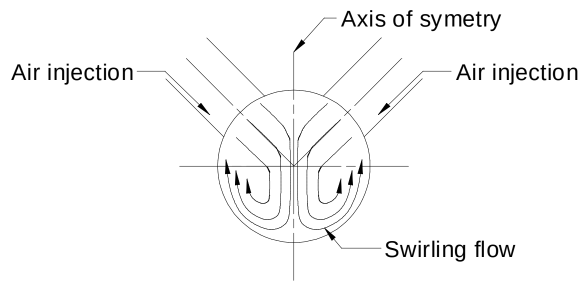

Figure 7 - Longitudinal vortical structures (end view)

The other basic flow phenomenon that generally appeared was a recirculation zone from the air inlet section into the dome region. Its exact shape was dependent on the strength of the fuel jet. At high air/fuel momentum ratios, the recirculation zone appeared to fill the entire height of the dome. However, when the fuel jet was relatively strong, this recirculation zone would decrease in height and turn back on itself below the fuel jet as shown in Fig. 8, and another recirculation region above the fuel jet rotating in the opposite direction occurred. At very high fuel momentums, though, mixing was relatively poor since the fuel jet would not break up in the air inlet section; it would continue, relatively intact, into the main combustor region.

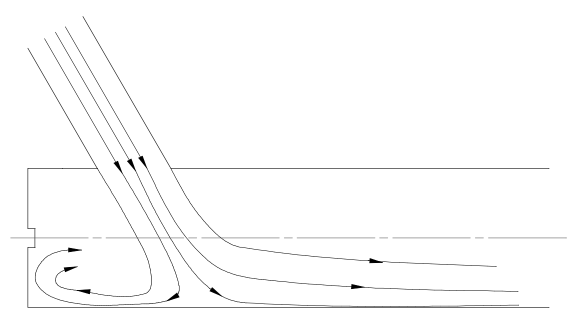

Figure 8 - Recirculation zone in dome

Flow stability

One important advantage of the water tunnel over the CFD modelling was that the unsteady flow phenomena could be observed. Figure 9 shows a sequence of images of configuration 9, taken at 30 frames per second.

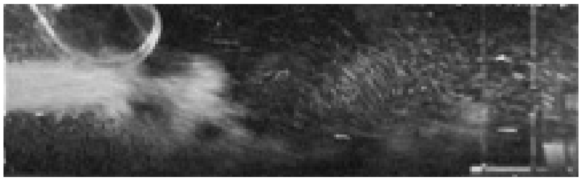

time = 0.000s

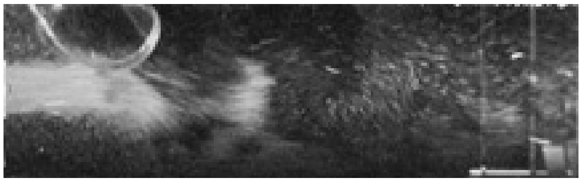

time = 0.033s

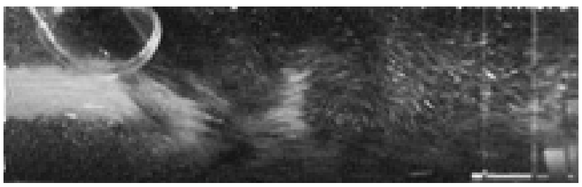

time = 0.067s

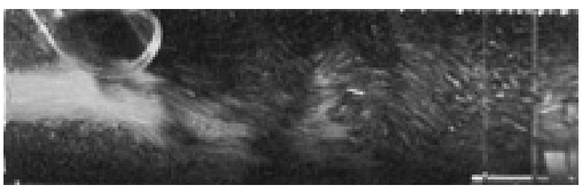

time = 0.100s

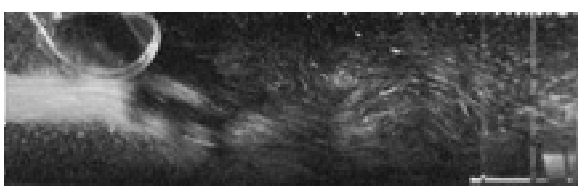

time = 0.133s

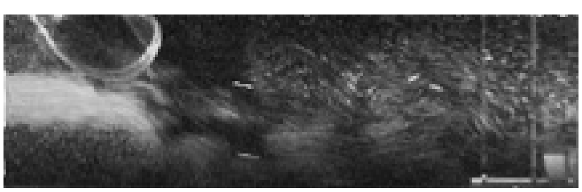

time = 0.167s

Figure 9 - Configuration 10, sequence of images.

These images were taken on the longitudinal centreline plane of the combustor where, assuming symmetry in the flows and the geometry, there should be no flow normal to the image. The fuel jet enters from the left, and the circular reflection just above is where the air inlet is attached to the combustor. This particular configuration used 51mm diameter air inlets with a 60^o injection angle, a dome height of 57mm, a centrally-located fuel inlet of 27mm diameter, an air/fuel mass flow ratio of 9.21, an air/fuel momentum ratio of 11.98, and a combustor Re = 40052. As can be seen in the first image, the end of the fuel jet has broken off and has passed through the air inlet section. As it moves downstream into the main combustor region it dissipates by the fourth and fifth image. In the third image, the end of the fuel jet appears to break off once again, but this time it is smaller and therefore dissipates more quickly than the one in the first image. This particular configuration was one of the least stable, meaning that it displayed a greater variability in the break-up of the fuel jet than most of the other configurations. From time-to-time, some relatively large pieces would break off. However, this type of behaviour was typical of all of the tests, though usually to a lesser extent, and occurred at regular intervals, increasing with Reynolds number.

Water tunnel and CFD comparison

To compare the CFD results with the water tunnel images, contour plots of fuel mass fraction on the centreline plane were chosen. Unfortunately, the apparent concentration of the simulated fuel in the water tunnel images is not only a function of the number of cavitation bubbles present, but also of how the laser light is scattered from these bubbles and the intensity of the laser light. Since forward-scattering of light from a bubble can be many times greater than the back-scattering, any bubbles to the right of the images are much brighter than those to the left. The apparent concentration of bubbles to the right of the image is therefore much greater than it should be. Since the laser beam intensity follows a Gaussian profile, the light sheet is less intense at the top and the bottom; this means than the apparent concentration at the top and the bottom is less than it should be. An additional problem is present in the top left hand corner of the image where reflections from the air inlet junction occur. Despite these limitations, however, the shape of the fuel jets can justifiably be compared in the CFD and the water tunnel images since the concentration gradients at the edges are quite sharp. If one takes these limitations into account, the differences between the images away from the fuel jets would certainly be reduced with the appropriate corrections.

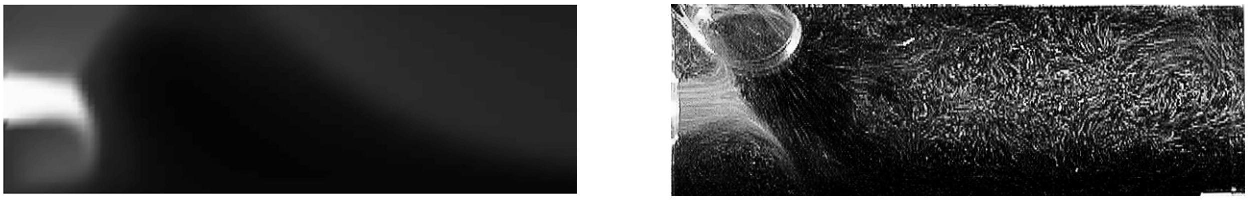

Configuration 5, air inlets 60^{o}, 38mm diameter, fuel inlet 27mm, centrally-located, dome height 57mm, air/fuel mass flow ratio = 9.07, air/fuel momentum ratio = 20.66, combustor Re = 80582.

Configuration 9, air inlets 60^{o}, 51mm diameter, fuel inlet 27mm, centrally-located, dome height 57mm, air/fuel mass flow ratio = 9.21, air/fuel momentum ratio = 11.98, combustor Re = 80104.

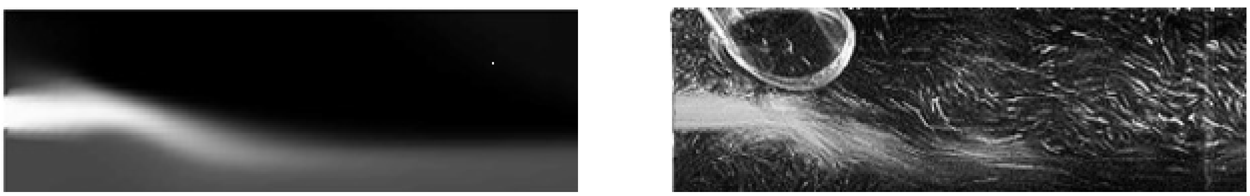

Configuration 11, air inlets 60^{o}, 51mm diameter, fuel inlet 18mm, centrally-located, dome height 57mm, air/fuel mass flow ratio = 9.19, air/fuel momentum ratio = 5.3, combustor Re = 80122.

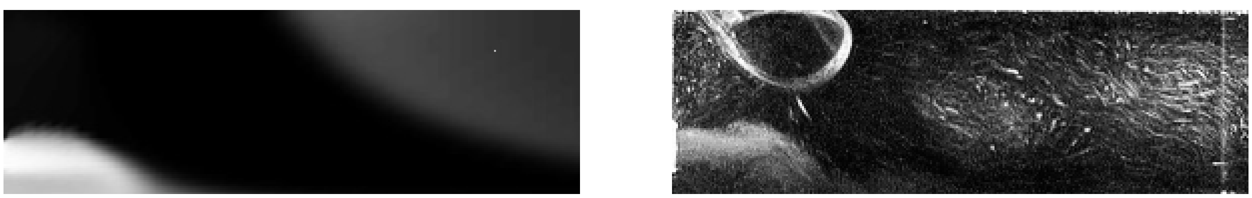

Configuration 13, air inlets 60^{o}, 51mm diameter, fuel inlet 18mm, located below air inlets, dome height 57mm, air/fuel mass flow ratio = 9.19, air/fuel momentum ratio = 5.3, combustor Re = 80122.

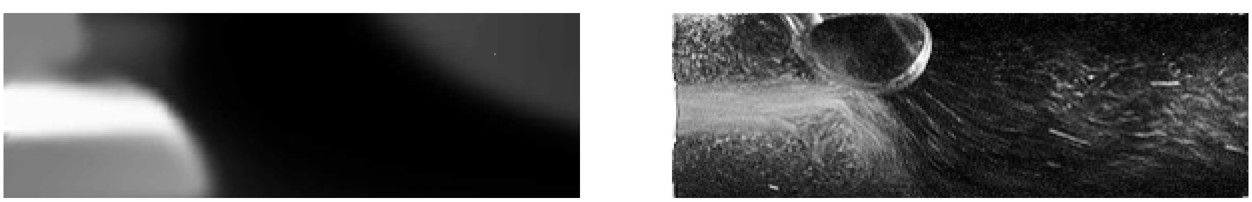

Configuration 17, air inlets 60^{o}, 51mm diameter, fuel inlet 27mm, centrally-located, dome height 100mm, air/fuel mass flow ratio = 9.21, air/fuel momentum ratio = 11.98, combustor Re = 80104.

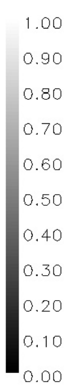

Figure 10 - Fuel mass fraction on centreline plane, CFD modelling and water tunnel tests for various configurations. Fuel mass fraction legend for CFD modelling to left.

The five pairs of images presented were chosen because they all have essentially the same air/fuel mass flow ratio and, compared to configuration 9 in the second pair, they each have only one parameter different. The top pair of images are for configuration 5 which has a small diameter air injector. This has the effect of increasing the air/fuel momentum ratio as compared to configuration 9, so the air jets are much more intense and abruptly cut off the fuel jet.

The third pair, configuration 11, has a smaller fuel injector than for configuration 9, so the air/fuel momentum ratio is smaller. Despite being deflected downward somewhat, the fuel jet shoots past the air jets and therefore its dissipation before the main combustor region is limited. In configuration 13, the fuel inlet port is lowered with respect to configuration 11, and this has a positive influence on the mixing. The fuel jet is cut off more abruptly by the air jets in this position.

The last configuration is the same as configuration 9 except the dome height is increased to 100mm. Since the fuel jet is already well cut off by the air jets and turns back toward the dome region by recirculation, increasing the dome height has no apparent advantage at this air/fuel momentum ratio.

In each case, areas of high fuel concentration in the water tunnel images correspond quite well to those in the CFD plots. Because the differences between the two techniques in the other regions of the flowfield could be explained by phenomena such as reflections, scattering, and variation in laser intensity, there was no evidence to doubt the CFD modelling results. As such, only CFD was used to evaluate the mixing for several additional configurations.

CFD visualization

Since the centreline contour plots provided only a limited view of the mixing within the combustor, much more extensive visualization was done with the CFD results. This visualization provided much better understanding of the mixing, but to generate the same number of images with the water tunnel would have not been practical. Figures 11-14 are contour plots of fuel mass fraction at many different cross-sections. In each case, the air/fuel mass flow ratio is essentially the same. A scale of 0% to 30% was chosen since this better highlighted the differences between the configurations. Completely mixed air and fuel at these mass ratios would correspond to a fuel mass fraction of approximately 10%. The fuel rich areas of 30% and above fuel mass fraction are white, and the lean areas are black. Configuration 5 shown in Fig. 11, with 38mm diameter air injectors and a 27mm diameter fuel injector, has a dome region that is fuel rich but has some entrained air from recirculation. In the air injector area there are zones of greatly varying concentration. The main fuel jet is swept along by the vortical structures created by the air jets from the air inlet section into the main combustor region. Toward the end of the combustor the cross-sections appear to have a uniform fuel mass fraction, except for a small leaner band against the wall.

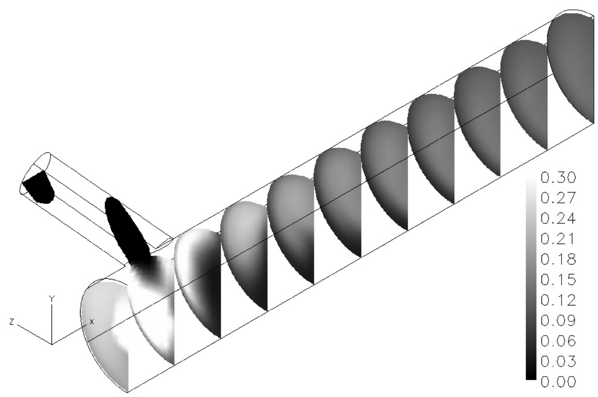

Figure 11 - Fuel mass fraction, configuration 5

Configuration 9, with 51mm air inlets and a 27mm diameter fuel injector, has a richer dome region mixture than for configuration 5 due to its lower inlet air velocities. The main mixture patterns are somewhat similar to the previous configuration, but the cross-sections are not as uniform in fuel concentration. There is also a larger lean area against the combustor wall.

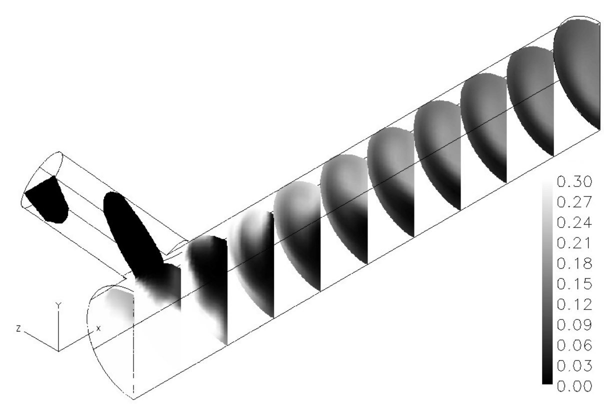

Figure 12 - Fuel mass fraction, configuration 9

Configuration 11 in Fig. 13 has the same air injector as configuration 9, but a smaller 18mm diameter fuel injector and therefore higher fuel momentum. As seen, there is more air at the top part of the dome region, and the fuel jet appears to remain intact as it passes through the air inlet section. The jet continues along the lower combustor wall, leaving a lean area on the top part of the main combustor all the way to the exit.

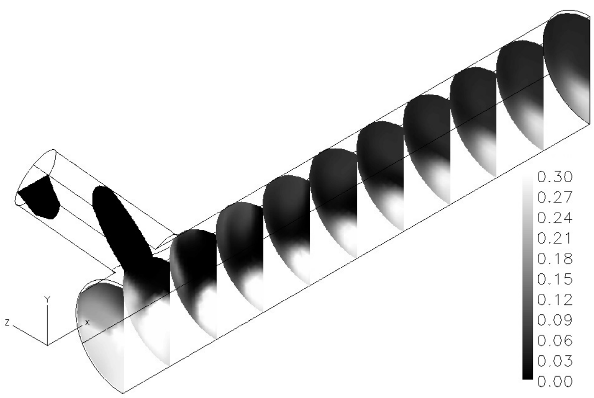

Figure 13 - Fuel mass fraction, configuration 11

Figure 14 shows a configuration that was not tested in the water tunnel. The previous results indicated that high injection velocities promoted better mixing as long as the air/fuel momentum ratio was high enough to prevent the fuel jet from passing through the air inlet section. A combination of the smaller air and fuel injectors was therefore modelled. The dome region has a fuel mass fraction almost everywhere above 30%, and while this mixture is swept along in a similar way to configurations 5 and 9, it is more uniform at the end of the combustor than for the other configurations.

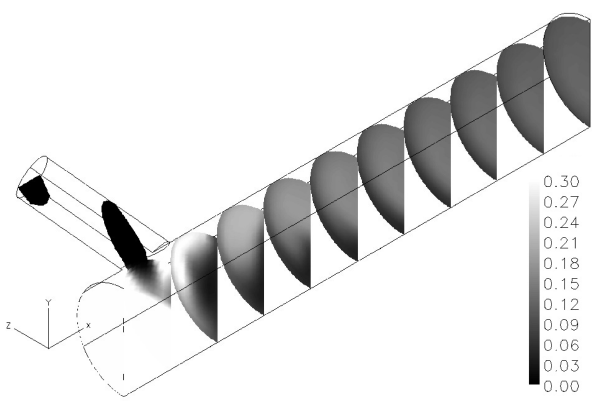

Figure 14 - Fuel mass fraction, configuration 39

CFD modelling: water tunnel versus air/fuel flowfield.

The water tunnel and CFD studies provided data to better choose several configurations worthy of further study in actual combustion tests. However, one question that remained was whether or not using the same air/fuel momentum ratio in the combustion tests, neglecting the effect of chemical reactions, would result in similar flowfields to those seen or modelled with the water tunnel. With the same geometry and combustor dimensions, realistic boundary conditions such as temperatures, densities, and velocities were chosen for the actual fuel and air inlet flows in a mass flow ratio that would give the same air/fuel momentum ratio as for the CFD and water tunnel studies. Configuration 1 was chosen for these calculations, and used 38mm diameter air inlets with an injection angle of 60^o, a 27mm diameter centrally-located fuel inlet, a dome height 57mm, and an air/fuel momentum ratio of 5.3. In the case of the water tunnel, properties of water were used. For the air/fuel tests, properties of gas generator exhaust (from a mainly glycidyl azide polymer fuel) were used for the fuel inlet flow, and properties of vitiated air for the air inlet flow. The flowfields were assumed to be non-reacting and incompressible. The following boundary conditions were used for the water tunnel and air/fuel test flowfield simulations:

	Water Tunnel	Air/fuel Tests
Air inlet velocity [m/s]	2.5	222.7
Fuel inlet velocity [m/s]	2.167	324.5
Air inlet density [kg/m^3]	1000	2.897
Fuel inlet density [kg/m^3]	1000	0.9537
Dyn. Viscosity [kg/ms]	0.0009	0.000025
Air/fuel mass flow ratio	4.59	8.02
Air/fuel momentum ratio	5.30	5.30
Combustor Re	88379	844565

Table II - Boundary conditions and properties for configuration 1, water tunnel and air/fuel tests

As seen, the Reynolds numbers varied by an order of magnitude, but as discussed previously the water tunnel results showed no Re-dependence between 40000 and 80000, and should not at values above. The air/fuel mass flow ratios differ greatly, and the velocity ratios somewhat, but the following graphs will indicate that the critical parameter to describe the flowfield is air/fuel momentum ratio. The next graph shows the mole fraction of fuel for both the water tunnel and the combustion tests on the centreline plane, 57mm from the head and in the middle of the air inlet section. Here

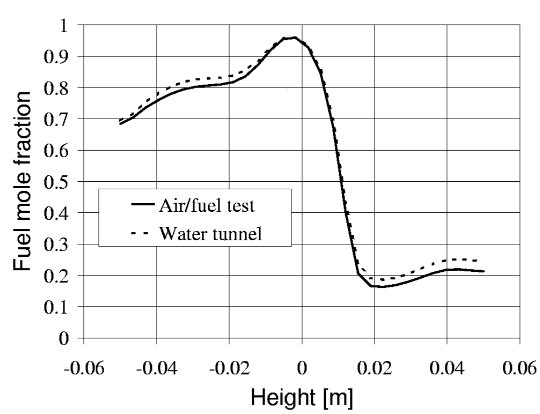

Figure 15 - Fuel mole fraction on centreline plane at X=0.057m

the fuel concentration and velocities vary greatly, and in the case of the combustion tests, density does as well. However, despite all of these differences in the fluid properties, Fig. 15 shows excellent agreement between the water tunnel and combustion test flowfields.

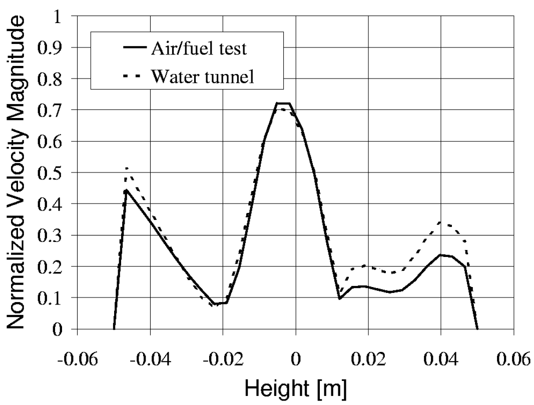

Figure 16 - Normalized velocity magnitude on centreline plane at X=0.057m

Figure 16 shows velocity magnitude normalized by the maximum velocity in the combustor for the two cases. The centres of the flowfields are virtually identical, but some differences exist toward the walls of the combustor. The greatest difference occurs near the top of the combustor where the velocities are very low. However, as seen previously in Fig. 15, the effect of this discrepancy is minor. For the contour plot on the centreline plane in Fig. 17, the fuel distributions are virtually identical.

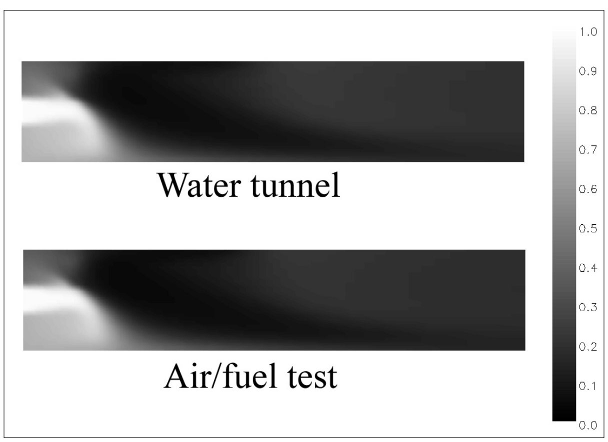

Figure 17 - Mole fraction of fuel on the centreline plane

CONCLUSIONS

The results from water tunnel experiments and CFD modelling provided credible data to choose geometries and test conditions configurations that could be expected to perform well in the direct-connect combustion tests.

The shapes of the fuel jets correlate well between the water tunnel images and the CFD modelling for fuel concentration on the centreline plane.

High inlet velocities were associated with good mixing, but only at high enough air/fuel momentum ratios.

Additional CFD modelling using boundary conditions expected in the combustion experiments confirmed that air/fuel momentum ratio was a critical parameter to describe the flowfield in the combustor. The mixing seen in the water tunnel CFD and experiments could therefore be expected in the combustion tests, as long as the air/fuel momentum ratio was the same. Differences in the velocity field occurred only where the velocities were low, and had little effect on the fuel distribution.

REFERENCES

1. Hawk, W.H., "Experimental Investigation of Pressure Oscillations in a Side Dump Ramjet Combustor", Journal of Spacecraft and Rockets, Vol. 19, No. 1, pp 47-53, January-February 1982.

2. Choudhury, P.R., "Characteristics of a Side Dump Gas Generator Ramjet", AIAA paper 82-1258, AIAA/SAE/ASME 18th Joint Propulsion Conference, Cleveland, Ohio, 1982.

3. Zetterström, K-A., Sjöblom, B., and Jarnmo, A., "Solid Ducted Rocket Engine Combustor Tests", Proceedings of the Sixth International Symposium of Air Breathing Engines, ISABE paper 83-7001, 1983.

4. Stull, F.D., Craig, R.R., Streby, G.D., and Vanka, S.P., "Investigation of a Dual Inlet Side Dump Combustor Using Liquid Fuel Injection", AIAA paper 83-0420, AIAA 21st Aerospace Sciences Meeting, Reno, Nevada, 1983.

5. Cherng, D.L., Yang, V., and Kuo, K.K., "Numerical Study of Turbulent Reaction Flows in Solid-Propellant Ducted Rocket Combustors", Journal of Propulsion and Power, Vol. 5, No. 6, pp 678-685, November-December 1989.

6. Dijkstra, F., Mayer, A.E.H.J., Smith, R.A., Wilson, K.J., and Schadow, K.C., "Ducted Rocket Combustion Experiments at Low Gas Generator Combustion Temperatures", AIAA paper 95-2415, AIAA/SAE/ASME 31st Joint Propulsion Conference, San Diego, California, 1995.

7. Schadow, K.C., "Boron Combustion Characteristics in Ducted Rockets", Combustion Science and Technology, Vol. 5, pp 107-117, 1972.

8. Tsujikado, N., Kashikawa, I., Harada, T., and Dohke, K., "Static Firing Tests of Experimental Ram-Rocket with Highly Boron Loaded Solid Propellant Type Fuels", ISABE paper 87-7028, 1987.

9. Vigot, C., Cochet, A., and Guin, C., "Combustion Behaviour of Boron-Based Solid Propellants in a Ducted Rocket", in *Combustion of Boron-based Solid Propellants and Fuels*, pp 386-401, CRC Press, Boca Raton, Florida, 1993.

10. Hebrard, P., Lavergne, G., Torgue, A., Bismes, F., and Heid, G. "Prédiction des Performances en Combustion de Stato-réacteurs et Stato-fusées par Expérimentations Isothermes et Modélisations", Paper No. 37 in *Airbreathing Propulsion for Missiles and Projectiles*, AGARD-CP-526, 79th AGARD PEP Symposium, Villepreux, France, 1992.

11. Brophy, C.M. and Hawk, C.W., "A Flow Visualization Facility for Ducted Rocket Engine Mixing Studies", AIAA paper 95-2934, AIAA 31st Joint Propulsion Conference, San Diego, California, 1995.

AIAA-2000-3728

MODELLING COMBUSTOR PERFORMANCE OF A DUCTED ROCKET

R.A. Stowe*, Defence Research Establishment Valcartier, Québec, Canada
A. De Champlain†, Université Laval, Québec, Canada
A.E.H.J. Mayer‡, TNO Prins Maurits Laboratory, The Netherlands

ABSTRACT

Under a co-operative program, the Defence Research Establishment Valcartier and Université Laval in Canada and the TNO Prins Maurits Laboratory in the Netherlands have studied the use of a ducted rocket for missile propulsion. Previously, non-reacting flow modelling using CFD (Computational Fluid Dynamics) and water tunnel tests were performed on a wide range of configurations to identify the geometries and flow rates necessary for good air/fuel mixing in the ramjet combustor. Hot-flow direct-connect combustion experiments using both simulated and solid fuels have since been carried out on these same configurations to measure actual combustor performance. Using a PDF (Probability Density Function) combustion model, reacting flow CFD modelling has also been done for each of these configurations with the goal of being able to analyze and predict combustor performance. Agreement between the measured and calculated temperature-based efficiencies was good for some configurations, but the overall tendency was to overestimate with the CFD. The differences are likely due to incorrectly specifying the boundary conditions and inaccuracies due to how the flowfield, turbulence and combustion were modelled.

INTRODUCTION

The Defence Research Establishment Valcartier (DREV) and Université Laval in Canada and the TNO Prins Maurits Laboratory (TNO-PML) in the Netherlands have undertaken a collaborative activity to study the use of a ducted rocket for missile propulsion. This type of motor has several advantages over solid fuel rocket motors including increased range, higher speed, and throttleability, but only a limited increase in complexity. Once launched, the ducted rocket missile is accelerated to supersonic speed with the integrated rocket booster (Fig. 1). Once the booster propellant is

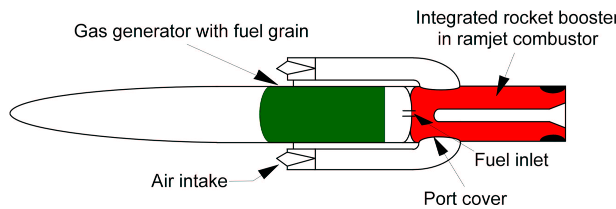

Figure 1 - Ducted rocket missile

completely burned to leave an empty ramjet combustor, the port covers that seal the air intakes from the ramjet combustor open and, simultaneously, the gas generator ignites. Fuel-rich exhaust from the gas generator is mixed with incoming air in the ramjet combustor, reacts, and is accelerated through a nozzle to provide thrust. This aspect of the overall ducted rocket propulsion system formed a major part of this collaboration, and included performing experiments at TNO-PML's direct-connect combustion test facility to determine combustor performance. Based on earlier non-reacting flow CFD (Computational Fluid Dynamics) modelling and water tunnel experiments, several simple configurations were identified for the direct-connect experiments. The geometries all had dual inlets spaced 90^{o} apart circumferentially since this is a favoured configuration for air-launched missiles. As Fig. 2 shows, they also used very long air inlets and main combustor bodies that would not be practical on a missile motor. However, they facilitated testing and determining the boundary conditions for the CFD modelling. A nozzle was added at the end of the combustor for the direct-connect combustion

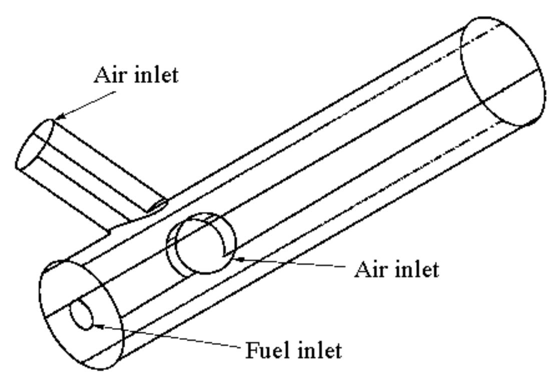

Figure 2 - Basic geometry

* Scientist, Propulsion Group, Senior Member AIAA
† Associate Professor, Mechanical Engineering
‡ Propulsion Engineer, Rocket Technology Group

experiments. A practical ducted rocket motor has inlets that hug the side of the combustor and their ends face directly forward, as shown in Fig. 1. During flight, the dual inlets would normally be below the missile as well.

This paper briefly describes the direct-connect combustion experiments, and then describes the particulars and the results of the reacting flow CFD modelling that was carried out. Estimates of combustor performance from the CFD modelling and experimental data are then compared. Reasons for the differences are given as well an assessment on the use of CFD modelling to analyze and predict ducted rocket combustor performance.

DIRECT-CONNECT COMBUSTION TESTS

All combustion experiments were carried out at TNO-PML's indoor direct-connect test facility. High-pressure air was heated by a methane-fuelled vitiator to produce stagnation conditions at the combustor representative of those downstream of the air intakes of an actual missile flying at supersonic speed. The ducted rocket hardware (Fig. 3) was based on an inside diameter of 100 mm and was modular so pieces could be easily changed to allow for different fuel and air injectors, combustor lengths, and nozzles. For all of the direct-connect experiments in this paper, the combustor was always 458 mm long from the head to the beginning of the nozzle. A 1-m diameter plenum surrounded the air injector and most of the combustor. It was designed to allow equal air mass flow rates through each of the arms of the air injector. Honeycomb in the entrance of each of the arms of the injector straightened the flow. For the fuel, the hot, reacted exhaust from the gas generator was expanded through a nozzle before entering fuel plenum upstream of the injector; this meant that the exhaust was not choked in the fuel injector before entering the ramjet combustor. More details on the experiments can be found in Reference 1.

CFD MODELLING

Computational fluid dynamics (CFD) modelling was carried out using a code known as FLUENT (Version 5). A control-volume-based technique is used within FLUENT to discretize the conservation equations for mass and momentum, otherwise known as the Navier-Stokes equations. If required, additional equations for turbulent transport, species, and energy conservation can be solved. The segregated solver option was used which means that the governing equations are solved sequentially. While FLUENT Version 5 can use unstructured meshes, all geometries were modelled as precisely as possible with structured grids of approximately 50,000 hexahedral cells (Fig. 4) for half the domain (symmetrical about the central longitudinal plane). These were the same meshes created for previous CFD modelling of the same geometries for the water tunnel work [Ref. 2]. FLUENT Version 4 was used for this earlier work and could handle only structured meshes.

FLUENT allows the user to choose from a variety of turbulence and combustion models. Flow in a ducted rocket combustor can be characterized as highly turbulent (Reynolds numbers on the order of 10^6). The Renormalized Group Theory (RNG) turbulence model was chosen rather than the more common k-ε model; the RNG model is thought to yield superior results to the k-ε model for the recirculating, swirling, and separated flow that occurs within a ramjet combustor. Since the fuel and air inlet streams are separate and the

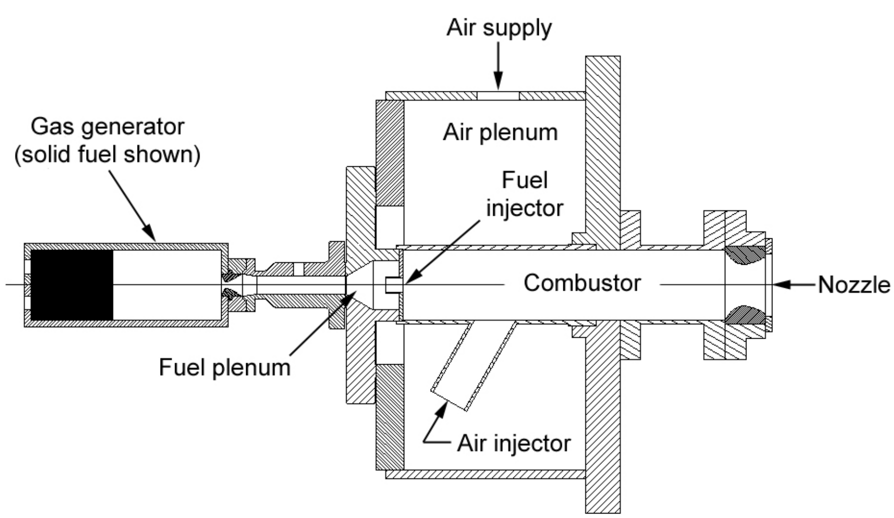

Figure 3 – Direct-connect test hardware

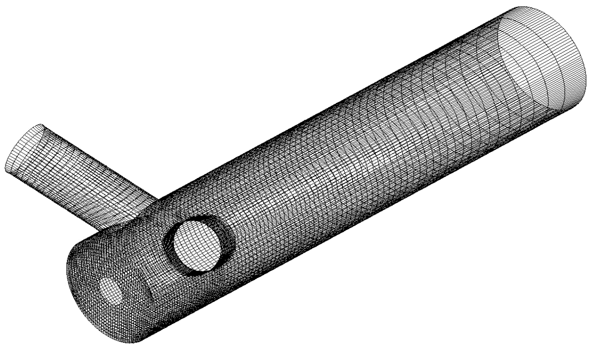

Figure 4 - Surface mesh of basic combustor geometry

flowfield highly turbulent, the combustion can be characterized as a turbulent diffusion flame. If the chemical reaction time is also much less than the time it takes for the reactants to mix, the combustion can be modelled using the PDF (Probability Density Function) approach [Ref. 3]. For the results presented here, a β-shaped PDF accounts for the turbulence-chemistry interaction. If the assumptions about the combustion hold, the advantage of the PDF approach is that only two additional transport equations have to be solved, rather than one equation for each chemical reaction in a finite-rate chemistry model. These two additional equations are for the transport of the mixture fraction and its variance. For the results presented in this paper, at each point in the combustor, up to a rich limit, the reactants are assumed to reach thermochemical equilibrium. For this assumption to be valid, temperatures in the combustor must be high enough. Another restriction in FLUENT's implementation of the PDF approach is that the flowfield is assumed incompressible. In most of the combustor the Mach number is less than 0.3, the exceptions being in the air and fuel inlets and at the nozzle. Since the flow had to be assumed incompressible, the nozzle at the end of the combustor was not modelled.

Also to keep in mind with the CFD modelling is that FLUENT, using the Reynolds averaged Navier-Stokes equations, gives a time-averaged output of the flowfield, whereas the combustor flowfields during the direct-connect experiments are unsteady and therefore change continuously with time.

The baseline dimensions for all of the modelling were a combustor diameter of 100 mm and a length of 500 mm. Adiabatic walls were assumed. The various geometries had different air and fuel inlet diameters, locations, and injection angles.

BOUNDARY CONDITIONS

Constant velocity inlet profiles at the fuel inlet and the beginning of the long air inlet tubes were assumed, along with a turbulence intensity of 10% and a turbulence characteristic length 25% of the inlet diameters. Vitiated air of approximately 600K entered at the air inlets. For all configurations, measured data from the direct-connect tests, including pressures and temperatures, were used to calculate and establish the boundary conditions as much as possible. Therefore the measured flow rates for the experimental tests were used as the flow rates for the CFD modelling for each configuration.

Characterizing the fuel inlet boundary conditions is much more challenging. Several of the direct-connect combustor experiments used a solid gas generator fuel based on glycidyl azide polymer (GAP), and included 10% carbon black (solid carbon particles). For the remainder of the tests, however, which formed the bulk of the experimental program and most of the results presented here, a partially reacted mixture of ethylene and air was used to simulate the solid fuel exhaust. Its flow rate was easier to control and it cost much less to use than solid fuel. The ratio of ethylene and air was chosen to give a composition similar to the solid fuel exhaust. However, thermochemical equilibrium, especially for these fuel rich conditions, may not be approached and the results of these calculations may not be a good estimate of the exhaust composition. Table I shows the results of these calculations from the CET 89 program for the gas generator fuel decomposing at a chamber pressure of 6.895 MPa and ideally expanded through a nozzle to ambient conditions (0.1 MPa). Some preliminary work on experimentally characterizing the exhaust has been

TABLE I
Calculated gas generator exhaust properties

	Chamber conditions	Nozzle exit, equilibrium	Nozzle exit, frozen flow
Temp [K]	1424.48	903.12	676.42
Vel [m/s]	0	1799.9	1742.8
	Mole fractions including condensed phase		
CH4	0.02962	0.03022	0.02962
CO	0.11527	0.04596	0.11527
CO2	0.00202	0.01977	0.00202
C2H4	0.00002	0	0.00002
C2H6	0.00001	0	0.00001
HCN	0.00013	0	0.00013
H2	0.26933	0.23522	0.26933
H2O	0.01067	0.04454	0.01067
NH3	0.00054	0.00011	0.00054
N2	0.18689	0.18726	0.18689
C(GR)	0.3855	0.43692	0.3855
Total	1	1	1

carried out for the solid fuel [Ref. 4] and the results indicate that thermochemical equilibrium may be reached in the gas generator chamber, but that the composition remains frozen during expansion. However, to simplify the modelling and in the absence of definitive temperature and species measurements of the exhaust, we have assumed that thermochemical equilibrium is maintained from the gas generator chamber and through expansion to the ramjet combustor pressure for the estimation of the fuel boundary conditions.

With the PDF combustion model, any inaccuracy in the exact species composition of the gas generator exhaust should not cause a large error in the energy released by the reactions where the assumption of thermochemical equilibrium holds in the ramjet combustor in the leaner, hotter regions. However, close to the fuel inlet, the exact species composition profoundly influences the physical properties of the fuel stream. Apart from geometry, the previous CFD modelling and water tunnel experiments [Ref. 2] showed the importance of the momentum ratio of the air and fuel streams on mixing. A change in the proportion of solids and/or the overall molecular weight of the gases in the exhaust will therefore alter this momentum ratio. For example, a small change in the mole fraction of hydrogen, a gas which may be present in significant quantities in the exhaust, can greatly change this momentum ratio since its molecular weight is an a order of magnitude less than most of the other gases present.

As Table I shows, solids make up a significant proportion of the fuel stream. Some results are shown here for particle samples taken from both ethylene/air and GAP/C solid fuel exhausts and analyzed in a Malvern Mastersizer 2000. Ethylene/air sampling has initially produced a wide range of particles from below 0.1 micron to 200 microns (Fig. 5). For the GAP/Carbon solid fuel, solids collected from earlier experiments [Ref. 4] and reanalyzed with this newer Malvern particle analyzer appear to be mainly carbon particles from less than one micron to 200 microns in diameter, with some larger particles as well. At the larger sizes, the residence time of the particles in the ramjet combustor may not be long enough for the particles to decompose and react. Modelling the combustion, if using the PDF approach, should include two fuel streams, one of gases and the other of particles. This also necessitates the use of a particle model so the time-dependence of energy release from the reacting particles is addressed correctly. Some preliminary CFD modelling has shown a strong dependence of particle size on heat release in the combustor. For the direct-connect experiments that used ethylene/air as the fuel, however, the simpler single stream PDF approach was used. The solid carbon or soot is assumed to act like the gaseous components of the fuel mixture, and must decompose and react instantaneously once in the ramjet combustor in the presence of oxygen. The ethylene/air experiments have therefore all been modelled using a single fuel stream.

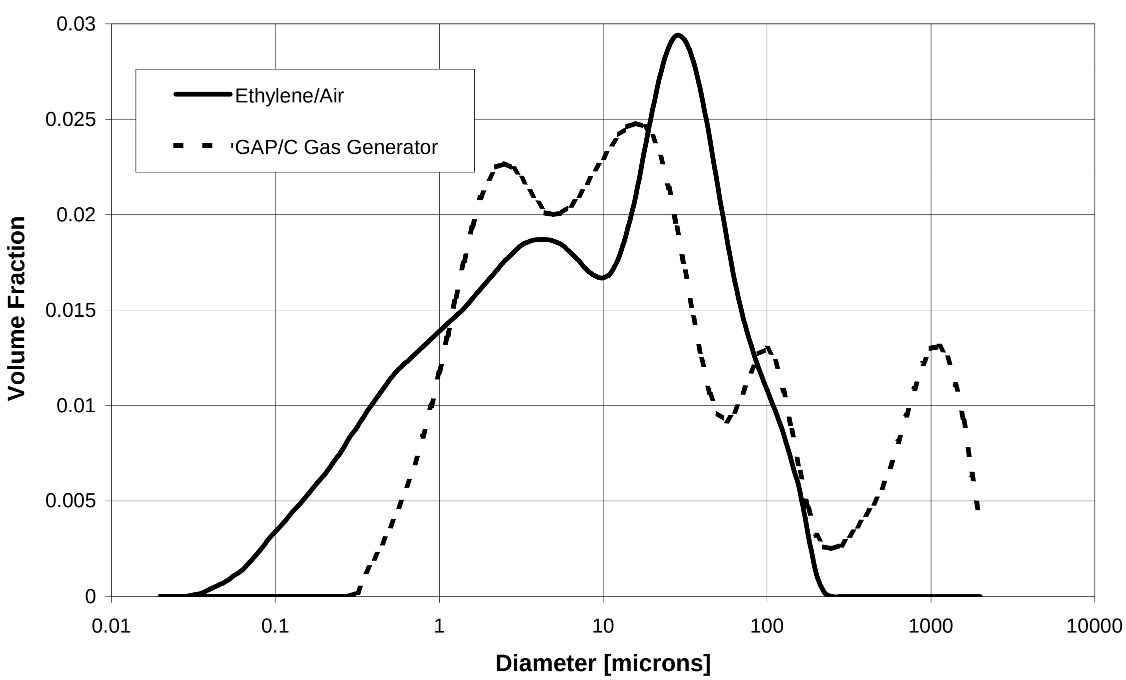

Figure 5 – Graph of particle sizes

SINGLE FUEL STREAM MODELLING RESULTS

Configurations

Several combustor configurations (Fig. 6) using three different fuel injectors and three different air injectors (Table II) were modelled and tested in the direct-connect facility. All combustion efficiencies calculated from the CFD results therefore used mass-averaged temperatures at the 458-mm cross section. The F1-18 fuel injector had its fuel port on the side of the combustor opposite to the air injector arms as shown in Fig. 6; the F1-18S fuel injector had its port on the same side as the arms.

Some of these configurations were modelled and tested at dome heights of 57 and 100 mm, and at different air/fuel momentum ratios. The configurations for which both CFD modelling and direct-connect ethylene/air experimental data are available are listed in Table III. The average fuel and air inlet velocities and the air/fuel momentum ratio are calculated from the experimental pressure and temperature data. Any numbers not listed are duplicate tests or used solid fuel, except for configuration 4 that was excluded because of a very low ethylene temperature.

TABLE II
Air injector geometries

Model	Air inlet angle	Air inlet diameter
A2	60^o	38.1 mm
A4	60^o	50.8 mm
A6	90^o	50.8 mm

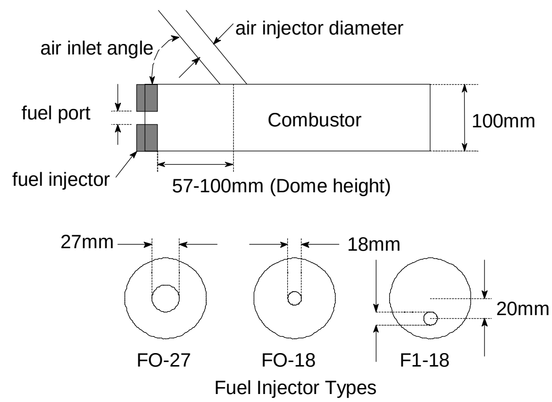

Figure 6 - Schematic of combustor and fuel injectors

TABLE III
Combustor configurations

No	Air Injector	Fuel Injector	Dome Height mm	Air/fuel Momentum Ratio	Air/fuel Mass Ratio	Combustor Pressure MPa	Fuel Velocity m/s	Air Velocity m/s
1	A4	F0-27	57	2.62	7.79	0.396	415.54	139.97
2	A4	F0-27	57	11.73	15.73	0.403	328.03	244.59
3	A4	F0-27	57	8.89	13.84	0.875	281.92	181.13
6	A2	F0-27	57	3.90	7.09	0.411	443.33	243.73
7	A2	F0-27	57	19.43	15.76	0.426	311.30	383.64
8	A2	F0-27	57	17.94	14.96	0.944	239.27	286.91
9	A2	F0-27	57	3.52	6.70	0.845	608.81	320.31
11	A4	F0-18	57	4.87	15.36	0.432	709.89	225.25
12	A4	F1-18	57	4.07	13.96	0.907	599.92	174.88
13	A6	F0-27	57	2.30	7.00	0.44	435.97	142.86
14	A6	F0-27	57	10.80	15.33	0.419	324.26	228.57
15	A6	F0-27	57	5.20	10.66	0.904	358.15	174.78
16	A6	F0-27	57	2.37	7.11	0.8	598.99	200.03
18	A4	F0-27	100	2.13	6.65	0.397	501.02	160.17
19	A4	F0-27	100	10.93	15.35	0.423	317.35	226.12
20	A4	F0-27	100	8.31	13.34	0.882	287.96	179.30
21	A4	F0-27	100	2.76	7.62	0.792	564.41	204.70
28	A4	F1-18	57	4.84	15.32	0.44	692.33	218.53
29	A4	F0-18	57	4.31	14.30	0.917	577.94	174.10
30	A4	F1-18S	57	4.29	14.34	0.921	578.52	173.09

Comparison of Two Configurations

A comparison of configurations 1 and 2 shows how the CFD results can help explain the combustor performance results for a change in configuration. Both configurations use a similar combustor geometry with an A4 air injector and a F0-27 fuel injector.

The previous water tunnel experiments and CFD modelling [Ref. 2] showed that while the exact flow patterns could vary greatly with each configuration, particularly with air/fuel momentum ratio, two basic flow features appeared to be common. The first is a recirculation zone from the air inlet section into the dome region. Its exact shape was dependent on the relative strength of the fuel jet. In Fig. 7, which compares mean mixture fraction, configuration 1 has an air/fuel momentum ratio of 2.62. Since the fuel momentum is relatively high, only part of the fuel jet, entering the combustor from the left, turns back into the dome region. However, in configuration 2, the air/fuel momentum ratio is 11.73 so the recirculation is much stronger; most of the fuel recirculates and has more opportunity to mix with the air. While Fig. 7 seems to show better mixing with configuration 1, this is only on the centreline plane. This can be seen in Fig. 8 which shows an isometric view of several cross-sections of the combustor, spaced at 100 mm intervals, from the head at the lower left to the end of the combustor at the upper right. Toward the nozzle end, configuration 2 has hotter cross-sections than configuration 1. Evidence of the second basic flow structure, which is a pair of longitudinal vortices structures that are a continuation of the high-speed flow from the air inlets, can be seen in the temperature field near the combustor wall towards the nozzle for configuration 2. These structures carry the mixture from the head end outward to the walls. Because of the higher fuel momentum in configuration 1, this does not occur. The greater recirculation of the fuel in the head end of configuration 2 therefore results in higher temperatures and efficiency in the combustor than for configuration 1.

Parametric Study

With configuration 1 as a baseline, several of the parameters that could be adjusted for the modelling were examined for their impact on the calculated combustion efficiency. The baseline parameters and models for the CFD calculations, also used for all the subsequent calculations to be shown later, used the same turbulence and combustion models and boundary conditions as previously described. The grid used 56688 cells and adiabatic walls were assumed. Figure 9 shows the calculated efficiencies based on combustor temperature rise at various cross-sections for the baseline CFD model for configuration 1 and for different turbulence parameters, models, and a doubled grid. As seen, doubling the turbulence length scale has a very small effect on calculated efficiency. Doubling the resolution of the grid in each direction so that there are eight times the number of cells will give an indication of the grid dependency of the solution. As seen, the finer grid reduces numerical diffusion, which has the same effect as reducing the mixing and therefore the efficiency by about 2% at the 458-mm cross-section. Going to a second order discretization scheme for the equations rather than the baseline first order scheme has a somewhat greater effect that depends on position in the combustor. The use of the k-ε turbulence model, not the

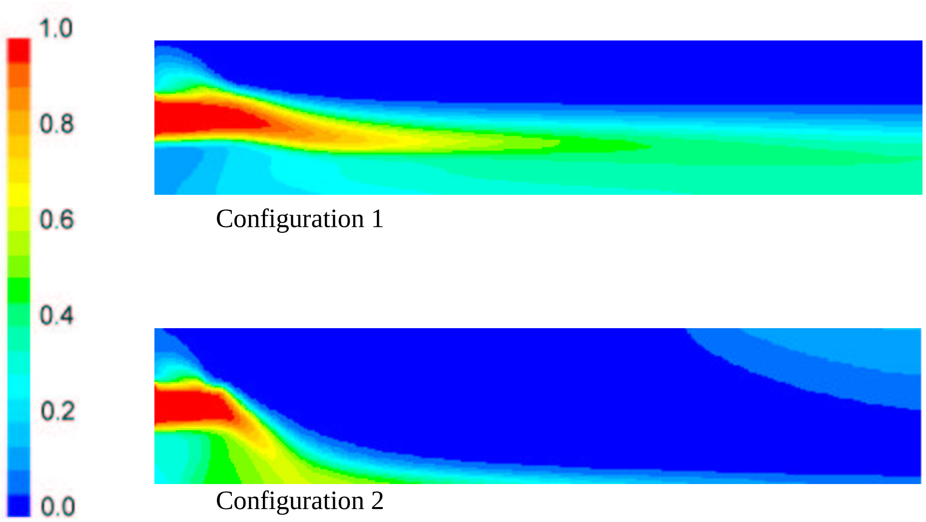

Figure 7 – Effect of momentum ratio on mean mixture fraction distribution, centreline plane, configurations 1 and 2

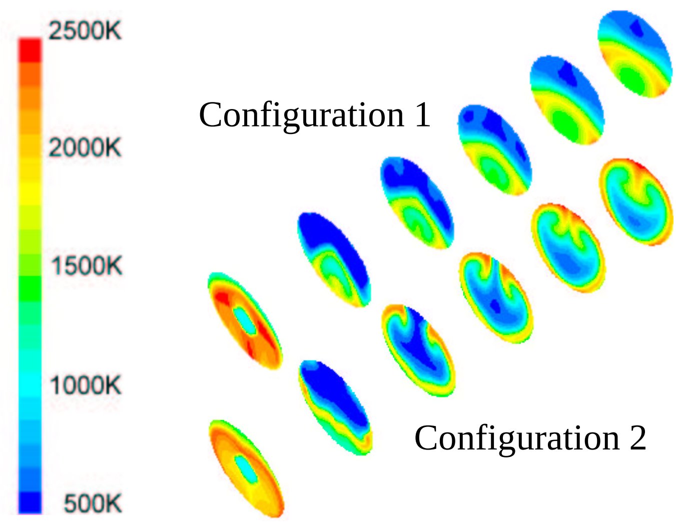

Figure 8 – Effect of momentum ratio on temperature distribution, configurations 1 and 2

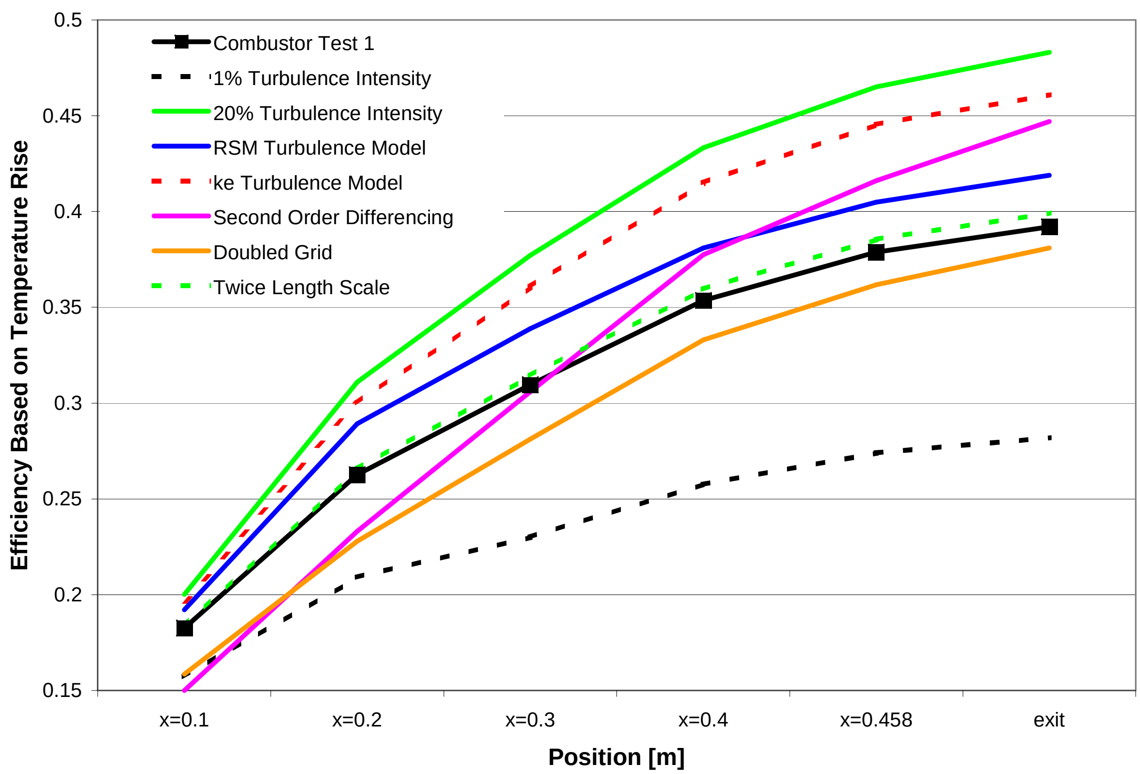

Figure 9 – Effect of turbulence parameters and models, grid, and discretization

best choice for this type of flow, increases the calculated efficiency by 6-7%. The Reynolds Stress Model (RSM) for turbulence has a much smaller impact on calculated efficiency, being only 2% at the 458 mm cross-section, but this model, like the RNG model, is better for this type of flow than the k-ε model. However, the largest effect comes from the turbulence intensity, and changing it to 1% or 20% from baseline 10% changes calculated combustion efficiency for this configuration up to 10%.

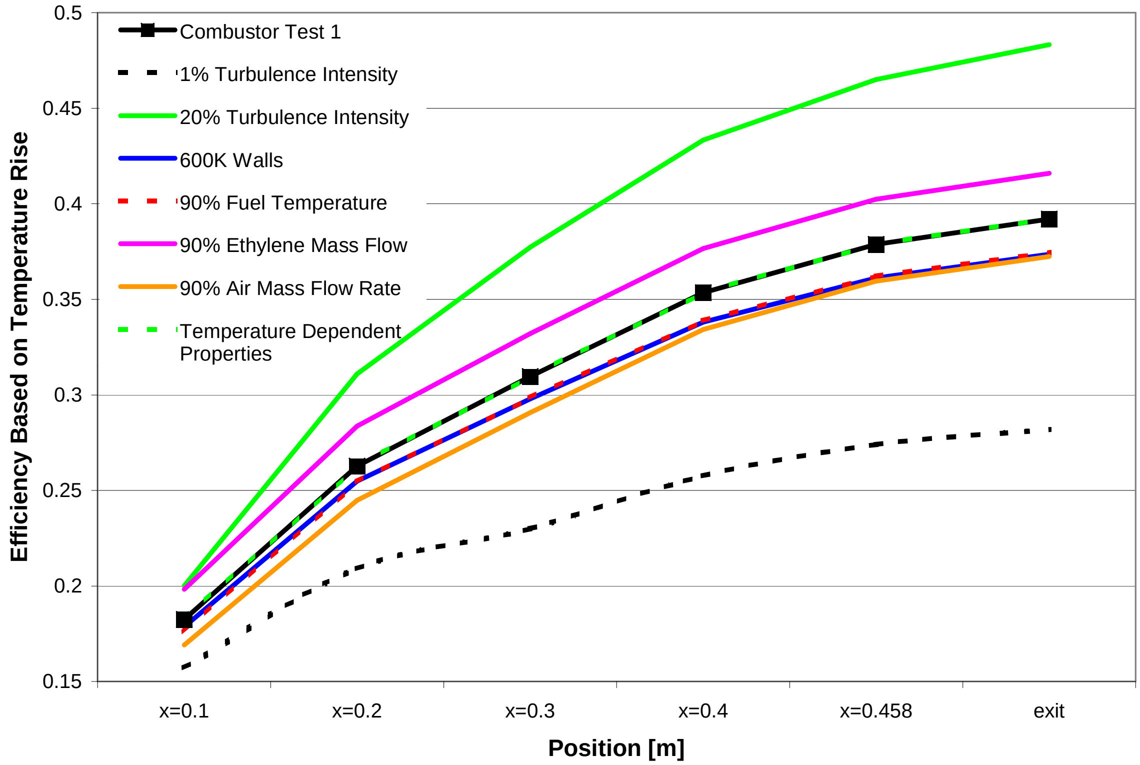

Figure 10 – Effect of temperature-dependent properties, isothermal walls, and changes in fuel temperature, ethylene mass flow rate, and air mass flow rate

Figure 10 shows the effect of using temperature-dependent fluid transport properties rather than constant values, the effect of using isothermal rather than adiabatic walls, and the effect of having a 10% change in fuel temperature, ethylene mass flow rate, or air mass flow rate. Since nitrogen is the predominate species in the combustor, the baseline model used constant values of $1.7894*10^{-5}$ kg/ms for viscosity and 0.0241 W/mK for thermal conductivity (nitrogen at 300K). The use of temperature-dependent polynomials for viscosity and thermal conductivity rather than these constant values had little effect, primarily because the conditions that render the situation suitable for modelling the combustion with a PDF approach also imply that these transport properties have little influence over the mixing. Next, the walls of the combustor were assumed to be isothermal at the same temperature as the incoming air at 600K (a good assumption for most of the combustor which was inside the plenum chamber). Allowing for this heat transfer from the flow only lowered calculated combustion efficiency by 2%. A similar 2% drop in combustion efficiency resulted from assuming a 10% drop in temperature of the fuel jet, which increases its density and decreases its velocity. Decreasing air mass flow rate also dropped combustion efficiency 2% at 458 mm, but lowering ethylene mass flow rate by 10% increased efficiency by a 2%. Also shown on the graph are the 1% and 20% turbulence intensity efficiencies, showing that turbulence intensity had a greater effect on the CFD results than any of the other parameters considered. Therefore properly characterizing the inlet turbulence intensities is a priority for improving the accuracy of the CFD modelling.

<u>Comparison with Experiments</u>

The direct-connect experiments for all configurations listed in Table III were reduced using the methods recommended by AGARD [Ref. 5]. Theoretical temperatures and characteristic velocities (c*) were calculated from static pressure measurements in the combustor and the CET89 thermochemical equilibrium combustion code. As previously mentioned, efficiencies based on temperature rise in the combustor were chosen to compare with the calculated CFD efficiencies from mass-averaged temperatures at the 458 mm cross-section, or at the beginning of the nozzle in the experimental combustor.

Figure 11 presents the results, and several of the configurations show very good agreement. However, for some of the combustors that have higher experimental efficiencies, the baseline CFD model for these configurations overestimates the temperatures and

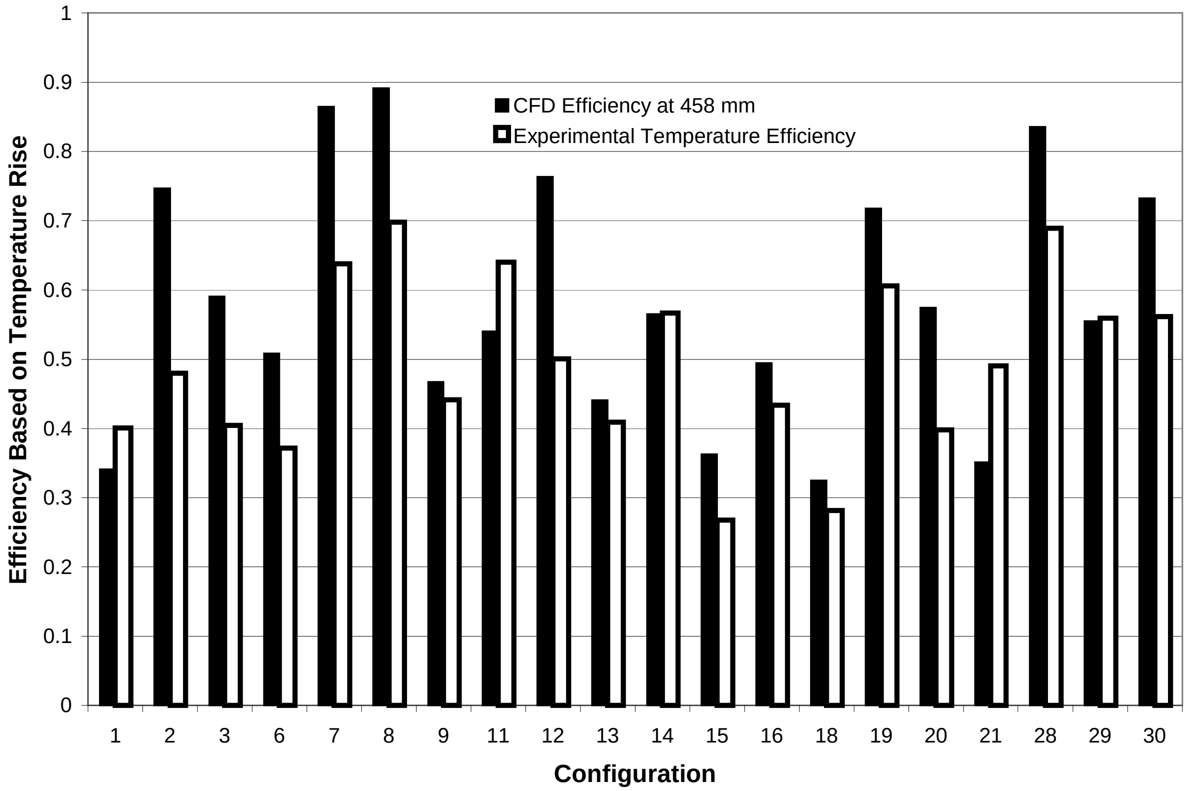

Figure 11 – Comparison of efficiencies based on temperature rise
between CFD modelling and direct-connect experiments

therefore the efficiencies. As seen from Figs. 9 and 10, though, overestimating the turbulence intensity could certainly account for some of the difference.

More evidence that the turbulence intensity may have been overestimated comes from the results for configurations 2 and 19. They are geometrically identical except that configuration 19 uses a longer dome height of 100 mm. Since a longer dome height enlarges the recirculation zone to improve the air/fuel mixing, a significant increase in efficiency was expected and was indeed seen in the experimental results. However, no such increase in efficiency is seen in the CFD results (Fig. 12). By redoing the CFD modelling for each configuration, but this time specifying inlet boundary conditions of 1% turbulence intensity rather than 10%, a clear difference in combustion efficiency results from an increase in dome height. This is because, at 10% turbulence intensity, the length of the recirculation zone for the shorter dome height is already sufficient for good air/fuel mixing and increasing the dome height provides no additional benefit. At 1% turbulence intensity, however, the benefit of increased dome height and a stronger recirculation zone is obvious with a significant increase in efficiency for the CFD results. The use of a lower turbulence intensity would also improve the agreement between the CFD and the experiments for these two configurations (Fig. 11).

Apart from turbulence intensity and other approximations and assumptions for the baseline CFD model already mentioned, other factors could also explain some of the difference between the CFD and experimental results. For the direct-connect tests, the uncertainty is estimated to be +/-5%, which is comparable to that estimated for temperature-based combustion efficiency in Refs. 5 and 6 for the AGARD method. Another important approximation in the modelling is that the CFD modelling gives a time-averaged output of the flowfield, whereas the flowfield in the experimental combustor is unsteady which results in pressure oscillations that are not considered in the model.

An important observation from the experimental results supports the assumption that mixing essentially controls the combustion and can justifiably be modelled with the PDF approach. Configurations 6 and 9, 7 and 8, 11 and 29, and 13 and 16 are pairs having identical geometries, similar momentum ratios, but one has a combustor pressure of approximately twice the other. If the combustion were kinetically controlled rather than mixing controlled, doubling the combustor pressure would result in a significant increase in reaction rate and therefore combustion efficiency. The decomposition of solid particles, if diffusion or kinetically controlled, will show

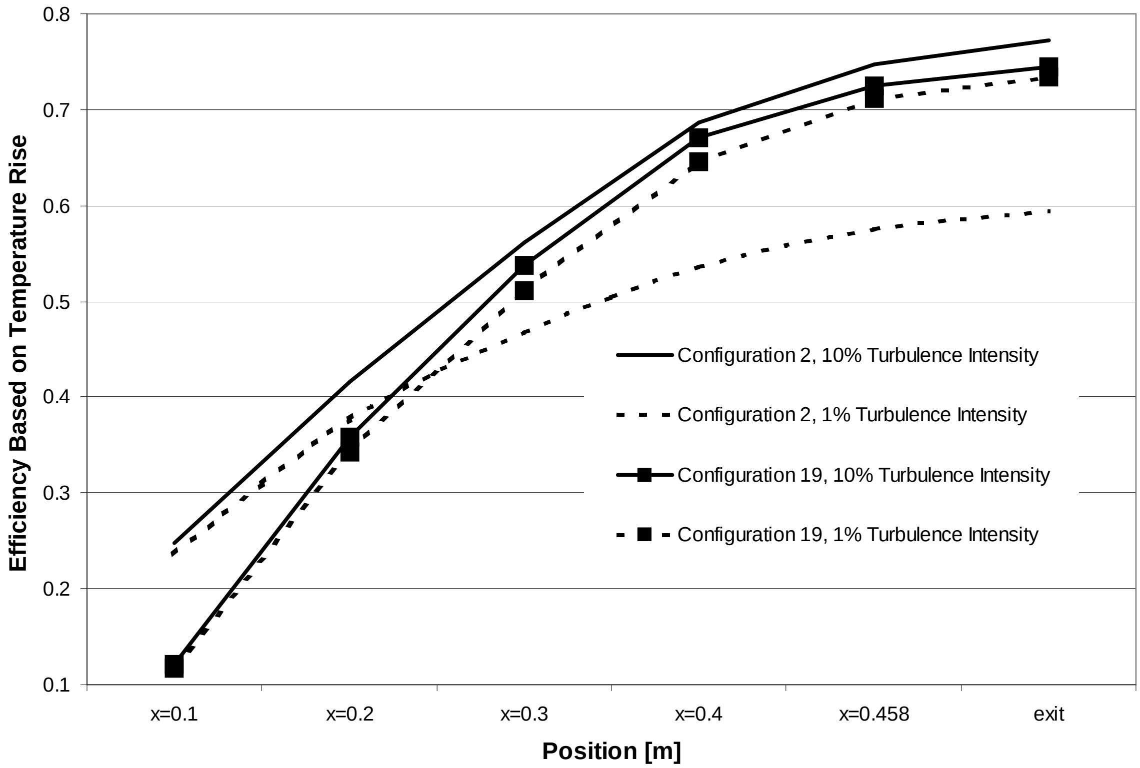

Figure 12 – Effect of turbulence intensity on configurations 2 and 19

pressure-dependency, but since solids account for only 25% (by mass) of the fuel, any dependence of efficiency on pressure should be overwhelmed by the increased reaction rate of the gases. In any case, significant differences in efficiency are not seen in the experimental results in Fig. 11.

Within the uncertainties and approximations mentioned above, the baseline CFD model can predict combustor efficiency. However, performance parameters of a ramjet-powered vehicle, such as cruising speed and range, are quite sensitive to the value assumed for combustion efficiency. Much effort should therefore be directed not only to accurately establishing the boundary conditions, particularly turbulence intensity, but also to reducing the uncertainty on the direct-connect experiments. Properly characterizing the gas generator exhaust, also critical to properly establishing the boundary conditions, should also be a priority.

TWO FUEL STREAM MODELLING RESULTS

As previously mentioned, to properly treat the decomposition of solids present in the fuel, modelling of the combustor should be done with a two fuel stream PDF approach. Some preliminary results are presented here to show the effect of carbon particle size on the temperature rise in the combustor. The configuration that was modelled used an A2 air injector with an F0-27 fuel injector and an air/fuel momentum ratio of 6.4. The gases in the gas generator exhaust were modelled as the primary fuel stream, and solid spherical particles of carbon as the second fuel stream. Both streams had the same initial temperature and velocity. The carbon particles make up about 25% of the entire fuel by mass. The decomposition of the particles is modelled as depending on the rate of oxygen diffusion to the surface. The product of the decomposition released as a gas from the particles is carbon monoxide. The calculation of the particle trajectories and decomposition was coupled with the flow of the gases.

As shown in Fig. 13, modelling the fuel as a single stream gives similar results to modelling it with a stream of gases and a separate stream of 1-micron carbon particles. The only significant differences are a smaller high temperature region and a larger moderate temperature region at the upper aft region of the combustor, which is due to the particles releasing their energy gradually. However, the fuel stream model with 100-micron particles shows no high temperature region at the aft end of the combustor because the residence time of this size particle is not long enough for it to decompose before exiting the combustor.

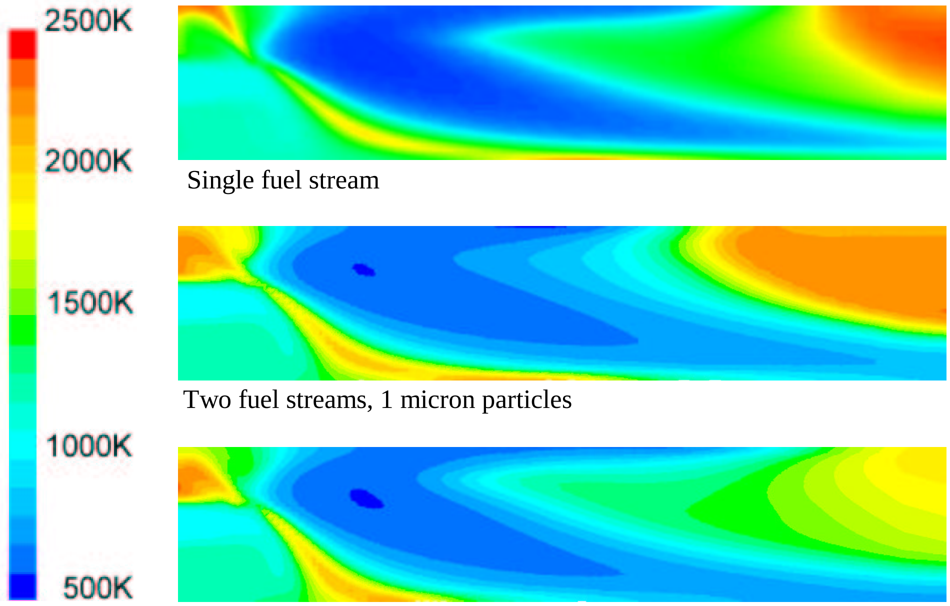

Single fuel stream

Two fuel streams, 1 micron particles

Two fuel streams, 100 micron particles

Figure 13 – Effect of fuel stream type on combustor temperature distribution, centreline plane

CONCLUSIONS

Efficiencies based on temperature rise calculated from the CFD results tend to be higher than those measured in the ethylene/air direct-connect experiments.

Characterizing the inlet boundary conditions properly, particularly the turbulence intensity and the fuel inlet species compositions and properties, would increase the accuracy of the CFD modelling the most.

The single fuel stream PDF model produced good results for the ethylene/air experiments. However, accuracy may be improved with a two fuel stream PDF and a suitable particle model.

For this program, the use of CFD modelling has helped analyze differences in combustor performance for the various configurations. Within the accuracy detailed in this paper, the baseline CFD model can predict ducted rocket combustor performance.

REFERENCES

1. Mayer, A.E.H.J., Stowe, R.A., and Dijkstra, F., “Experimental Study Into Mixing in a Solid Fuel Ducted Rocket Combustion Chamber”, AIAA-2000-3346, 2000.
2. Stowe, R.A., De Champlain, A., Mayer, A.E.H.J., and Niemeijer, S.F., “Modelling and Flow Visualization of Mixing in a Ducted Rocket Combustor”, AIAA-98-3768, 1998.
3. Kuo, K.K., “Principles of Combustion”, Chapter 7, John Wiley and Sons, New York, 1986.
4. Stowe, R.A., Dubois, C., Smithson, T., and De Champlain, A., “Preliminary Exhaust Characterization of a GAP/Carbon Ducted Rocket Fuel”, 24th Meeting of The Technical Cooperation Program, Technical Panel WPN/TP-4 Workshop, NSWC, Indian Head, Maryland, 15-16 April 1999.
5. Advisory Group for Aerospace Research and Development, “Experimental and Analytical Methods for the Determination of Connected-Pipe Ramjet and Ducted Rocket Internal Performance”, Propulsion and Energetics Panel Working Group 22, AGARD-AR-323, 1994.
6. Blevins, J.A. and Coleman, H.W., “Uncertainty Assessment of Ramjet Performance Determination in Connected-Pipe Testing”, AIAA-95-3074, 1995.

TWO PHASE FLOW COMBUSTION MODELLING OF A DUCTED ROCKET

R.A. Stowe*, C. Dubois†, and P.G. Harris‡, Defence Research Establishment Valcartier, Québec, Canada
A.E.H.J. Mayer§, TNO Prins Maurits Laboratory, The Netherlands
A. De Champlain¶ and S. Ringuette#, Université Laval, Québec, Canada

ABSTRACT

Under a co-operative program, the Defence Research Establishment Valcartier and Université Laval in Canada and the TNO Prins Maurits Laboratory in the Netherlands have studied the use of a ducted rocket for missile propulsion. Hot-flow direct-connect combustion experiments using both simulated and solid fuels have been carried out on a wide range of configurations to identify the geometries and flow rates necessary for good combustor performance. The experiments using a simulated ducted rocket fuel, a reacted mixture of ethylene and air, have all been modelled using reacting flow Computational Fluid Dynamics (CFD) with the goal of being able to analyze and predict combustor performance. The combustion was modelled with onestream and twostream PDF (Probability Density Function) models. With the onestream model, all of the fuel components, both gaseous and solid carbon, were injected together and were assumed to react instantaneously in the presence of the oxidizer. Because of this, the onestream model overpredicted the combustion efficiency with respect to the experimental results for most of the combustor configurations examined. With the twostream model, however, the fuel stream was separated into gaseous and solid carbon components, with the carbon injected as a series of 75 nm particles. These particles decompose gradually into carbon monoxide gas, based on a model using both the kinetics of the surface reactions and the diffusion of oxygen to the surface of the particles. For the majority of the configurations, better predictions of combustion efficiency were obtained with the twostream approach when compared to the experimental results than for the onestream PDF model.

* Scientist, Propulsion Group, Senior Member AIAA
† Scientist, Emerging Materials/Energetics Section
‡ Leader, Propulsion Group, Member AIAA
§ Propulsion Engineer, Rocket Technology Group
¶ Professor, Mechanical Engineering, Member AIAA
\# Graduate Student, Chemistry

INTRODUCTION

The Defence Research Establishment Valcartier (DREV) and Université Laval in Canada and the TNO Prins Maurits Laboratory (TNO-PML) in the Netherlands have collaborated to study the use of a solid fuel ducted rocket for missile propulsion. This type of motor has several advantages over solid fuel rocket motors including increased range, higher speed, and throttleability with only a limited increase in complexity. Once launched, the ducted rocket missile is accelerated to supersonic speed with the integrated rocket booster (Fig. 1). When the rocket propellant is completely burned at the end of the boost phase, the port covers that seal the air intakes from the ramjet combustor open and, simultaneously, the gas generator ignites. The effluent from the decomposition of the solid fuel in the gas generator is what acts as fuel for the ramjet phase of the flight. It includes gases and a substantial proportion of condensed phase material such as solid carbon. It is injected through the fuel inlet into the ramjet combustor where it is mixed with incoming air, reacts, and is accelerated through a nozzle to provide thrust.

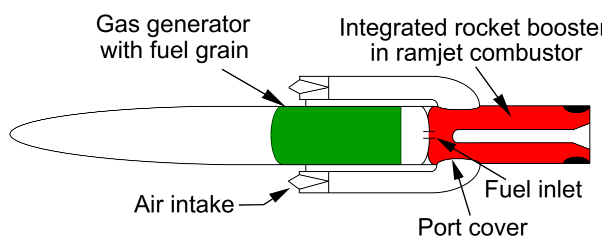

Figure 1 - Ducted rocket missile

A major focus of this work has been the ramjet combustor and to date has included water tunnel visualization, direct-connect combustion experiments, and CFD modelling of the non-reacting flow.[1,2] Reacting flow CFD modelling[3] has also been carried out with a onestream PDF model in which the gas generator exhaust, including gases and solid carbon, was injected into the combustor as a single homogeneous stream and assumed to react instantaneously with any oxidizer present. This approach, unfortunately, tended to overestimate the combustion efficiency when compared to the direct-connect experiments. To improve these predictions, a twostream PDF model was used with the gases and the solid carbon injected as two separate fuel streams. The solid stream was assumed to consist of 75-nm diameter carbon spheres which gradually decomposed into carbon monoxide, controlled mainly by surface oxidation, as they flowed through the combustor. The emphasis of this paper is therefore on the twostream PDF modelling methodology, and will be presented after descriptions of the combustor configurations and the direct-connect experiments. Results of the modelling will not only be compared with the experiments but also with the earlier onestream PDF modelling results.

COMBUSTOR CONFIGURATIONS

The basic geometry (Fig. 2) has dual inlets spaced 90^{o} apart circumferentially, with the main body of the combustor being 100 mm in diameter. The long air inlets would not be practical on a missile, but they were chosen specifically to facilitate testing and the characterization of the boundary conditions. For the direct-connect experiments the combustor was 458 mm long; any calculated efficiencies reported from the reacting flow CFD modelling was done for this combustor length. A converging/diverging nozzle was mounted at the end of the combustor only for the direct-connect tests; it was not modelled.

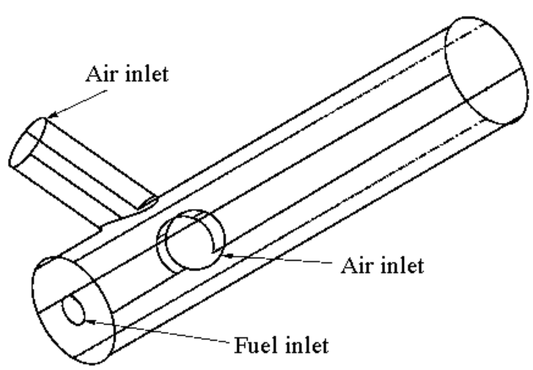

Figure 2 - Basic geometry

A schematic of the combustor configurations, including the fuel injector geometries, is shown in Fig. 3. The F1-18S fuel injector is similar to the F1-18 fuel injector except that it had its port on the same side as the air inlets rather than opposite to them. The basic geometries of the air injectors are presented in Table II. Two different dome heights as defined in Fig. 3, 57 and 100 mm, were used.

DIRECT-CONNECT COMBUSTION TESTS

Table III presents the geometries, as well as combustor pressure and characteristics of the air and fuel flows, of all the configurations that were tested in the direct-connect facility and for which the CFD combustion

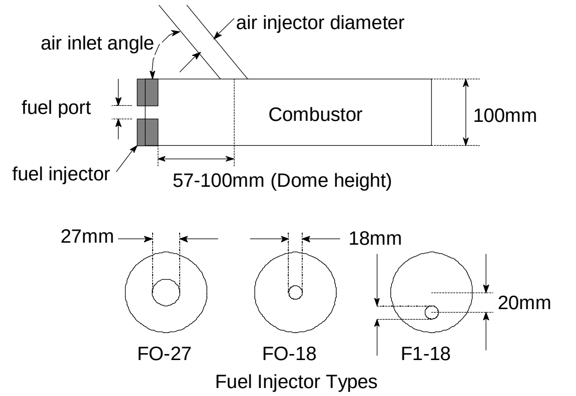

Figure 3 - Schematic of combustor and fuel injectors

TABLE II
Air injector geometries

Model	Air inlet angle	Air injector diameter
A2	60^{o}	38.1 mm
A4	60^{o}	50.8 mm
A6	90^{o}	50.8 mm

modelling was done. Apart from geometry, the previous water tunnel experiments and CFD modelling showed the importance of the momentum ratio of the air and fuel streams on the flowfield and the mixing; this key parameter is also listed.

All of the combustion experiments were carried out at TNO-PML's direct-connect test facility. High-pressure air was heated by a methane-fuelled vitiator to produce stagnation conditions at the combustor representative of those downstream from the air intakes of an actual missile flying at Mach 2.5 and 6000 m altitude (0.5 MPa and 600K). Additional oxygen was injected at the vitiator to replace that used for the combustion of the methane. A plenum of 0.5-m internal diameter surrounded the air injector to distribute the air as evenly as possible through each of its arms (Fig. 4). This arrangement was chosen to facilitate the changing of the air and fuel injectors and the nozzle at the end of the combustor.

For the solid fuel in the gas generator, a formulation of 90% by mass glycidyl azide polymer (GAP) and 10% carbon was specified and developed. Some direct-connect tests were carried out with this solid fuel, but its mass flow rate proved to be difficult to control and characterize to a sufficient degree of accuracy for these purposes. In the correct proportions, however, the calculated equilibrium exhaust properties of an ethylene/air mixture can be close to those of the GAP/Carbon solid fuel.[4] Since the mass flow rates of the ethylene and the air were controlled and measured in the same way as the vitiator gases, the boundary conditions of the effluent injected through the fuel inlet could be estimated with more confidence. All of the results presented here therefore use the ethylene/air mixture as the fuel.

TABLE III
Combustor configurations

No	Air Injector	Fuel Injector	Dome Height mm	Air/fuel Momentum Ratio	Air/fuel Mass Ratio	Combustor Pressure MPa	Fuel Velocity m/s	Air Velocity m/s
1	A4	F0-27	57	2.62	7.79	0.396	416	140
2	A4	F0-27	57	11.73	15.73	0.403	328	245
3	A4	F0-27	57	8.89	13.84	0.875	282	181
6	A2	F0-27	57	3.90	7.09	0.411	443	244
7	A2	F0-27	57	19.43	15.76	0.426	311	384
8	A2	F0-27	57	17.94	14.96	0.944	239	287
9	A2	F0-27	57	3.52	6.70	0.845	609	320
11	A4	F0-18	57	4.87	15.36	0.432	710	225
12	A4	F1-18	57	4.07	13.96	0.907	600	175
13	A6	F0-27	57	2.30	7.00	0.44	436	143
14	A6	F0-27	57	10.80	15.33	0.419	324	229
15	A6	F0-27	57	5.20	10.66	0.904	358	175
16	A6	F0-27	57	2.37	7.11	0.8	599	200
18	A4	F0-27	100	2.13	6.65	0.397	501	160
19	A4	F0-27	100	10.93	15.35	0.423	317	226
20	A4	F0-27	100	8.31	13.34	0.882	288	179
21	A4	F0-27	100	2.76	7.62	0.792	564	205
28	A4	F1-18	57	4.84	15.32	0.44	692	219
29	A4	F0-18	57	4.42	14.54	0.917	568	173
30	A4	F1-18S	57	4.29	14.34	0.921	579	173

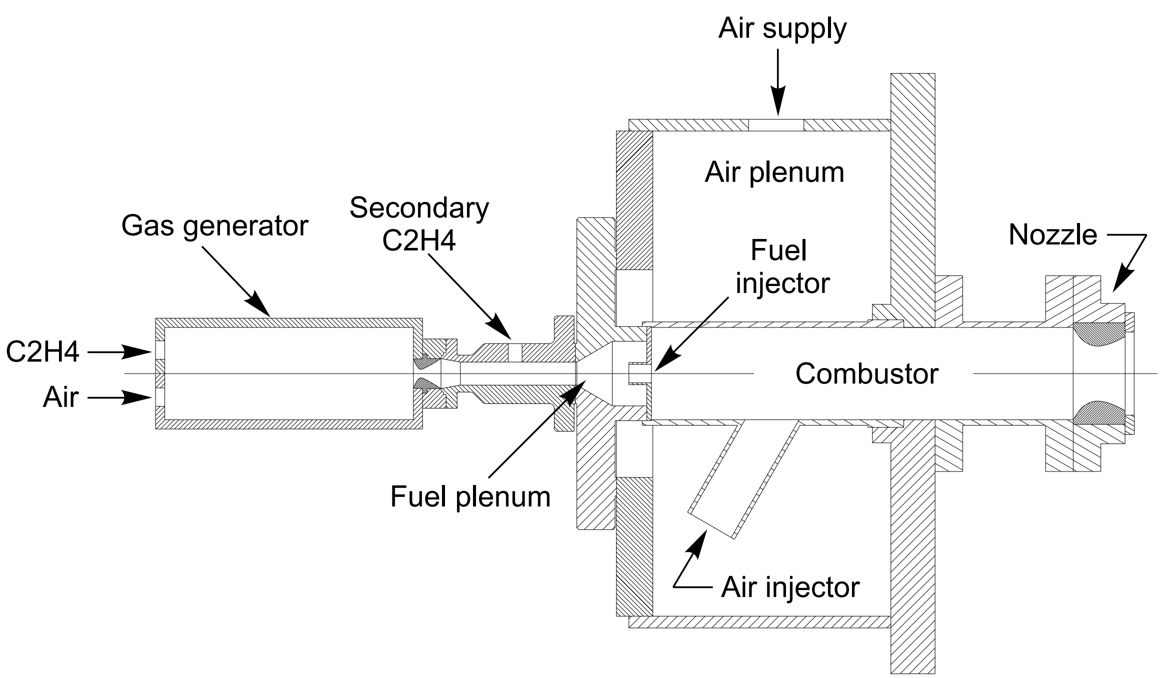

Figure 4 – Direct-connect test hardware

However, while an actual solid fuel must decompose by itself inside the gas generator once ignited, the mixture of ethylene and air is much too rich to react at the conditions present. About 10% of the ethylene is therefore injected into the head of the gas generator where it reacts with the air in a combustible mixture, and the remainder is injected into the transition assembly where it can react with the hot exhaust from the gas generator. The main assumption here, of critical importance to the reacting flow CFD modelling, is that conditions are appropriate to allow the mixture to approach thermochemical equilibrium before being injected into the combustor. Another important point for the CFD modelling is that flow of the reacted ethylene/air mixture is not choked in the fuel inlet before entering the ramjet combustor; the fuel plenum pressure is only slightly higher than the combustor. As to be explained later, this means that the flow can be approximated as being incompressible.

CFD MODELLING

CFD modelling was carried out using a code known as FLUENT (Version 5). A control-volume-based technique is used within FLUENT to discretize the conservation equations for mass and momentum, otherwise known as the Navier-Stokes equations. If required, additional equations for turbulence, species, energy, radiation, and particle tracking can be solved. The segregated solver option was used which means that the governing equations are solved sequentially. All geometries were modelled as precisely as possible with structured grids of approximately 50,000 hexahedral cells (Fig. 5) for half the domain (symmetrical about the central longitudinal plane).

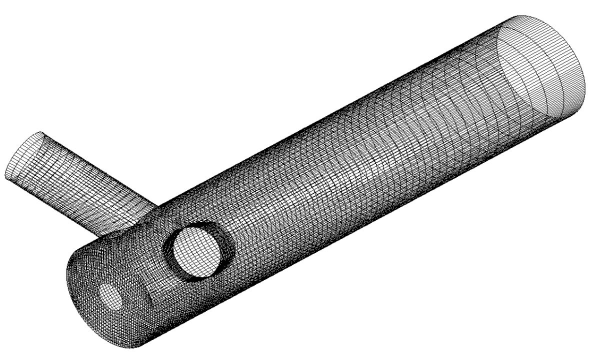

Figure 5 - Surface mesh of basic combustor geometry

Flow in a ducted rocket combustor can be characterized as highly turbulent (Reynolds numbers on the order of 10^6). The Renormalized Group Theory (RNG) model was chosen to model the turbulence since it gives better results than the k-ε model for the recirculating, swirling, and separated flow that occurs within a ramjet combustor. An equilibrium-chemistry Probability Density Function approach[5] was chosen to model the reacting flow in the ducted rocket combustor. It is well suited for problems where the fuel and oxidizer inlet streams are separate and the combustion is controlled by turbulent mixing rather than the kinetics of the chemical reactions. With the use of β-shaped PDF's, properties of the reacted mixture anywhere in the combustor can be determined by solving two additional transport equations for the mixture fraction and its variance for each fuel stream. For this approach to give good results, temperatures in the combustor must be high enough so that the characteristic chemical reaction time is short compared to the characteristic mixing time; this is also necessary for the equilibrium chemistry assumption to be valid.

A restriction in FLUENT's implementation of the PDF approach in Version 5 is that the flowfield must be modelled as being incompressible. This is a good assumption in most of the combustor since the Mach number is less than 0.3 almost everywhere. There are exceptions, though. One is the nozzle; it has intentionally not been modelled. The other exceptions are in the air and fuel inlets where the calculated flow velocities exceed the Mach 0.3 limit for some of the configurations. However Spalding[6] states that even flow velocities of up to Mach 0.8 need not be reproduced exactly between a model and a prototype combustor. This implies that the flow in the inlets can be treated as incompressible as long as this higher limit is respected (it has been exceeded slightly in only a couple of instances for the unchoked flow in the fuel inlets).

BOUNDARY CONDITIONS

As previously indicated, the direct-connect hardware and experiments were intentionally set up in such a way to facilitate the characterization of the boundary conditions for the CFD modelling. For the air inlets, the tubes were lengthened as much as possible within the air plenum and honeycomb installed to straighten the flow and produce a uniform velocity profile at the combustor. Mean velocities at the entrance to the air inlet tubes were calculated from the measured vitiated air mass flow rate and composition, air plenum temperature, and combustor pressure during the direct-connect experiments. While most ramjets with side-mounted inlets have curved inlet ducts, the velocity profiles downstream from these curves depend heavily on the exact geometry. Laser Doppler Velocimetry (LDV) measurements of flow within a plexiglass model of a curved inlet duct[7], also supplied with air from a large chamber, showed a uniform velocity profile uniform in the lengthy (370 mm) horizontal portion of the duct upstream of the curve, but non-uniform downstream from it. A CFD study of a ducted rocket combustor that included a curved inlet diffuser[8] predicted a uniform velocity profile downstream from the normal shock but upstream of the curve in the duct, and non-uniformity downstream from it. Therefore, since the air inlet tubes are straight, the desired uniform velocity profiles can be expected throughout, so this should be a good assumption at the air inlet entrances for the CFD modelling.

Because the air from the vitiator arrives at the air plenum in a small-diameter pipe and is suddenly dumped, its turbulence level is likely high. Since no measurements of the turbulence characteristics of the air entering the inlets could be made, estimates of a turbulence intensity of 10% and a turbulence characteristic length of 25% of the air inlet tube diameter were made for the CFD modelling.

Characterizing the fuel inlet boundary conditions is much more challenging. As for the air inlets, a constant velocity profile at the fuel inlet was assumed, along with a turbulence intensity of 10% and a turbulence characteristic length 25% of the fuel inlet diameter. For all configurations, measured data from the direct-connect tests, including pressures and temperatures, were used to calculate the measured flow rates and mixture ratio for the ethylene and vitiated air. Table IV shows the equilibrium exhaust compositions, calculated with the CET89 thermochemical equilibrium code,[9] of an ethylene/air mixture (1.3823 air/fuel ratio) expanded from a chamber pressure of 1.175 MPa to the ramjet combustor pressure of 0.5 MPa. The critical assumption is that thermochemical equilibrium is reached in the fuel plenum. The best way to validate this assumption is to directly sample the gases within the fuel plenum and analyze them with gas chromatography, but unfortunately attempts to do this have not yet been successful. However, exhaust temperature measurements made on small GAP/Carbon solid fuel gas generators[10] suggested that thermochemical equilibrium being reached in the gas generator chamber was a good possibility. If the GAP/Carbon fuel is likely in thermochemical equilibrium within its gas generator, so should be the more reactive ethylene/air mixture. Furthermore, although the sampling and characterization of the gases was not successful for the ethylene/air mixture, there was a significant amount of solid carbon observed, as predicted by CET89. This solid carbon was in the form of soot particles, and its presence supports the assumption that equilibrium has been reached in the fuel plenum.

TABLE IV

Calculated gas generator exhaust properties

Oxidizer/fuel ratio 1.3823

	Gas generator chamber conditions	Fuel plenum conditions, equilibrium
Pressure [MPa]	1.175	0.5
Temp [K]	1274.33	1132.07
Mass fraction AR	0.00829	0.00828
Mass fraction CH4	0.02354	0.02786
Mass fraction CO	0.24107	0.21598
Mass fraction CO2	0.00519	0.01329
Mass fraction HCN	0.00008	0.00002
Mass fraction H2	0.05421	0.05208
Mass fraction H2O	0.01095	0.02043
Mass fraction NH3	0.00029	0.00022
Mass fraction N2	0.41620	0.41628
Mass fraction C(GR)	0.24020	0.24555
Total	1	1

TWO PHASE FLOW

For the combustion modelling results previously reported,[3] the boundary conditions for each experiment were used to generate single fuel stream PDF data. This means that all of the fuel, including both the gaseous and solid phases, was injected into the combustor as a single homogeneous stream. The solid carbon was therefore assumed to react instantaneously, as were the gases, once there was any oxidizer present. While a few of the calculated temperature-based combustion efficiencies with the "onestream" PDF were in agreement with the experimental results, most of them were higher. However, brilliant orange-yellow exhaust plumes, a likely indication of soot particles and incomplete combustion, were observed for some of the direct-connect experiments. This indicates that the soot particles were too large to be assumed to react instantaneously, and this can explain the overestimation of the combustion efficiencies. Therefore, by using a two fuel stream PDF approach,[5] with separate gaseous and solid phase streams, along with a model to describe the flow paths and decomposition of the solid carbon soot, improvements to the estimates of the calculated combustion efficiencies were possible.

The first step to develop a model to describe the motion and decomposition of the particles was to collect and measure some of the solid material during an actual direct-connect combustion experiment. This was accomplished by trapping some of the material from the fuel plenum in an in-line filter. This material was then dispersed in some ethanol using an ultrasonic bath and analyzed in a Malvern Mastersizer 2000. The resulting size distribution, which assumes that the particles are spherical, is shown in Fig. 6. A wide range of particles is indicated, from below 0.1 to above 200 μm.

Soot from typical hydrocarbon/air combustion consists of minute carbon spheres usually less than 60 nm

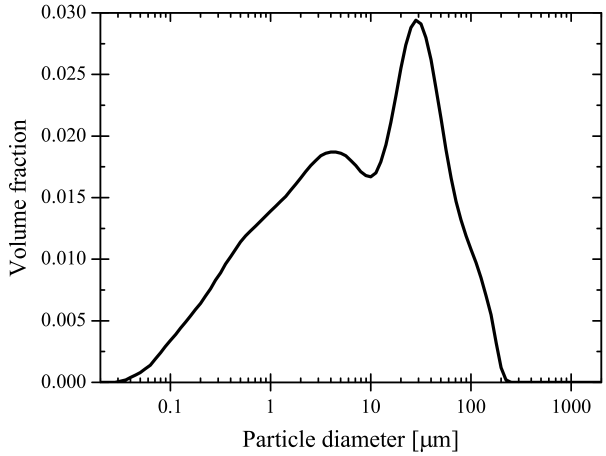

Figure 6 – Particle size distribution, ethylene/air soot

in diameter. These spheres are grouped together as much larger agglomerates that can be as large as several microns.[11] A scanning electron microscope (SEM) image of the soot collected from the fuel plenum of the reacted ethylene/air mixture is presented in Fig. 7. It shows that the majority of the particles present are composed of spheres of about 75 nm in diameter, close to that usually reported for soot from typical hydrocarbon flames.

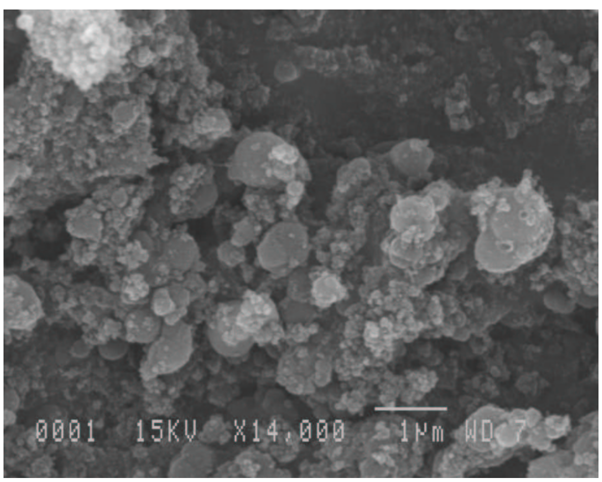

Figure 7 – SEM picture of the ethylene/air soot

While the trajectories of the particles are closely related to their mass and overall dimensions, their decomposition is a function of their total surface area exposed to the oxidizer. This total surface area is related more to the number and diameter of the minute spheres that make up each soot particle rather than the overall size of the particle. To determine the sensitivity of the size of the particles on their trajectories, twostream PDF modelling (with the particle model described below) for configuration 1 was carried out for a wide range of particle sizes. The trajectories of the particles injected from the fuel inlet hole were calculated using a Lagrangian reference frame[5] and stochastic particle tracking so that the effects of turbulent fluctuations from the flowfield were included. The continuous phase flowfield and dispersed (solid) phase calculations were coupled, meaning that not only did the flowfield affect each particle's trajectory and decomposition, but each particle could also affect the flowfield.

The results for the trajectories of these various particle sizes and how much they decompose are shown in Fig. 8. In the side views of the trajectories, the particles from 1 nm to 1 μm diameter appear to fill the bottom half of the combustor and abruptly change direction when deflected by the incoming air jets. The 10 and 100 μm particles, however, do not seem to follow the flow as faithfully and take much straighter trajectories toward the end of the combustor. The isometric views show that the ensembles of trajectories for particles smaller than 10 μm are similar. The particle trajectories are coloured by particle density that changes as the particles decompose, and it can be seen that the smaller the particle is, the faster it decomposes. In fact, for the 1-nm particles, about half decompose completely before reaching the end of the combustor. About 10-20% of the 10 nm particles and less than 5% of the 75 nm particles decompose completely before the end of the combustor. For particle diameters of 1 μm and above, all of the particles leave the combustor before they decompose completely.

The results from Fig. 8 therefore imply that the all of the particles can be modelled as 75 nm spheres with little consequence on their average trajectories, particularly for those from 1 nm to over 1 μm in diameter. This is probably valid for the larger particles as well. Figure 6 shows the existence of many particles with overall diameters of 10 μm and larger, but Fig. 7 shows that they must be made up of agglomerates of much smaller spheres. Their aerodynamic drag would therefore be much higher than spheres of equivalent overall diameter, so then particles of even several microns in diameter could be expected to follow the flow as well as the 1 μm diameter and smaller particles. Furthermore, because they are agglomerates, they likely break up as well.

A kinetics/diffusion model in FLUENT[5] was used to describe the decomposition of the carbon particles. The change in mass of the particles is described by:

$$\frac{dm_p}{dt} = -\pi d_p{}^2 \frac{\rho R T m_o}{Mo} \frac{R_1 R_2}{R_1 + R_2}$$

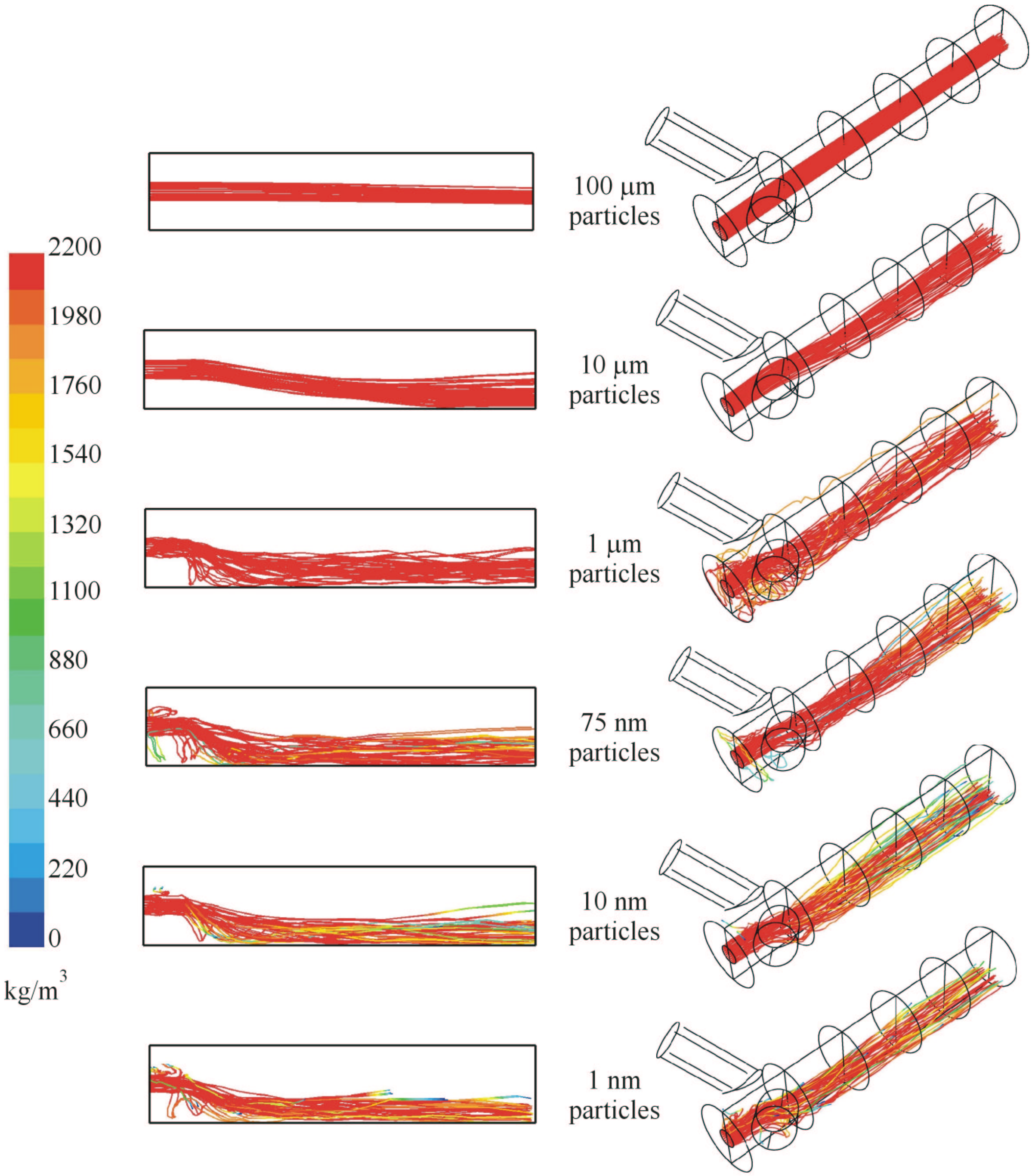

Figure 8 – Particle trajectory versus diameter, side and isometric views, coloured by particle density

where m_p is the mass of the particle and d_p is its diameter, ρ and T are the density and temperature of the surrounding gas, R is the Universal Gas Constant, m_o and M_o are the mass fraction and the molecular mass of the oxidant in the surrounding gas near the particles, and R_1 and R_2 are the diffusion controlled and the surface kinetics controlled rates respectively. The diffusion controlled decomposition rate is derived from an expression for pulverized coal particles over a wide range of temperatures where the particles give off carbon monoxide rather than carbon dioxide:[12]

$$R_1 = C_1 \frac{\left[\left(T_p + T_\infty\right)/2\right]^{0.75}}{d_p}$$

where C_1 is 4.993868X10^{-12} kg/(m·s·Pa·K$^{0.75}$), and T_p and T_∞ are the temperatures of the particle and the surrounding gas. The kinetics of the surface reaction come from an approximation[13] to the Nagel-Strickland-Constable formula for soot oxidation[14] at temperatures below approximately 2000K:

$$R_2 = C_2 \exp\left(-E / RT_p\right)$$

where C_2 is 1.11531X10^{-3} kg/(m^{2}s·Pa) and E is the activation energy, 1.42537X10^8 J/kg-mol, of the surface reaction. As the particle gets very small, the diffusional rate R_1 becomes very large, and the decomposition of the particles becomes controlled by the surface reaction rate. For particles of 75-nm diameter, the decomposition is essentially controlled by the surface reaction rate.

An important feature of the particle decomposition model is that rather than having each particle decrease in diameter as its mass decreases, the diameter remains the same while the density decreases. The particle therefore becomes more porous. Also, approximately 500 particles had to be injected every 10 flowfield iterations to attain a "quasi-steady" state and convergence after several hundred iterations. (For clarity, Fig. 8 shows the paths of only 30 of these particles.)

RESULTS

The purpose of the twostream PDF model was to more accurately model the distribution and decomposition of the solid carbon in the gas generator exhaust and hopefully reduce the overprediction of the temperatures that occurred with the onestream model. The success of this approach will be shown later. An example of how the twostream model can change the distribution of temperature in the combustor is shown in Fig. 9. In configuration 1, the twostream model shows a less intense, but more diffuse release of energy on the centreline plane right near the head end of the combustor. Further downstream, however, the temperatures are higher for the twostream model in the lower half of the combustor than for the onestream model.

To show the improvement of the twostream model over the onestream model in predicting combustor performance, the results were compared with the results from the direct-connect experiments for all configurations listed in Table III. The chosen measure to express combustor performance is the efficiency based on temperature rise in the combustor:

$$\eta_{\Delta T} = \frac{T_{t4,\exp} - T_{t2}}{T_{t4,theo} - T_{t2}}$$

For the direct-connect experiments, the combustion efficiency was estimated using the methods recommended by AGARD.[15] T_{t2} is the air inlet stagnation temperature, and $T_{t4,exp}$ is the stagnation temperature at the end of the combustor. $T_{t4,exp}$ is determined from static pressure measurements in the combustor and calculations of theoretical temperatures and characteristic velocities from the CET89 thermochemical equilibrium combustion

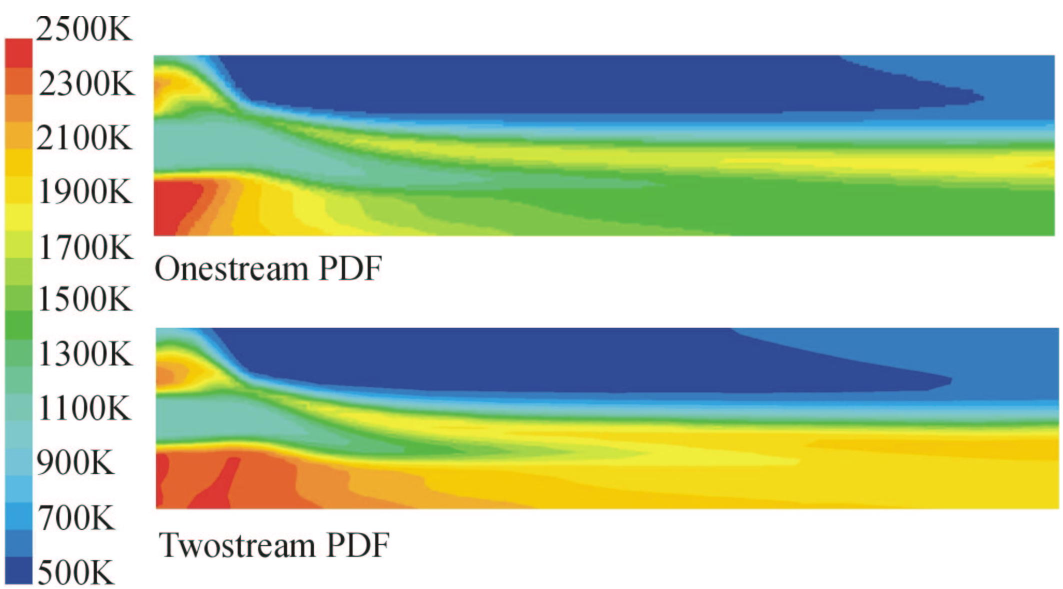

Figure 9 – Temperature distribution on the centreline plane for onestream and twostream PDF models, configuration 1

code. For the CFD results, $T_{t4,exp}$ is the mass-averaged stagnation temperature at the 458 mm cross-section of the combustor to correspond with the length of the combustor for the direct-connect experiments. For both the direct-connect and CFD results, $T_{t4,theo}$ is calculated from CET89 using the static pressure in the combustor, the nozzle entrance-to-throat area ratio and the compositions, temperatures, and mass flow rates of the vitiated air and gas generator exhaust as inputs. The average uncertainty for the direct-connect tests is estimated to be +/-13% of the value given for the combustion efficiency.

Figure 10 shows the calculated temperature-based combustion efficiency results for the experiments and the onestream and twostream PDF models. Under careful scrutiny, the onestream PDF model can be seen to overpredict combustion efficiency for several of the configurations, as previously reported.[3] However, the twostream PDF model improves the prediction of combustion efficiency for most of the configurations. In fact, the average difference between the twostream and experimental results is 16%, or nearly the same as the experimental uncertainty, while it is 27% between the onestream and experimental results. Furthermore, with the twostream model exactly half of the configurations are overpredicted and the remainder underpredicted, rather than being consistently overpredicted as with the onestream model.

While the twostream PDF model improves the agreement between the experiments and the predictions significantly over the onestream PDF model, there are still large differences in the results for some of the configurations. An explanation for this may be the fact that the CFD modelling gives a time-averaged output of the flowfield, whereas the flowfield in the experimental combustor is unsteady and results in pressure oscillations that are not considered in the model. These oscillations have now been properly measured using piezoelectric pressure transducers, sampled at 80 kHz, which were flush mounted to the inner combustor wall. Figure 11 shows the magnitude of the pressure oscillations from one of the transducers versus time. The magnitude of the pressure oscillations due to flow noise, about 50 kPa, can be seen before the spike from the ignition of the gas generator that occurs at 3.0 s. Shortly afterwards at about 3.3 s, the fuel-rich exhaust from the gas generator and the vitiated air ignites in the ramjet combustor, and the pressure oscillations are about 100 kPa in magnitude. Given that the average static pressure in the combustor for this test was 0.42 MPa, the magnitude of the pressure oscillations is indeed significant.

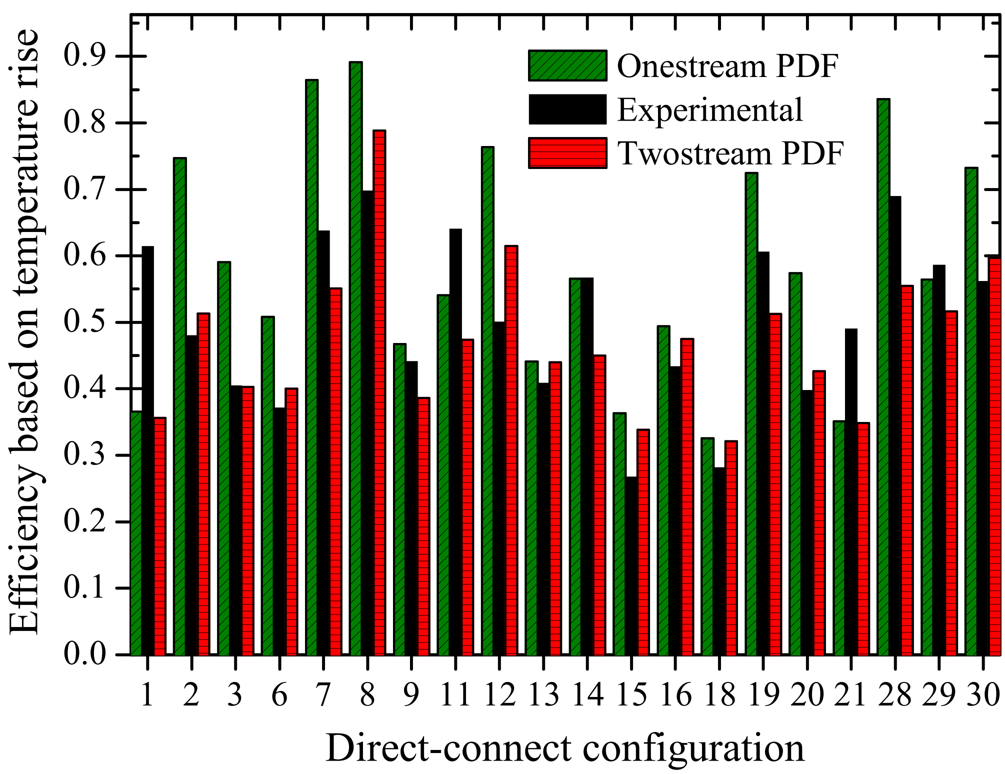

Figure 10 – Comparison of efficiencies based on temperature rise between CFD modelling and direct-connect experiments

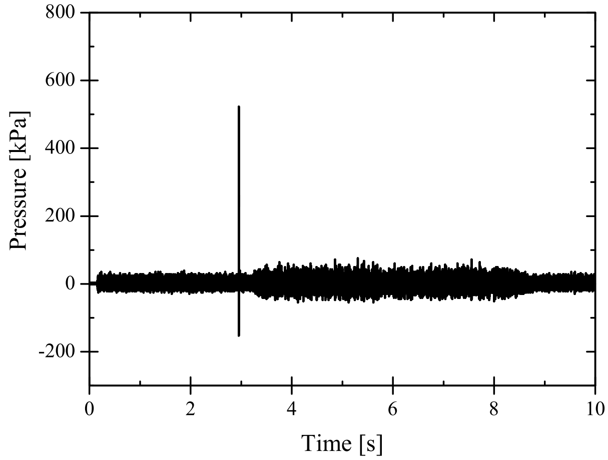

Figure 11 - Pressure variation versus time

While the magnitude of the oscillations obviously changes before and after ignition of the mixture in the ramjet combustor, Fast Fourier Transform (FFT) analysis of the signal was done at one-second intervals to see if the frequencies of the oscillations and the magnitude of each frequency also change. At 2.0 s, before ramjet ignition, Fig. 12 shows that there are two significant frequencies at 520 and 2890 Hz. Figure 13 shows an FFT at 6.0 s, well after ramjet ignition, and the frequencies and magnitudes have changed significantly. There are dominant frequencies at approximately 250, 800, 920, 1500, 2420, and 4820 Hz, some of which may be harmonics of the others. The magnitude of the lowest frequency component has also doubled with respect to the 520 Hz peak at 2.0 s.

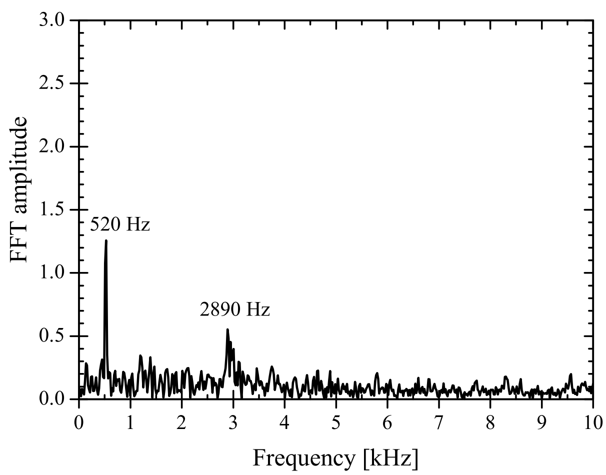

Figure 12 - FFT amplitude versus frequency at 2.0 s

Apart from showing that the combustor pressure oscillations can be significant, these data have demonstrated that the magnitude and frequency of the pressure oscillations change when combustion occurs in the ramjet, and that there is a strong possibility that they are coupled to the combustion processes taking place. The effect of these pressure oscillations on combustor performance has not been considered in the CFD modelling, and therefore may help explain differences between the experimental and predicted results. While time-dependent CFD modelling is possible in theory and could take these oscillations into account, this type of modelling would not have been practical for the three-dimensional, turbulent reacting flowfield of interest here.

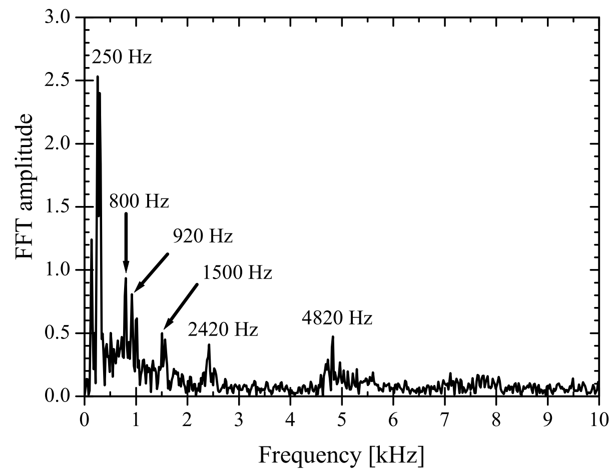

Figure 13 - FFT amplitude versus frequency at 6.0 s

CONCLUSIONS

Modelling the combustion using a twostream PDF model rather than a onestream PDF model improved predictions of temperature-based combustion efficiency significantly. The average difference between the twostream model predictions with the direct-connect experimental results was 16%, or slightly higher than the experimental uncertainty. For the onestream PDF model, this difference was 27%.

Not properly modelling pressure oscillations in the combustor may account for not being able to predict combustion efficiency accurately for some of the configurations. Pressure oscillations of 25% of the mean static pressure in the combustor were recorded, and FFT analyses revealed that they might be coupled to the combustion processes.

The use of the twostream PDF model results in a change of the temperature distribution in the combustor when compared to that of the onestream model.

REFERENCES

1. Stowe, R.A., De Champlain, A., Mayer, A.E.H.J., and Niemeijer, S.F., “Modelling and Flow Visualization of Mixing in a Ducted Rocket Combustor”, AIAA-98-3768, 1998.
2. Mayer, A.E.H.J. and Stowe, R.A., “Experimental Study Into Mixing in a Solid Fuel Ducted Rocket Combustion Chamber”, AIAA-2000-3346, 2000.
3. Stowe, R.A., De Champlain, A., and Mayer, A.E.H.J., “Modelling Combustor Performance of a Ducted Rocket”, AIAA-2000-3728, 2000.
4. Dijkstra, F., “Conceptual Design of a Ducted Rocket Combustor”, Thesis A2R-P21, Delft University of Technology, Faculty of Aerospace Engineering, The Netherlands, 23 July 1993.
5. *FLUENT 5 User's Guide*, Fluent Inc., Lebanon, New Hampshire, U.S., July 1998.
6. Spalding, D.B., “The Art of Partial Modeling”, in *Ninth Symposium on Combustion*, pp 833-843, Academic Press, London, U.K., 1963.
7. Liou, T.M. and Liao, C.C., “Flows in a Curved Combustor Inlet With and Without a Guide Vane”, Journal of Propulsion and Power, Vol. 11, No. 3, May-June 1995.
8. Hsieh, S.Y., Yang, V., Cherng, D.L., and Yang, H.T., “A Unified Flow Analysis of Ramjet Propulsion Systems”, AIAA-94-3326, 1994.
9. McBride, B.J., “CET89 - Chemical Equilibrium with Transport Properties”, Cosmic Program LEW-15113, Lewis Research Center, 1989.
10. Stowe, R.A., Dubois, C., Smithson, T., and De Champlain, A., “Preliminary Exhaust Characterization of a GAP/Carbon Ducted Rocket Fuel”, 24th Meeting of The Technical Cooperation Program, Technical Panel WPN/TP-4 Workshop, NSWC, Indian Head, Maryland, U.S., 15-16 April 1999.
11. Faeth, G.M. and Köylü, Ü.Ö., "Soot Morphology and Optical Properties in Nonpremixed Turbulent Flame Environments", Combustion Science and Technology, Vol. 108, pp. 207-229, 1995.
12. Field, M.A., “Rate of Combustion of Size-Graded Fractions of Char from a Low Rank Coal between 1200K - 2000K”, Combustion and Flame, Vol. 13, pp. 237-252, 1969.
13. Glassman, I., *Combustion*, Second Edition, Academic Press, Orlando, Florida, U.S., 1987.
14. Nagel, J., Strickland-Constable, R.F., "Oxidation of Carbon Between 1000-2000^{o}C", Proceedings of the Fifth Conference on Carbon, London, 1962.
15. Advisory Group for Aerospace Research and Development, “Experimental and Analytical Methods for the Determination of Connected-Pipe Ramjet and Ducted Rocket Internal Performance”, Propulsion and Energetics Panel Working Group 22, AGARD-AR-323, 1994.

INTERNAL DISTRIBUTION

DREV TR 2001-200

(Bound paper copies unless otherwise noted)

1	-	Director General
1	-	Deputy Director General
6	-	Document Library
1	-	Head, Precision Weapons Section
1	-	Head, Emerging Materials/Energetics Section
1	-	Head, Weapon Effects Section
2	-	Dr. R.A. Stowe (author, 1 CD and 1 bound paper copy)
1	-	Dr. A. De Champlain
1	-	Mr. P.G. Harris
1	-	Mr. R. Farinaccio
1	-	Ms. S. Ringuette
1	-	Lt. C.E. Galligan
1	-	Mr. P. Twardawa
1	-	Dr. C. Dubois
1	-	Dr. J. Rapanotti

EXTERNAL DISTRIBUTION

DREV TR 2001-200

(CD copies unless otherwise noted)

2	-	DRDKIM (1 CD and 1 unbound paper copy)
1	-	DRDB
1	-	DSTM
1	-	DSTL
1	-	DSTA
1	-	DAR 5
1	-	Dr. J. Margetson Defence Research Consultancy Ltd Roundwood Farm Barton Hartshorn Bucks MK18 4JS United Kingdom
1	-	Dr. M.F. Bardon Royal Military College of Canada Department of Mechanical Engineering Kingston, ON K7K 7B4
1	-	Dr. J.E.D. Gauthier Carleton University Dept. of Mechanical and Aerospace Engineering 1125 Colonel By Drive, Ottawa, ON K1S 5B6
1	-	Dr. G.M.H.J.L. Gadiot Netherlands Agency for Aerospace Programmes Market Research & Strategy Division Kluyverweg 1 PO Box 35 2600 AA DELFT The Netherlands
5	-	Mr. R. Calzone (4 CD's and 1 bound paper copy) TNO Prins Maurits Laboratory Group Rocket Technology PO Box 45 2280 AA Rijswijk The Netherlands

1 - Mr. Mark Ivey
DSTL Integrated Systems
Guided Weapon Propulsion
Building A2
Ively Road
Farnborough, Hampshire
GU14 OLX
United Kingdom

1 - Dr. Keith Atkinson
QinetiQ
Cody Technology Park
Building A57
Ively Road, Farnborough
Hampshire GU14 0LX
United Kingdom

1 - Mr. R.B. Norris
AFRL/PRA Bldg 18
1950 Fifth Street
Wright-Patterson AFB OH 45433-7251
USA

1 - Dr. K. Thalassoudis
Defence Science and Technology Organisation
Weapons Systems Division
PO Box 1500
Edinburgh, SA 5111
Australia

1 - Mr. Rod Keyser
Manager: Rocket Propulsion
Somchem Division of DENEL
PO Box 187
Somerset West
7130
Rep. of South Africa

DOCUMENT CONTROL DATA

1. ORIGINATOR (name and address) Defence Research Establishment Valcartier 2459 Pie XI Blvd. North Val-Bélair, QC G3J 1X5	2. SECURITY CLASSIFICATION (Including special warning terms if applicable) Unclassified

3. TITLE (Its classification should be indicated by the appropriate abbreviation (S, C, R or U)
Performance Prediction of a Ducted Rocket Combustor

4. AUTHORS (Last name, first name, middle initial. If military, show rank, e.g. Doe, Maj. John E.)
Stowe, Robert A.

5. DATE OF PUBLICATION (month and year) November 2001	6a. NO. OF PAGES 274	6b. NO. OF REFERENCES 88

7. DESCRIPTIVE NOTES (the category of the document, e.g. technical report, technical note or memorandum. Give the inclusive dates when a specific reporting period is covered.)
DREV Technical Report (Doctoral Thesis, Université Laval)

8. SPONSORING ACTIVITY (name and address)

9a. PROJECT OR GRANT NO. (Please specify whether project or grant) 3eb13	9b. CONTRACT NO.
10a. ORIGINATOR'S DOCUMENT NUMBER DREV TR 2001-200	10b. OTHER DOCUMENT NOS N/A

11. DOCUMENT AVAILABILITY (any limitations on further dissemination of the document, other than those imposed by security classification)

- [x] Unlimited distribution
- [ ] Contractors in approved countries (specify)
- [ ] Canadian contractors (with need-to-know)
- [ ] Government (with need-to-know)
- [ ] Defense departments
- [ ] Other (please specify)

12. DOCUMENT ANNOUNCEMENT (any limitation to the bibliographic announcement of this document. This will normally correspond to the Document Availability (11). However, where further distribution (beyond the audience specified in 11) is possible, a wider announcement audience may be selected.)

13. ABSTRACT (a brief and factual summary of the document. It may also appear elsewhere in the body of the document itself. It is highly desirable that the abstract of classified documents be unclassified. Each paragraph of the abstract shall begin with an indication of the security classification of the information in the paragraph (unless the document itself is unclassified) represented as (S), (C), (R), or (U). It is not necessary to include here abstracts in both official languages unless the text is bilingual).

The ducted rocket is a supersonic flight propulsion system that takes the exhaust from a solid fuel gas generator, mixes it with air, and burns it to produce thrust. To develop such systems, the use of numerical models based on Computational Fluid Dynamics (CFD) is increasingly popular, but their application to reacting flow requires specific attention and validation. Through a careful examination of the governing equations and experimental measurements, a CFD-based method was developed to predict the performance of a ducted rocket combustor. It uses an equilibrium-chemistry Probability Density Function (PDF) combustion model, with a gaseous and a separate stream of 75 nm diameter carbon spheres to represent the fuel. After extensive validation with water tunnel and direct-connect combustion experiments over a wide range of geometries and test conditions, this CFD-based method was able to predict, within a good degree of accuracy, the combustion efficiency of a ducted rocket combustor.

Le statofusée est un système de vol à propulsion supersonique qui prend l'échappement d'un générateur à gaz, le mélange avec de l'air, et le fait réagir dans un foyer de combustion à statoréacteur afin de produire de la poussée. Pour développer ces systèmes, des modèles numériques basés sur la simulation numérique des fluides (CFD) sont devenus très populaires, mais leur développement pour les écoulements réactifs pose toujours un défi important, et il faut porter attention à chaque application et bien la valider. Par une étude approfondie des lois qui régissent la dynamique des fluides et la combustion, et des données expérimentales, une méthode basée sur le CFD a été développée pour prédire la performance du foyer de combustion d'un statofusée. Elle utilise un modèle de combustion préconisant l'équilibre chimique mais avec une fonction de densité des probabilités (PDF) pour tenir compte de l'influence de la turbulence, pour deux écoulements de carburant, l'un qui est gazeux et l'autre qui est qui est composé des sphères solides en carbone de diamètre de 75 nm. Après avoir validé la méthode avec la visualisation dans un tunnel à eau et des expériences de combustion à connexion-directe pour beaucoup de géométries et de conditions variées, cette méthode basée sur le CFD pouvait prédire, avec une bonne précision, le rendement de combustion dans le foyer d'un statofusée.

14. KEYWORDS, DESCRIPTORS or IDENTIFIERS (technically meaningful terms or short phrases that characterize a document and could be helpful in cataloguing the document. They should be selected so that no security classification is required. Identifiers, such as equipment model designation, trade name, military project code name, geographic location may also be included. If possible keywords should be selected from a published thesaurus, e.g. Thesaurus of Engineering and Scientific Terms (TEST) and that thesaurus-identified. If it is not possible to select indexing terms which are Unclassified, the classification of each should be indicated as with the title.)

ducted rocket
ramrocket
water tunnel
Computational Fluid Dynamics, CFD
ramjet
solid fuel
gas generator
mixing
combustor
direct connect
airbreathing propulsion
missile
Probability Density Function, PDF
GAP
Glycidyl Azide Polymer
soot
oxidation
particle decomposition model
FLUENT
scaling